

APPLICATION OF LASER-BASED DIAGNOSTICS FOR
NANOMATERIALS SYNTHESIS

By

XIAOFEI LIU

A Dissertation submitted to the
Graduate School-New Brunswick
Rutgers, The State University of New Jersey
in partial fulfillment of the requirements

for the degree of

Doctor of Philosophy

Graduate Program in Mechanical and Aerospace Engineering

Written under the direction of

Professor Stephen D. Tse

and approved by

New Brunswick, New Jersey

October, 2009

ABSTRACT OF THE DISSERTATION

APPLICATION OF LASER-BASED DIAGNOSTICS FOR NANOMATERIALS SYNTHESIS

By XIAOFEI LIU

Dissertation Director:
Professor Stephen D. Tse

Spectroscopic laser-based diagnostics are applied in the gas-phase synthesis of nanostructured materials to make non-intrusive, *in-situ*, spatially-precise measurements of gas-phase temperatures and relevant chemical species. For the nanomaterials themselves, a novel application of Raman spectroscopy is developed to characterize nanoparticles *in-situ*, during flame and plasma synthesis. As result, the local conditions for gas-phase synthesis can be determined for a given nanomaterial property, so that fundamental mechanisms can be revealed and process conditions can be optimized.

The synthesis configurations investigated in this work are (i) the inverse co-flow diffusion flame (IDF), (ii) the counter-flow diffusion flame (CDF), (iii) the low-pressure burner-stabilized premixed stagnation-point flame, and (iv) the inductively-coupled plasma (ICP) impinging on a cold substrate.

Spontaneous Raman spectroscopy (SRS) is used to measure local gas-phase conditions in the 2-D axi-symmetric IDF and the quasi 1-D CDF, where nanomaterials are grown on

inserted substrates of various compositions. Nitrogen-diluted methane-air flames are examined. Carbon nanotubes (CNTs) are grown catalytically on metal-alloy substrates, and their morphologies are correlated with the local gas-phase temperature and the concentrations of carbon-based precursor species (e.g. C_2H_2 , CO). Zinc oxide (ZnO) nanostructures are grown directly on zinc-plated steel substrates, and their morphologies are correlated with the local gas-phase temperature and the concentrations of oxidative (e.g. O_2 , H_2O , and CO_2) and reducing (e.g. H_2) species. Computational simulations in 1-D, involving detailed chemical kinetics and transport properties, and in 2-D, using simplified kinetics and transport, are used to validate and improve the measurements.

Laser-induced fluorescence (LIF) is employed to measure the gas-phase temperature profile and OH radical species concentration distribution in a low-pressure, premixed, nitrogen-diluted hydrogen-oxygen, burner-stabilized, stagnation-point flame. Titania nanoparticles are synthesized using a metalorganic precursor. The LIF measurements are compared with computational simulations with detailed chemical kinetics and transport, to affirm the quasi 1-D flow field, as well as to investigate the effects of precursor addition and uniform electric-field application.

SRS is utilized to characterize *in-situ* the composition and crystallinity of nanoparticles, in aerosol form, produced in the aforementioned low-pressure premixed flame and in the ICP synthesis setup. The Stokes spectra are identified for crystalline phases of TiO_2 (and Al_2O_3 in a different flame setup) and *c*-BN based on *ex-situ*-taken spectra from the literature. The *in-situ* technique is able to delineate the phase conversion of nanoparticles (including amorphous to crystalline) as they evolve in the flow field.

ACKNOWLEDGEMENTS

I am grateful to all of those who made this dissertation possible. First and foremost, I would like to express my sincere gratitude to my advisor, Prof. Tse, for his guidance and help during this work. Appreciation is also expressed to other members of my dissertation committee, Prof. Guo, Prof. Shan, and Prof. Mann. I am indebted to fellow lab members Dr. Hong Zhao, Dr. Fusheng Xu, Dr. Geliang Sun, Ms. Megan Smith for their helps with the various synthesis experiments and Mr. Justin Fernandez for his help with the Fluent simulations. The help from many other students in the lab throughout the years is also appreciated.

Financial support from the National Aeronautics and Space Administration (through Grant NCC3-1052), the National Science Foundation (through Grants NSF-CTS-0213929, NSF-CTS-0325057, and NSF-CTS-0522556), the Army Research Office (through Grant W911NF-08-1-0417), the Office of Naval Research (through Grant N00014-08-1-1029), and the Rutgers Mechanical and Aerospace Engineering Department, including the Raisler Fellowship, is gratefully acknowledged.

PREFACE

All the materials-synthesis experiments in this dissertation were performed by Dr. Fusheng Xu (carbon nanotubes¹, nanowires²), Dr. Hong Zhao (TiO₂ nanoparticles^{3,4}), Ms. Megan Smith (TiO₂ nanoparticles⁵), and Dr. Geliang Sun (*c*-BN nanoparticles⁶). They are listed as co-authors for the papers related to this work.

Portions of the content in Chapters 4, 5, 6, and 7 are verbatim from published and submitted papers, corresponding to Refs. 1, 2, 3,4, 5, and 6. I have obtained permission from the co-authors to present the results related to my thesis work in this dissertation.

References

¹ Xu F., Liu X., and Tse S.D., Synthesis of Carbon Nanotubes on Metal Alloy Substrates with Voltage Bias in Methane Inverse Diffusion Flames, *Carbon*, 44(3), 570-577,(2006).

² Xu, F., Liu, X., Tse, S.D., Cosandey, F., and Kear, B.H., Flame Synthesis of Zinc Oxide Nanowires, *Chemical Physics Letters* 449, 175-181 (2007).

³ Zhao, H., Liu, X., and Tse, S.D., Control of Nanoparticle Size and Agglomeration through Electric-Field-Enhanced Flame Synthesis, Invited paper, *Journal of Nanoparticle Research* 10, 907-923 (2008).

⁴ Zhao, H., Liu, X., and Tse, S.D., Effects of Pressure and Precursor Loading in the Flame Synthesis of Titania Nanoparticles, *Journal of Aerosol Science*, in press (available online 6 Aug 2009).

⁵ Liu X., Smith M., and Tse S.D., *In-Situ* Raman Characterization of Nanoparticle Aerosols during Flame Synthesis, submitted to *Applied Physics B* (2009).

⁶ Tse, S.D., Sun, G., Liu, X., *et al*, Development of RE-Doped III-Nitride Nanomaterials for Laser Applications, *Symposium D: Rare-Earth Doping of Advanced Materials for Photonic Applications*, 2008 MRS Fall Meeting, December 1 - 5, Boston, MA.

TABLE OF CONTENTS

Abstract	ii
Acknowledgements	iv
Preface	v
List of Tables	xii
List of Illustrations	xiii
Chapter 1 Introduction	1
1.1 Background and Motivation	2
1.1.1 Laser based diagnostics	2
1.1.2 Flame synthesis	5
1.2 Strategies and innovations in this work	6
1.3 Overview	7
1.4 Outline of this dissertation	9
References	10
 Chapter 2 Theoretical and Experimental Background	 11
2.1 Spontaneous Raman Scattering (SRS)	11
2.1.1 Raman spectroscopy of gas phase combustion species	14
2.2 Laser Induced Fluorescence (LIF)	23
2.2.1 Spectroscopy of diatomic molecules	24
2.2.2 Experimental strategy	26
2.2.3 Interference	28

2.2.4 Two-line temperature measurement	30
2.2.5 OH concentration measurement	33
2.3 Other Diagnostic Techniques	35
2.3.1 Chemiluminescence.....	35
2.3.2 Photoluminescence (PL).....	35
2.3.3 Laser light scattering (LLS).....	36
2.3.4 <i>In-situ</i> sampling and nano-scanning mobility particle sizer (nano-SMPS)	36
2.4 <i>Ex-situ</i> Nanopowder Characterization	36
2.4.1 X-Ray diffraction (XRD).....	37
2.4.2 Transmission electron microscopy (TEM).....	37
2.4.3 Scanning electron microscopy (SEM).....	37
2.4.4 Energy-dispersive X-ray spectroscopy (EDXS).....	38
2.4.5 Raman microscopy	38
2.4.6 Thermogravimetric analysis (TGA).....	38
References	39

Chapter 3 Literature Review of the Application of *In-situ* Laser-based Diagnostics to

Gas-phase Synthesis.....41

3.1 Introduction	41
3.2 Literature Review.....	42
3.2.1 Laser induced fluorescence (LIF).....	42
3.2.2 Spontaneous Raman spectroscopy (SRS).....	45
3.2.3 Fourier transform infrared (FTIR)	47
3.2.4 Laser-induced breakdown spectroscopy (LIBS)	49

3.2.5 Laser induced incandescence (LII).....	51
3.2.6 Ultra-small-angle x-ray scattering (SAXS)	52
3.2.7 Laser light scattering (LLS).....	53
References	54

Chapter 4 Application of Gas-Phase Spontaneous Raman Spectroscopy to Study the Synthesis of 1-D Nanostructures.....59

4.1 Introduction	60
4.2 Spontaneous Raman scattering of methane inverse diffusion flames	62
4.2.1 Experiment arrangement.....	63
4.2.2 Results	69
4.3 ZnO nanowires	78
4.3.1 Experiment arrangement.....	79
4.3.2 N ₂ Profiles from FLUENT simulation.....	80
4.3.3 Results and discussion	83
4.4 Spontaneous Raman scattering of counter flow diffusion flame	99
4.4.1 Experiment arrangement.....	100
4.4.2 Fluorescence Interference on Raman measurement	101
4.5 Results and Discussions	109
4.6 Error analysis.....	111
4.6.1 Species concentration	111
4.6.2 Temperature.....	116
4.6.3 Flame position	120
4.7 Conclusions	121

References	122
Chapter 5 Application of Gas-Phase Laser-Induced Fluorescence to Study Low-Pressure Synthesis of Nanoparticles.....	124
5.1 Introduction	124
5.2 Experiment	126
5.2.1 Flame synthesis setup	126
5.2.2 LIF diagnostics systems	128
5.3 Flame simulation – CHEMKIN	132
5.4 Results and discussions	134
5.4.1 Isolation of the electrophoretic effect	134
5.4.2 Effect of the precursor loading on T and OH concentration	136
5.5 Error analysis.....	139
5.5.1 Relative OH concentration errors from systematic uncertainty	139
5.5.2 Temperature errors from systematic uncertainty	140
5.5.3 Temperature errors from photoelectron statistics	141
5.6 Conclusion.....	142
References	143
Chapter 6 <i>In-situ</i> Raman Characterization of Nanoparticle Aerosols during Flame Synthesis.....	145
6.1 Introduction	146
6.2 Experimental Arrangement	148
6.2.1 <i>In-situ</i> Spontaneous Raman Scattering Setup.....	148
6.2.2 Gas-phase SRS	149

6.2.3 Nanoparticle SRS	150
6.3 Validation and Calibration of Technique	151
6.3.1 <i>Ex-Situ</i> TiO ₂ nanoparticle characterization on glass slides at room temperature.....	151
6.3.2 <i>In-Situ</i> Aerosol Characterization	155
6.3.2.1 Setup of Nanoparticle-Seeded Calibration Flame.....	155
6.3.2.2 Results and Discussions.....	156
6.4 Application of Technique to Flame Synthesis of Nanoparticles.....	163
6.4.1 TiO ₂ Nanoparticle Synthesis Flame Setup	163
6.4.2 Results and Discussions.....	165
6.5 Error Analysis	171
6.6 Conclusions	172
References	173

Chapter 7 Application of *In-Situ* Raman Spectroscopy to Study the Plasma Synthesis of Cubic Boron Nitride Nanoparticles.....176

7.1 Introduction	176
7.2 Experiment Arrangement	178
7.2.1 <i>In-situ</i> Spontaneous Raman Scattering Setup.....	178
7.2.2 Gas-phase SRS	178
7.2.3 <i>c</i> -BN nanoparticle SRS.....	179
7.2.4 <i>c</i> -BN Nanoparticle Plasma Synthesis Setup.....	180
7.2.5 <i>Ex-Situ c</i> -BN nanoparticle characterization on glass slides at room temperature.....	183

7.3 Results and discussion.....	183
7.3.1 <i>Ex-situ</i> characterization	183
7.3.2 <i>In-situ</i> characterization	186
7.4 Conclusion.....	191
References	191
Chapter 8 Concluding Remarks.....	194
8.1 Review of results and conclusions	194
8.1.1 Flame structure for nanostructure synthesis by SRS.....	194
8.1.2 Flame structure for nanoparticle synthesis by LIF	195
8.1.3 <i>In-situ</i> laser diagnostics of nanoparticle growth in flame synthesis.....	195
8.1.4 <i>In-situ</i> laser diagnostics of energetic material growth in aerodynamically-assisted plasma synthesis	196
8.2 Suggestions for future work	196
Appendix A Resonance Raman Spectroscopy Characterization on Single-Wall Carbon Nanotubes (SWNT).....	198
Appendix B Laser Diagnostics Applied to Low-Grashof Nearly Spherical Inverse Flames.....	201
Appendix C Intensity Calibration of Raman Spectroscopy System.....	211
Appendix D Standard Operation Procedure for Laser-Based Diagnostics.....	216
Curriculum Vita.....	220

LISTS OF TABLES

Table 2.1. Raman shift and frequency range for the species in SRS study.....	20
Table 2.2. The values of $\frac{kf_i(T_0)}{kf_{N_2}(T_0)}$ for different species in SRS study.....	20
Table 2.3. Probing schemes for LIF.....	34
Table 5.1. Parameters used in temperature measurement.....	131

LIST OF ILLUSTRATIONS

Figure 2.1. Energy level diagram showing the states involved in Raman signal. The line thickness is roughly proportional to the signal strength from different transitions. (Reproduced from Ref. 6)	13
Figure 2.2. A plot of $-\log \sigma$ (cross section in cm^2 per molecule) for the most common optical processes in linear spectroscopy. (Reproduced from Ref. 7).....	14
Figure 2.3. A schematic of a typical experimental arrangement for SRS measurements in steady-state flames (Reproduced from Ref. 4).....	15
Figure 2.4. Energy level diagram of LIF.....	24
Figure 2.5. Generalized experimental schematic for LIF with a simple two mirror scheme for image rotation. (Reproduced from Ref. 4).....	27
Figure 2.6. Boltzmann distribution for different rotational levels of OH diatomic molecule at various temperatures. (Reproduced from Ref.23).....	34
Figure 4.1. (a) Methane inverse co-flow jet diffusion flame. (b) Spontaneous Raman spectroscopy (SRS) diagnostic setup. (c) Experimental timing diagram (d) Time gate diagram on oscilloscope.....	68
Figure 4.2. Representative Raman spectra of major species at 1794K in flames.	70
Figure 4.3. Experimental spectra of CO_2 and O_2 at $T=1794\text{ K}$, showing the overlap of O_2 spectrum by the wing of CO_2 spectrum at high temperature.....	72
Figure 4.4. Gas-phase temperature (Raman) and species mole fraction profiles as measured by SRS, including thermocouple temperature (TC), at investigated sampling heights within	

the flame structure of Fig. 1: (a) $z = 6$ mm, (b) $z = 9$ mm, (c) $z = 12$ mm, and (d) $z = 15$ mm.....	75
Figure 4.5. FESEM images of CNT morphology corresponding to catalytic probe composition (column) and flame sampling height (row) of Figure 4.1. (from Ref.28)...	76
Figure 4.6. An IDF with investigated positions for ZnO nanostructure growth.....	80
Figure. 4.7. Comparisons of simulated and experimental results of flame temperature....	85
Figure 4.8. N_2 profile simulation results from Fluent (■) vs. linear assumption (▲) and the comparisons of major species.....	90
Figure 4.9. Comparisons of simulated and experimental results of O_2 mole fraction.....	91
Figure 4.10. Comparisons of simulated and experimental results of CH_4 , CO_2 , and H_2O at various heights in the flame.....	94
Figure 4.11. The profiles of temperature and major species measured by SRS for the production of ZnO nanostructures, at (a) $z=6$ mm, (b) $z=7$ mm, (c) $z=8$ mm, (d) $z=9$ mm, (e) $z=12$ mm and (f) $z=15$ mm, along with the temperatures measured by thermocouple (TC)	97
Figure 4.12. FESEM images corresponding to growth characteristics of (a) 100-400nm diameter nanowires, where arrows show interpenetrative growth, (b) < 50 nm diameter nanowires, and (c) nanowires with transition to nanoribbons at the tips. (d) EDX spectra of as-grown nanowires. (from Ref. 27).....	98
Figure 4.13. A CDF flame is established between the two burners.....	100
Figure 4.14. Linear distribution assumption (▲) and CHEMKIN simulation results (■) of N_2 profile and the comparisons for major species.....	105

Figure 4.15. Concentration results from Raman scattering measurements with and without fluorescence interferences and their comparisons with computation simulation.....	107
Figure 4.16. Flame structure with 50% CH ₄ measured by SRS and compared with simulations, (a) temperature profile along the axial z direction, and (b) the molar fractions of major species along the axial z direction.....	108
Figure 4.17. A typical theoretical least-squares fit to the experimental Raman spectrum of N ₂	117
Figure 4.18. (a) Real spectrum of a monochromatic light source (b) Recorded spectrum of a monochromatic light source with a perfect instrument (c) Recorded spectrum of a monochromatic light source with a real instrument.....	118
Figure 4.19. Instrumental line profile of a spectrograph system used in Raman spectroscopy measurements.....	119
Figure 4.20. An N ₂ Raman spectrum at 1794 K and its convoluted spectrum (1799 K).	120
Figure 5.1. Outline of flame synthesis of nanoparticle research and the function of laser diagnostics techniques.....	126
Figure 5.2. Premixed synthesis flame setup.....	127
Figure 5.3. Laser induced fluorescence (LIF) measurement setup.....	129
Figure 5.4. OH LIF spectra at the middle point between the burner and the substrate, with and without the precursor.....	130
Figure 5.5. “Dead distance” in LIF when approaching surfaces.....	132
Figure 5.6. Axial temperature profile without precursor. Comparison between simulation, with and without an electric field at 20torr. The symbols are the results of LIF	

measurements and the line is model prediction. –500V is applied to the substrate and the burner is grounded.....	135
Figure 5.7. Axial OH concentration without precursor. Comparison between simulation, with and without an electric field at 20torr. The symbols are the results of LIF measurements and the line is the model prediction. –500 V is applied to the substrate and the burner is grounded.....	135
Figure 5.8. Comparison of visible luminescence of the synthesis flames, (a) with, and (b) without precursor loaded.....	137
Figure 5.9. Axial temperature profile. Comparison between simulation, with and without precursor, at 20torr. The symbols are the results of the LIF measurement and the line is the model prediction.....	138
Figure 5.10. Axial OH concentration. Comparison between simulation, with and without precursor at 20torr. The symbols are the results of the LIF measurement and the line is the model prediction.....	138
Figure 6.1. Schematic of the <i>in-situ</i> Raman scattering system. BS: beam splitter; L: lens; M: mirror; PD: photodiode.....	149
Figure 6.2. Schematic of the setup for the nanopowder on glass slide calibration configuration.....	152
Figure 6.3. Raman spectrum of anatase titania on a glass slide: (a) taken using our <i>in-situ</i> Raman setup. Spectrum is composed of two smaller coverage spectra, with the grating centered at 350 cm^{-1} and 500 cm^{-1} ; (b) taken using Renishaw inVia Raman microscope. Known spectra of anatase and rutile films given in Ref. 44 are also shown.....	154

Figure 6.4. Schematic of the setup for the nanoparticle-seeded co-flow jet diffusion flame.....	156
Figure 6.5. Typical N ₂ rotational Raman spectrum detected <i>in-situ</i> in the co-flow jet diffusion flame without TiO ₂ nanoparticle seeding.....	157
Figure 6.6. <i>In-situ</i> Raman spectra of seeded TiO ₂ nanoparticles flowing through the co-flow jet diffusion flame, along the axial centerline at different heights above the burner exit. Gas-phase temperature is given and made by SRS on N ₂ . Figure shows the transformation from anatase to rutile of the originally anatase seeded nanoparticles.....	160
Figure 6.7. <i>In-situ</i> Raman spectra of seeded Al ₂ O ₃ nanoparticles nanoparticles flowing through the co-flow jet diffusion flame, along the axial centerline at two heights above the burner exit. Gas-phase temperature is given and made by SRS on N ₂ . Figure shows the transformation from γ -alumina (no Raman signature) to α -alumina of the originally γ -alumina seeded nanoparticles.....	161
Figure 6.8. Schematic of the axisymmetric, stagnation-point premixed flame synthesis setup.....	163
Figure 6.9. <i>In-situ</i> Raman spectra of TiO ₂ nanoparticles formed during low-pressure premixed flame synthesis (see Fig. 6.8), along the axial centerline at different distances from the substrate (0mm). Burner exit is located at 40mm. Gas-phase temperature is given and made by LIF on OH. Figure shows the increasing anatase content as the nanoparticles approach the substrate.	166
Figure 6.10. XRD of TiO ₂ (A for anatase, R for rutile) (From Ref.51).....	167
Figure 6.11. TEM image of TiO ₂ nanoparticles and the insert showing the SAD pattern (From Ref. 51)	168

Figure 6.12. Elastic laser light scattering from nanoparticles synthesized in the flame, as a function of distance from the substrate. Burner exist is located at 4cm. A relative number density is computed using nano-SMPS data for the aggregate particle size.....	169
Figure 6.13. Computed particle residence time and temperature between the substrate and burner.....	171
Figure 7.1. TO mode of <i>c</i> -BN and the LO mode of <i>h</i> -BN Raman spectra. (Reproduced from Ref. 32)	180
Figure 7.2. The schematic diagram of the r.f. ICP–CVD system inside the plasma chamber measurement locations for temperature and <i>c</i> -BN characterization by SRS.....	182
Figure 7.3. Raman spectrum of <i>c</i> -BN powder samples on the slides.....	184
Figure 7.4. TEM image of <i>c</i> -BN powders (from Ref.1).....	185
Figure 7.5. XRD pattern of <i>c</i> -BN powders shows the dominant phase of <i>c</i> -BN (from Ref. 1).....	185
Figure 7.6 Temperature measurements in post-plasma region using SRS of N ₂	188
Figure 7.7 Ar I emission lines in plasma region at 5cm above the cold substrate.....	189
Figure 7.8 Raman spectra of <i>c</i> -BN detected in the region nearby the substrate.....	191
Figure A.1. Raman spectra of single-wall carbon nanotubes: a. G/D mode of sample 1; b. G/D mode and c. RBM mode of sample 2.....	200
Figure B.1. a: Schematic of spherical inverse diffusion flame combustion apparatus. Inner dimension is 40×40×40 cm ³ . b: Design of 1.27 cm spherical diameter porous, bronze burner.....	202
Figure B.2. Spherical diffusion flames of different fuels. a) Pure hydrogen. b) Hydrogen/methane mixture. c) Pure methane.....	207

Figure B.3. Comparison of temperature profile along downward direction between three flames.....	209
Figure B.4. Temperature distribution profile along three directions in the methane inversed spherical flame.	209

Chapter 1 Introduction

Spectroscopic laser-based diagnostics provide researchers with the capability for remote, non-intrusive, *in-situ*, spatially- and temporally-precise measurements of important chemical and thermodynamic parameters. They provide improved understanding of a wide variety of gas-phase processes¹.

A synthesis method that has drawn interest from the materials community is combustion synthesis of nanostructured materials^{2,3}. With smaller size and larger surface area, nanomaterials have many unique physical, optical, and electromagnetic properties different from bulk materials⁴. Flame synthesis of nanomaterials, including nanoparticles and various nanostructures, has demonstrated the potential for continuous, efficient, high-volume production, using low-cost raw materials.

However, flame synthesis can involve complex chemistry and transport processes⁵, where fundamental scientific understanding remains a major challenge. Yet, specially-defined flame configurations, along with laser-based spectroscopy, allow the material processing flow field to be quantified (which has been surprisingly limited in the materials science field) so that meaningful relationships can be drawn between input conditions, growth properties, and final material characteristics. Thus, laser-based optical diagnostics can be a powerful tool in gas-phase synthesis research.

In this chapter, motivations and objectives are addressed first. Then, the dissertation work is overviewed, which includes experimental methods and simulation models applied to a variety of flame synthesis systems. Finally, major findings and conclusions are presented, along with Appendices. Highlights of this work are summarized followed

by the content outlines of each chapter.

1.1 Background and Motivation

Given the interdisciplinary nature of the current research, a brief introduction on laser-based diagnostics and gas-phase materials synthesis is presented in the context of flame and plasma applications.

1.1.1 Laser based diagnostics

Electromagnetic radiation--infrared, visible, or ultraviolet light--interacts with the molecule under investigation and is scattered. The diagnostic methods differ in scattering angle, in the energetics of the scattering process, the polarization of the scattered light, the temporal evolution of the signal, and the efficiency ("cross section") of the process. They are usually classified into two basic types: optical methods and spectroscopic methods.

Optical methods, including interferometry, holography, laser Doppler anemometry (LDA), particle imaging velocimetry (PIV), etc., do not have specific requirements on the exact value of the wavelength of the light. However, most of them do require monochromaticity or coherence of the light such as that provided by lasers. The spectroscopic methods, on the other hand, use specific wavelengths for the light source, or they analyze the emerging signal with respect to its spectral composition, or both. These wavelengths closely relate to the molecules under investigation.

Spectroscopic methods have a couple of advantages over conventional techniques. Spectroscopic methods are non-intrusive, and they can be applied to situations inaccessible by conventional methods, e.g. harsh and hostile environments. By

employing spectroscopic diagnostics, both major and minor/trace species (such as pollutants) are detectable, which is favorable in flame or plasma synthesis studies⁶. Properly designed, *in-situ* measurements can be made for gas-phase synthesis systems with suitable optical access.

Quantitative measurements are important to understand the synthesis mechanisms. Temperature and chemical species concentrations are two major concerns which are generally difficult to resolve precisely in flames. In our spectroscopic laser-based diagnostics for gas-phase synthesis, these problems are addressed by tailoring the flames and by carefully choosing diagnostic techniques, experimental designs, and data processing methods. Major laser spectroscopy techniques used in flame synthesis studies include laser induced fluorescence (LIF) and spontaneous Raman scattering (SRS).

Laser induced fluorescence (LIF) is spontaneous emission from atoms or molecules that have been excited by laser radiation. In a simple two-level model of a molecule, if the molecule is resonantly stimulated by the laser source, then a photon of energy $h\nu$ will be absorbed, bringing the molecule to an excited state. Such a state is unstable and will decay, spontaneously emitting another photon of energy $h\nu$. If the fluorescence is observed at 90 degrees to a collimated laser source, then a very small focal volume, V_c , may be used, defining a fine spatial resolution.

The fluorescence signal can be used in a number of ways. Most simply, it provides a measure of the population of the excited state(s). In addition, if a relationship can be found between the number densities of all the quantum states under excitation conditions, then the total number density of the species can be deduced. By examining the excitation spectrum of a molecular species, one can deduce the ground state distribution function,

and thus the temperature. Also, if one can predict the population distribution in the atom or molecule under excitation, then one can use the observed fluorescence spectrum to deduce the temperature.

LIF can be modified into a 2-D diagnostic method called planar laser-induced fluorescence (PLIF). The difference lies in that a laser sheet instead of a focus point generates the excited atoms/molecules. The sheet passes through the flow field, and the resulting fluorescence is imaged by an intensified digital camera.

Spontaneous Raman scattering (SRS) is an inelastic, non-resonant scattering process that occurs simultaneously on all Raman active transitions of the molecules in the probe volume. For any laser wavelength, Raman scattered photons will be emitted at characteristic frequencies associated with the vibrational energy of the Raman active modes of the various molecules in the problem volume. The red-shifted spectrum (Stokes) results from scattering where vibrational quanta from the laser source are deposited in the molecule and arise from the ground vibrational levels of the molecule. The blue-shifted spectrum (anti-Stokes) results from scattering where vibrational quanta from the molecule are added to the photon energy and arise from excited vibrational levels of the molecule. The anti-Stokes scattering is usually much weaker than the Stokes scattering (due to the relatively small population in the vibrationally excited molecular states), but can be used to infer the vibrational temperature of the scattering molecule.

SRS is well suited for flame-based research. The major species O_2 , N_2 , H_2 , CH_4 , CO_2 , H_2O , which are not easily, or not at all, accessible by LIF, are observable by Raman scattering. A single laser line can be used for Raman excitation; the different species identify themselves by different shifted scattered wavelengths. Therefore simultaneous

multi-species detection is inherent to Raman spectroscopy. Quantitative information on concentration distribution is more easily extracted out of Raman data than LIF data.

For Raman, the low scattering cross section is the main disadvantage. The cross section can be increased somewhat by decreasing the wavelength of the excitation light, since Raman cross-section is proportional to the fourth power of the scattering frequency. However, the lower the excitation wavelength, the closer the Raman lines identifying the different species lie together. With (a) correct selection of high energy, long pulse, and wavelength-tunable laser system, (b) recent development of larger spectrometers having a greater dispersion and a lower light throughput, and (c) advancement of ICCD cameras with gating abilities, this disadvantage of Raman spectroscopy can be overcome.

1.1.2 Flame synthesis

In the research of flame synthesis of nanoparticles and nanostructures, one of the objectives is the fundamental understanding of the mechanism involved in nanomaterials formation, growth, and aggregation. *In-situ* laser diagnostics aid the investigation by characterizing the gas-phase flow field, as well as the nanomaterials themselves.

Nanomaterials have been successfully produced using various techniques such as arc discharge (AD), laser ablation (LA), chemical vapor deposition (CVD), and molecular beam epitaxy (MBE). However, these techniques can be energy intensive (e.g., CVD and LA), characterized by batch-to-batch inconsistencies (e.g., AD and LA), or require expensive vacuum equipment (e.g., AD, CVD and MBE). Moreover, they may not be readily or economically scalable for large-scale manufacturing.

In contrast, flame synthesis can be a cost effective technique with a demonstrated history of scalability (e.g., commercial production of titania, silica, carbon black, etc.).

Flame synthesis features energy-efficiency (by providing both heat and chemical reagents), large parameter space (by offering examination of key affecting factors in a single flame condition), high growth rate (by operating at non-vacuum pressures), controllability (by adjusting flame stoichiometries and velocities), and processing continuity (by maintaining a constant flow process)⁷. As a result, flames can be tuned to specify the local temperatures and chemical species concentrations that are optimal for nanoparticle, carbon nanotube (CNT), and metal-oxide nanowire growth—the topics investigated in this thesis.

1.2 Strategies and innovations in this work

Spectroscopic laser-based measurements probe the controlling parameters to better understand the fundamental mechanisms involved in our flame and plasma synthesis processes. Due to the “harsh” environment of our synthesis configurations, the setup of spectroscopic detection instruments needs to be away from measurement points in the flow field. An obvious advantage of the remote configuration is its non-intrusive feature. Using the laser beam as a probe, flow field and chemical processes in a flame will not be disturbed, and isolated (e.g., low-pressure) systems can be examined. The most important feature of the spectroscopic laser-based diagnostics systems is that *in-situ* characterization is realized. The versatile system is easy to redesign for any new synthesis flames/plasmas with practical layout and measurement considerations. Finally, by using advanced spectroscopic instruments with careful experimental strategy, it is possible to make measurements with spatial, spectral, and temporal precision.

Materials characterization techniques have been developed to determine the size, morphology, crystallinity, phase, and even chemical composition of various new

nanomaterials. Most of the techniques, however, due to the limitation of the instruments or metrology, only allow the test to be conducted *ex-situ* instead of *in-situ*. In this work, *in-situ* measurements are made at the local conditions where synthesis occurs. Local information obtained in this way provides insight into the fundamental growth mechanisms.

Additionally, the precision of the Raman spectroscopy measurements is improved by including key parameters (e.g., N_2 profile) from computational simulations into the data processing. As such, calculation of relative species concentrations can be better made.

Finally, the SRS technique is developed to diagnose the nanoparticles themselves during gas-phase synthesis. This is examined in low-pressure premixed flat flame synthesis and extended to inductively coupled RF plasma synthesis. Such measurements mark the first time Raman has been used to characterize nano-aerosols *in-situ* during synthesis.

1.3 Overview

In the flame synthesis of 1-D nanostructures at atmospheric pressure, local conditions play the key role in determining the growth of CNTs and semi-conducting metal-oxide nanowires. SRS is used to determine local gas-phase temperatures, as well as the concentrations of carbon-based precursor species (e.g., CO, C_2H_2) at specific locations where CNTs grow and the concentrations of oxidizer species (e.g., O_2 , H_2O , CO_2) where ZnO nanowires grow. Two flame configurations are studied by SRS: the co-flow inverse diffusion flame (IDF) and the counter-flow diffusion flame (CDF). The variation of the obtained parameters strongly affects the formation, diameter, growth rate, and morphology of the nanomaterials. Nanostructures grown under similar local conditions

in different flames possess similar morphology, indicating that the local conditions can be translated between different synthesis configurations.

In low-pressure flame synthesis of nanoparticles, LIF is employed to map gas-phase temperature and OH radical species concentrations. The LIF measurements are compared with computational simulation (using a modified Sandia SPIN code) for temperature, chemical species, and flow-velocity distributions. The agreement between the one-dimensional simulation and the experimental measurements is excellent for the stagnation point flame, especially without precursor loading, verifying the quasi-1-D flow field. The measurements also show that the application of uniform electric fields have virtually no effect on the flame structure for our geometry, isolating the study of electrophoretic transport of nanoparticles.

A particularly novel aspect of this thesis is the application of Raman spectroscopy to diagnose nanoparticle presence and characteristics in a gaseous flow field. Specifically, *in-situ* monitoring of the Raman-active modes of TiO_2 and Al_2O_3 nanoparticles in aerosol form is demonstrated in high-temperature flame environments. This technique serves as a sensitive and reliable way to characterize particle composition and crystallinity (e.g., anatase versus rutile) and delineate the phase conversion of nanoparticles as they evolve in the flow field. The effect of temperature on the solid-particle Raman spectra is investigated by seeding nanoparticles into a co-flow jet diffusion flame, where local gas-phase temperatures are correlated by shape-fitting the N_2 vibrational Stokes Q-branch Raman spectra. Applying the technique to a flame synthesis environment, the results demonstrate that *in-situ* Raman of as-formed nanoparticles can be readily applied to other gas-phase synthesis systems, especially as an on-line diagnostic.

Application of *in-situ* SRS is extended to examine processes involved in the inductively-coupled plasma synthesis of Group-III-Nitride nanoparticles (e.g., boron nitride). The Raman spectra shows that the powders deposited are mainly cubic-BN, as confirmed by XRD. TEM shows that the particles are 50-100 nm in size, consistent with the broadening of the Raman peaks due to small crystallite sizes. The gas-phase temperature measurements (using recombined N₂) reveal the steep temperature gradient needed for the formation of the material in a metastable state.

1.4 Outline of this dissertation

Chapter 2 gives the theoretical and experimental background on various laser-based spectroscopy techniques, focusing on LIF and SRS. Chapter 3 provides a literature review of the application of laser-based diagnostics to gas-phase synthesis. Chapter 4 demonstrates the utilization of SRS to measure local gas-phase temperatures, as well as concentrations of key species, involved in the synthesis of CNTs and ZnO nanowires in diffusion flames. Chapter 5 presents the employment of LIF to measure gas-phase temperatures, as well as OH radical species concentrations, involved in the synthesis of anatase titania nanoparticles. Chapter 6 addresses the development of Raman spectroscopy to characterize TiO₂ nanoparticles *in-situ* during flame synthesis. Chapter 7 presents the utilization of the SRS system of Chapter 6 to diagnose *c*-BN nanoparticles synthesized using an inductively coupled RF plasma. Chapter 8 offers some concluding remarks and suggestions for future work. Appendix A presents some preliminary results using our Raman setup to characterize single-wall carbon nanotubes (SWNT). Appendix B presents preliminary work conducted using LIF and PLIF to study weakly buoyant, spherical flames—a promising 1-D synthesis geometry. Appendix C provides some

details about the calibration of the spectroscopy system. Appendix D gives standard operating procedures for the laser-based diagnostics and spectroscopy.

References

-
- ¹ K. Kohse-Hoinghaus and J.B. Jeffries, *Applied combustion diagnostics* (Taylor & Francis, New York, 2002).
- ² M.T. Swihart, Vapor-phase synthesis of nanoparticles, *Current Opinion in Colloid & Interface Science* 8, 127 (2003).
- ³ M. S. Wooldridge, Gas-phase combustion synthesis of particles, *Progress in Energy and Combustion Science* 24, 1, 63-87 (1998).
- ⁴ H. Gleiter, Nanocrystalline materials, *Progress in materials science* 33, 4, 223-315 (1989).
- ⁵ F.A. Williams, *Combustion theory: the fundamental theory of chemically reacting flow systems* (Perseus Books, Cambridge, Mass, 2000).
- ⁶ A.C. Eckbreth, *Laser Diagnostics for Combustion Temperature and Species* (Gordon and Breach Publishers, Amsterdam, The Netherlands, 1996).
- ⁷ K.C. Patil, S.T. Aruna, and S. Ekambaram, Combustion synthesis, *Current Opinion in Solid State and Materials Science* 2, 158 (1997).

Chapter 2

Theoretical and Experimental Background

Laser-spectroscopy-based diagnostics techniques can provide non-intrusive, *in-situ*, spatially- and temporally-precise measurements of important chemical and thermodynamic variables. In this chapter, two laser spectroscopy techniques are reviewed in detail. Spontaneous Raman scattering (SRS) is employed to measure major species concentrations and gas-phase temperatures, as well as to characterize solid-phase nanomaterials during high-temperature synthesis at atmospheric pressure. Laser induced fluorescence (LIF) is used at low pressures to measure temperature and radical/intermediate species, which play important roles in the transition from gas phase to solid phase nanoparticles. Other *in-situ* laser diagnostics and *ex-situ* material characterization methods are also reviewed briefly. Measurements using these methods reveal a more complete understanding of the synthesis process.

2.1 Spontaneous Raman Scattering (SRS)

Raman spectroscopy is a valuable tool for studying molecular vibrations, both in industrial and laboratory settings^{1,2,3}. Raman spectra from samples of different phases, including liquids, solids, and gases, provide rich information about their structures and thermodynamic properties. Raman spectroscopy is widely applied to gas-phase combustion research^{4,5}.

Raman scattering is the result of interaction of light with matter. There are both elastic and inelastic processes in the interaction. An elastic scattering process, i.e., no energy exchange between the molecule and light, is termed Rayleigh scattering. The

other process, the inelastic scattering of light from molecules includes energy exchange and is instantaneous in nature. If a molecule gains energy from the incident light, the resulting lower frequency shift is termed Stokes Raman scattering; the opposite is termed anti-Stokes Raman scattering. Depending on the nature of the energy exchange between the light and the molecules, Raman scattering can also be termed rotational or vibrational. Pure rotational Raman scattering ($\Delta v = 0$) is not widely used for combustion diagnostics due to its small frequency shifts, which makes interpretation difficult. In vibrational Raman scattering ($\Delta v = \pm 1$), each shift component is associated with three rotational branches: $Q(\Delta J=0)$, $O(\Delta J=-2)$ and $S(\Delta J=+2)$, which are normally not resolved. As a result, vibrational Raman scattering is often termed vib-rotational Raman scattering. The frequency shift of vibrational Raman depends on the vibrational frequency of the molecule, and therefore is species specific, contrary to Rayleigh scattering. This feature makes Raman scattering well suited for species detection in combustion diagnostics.

The three light scattering processes are shown in Fig. 2.1, where the thickness of the arrow represents the relative intensity of each process. Raman scattering is much weaker than Rayleigh scattering. In most cases, Stokes Raman scattering is the stronger of the two Raman scattering processes because more molecules generally reside in the ground vibrational state. For this reason, Raman scattering applications in this study use the Stokes shift.

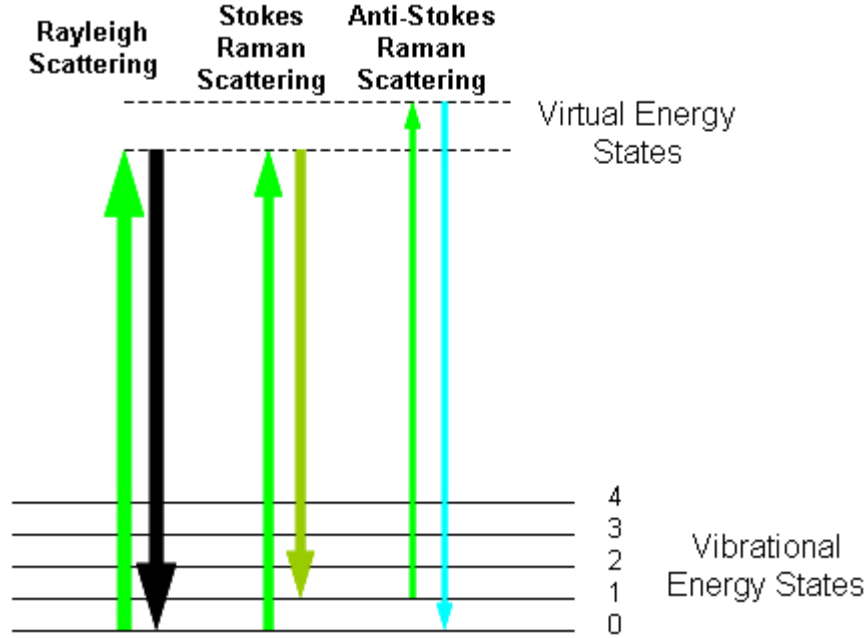


Figure 2.1. Energy level diagram showing the states involved in Raman signal. The line thickness is roughly proportional to the signal strength from different transitions. (Reproduced from Ref. 6)

The intensities of Raman scattering can formally be written as

$$I = P_l N_j \left(\frac{d\sigma}{d\Omega} \right)_j \Delta\Omega l \varepsilon \quad (2.1)$$

where $(d\sigma/d\Omega)_j$ is the Raman (differential) cross-section of species j at certain temperature, $\Delta\Omega$ the collecting solid angle, P_l the incident laser power, N_j the number density of molecules of j , l the sampling extent, and ε the quantum efficiency of the detecting system. The integration of (differential) cross section over all directions gives σ . The units of σ are m^2 , and the cross section can be interpreted as the target area of a molecule (or particle) for scattering or absorption. In general, the Raman and Rayleigh cross-sections depend on the excitation frequency, molecular structure, and direction of observation. Specifically, the Raman cross-section is proportional to the square of the polarizability derivatives for the $m \rightarrow n$ vibrational transition $\alpha' = (\partial\alpha/\partial Q)_0$, and the fourth

power of the scattering frequency ω_S : $\sigma_{RS}=C\omega_S^4|\alpha'_{mn}|^2$. C contains numerical constants.

From Eqn. 2.1, we know that the cross section will determine the efficiencies of absorption or scattering processes and is the meeting point of experiments and theory. The typical cross sections of several spectroscopy processes are shown in Fig. 2.2 for comparison⁷. Note that the y-axis is presented by $-\log \sigma$ (cross section in cm^2 per molecule). By comparison, Raman spectroscopy has much weaker cross section than several other linear spectroscopy including Rayleigh scattering and fluorescence. The cross section values for various molecule vibrations are readily available in modern spectroscopy books^{3,4}.

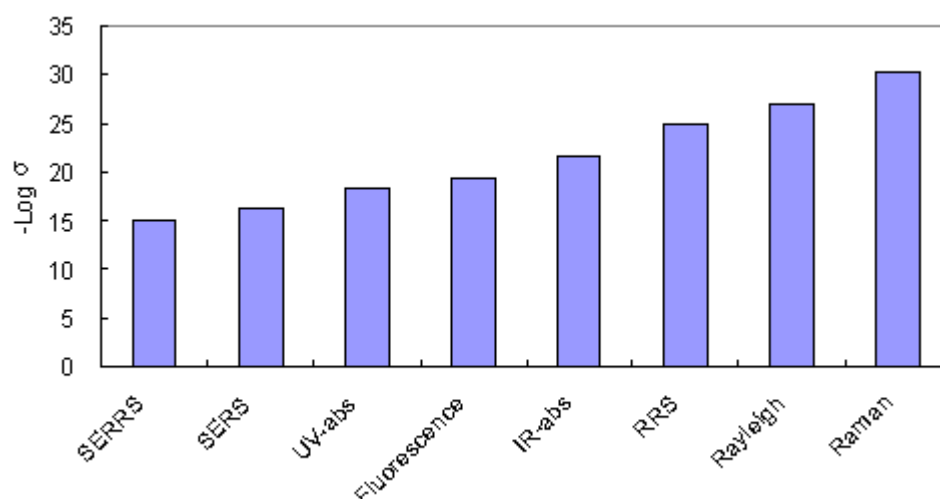


Figure 2.2 A plot of $-\log \sigma$ (cross section in cm^2 per molecule) for the most common optical processes in linear spectroscopy. (Reproduced from Ref. 7)

2.1.1 Raman spectroscopy of gas phase combustion species

SRS has been implemented to measure major species concentrations and temperature in combustion research and other fields. A generic experimental arrangement, with a focus on combustion applications, is discussed as follows. A schematic of a typical SRS

experimental arrangement is shown in Fig. 2.3.

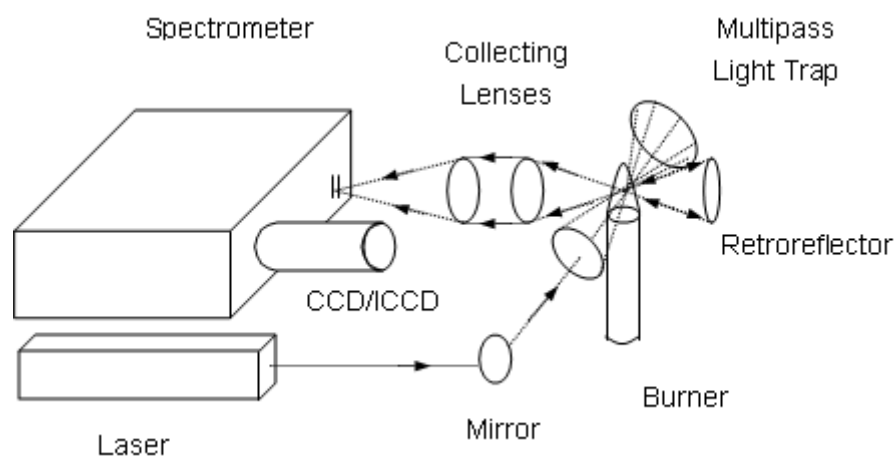


Figure 2.3. A schematic of a typical experimental arrangement for SRS measurements in steady-state flames (reproduced from Ref. 4)

A modern Raman spectroscopy system consists of four major sub-systems: a light source, a signal collection system, a wavelength separator/selector, and a detector. A laser is usually used as light source due to its high-intensity monochromatic characteristics, given the small cross section of Raman scattering. In combustion applications, the required temporal resolution and the luminosity in the flame will determine the selection of the type of laser (CW or pulsed, UV or visible). Since the Raman cross-section is proportional to the fourth power of the scattering frequency, the Raman signals excited by ultraviolet lasers can be greatly enhanced over visible ones.

Because the Raman scattering is inherently weak, the laser beam must be focused properly onto the sample, and the scattered radiation must be collected efficiently. Excitation and collection from the sample can be configured to the 90° and 180° scattering geometries. Collection optics in the detection systems determine the collection power, which may be defined as $F=f/D$ (f , the focal length of the lens and D , the lens diameter). It is important to match the F -number with the wavelength separator to

maximize the total light throughput. To filter out the radiation at the laser wavelength from weak Raman signal, a laser-line rejection device, e.g., edge filter or notch filter, is an important component in the Raman detection system.

A spectrograph is used as the wavelength separator/selector. A dispersive spectrograph consists of an input aperture, an input collimator, a grating, and an output collimator. Light enters the spectrograph through a slit or entrance aperture, which serves to spatially localize the light. The input collimator collimates the light from the slit and directs it to the grating where it is dispersed, or angularly separated, into its constituent wavelengths. The output collimator images the light from the grating onto the detector. The grating produces a different laterally displaced image of the slit at each wavelength of the input light. The term spectrograph implies a two-dimensional, or "imaging" device. Its usage in spectroscopy applications is closely related to the development of multichannel detectors. Initially photodiode arrays and, subsequently, charge-coupled device (CCD) arrays have been the major detection devices, although photomultiplier tubes (PMTs), which have only a single detecting element, are still in use. A CCD is a silicon-based semiconductor arranged as an array of photosensitive elements, each one of which generates photoelectrons and stores them as a small charge. The major advantages of the CCD relative to other multichannel detectors are the low readout noise (which makes optical intensification unnecessary) and the high quantum efficiency and sensitivity in a wide wavelength range (120-1000 nm). Thus, CCDs find increasing use in Raman spectroscopy. For ultra low light measurements as Raman spectroscopy, intensified CCD (ICCD) is used to amplify the weak light. An ICCD camera uses a proximity-focused microchannel plate (MCP) image intensifier fiber-optically coupled to

a CCD array. The image at the output of the image intensifier is translated to the input of the CCD at the same size.

2.1.1.1 Major species concentration

Species concentration measurements are obtained from the strength of the Raman signal. The Raman signal is not affected by collisional quenching and is linearly dependent on the number density of the Raman active species, the Raman cross section, the incident laser energy, the optical collection efficiency, and the bandwidth factor^{4,8}. The intensity of Raman signal is determined by the following relation:

$$P_{Raman} = P_{Laser} N_i K f_i(T) \quad (2.2)$$

where P_{Raman} is Raman signal of species i , P_{Laser} laser power, N_i the number density of species i , K the instrument constant, and $f_i(T)$ the the bandwidth factor of species i under temperature T .

To ensure that the Raman detection system is linear as well, it is run in the accumulation mode for rather short duration (~30s). This mode avoids the saturation problem and improves the S/N. The linearity of the entire system is satisfactorily confirmed by measuring the signal intensity as functions of incident laser power and accumulation time.

The system calibration constants are determined at room temperature to identify the Raman cross section and optical collection efficiency for each species relative to that for N_2 . N_2 spectra are taken at the beginning and end of each experiment in order to monitor any variation in calibration during the experiment and correct for any day-to-day variations in the optical system.

The bandwidth factor is mainly determined by the temperature-dependent distribution

of molecules in their allowed quantum states, and depends on laser line width, spectral location, shape, and bandwidth of the detection system. Detection bandwidths are chosen so that the bandwidth factors are nearly constant over a wide range of temperatures, reducing the uncertainty in temperature. The Sandia Raman code CARSFT⁹ is reliable for calculation of bandwidth factors of diatomic molecules such as N₂, O₂, CO, and H₂¹⁰. The product of the bandwidth factor and the instrument constant, $K f_i(T)$, yield a calibration factor that is used for further data analysis, as explained in the following paragraphs.

From Eqn. 2.3, we have the number density of species i :

$$N_i = P_{Raman} / P_{Laser} K f_i(T) \quad (2.3)$$

in which P_{Raman} and P_{Laser} can be obtained directly from measurement. $K f_i$ can be obtained from calibration. In real experiments, practical issues, including beam steering and defocusing effects, will cause variations in collection efficiency for various spatial locations. A correction factor $c(x)$ is then used to correct the effects. By assuming the mole fraction profile of N₂ in the flame (often assumed to be a linear distribution in counterflow flames), $c(x)$ can be determined from the following relation:

$$\frac{c(x)}{c(x_0)} = \frac{X_{N_2}}{X_{N_2,0}} \frac{T}{T_0} \frac{k f_i(T)}{k f_i(T_0)} \frac{(P_R / P_L)_0}{(P_R / P_L)} \quad (2.4)$$

The subscript 0 stands for reference point; usually it is at the nozzle exit of the flame burners. X is the molar fraction of N₂.

Once the correction factors are determined, the concentrations of fuel and oxidizer can be readily calculated from their reference concentrations at the nozzle exit:

$$n_{F,O} = \frac{\left(\frac{P_R}{P_L}\right) \frac{1}{kf_i(T)} c(x)}{\left(\frac{P_R}{P_L}\right)_0 \frac{1}{kf_i(T_0)} c(x_0)} n_{F,O,0} \quad (2.5)$$

where F, O stands for fuel or oxygen. The mole fraction is then:

$$X_i = \left(\frac{n_i T_i}{n_{i,0} T_0} \right) X_{i,0} \quad (2.6)$$

For other products, the concentrations are calculated from the intensities relative to that of N_2 :

$$X_i = \frac{n_i T_i}{(n_i T_i)_{N_2,0}} \frac{kf_{N_2}(T_0)}{kf_i(T_0)} X_{N_2,0} \quad (2.7)$$

P_{Raman} is the Raman peak area of each species and can be obtained from the spectra. In the spectrometer, a center frequency of spectrum (Raman shift) is preset for each species in the control software WinSpec/32. On the spectrum obtained on the spectrometer, a Raman shift range (low and high Raman shift) are also preset for the peak area calculation. In the calculation of concentration, the peak area within the Raman shift range is then the input of P_{Raman} for specific species. Table 2.1 lists the Raman shift and frequency range for the species measured in this study. Table 2.2 gives $\frac{kf_i(T_0)}{kf_{N_2}(T_0)}$ values of different species.

Table 2.1. Raman shift and frequency range for the species in SRS study

	Cen. Freq. (nm)	Raman Shift (cm ⁻¹)	Low Freq. (nm)	Low Shift (cm ⁻¹)	High Freq (nm)	High Shift (cm ⁻¹)
N ₂	607.3	2330	603.67	2231.69	608.79	2370.93
CO ₂	572.8	1338	568.89	1219.05	574.06	1377.29
H ₂ O	660.5	3657	655.71	3546.31	662.15	3694.70
O ₂	572.8	1338	574.67	1395.85	577.34	1476.29
CH ₄	629.6	2915	623.74	2764.80	631.04	2950.08
H ₂	683.2	4160	677.15	4029.18	683.97	4176.37
C ₂ H ₂	594.6	1980	588.87	1815.42	595.71	2010.24
CO	594.6	1980	588.87	1815.42	595.71	2010.24

Table 2.2. The values of $\frac{kf_i(T_0)}{kf_{N_2}(T_0)}$ for different species in SRS study

Species	CH ₄	O ₂	CO ₂	CO	H ₂ O	C ₂ H ₂	H ₂
$\frac{kf_i(T_0)}{kf_{N_2}(T_0)}$	6.77	1.64	2.56	1.03	1.24	7.63	1.34

Because Raman scattering is generally very weak, in practical combustion situations, only major species with high enough concentrations can be measured. The minimum detection threshold is approximately 0.1% for combustion measurements. There are several methods to improve the signal-to-noise (S/N) ratio in Raman measurements: (1) installing a depolarizer in front of the entrance slit of the spectrometer/spectrograph to scramble the polarization of the Raman signal and improve the overall efficiency of the holographic gratings, (2) rejecting the background luminosity¹¹ and hydrocarbon fluorescence¹², by gating the intensified-CCD (ICCD) camera, (3) mounting a high-attenuation holographic Raman notch filter to reject elastically scattered light, and (4) collecting data for long periods of time, typically 5 to 10 minutes (for very steady flames). In situations where interferences cannot be suppressed any further by methods mentioned

above, sampling and subtracting the interference could be attempted during the data processing, which will be elaborated in Chapter 4.

2.1.1.2 Temperature measurement from Raman spectroscopy

As described in the theory for Raman spectroscopy, scattering can be detected in two different kinds of spectra: pure rotational Raman transitions close to both sides (Stokes and anti-Stokes) of the exciting wavelength, and the ro-vibrational spectra shifted from the exciting wavelength by the molecule-specific vibrational Raman frequency, usually expressed in Raman shift or wavenumber (cm^{-1}).

To determine the temperature from Raman scattering, different approaches can be adopted. First, the temperature is deduced from a total number density measurement in the flame investigated, using a state equation, e.g. the ideal gas law, and assuming isobaric conditions. Here, the total number density of the gas mixture has to be deduced from the integrated Q-branch spectra of all major species in the flame, and the conversion of measured optical signal intensity into temperature demands calibration.

Second, from the spectral shape of pure rotational spectrum (S branch) or ro-vibrational spectrum (Q branch) of N_2 , a theoretical Raman spectrum (S or Q branch, respectively) is calculated and then convoluted with the exciting laser linewidth, taking also into account the influence of the Raman transfer function of the detection system. From a contour fit of the calculated spectrum to the experimental data, the temperature is deduced by employing a least-square fitting routine and minimizing the residuals with the temperature as the fit parameter. When Q-branch ($J'' = 0$) Raman scattering is considered, the characteristic Raman frequency shift ν_R is related to the initial and final energy states by

$$h\nu_R = E(\nu'' + 1, J'') - E(\nu'', J) \quad (2.8)$$

where h is Planck's constant, J'' and ν'' the rotational and vibrational quantum numbers of the initial state, and $E(\nu'', J'')$ and $E(\nu'' + 1, J'')$ the energy of the initial and final states.

Lapp *et al.*¹³ found that Raman scattering intensity $I(\nu_R)$ to be given by

$$I(\nu_R) \propto \frac{C(2J''+1)(\nu''+1)\exp\left[-\frac{E(\nu'', J'')}{kT}\right](\nu_{LASER} - \nu_R)^4}{TQ_{VIB}Q_{ROT}} \quad (2.9)$$

where C is a constant that depends on the mole fraction, nuclear spin, and the incident light intensity. The vibrational partition function is Q_{VIB} , and the rotational partition function is Q_{ROT} .

The complete frequency dependence of the Raman scattering signal is determined by summing over all occupied rotational and vibrational energy levels. In general, the Raman frequency shift from each rotational and vibrational state is different due to the molecular vibrational anharmonicity and the vibrational rotational interactions. Moreover, the population distribution of the different energy levels is different at different temperatures. Therefore, the Raman scattering signal as a function of frequency is strongly temperature dependent. The temperature of the molecule may thus be determined by fitting the experimental Raman scattering signals to the convolution of the spectrometer slit function and Eqn. 2.9 summed over all occupied states.

This method is most successful in steady, laminar flames, where integration over a longer period of time (CW excitation) or a summation over many laser pulses can produce high quality, noise-free spectra. The measurement is self-calibrating, because the relative intensity distribution of the rotational lines or the spectral envelope of the vibrational band mirrors the Boltzmann distribution of the energy states.

Third, temperature can be deduced by the ratio of the integral intensities of Stokes and anti-Stokes transitions (with the restriction to higher temperature), because at low temperatures, the thermal population of the excited vibrational state is low.

In the current research, for steady laminar flames with the temperature range from room temperature to as high as 2200 K, temperature measurements by spontaneous Raman scattering is then relatively straightforward by using the shape of the Q-branch N_2 Raman spectra, as mentioned in the second approach. Once the detection of the vibrational Stokes Q-branch Raman signal of N_2 is achieved, temperature is then determined by least-square fitting the measured spectrum for N_2 to a library of theoretical spectra at different temperatures. A computer code CARSFT developed at Sandia¹⁴ for coherent anti-Stokes Raman spectroscopy is modified to analyze the Raman spectra. The quick-fit approach of Hall and Boedeker¹⁵ is used. Specifically, a library of nitrogen spectra spaced 50 K apart is first generated by convolving the spectra with the experimental instrument functions. Then the experimental spectra are least-square fitted to the library spectra. The fitting error is estimated conservatively by the temperature bounds where the experimental and theoretical spectra clearly differ¹⁶. The uncertainty in the fitted temperature is determined to be less than ± 50 K and the reproducibility of the measurements is within ± 20 K.

2.2 Laser Induced Fluorescence (LIF)

Raman spectroscopy cannot detect some important radical species in combustion processes, such as OH, CH, and pollutants NO, CO, which are often present with concentrations under the level of 0.1%. LIF spectroscopy, on the other hand, can resolve these intermediate at ppm or even sub-ppm levels.

LIF, as shown in Figure 2.4, can be viewed as absorption followed by spontaneous emission from the excited energy states of a molecule. More details can be obtained from Ref. 4 and Ref. 17.

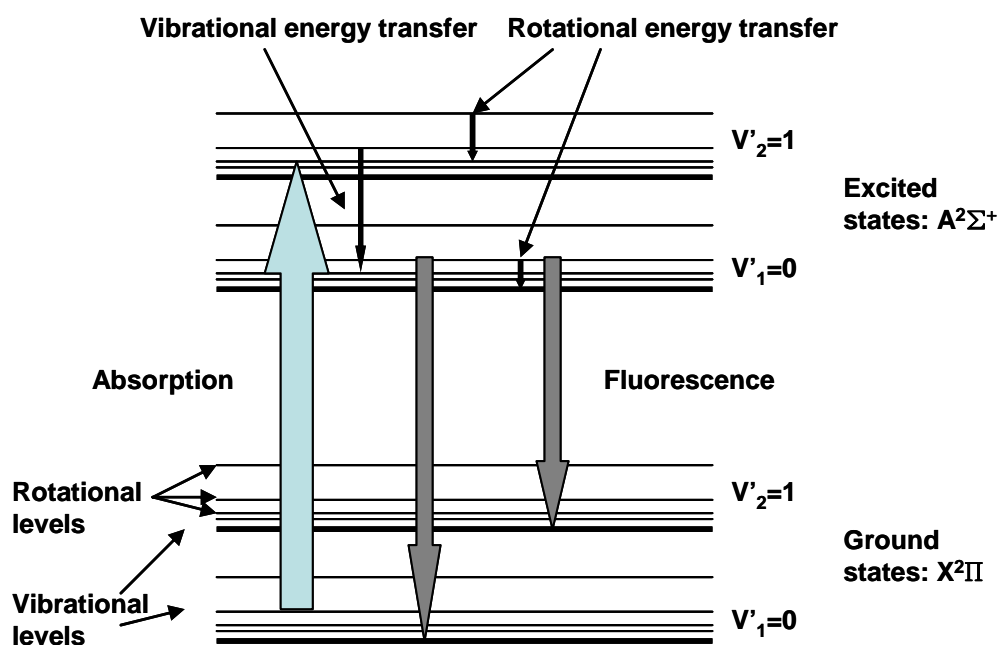


Figure 2.4. Energy level diagram of LIF

2.2.1 Spectroscopy of diatomic molecules

2.2.1.1 Notation for electron orbital in a molecule

Transitions between electron states are important in the study of LIF spectroscopy. The quantum state of an atom is characterized by principle quantum number n , the orbital angular momentum quantum number l , the magnetic quantum number m_l , and the electron spin quantum number s . The electron orbital in an atom is named as s, p, d, f, \dots with respect to orbital angular momentum quantum number $l = 0, 1, 2, 3, \dots$. Similarly, the electron orbital in a molecule is named as $\sigma, \pi, \delta, \varphi, \dots$ with respect to the angular momentum quantum number $\lambda = 0, 1, 2, 3, \dots$. The value of angular momentum quantum number λ for diatomic molecules is similar to the value of magnetic quantum number

$|m_l|$ for atoms, since the angular momentum for diatomic molecules strongly coupled with internuclear axis. There are at most two electrons at σ orbital while the maximum electrons for other orbitals are four, due to the double degeneracy of total orbital angular momentum.

In this chapter, the bold letters represent quantum vectors while regular letters represent quantum number. The Roman letters represent orbitals in an atom while Greek letters represent orbitals in a molecule. The letters in the lower case is the quantum value for a single electron, while the upper case is for the total quantum value for multielectron.

2.2.1.2 Multielectron atom

In a multielectron atom, the orbital angular momentum vector, \mathbf{L} , is the vector summation of l of each electron; the spin angular momentum vector, \mathbf{S} , is the vector summation of s of each electron. A closed inner shell has zero total orbital or spin angular momentum of an atom. Only the electrons in the outer partially filled shell are important for the coupling of angular momentum.

Russell-Saunders coupling (LS coupling): Russell-Saunders coupling or L-S coupling has an electron coupling vector $\mathbf{J}=\mathbf{L}+\mathbf{S}$, which is determined by $L=\sum l_i$ and $S=\sum s_i$. It is most often followed by light atoms since the spin-orbit interaction is weak for light atoms.

j-j coupling: The *j-j* coupling follows $\mathbf{j}_i=\mathbf{l}_i+\mathbf{s}_i$, and $\mathbf{J}=\sum \mathbf{j}_i$. It is usually followed by heavy atoms because the magnetic interaction of the orbital and spin angular momentum of a single electron is larger for heavy atoms. The shielding electrons in heavier atoms will increase the electric field in the electron cloud and enhance the magnetic field.

2.2.1.3 Diatomic molecule

Four coupling schemes, Hund's cases (a), (b), (c), and (d), are described as follows.

Cases (a) and (b) are the most common cases.

Hund's case (a): the electronic motion (spin and orbital) is coupled strongly with the inter-nuclear axis, but coupled weakly with nuclear rotation. This case is denoted as $\mathbf{L} \rightarrow \mathbf{\Lambda}$ and $\mathbf{S} \rightarrow \mathbf{\Sigma}$, where \rightarrow means the projection onto the internuclear axis.

Hund's case (b): the spin is weakly coupled to the inter-nuclear axis, so $\mathbf{\Lambda}$ is coupled with rotational angular momentum first. This case is denoted as $\mathbf{N} = \mathbf{\Lambda} + \mathbf{R}$ and $\mathbf{J} = \mathbf{N} + \mathbf{S}$.

Hund's case (c): both the spin and the orbital angular momentum are weakly coupled with the internuclear axis; however, both angular momenta are strongly coupled. This case is denoted as $\mathbf{J}_n = \mathbf{L} + \mathbf{S}$, $\mathbf{J}_n \rightarrow \mathbf{\Omega}$, and $\mathbf{J} = \mathbf{\Omega} + \mathbf{R}$.

Hund's case (d): the electronic motion is coupled strongly with the rotational axis rather than the internuclear axis. This case is denoted as $\mathbf{L} = \mathbf{R} + \mathbf{L} + \mathbf{S}$.

Hund's case (e): a variation of case (d) is that \mathbf{L} and \mathbf{S} are coupled to \mathbf{J}_n , and \mathbf{J}_n is coupled with \mathbf{R} to \mathbf{L} . No practical examples of this case (e) have been observed.

2.2.2 Experimental strategy

An LIF experimental arrangement includes two major systems: a wavelength-tunable laser and a fluorescence detection system (Fig. 2.5).

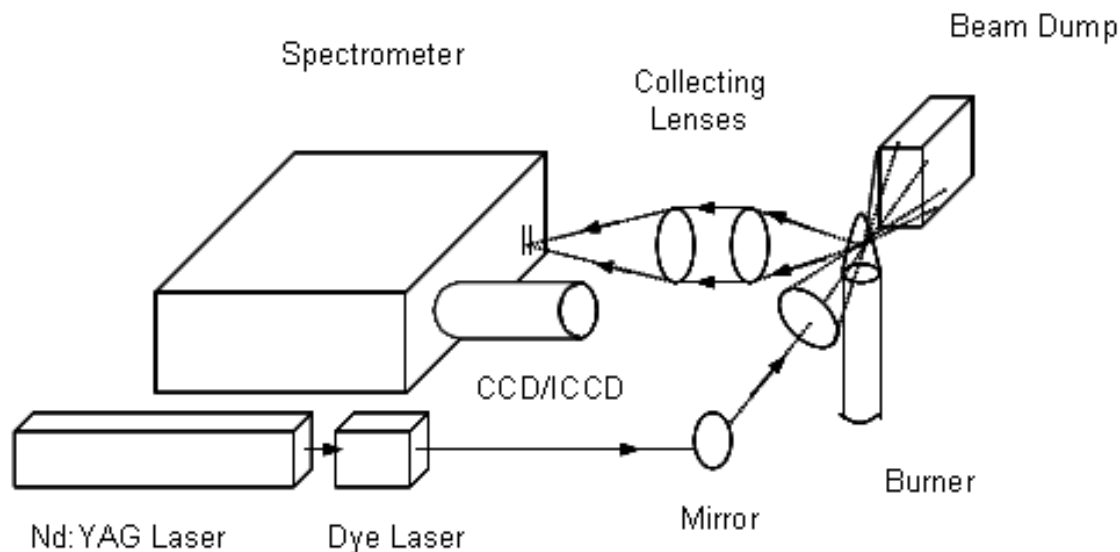


Figure 2.5. Generalized experimental schematic for LIF with a simple two mirror scheme for image rotation. (Reproduced from Ref. 4)

The wavelength tunable laser system typically consists of a pump laser, a dye laser, and a frequency converter to the dye laser. High quality, high energy Nd:YAG laser is available for a variety of LIF excitation. The pump beam from the Nd:YAG laser at the second (532 nm) or third (355 nm) harmonic is used for dye laser pumping. The choice of pumping laser wavelength is based on the dye type in the dye laser and the final frequency needed. The Nd:YAG laser is often injection seeded for a temporally smooth dye laser profile. The dye laser consists of a transversely pumped oscillator and one or two stages of amplification, transversely or longitudinally pumped. Prism or grating beam expansion will typically produce dye linewidths on the order of $0.1\text{--}0.2\text{ cm}^{-1}$. With etalons inserted into the cavity, linewidths in the range of $0.01\text{--}0.05\text{ cm}^{-1}$ can be achieved at the expense of laser energy. The tunable dye laser beam enters the frequency converter for frequency doubling or mixing, to obtain the desired output frequency.

There are basically two ways of obtaining fluorescence spectra. One is to tune the

laser to a specific absorbing transition, and monitor the fluorescence. The other is to perform excitation scans; in this case, the laser is tuned across the absorbing transitions in a given spectral region, and the excited fluorescence is monitored over a broad spectral range using wide spectrometer slits or a broadband interference filter. The absorption spectrum obtained through the excitation provides information about the ground or lower state population distribution. The laser-induced fluorescence spectrum reveals upper state population dynamics. This is the basis for LIF measurement in this study.

The tunable laser excitation is focused into the measurement region, and the LIF signal is collected, typically at right angles. Usually, tight, low $f/\#$ focusing optics is employed to achieve high spatial resolution, and high laser spectral irradiances are required to reach saturation. Since most monochromators or spectrometers possess vertical slits but most scattering experiments are arranged in a horizontal scattering plane, an image rotation is required for the measurements. A design of two mirrors arranged to achieve a 90 degree deviation and beam elevation change¹⁸ or dove prisms solve the problem.

A photomultiplier tube or CCD camera is used as detector for LIF signals. The requirement for the detector is to have sufficient time response to temporally resolve the LIF signal. The detector output can be accumulated over many pulses in the gated integrator or sent to a computer pulse by pulse for subsequent manipulation and processing.

2.2.3 Interference

Laser-induced fluorescence may encounter interference by other light sources. There are

four main interferences: (1) elastic scattering (Mie) from particles, (2) laser-induced incandescence, (3) thermal radiation, and (4) laser scattering. Beam absorption and fluorescence self-absorption can also influence the interpretation of the LIF signal. The choice of the excitation and collection strategy is critical to reduce the magnitude of the above interferences and to obtain a good LIF result.

The elastic Mie scattering can be reduced by the following three ways. First, using a polarized excitation laser and collecting only the LIF that has a polarization perpendicular to the laser polarization direction, most of the Mie scattering will be rejected while the LIF intensity will only be reduced by half. A second option is to collect the fluorescence perpendicular to the incident beam and parallel to the polarization direction. A third option is to collect LIF at a wavelength different from the excitation wavelength, as is adopted in the current study.

Laser-induced incandescence can be neglected, since the particles do not absorb appreciably at the excitation wavelength. A pulsed laser is helpful to reduce the thermal radiation effect. Collecting LIF in ~ 100 ns immediately after the laser pulse will reduce background signal by 10^7 , greatly minimizing the background signal by thermal radiation. Beam absorption is minimized by choosing a transition with minimal absorption coefficient. For example, the (1,0) transition for excitation of OH molecules is chosen so that only $\sim 1\%$ is absorbed along the path. For the reduction of fluorescence self-absorption, the fluorescence that can only excite less populated states is chosen. For OH LIF is collected for the (1,1) transition since the fractional population at $v''=1$ is only ~ 0.001 .

Rayleigh scattering and beam scattering can be blocked by spectral filters. Lucht et

al¹⁹ and Eckbreth found that the interference from rotational Raman scattering of N₂ becomes significant for low OH concentrations (~5 ppm). Radiative transitions from a given upper level should be selected to avoid rotational Raman bands. For OH, this can be accomplished by pumping the (1,0) band and collecting fluorescence in the (1,1) band, as recommended by Refs. 4 and 20.

2.2.4 Two-line temperature measurement

According to the knowledge of spectroscopy of diatomic molecules, the hetero-nuclear diatomic molecule OH, has 9 electrons, represented as $(ls\sigma)^2(2sa)^2(2pa)^2(2p\pi)^3$ using the united-atom model notation. There are 3 electrons in this partially filled orbital $2p\pi$, so we have $L=1-1+1=1$ and $S=(1/2)-(1/2)+(1/2)=(1/2)$. Since $\Lambda=0, 1 \dots L$, and $\Sigma=S, S-1 \dots -S$, we obtain $\Lambda=0$ or 1 , and $\Sigma=(1/2)$ or $-(1/2)$ for the molecule OH. If $\Lambda=0$, the electron level is denoted as $^2\Sigma^+$, while if $\Lambda=1$, the electron level is $^2\Pi$. The ground electronic state, $^2\Pi$, is also denoted as $X^2\Pi$; the next lowest level, $^2\Sigma$ is denoted as $A^2\Sigma^+$.

The fluorescence signal is proportional to the population density n_j of the ground state probed, and the Einstein coefficient A and B. The coefficients are determined by specific electron levels, while the population density n_j is an exponential function of temperature and the degeneracy. Therefore, if the degeneracy is known, the temperature can be obtained by combining the fluorescence equation with fluorescence measured at two different transitions. Specifically, we excite $^2\Pi$ to $^2\Sigma^+$ of the (1,0) transition and collect the fluorescence of the (1,1) transition. In this case, Einstein's coefficient B of the excitation is obtained from Ref. 21; Einstein's coefficient A of spontaneous emission is estimated by summing A coefficients for all allowed transitions from the excited upper state. The parameters are shown in Chapter 5 where the

calculation is carried out.

The fluorescence signal is acquired within the collection interval of 100 ns, compared with the fluorescence lifetime of 50 ns. The short collection time will minimize the effect of quench rate variations, and therefore the decay of the fluorescence. The total signal S_f is the integration of fluorescence I_f over the collection interval t :

$$S_f = \int I_f dt \quad (2.10)$$

The relationship between upper level and ground level populations under linear region or saturated conditions are different:

Linear:

$$N_2 \propto B_{12} N_1 \quad (2.10)$$

Saturated:

$$N_2 \propto \frac{g_2}{g_1 + g_2} N_1 \quad (2.11)$$

For the two excitation schemes, the ratio of lower levels is represented in the following equations according to either region, i.e., linear and steady state, respectively.

Linear:

$$\left(\frac{N_{1,A}}{N_{1,B}} \right)_{linear} = \frac{N_{2,A} B_{12,B}}{N_{2,B} B_{12,A}} \quad (2.12)$$

Saturated

$$\left(\frac{N_{1,A}}{N_{1,B}} \right)_{saturated} = \frac{N_{2,A} \left(\frac{g_2}{g_1 + g_2} \right)_B}{N_{2,B} \left(\frac{g_2}{g_1 + g_2} \right)_A} \quad (2.13)$$

The ratio of excited state populations will be independent of whether the excitation is in the linear or saturated regime, if Equation 2.14 is valid:

$$\left(\frac{B_{12}(g_1 + g_2)}{g_2} \right)_B = \left(\frac{B_{12}(g_1 + g_2)}{g_2} \right)_A \quad (2.14)$$

From Equations 2.12 to 2.14, it is deduced that the constant of proportionality between $N_{2,A}/N_{2,B}$ (which we measure) and $N_{1,A}/N_{1,B}$ (which we use to infer temperature) is the same whether it is in the linear or saturated region. For $P_2(7)$ and $P_2(9)$ transitions this equality in Equation 2.14 holds to about 3%.

Now, by assuming linear conditions:

$$S_f = \int I_f dt \propto N_2 A_{21} = N_1 B_{12} A_{21} \quad (2.15)$$

The temperature can be obtained by comparison between populations of two ground rotational levels. The rotational population is governed by Boltzmann equation:

$$N_j = N \frac{g_j e^{-\epsilon_j/kT}}{\sum_j g_j e^{-\epsilon_j/kT}} \quad (2.16)$$

The fluorescence signal can be related to the ground level population, and thus the temperature (Equation 2.17).

$$\frac{(S_f)_{J'=5.5}}{(S_f)_{J'=7.5}} = \frac{(gB_{12}A_{21})_{J'=5.5}}{(gB_{12}A_{21})_{J'=7.5}} e^{-(E_7-E_9)/kT} \quad (2.17)$$

Equation 2.18 gives the gas-phase temperature once the fluorescence intensity of $P_2(7)$ and $P_2(9)$ transitions (S_9/S_7) are known.

$$T = \frac{(E_9 - E_7)/k}{\ln \left[\frac{(gB_{12}A_{21})_{P_2(7)} S_9}{(gB_{12}A_{21})_{P_2(9)} S_7} \right]} \quad (2.18)$$

2.2.5 OH concentration measurement

For concentration measurements, the rotational transition state is chosen so that the fractional population is relatively insensitive to temperature fluctuations. The signal intensity is then only proportional to the number density. The detailed procedure for choosing such a state is as follows.

Calculate the fractional population for all rotational states at a given temperature, assuming all rotational states are in thermal equilibrium, i.e., Boltzmann equilibrium. For the fraction of molecules in state J , from the Boltzmann expression⁴,

$$f_J = \frac{hcB_v}{kT} (2J+1) \exp[-B_v J(J+1)hc / kT] \quad (2.19)$$

we can find the rotational state that is least sensitive to temperature fluctuations by evaluating the derivative of f_J with respect to temperature and equating it to zero:

$$J^2 + J - \left(\frac{k}{hcB_v} \right) T = 0 \quad (2.20)$$

In the case of OH molecules, this gives $J=7.5$. In Figure 2.6, the Boltzmann distribution is also plotted for a series of temperatures from 1000 K to 2600 K. Here the temperature dependence of the Boltzmann fraction of the absorbing state plays a relatively minor role in interpreting the signal in the regions observed to contain OH, and the fluorescence intensity can be qualitatively linked to OH mole fraction. So in this study, the $Q_1(7)$ line (283.222 nm from LIFBASE²²) is excited, and LIF spectra are collected at 314.695 nm (from LIFBASE).

Table 2.3 summarizes the excitation and collection schemes for various diatomic molecules.

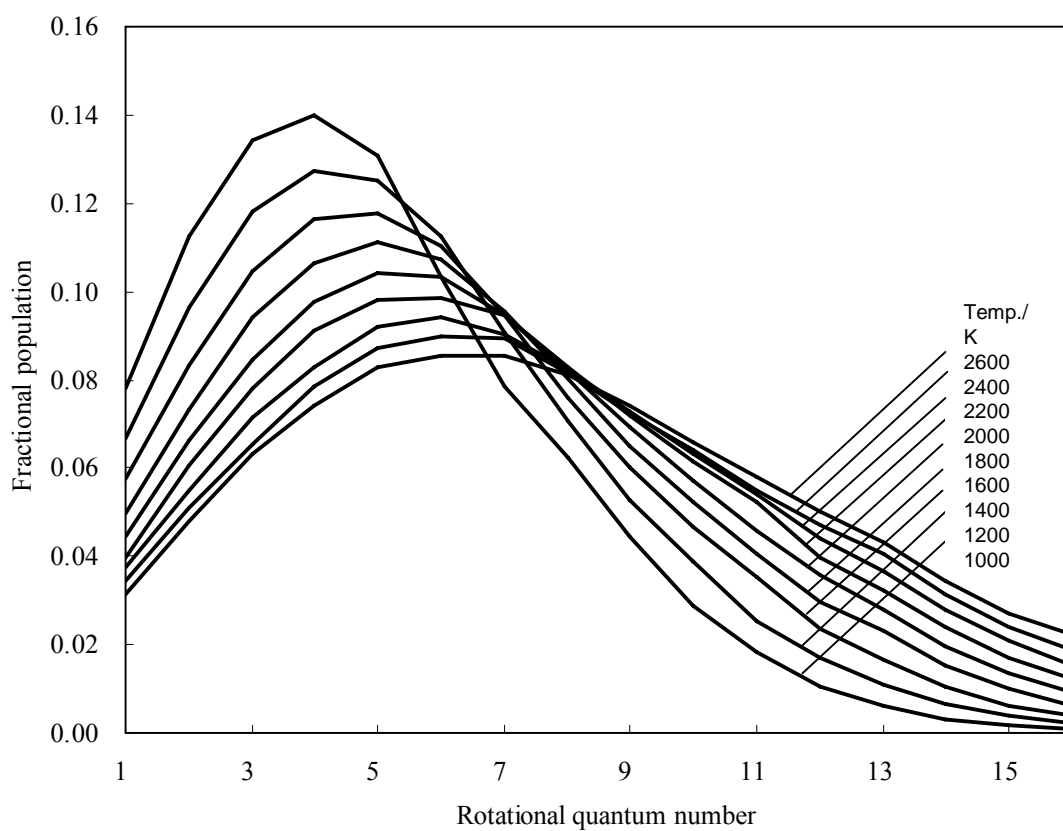


Figure 2.6. Boltzmann distribution for different rotational levels of OH diatomic molecule at various temperatures. (Reproduced from Ref.23)

Table 2.3 Probing schemes for LIF

Function	Molecule	Excitation wavelength	Electronic state	Vibrational state	Rotational state	Electronic state	Vibrational state
Intensity	OH	282	$A^2\Sigma^+ \leftarrow X^2\Pi$	(1-0)	$Q_1(7)$	$A^2\Sigma^+ \leftarrow X^2\Pi$	(1-1)
T	OH	282	$A^2\Sigma^+ \leftarrow X^2\Pi$	(1-0)	$P_2(7) P_2(9)$	$A^2\Sigma^+ \leftarrow X^2\Pi$	(1-1)

2.3 Other Diagnostic Techniques

2.3.1 Chemiluminescence

Specific chemical reactions in flames result in optical flame emission, indicating non-equilibrium concentrations of molecules and their electronic transitions from the excited states. As a result of such chemical reactions, chemiluminescence has been used to characterize the spectroscopy and the reactions producing identified emissions. Gaydon²⁴ provides an excellent summary of the emission spectra of flames and possible reactions. For hydrocarbon flames, most light comes from OH (A-X) at 280 to 310 nm, CH (A-X) at 430 nm, CH (B-X) at 390 nm, C₂ (d-a) Swan bands found mostly between 470 to 550 nm, CO₂ band continuum, HCO hydrocarbon bands between 300 to 500 nm, and polynuclear aromatic molecules and luminescent soot emitting in the visible in fuel rich systems²⁵.

2.3.2 Photoluminescence (PL)

Photoluminescence is the spontaneous emission of light from a material under optical excitation²⁶. When light of sufficient energy is incident on a material, photons are absorbed and electronic excitations are created. Eventually, these excitations relax and the electrons return to the ground state. The photoluminescence in this process can be collected and analyzed to yield information about the photo-excited material. The photoluminescence spectrum provides the transition energies, useful to determine electronic energy levels. Compared with other optical methods of characterization like reflection and absorption, PL is less stringent about beam alignment, surface flatness, and sample thickness.

2.3.3 Laser light scattering (LLS)

In addition to various electron microscopes, light scattering techniques are also employed for particle size measurement. One of the easiest is laser light scattering (LLS), using scattering of visible laser light to characterize particles in the size range from a few nanometers to a few microns. Scattered laser light has been used for several decades in combustion systems for particle sizing²⁷. In the current research, strong LLS signal along the flame synthesis path reveals the presence of nanoparticles.

2.3.4 *In-situ* sampling and nano-scanning mobility particle sizer (nano-SMPS)

A nano-SMPS is a combination of a nano-differential-mobility analyzer (nano-DMA, model 3085) and a condensation particle counter (CPC, model 3025A). The nano-DMA separates particles according to charge and electrical mobility for size classification. The CPC grows the particles to a detectible size for counting. During synthesis, the synthesized nanoparticles can be *in-situ* characterized by sampling the aerosol from the flame, quenching it quickly (to freeze further chemical reactions and particle growth through large volume dilution), and then sending the well-diluted aerosol to a nano-scanning mobility particle sizer (nano-SMPS). A low-pressure aerosol sampling system specially designed to couple the low-pressure synthesis reactor to the commercial nano-SMPS instrument that operates only at atmospheric pressure is employed²⁸.

2.4 *Ex-situ* Nanopowder Characterization

The as-synthesized particles are characterized to obtain the important nanopowder properties including aggregate particle size, primary particle size, specific surface area, particle morphology, crystallinity, and phase composition.

2.4.1 X-Ray diffraction (XRD)

XRD is a powerful quantitative tool for identifying crystal structure in powder or film samples²⁹. The crystalline phases diffract X-rays according to Bragg's equation,

$$n\lambda = 2d \sin q \quad (2.21)$$

which relates lattice spacing d to X-ray wavelength λ (q is the angle of diffraction). The Scherrer equation can be used to relate the widths of the peaks to the crystallite size:

$$d = \frac{k \times \lambda}{FWHM \times \pi / 180 \times \cos \theta} \quad (2.22)$$

where k is the shape factor of the average crystallite, λ the wavelength, and θ the diffraction angle.

2.4.2 Transmission electron microscopy (TEM)

Transmission electron microscopy (TEM) is a technique using electrons instead of light as transmitted beam to form a high resolution image of the specimen³⁰. In the synthesis of TiO₂ and *c*-BN nanoparticles, TEM (model TOPCON 002B) is used to get the morphologies and the grain sizes^{28,31}. The atomic-level structures of these particles can be examined using high resolution TEM (HRTEM). Selected area diffraction (SAD) is performed to evaluate the crystallinity and phase composition of individual (or a group of) nanoparticles.

2.4.3 Scanning electron microscopy (SEM)

Scanning electron microscopy (SEM) is a basic tool to observe the morphologies of as-grown nanostructures, and estimate the size and yield of those nanostructures³². Our SEM is used with a field emission electron source (FESEM, LEO Zeiss Gemini 982) to investigate the morphologies of 1D nanostructures produced from flames, and estimate

the size and yield of these structures at various magnifications ranging from 1000 to 50000.

2.4.4 Energy-dispersive X-ray spectroscopy (EDXS)

The elemental compositions of as-prepared nanomaterials from flames are analyzed using EDXS attached to either TEM or FESEM. EDXS is conducted for nanomaterials ranging from a single nanostructure to bundles of nanostructures.

2.4.5 Raman microscopy

Raman microscopy is a specialized optical microscopy using lasers as monochromatic light source. A Raman spectrometer is coupled to it to detect the scattered Raman signals from the material. Raman microscopy can resolve parts with different chemical composition in a sample, and, together with infrared microscopy, is sometimes referred as *chemical imaging*. The as-synthesized TiO₂ nanoparticles are analyzed by a Raman microscope (Renishaw inVia) to determine the specific phase information.

2.4.6 Thermogravimetric analysis (TGA)

TGA calculates the weight loss of nanopowders upon temperature change. Model Perkin-Elmer TGA 6 is used to determine the extent of precursor decomposition/conversion in as-synthesized TiO₂ nanoparticles. The atmosphere is oxygen, and the heating rates are: 30-200 °C at 5 °C /min, and then 200-900 °C at 10 °C /min.

References

- ¹ J.R. Ferraro, and N. Kazuo, *Introductory Raman Spectroscopy* (Academic Press, Boston, 1994).
- ² I.R. Lewis, and G. M. Howell, *Handbook of Raman Spectroscopy: From the Research Laboratory to the Process Line* (Marcel Dekker, New York, 2001).
- ³ R.L. McCreery, *Raman Spectroscopy for Chemical Analysis, Chemical analysis*, v. 157 (John Wiley & Sons, New York, 2000).
- ⁴ A.C. Eckbreth, *Laser Diagnostics for Combustion Temperature and Species* (Gordon and Breach Publishers, Amsterdam, The Netherlands, 1996).
- ⁵ K. Kohse-Hoinghaus, and J. B. Jeffries, *Applied combustion diagnostics* (Taylor & Francis, New York, 2002).
- ⁶ http://en.wikipedia.org/wiki/Raman_spectroscopy, accessed on August 30, 2009.
- ⁷ R. Aroca, *Surface Enhanced Vibrational Spectroscopy* (Wiley, Hoboken, NJ, 2006).
- ⁸ D.A. Long, *The Raman Effect A Unified Treatment of the Theory of Raman Scattering by Molecules* (Wiley, Chichester, 2002).
- ⁹ R.E. Palmer, The CARSFT Computer Code for Calculating Coherent Anti-Stokes Raman Spectra: User and Programmer Information, Sandia Nat'l Lab Report SAND89 8206 (1989).
- ¹⁰ R.W. Dibble, et al., The spontaneous Raman scattering technique applied to nonpremixed flames of methane, *Combust. Flame* 67, 189-206 (1987).
- ¹¹ PF Jessen, and AG Gaydon, Estimation of carbon radical concentrations in fuel-rich acetylene-oxygen flames by absorption, *Proceedings of the Combustion Institute* 27, 764 (1998)
- ¹² Masri, A.R. and Bilger, R.W., ``Fluorescence`` interference with Raman measurements in nonpremixed flames of methane, *Combust. Flame* 68, 2, 109-120 (1987).
- ¹³ M. Lapp, L. M. Goldman, and C. M. Penney, *Science* 175, 1112 (1972).
- ¹⁴ R. L. Farrow, R. P. Lucht, G. L. Clark, and R. E. Palmer, Species concentration measurements using CARS with nonresonant susceptibility normalization, *Appl. Opt.* 24, 2241-2251 (1985).
- ¹⁵ R. J. Hall, and L. R. Boedeker, CARS thermometry in fuel-rich combustion zones, *Appl. Opt.* 23, 1340-1346 (1984).
- ¹⁶ M. D. Allendorf, et al., Temperature measurements in a vapor axial deposition flame by spontaneous Raman spectroscopy, *J. Appl. Phys.* 66, 5046 (1989).
- ¹⁷ J. W. Daily, Laser induced fluorescence spectroscopy in flames, *Progress in Energy and Combustion Science*, 23, 133 (1997).
- ¹⁸ R.P. Lucht, Laser-Saturated Fluorescence Measurements of OH Concentration in Flames, *Combust. Flame* 50, 189-205 (1983).
- ¹⁹ R.P. Lucht, et al., Laser-Saturated Fluorescence Measurements of OH in Atmospheric Pressure CH₄/O₂/N₂ Flames Under Sooting and Non-Sooting Conditions, *Combust. Sci. Tech.* 42, 5 (1985).
- ²⁰ N. M. Laurendeau, and J. E. M. Goldsmith, Comparison of Hydroxyl Concentration Profiles using Five Laser-Induced Fluorescence Methods in a Lean Subatmospheric-Pressure H₂/O₂/Ar Flame, *Combustion Science and Technology* 63, 1 (1989).
- ²¹ I. L. Chidsey and D. R. J. Crosley, Calculated rotational transition probabilities for the A-X system of OH, *Quant. Spectrosc. Radiat. Transf.* 23, 187 (1980).
- ²² J. Luque, and D. R. Crosley, *LIFBASE: database and spectral simulation program* (Version 2.0), SRI. International Report MP, 99-009 (1999).
- ²³ M.R. Zachariah, and D.R.F. Burgess, Strategies for laser excited fluorescence spectroscopy. Measurements of gas phase species during particle formation, *J. Aerosol. Sci.* 25, 487 (1994).
- ²⁴ A.G. Gaydon, *The Spectroscopy of Flames*, 2nd ed. (John Wiley & Sons, New York, 1974).
- ²⁵ G.P. Smith, et al., Low pressure flame determinations of rate constants for OH(A) and CH(A) chemiluminescence, *Combust. Flame* 131, 59-69 (2002).
- ²⁶ D. A. McQuarrie, and J. D. Simon, *Physical Chemistry, a molecular approach* (University Science Books, 1997).
- ²⁷ J. M. Bernard, *Particle Sizing in Combustion Systems Using Scattered Laser Light*. (The Aerospace Corp, El Segundo, CA, 1988).
- ²⁸ H. Zhao, X. Liu, and S.D. Tse, Effects of Pressure and Precursor Loading in the Flame Synthesis of Titania Nanoparticles, *Journal of Aerosol Science*, in press (available online 6 Aug 2009).

-
- ²⁹ B. E. Warren, *X-Ray Diffraction* (Dover Publications, New York, 1990).
- ³⁰ D. B. Williams, and C. B. Carter., *Transmission Electron Microscopy: A Textbook for Materials Science* (Plenum Press, New York, 1996).
- ³¹ H. Zhao, X. Liu, and S.D. Tse, Control of Nanoparticle size and Agglomeration through Electric-field-enhanced Flame Synthesis, invited paper, *Journal of Nanoparticle Research* 10, 907-923 (2008).
- ³² Z. L. Wang, *Characterization of Nanophase Materials* (Wiley-VCH, Weinheim, 2000).

Chapter 3

Literature Review of the Application of *in-situ* Laser-based Diagnostics to Gas-phase Synthesis

In Chapter 2, two spectroscopic laser-based techniques (SRS and LIF) were reviewed in detail for the *in-situ* diagnostics used to measure gas-phase species concentrations and temperatures in this work. Both *ex-situ* characterization of as-synthesized nanomaterials (i.e. aggregate particle size, primary particle size, specific surface area, particle morphology, crystallinity, and phase composition) and *in-situ* laser-based diagnostics are necessary to reveal the fundamental mechanisms of the synthesis process.

In this chapter, major advantages of laser-based diagnostics for *in situ* measurements are introduced, followed by a review of *in-situ* laser-based diagnostics that have been applied to gas-phase synthesis.

3.1 Introduction

Laser-based diagnostics have several advantages which make them suitable for gas-phase synthesis of nanomaterials. Laser-based diagnostics are non-intrusive probes to measure the target, as well as the synthesis conditions. In most cases, the laser energy is not high enough to change the environment or the materials inside. It does not disturb the flow field, temperature, or chemical composition in the synthesis system where the measurement is taken. The configuration is often flexible, permitting investigation of high temperature or high/low pressure systems.

Another advantage of laser-based diagnostics lies in its spatial-precision. The laser probe can be manipulated to form a tiny measurement volume of 10^{-12} m^3 . The third

advantage is that temporally-precise measurements are available considering today's ultra short pulse lasers (picoseconds (10^{-12} s) or femtoseconds (10^{-15} s)). This is helpful to study the dynamics of some very fast processes.

For gas-phase synthesis, a variety of *in-situ* laser-based diagnostics techniques have been applied. In this chapter, laser-induced fluorescence (LIF)^{1,2,3}, Raman scattering (SRS)^{4,5,6,7,8}, Fourier transform infrared (FTIR) spectroscopy^{9,10}, ultra-small-angle x-ray scattering (SAXS)¹¹, laser light scattering (LLS)¹², laser-induced breakdown spectroscopy (LIBS)¹³, and laser-induced incandescence (LII)¹⁴ are reviewed for their applications to *in-situ* laser-based diagnostics, mostly related to flame synthesis. No single technique can provide all the information for the synthesis process. The arrangement of the following introduction will base on both the specific technique and its measurement capability.

3.2 Literature Review

3.2.1 Laser induced fluorescence (LIF)

Laser induced fluorescence (LIF) as a laser diagnostic technique for combustion research has been widely adopted for a long time¹⁵. More general knowledge including spectroscopic and thermodynamic background, and experimental methods can be found in Refs. 16 and 17. LIF was found to be a valuable technique for gas-phase species measurement in a variety of chemical reacting systems^{18,19,20, 21}, and is both highly sensitive and selective for atoms and small molecules. In gas-phase particle synthesis, the non-intrusive diagnostics has been utilized to obtain temperature and radial species concentration in gas phase^{1,22}, and metalorganic monoxides profiles^{2,3,22}.

The concentration a molecule is related to the Boltzmann distribution of its rotational

states, which is dependent upon temperature. Therefore any concentration measurement must account for this effect, particularly if the probed system is not isothermal. The most convenient way to correct for this effect is to probe a rotational state which is only weakly dependent on temperature. Zachariah and Burgess²² used the $P_1(8)$ OH rotation line for the concentration measurements, with the uncertainty in the concentration measurement only $\pm 5\%$ over the range $T = 1500\text{-}2500$ K assuming no knowledge of the temperature.

Near-surface laser induced fluorescence (LIF) measured the radial OH in the post-flame region of a low-pressure hydrogen/oxygen stagnation flames above catalytic¹ and non-catalytic surfaces and NO in $H_2/O_2/NH_3$ stagnation point flames over platinum substrates²³. The measured number densities of OH and NO near the substrate were sensitive to the changes in surface reaction rates, and were used as a test of surface chemical mechanisms^{1,23}. LIF was also used to study the catalytic removal of NO from post-flame gases in low-pressure stagnation-point flames over platinum and palladium substrates^{24,25}. The results helped to further study the effect of synthesis parameters on the nanoparticles. Qualitative 2-D measurements of OH radical concentrations were made by using a planar laser-induced fluorescence (PLIF) technique in a silica-generating flame²⁶. In their PLIF technique²⁷, they excited the OH radical using the $Q_1(6)$ line at 282.95 nm with $A^2\Sigma^+ - X^2\Pi$ (1, 0) transition, which has been reported^{28, 29} to result in the weakest temperature dependence of the fluorescence signal across the flame flow field.

Flame temperature can affect the flame structure and the process of aerosol formation/growth including chemical reactions, surface growth, coagulation, sintering, transport, and deposition of particles. Therefore, accurate measurement of the temperature distribution in particle synthesis flames is useful to understand particle

formation mechanisms and to control particle growth^{26,30}. Laser-induced fluorescence of OH was applied to measure the actual temperatures in high-flow rate, fuel-rich acetylene/oxygen flames and to compare them with the predictions of a 1-D stagnation flame model^{1,31}. Two-line temperature technique was usually used by exciting two strategically selected transitions of the (1-0) OH band, which reduced the effect of saturation on the derived temperatures. As an alternative, two-line^{32,33} or multiline^{34,35} laser-induced fluorescence of NO seeded into low-pressure methane synthesis flames were also measured. The gas phase LIF measurements on OH/NO concentrations and temperatures validated the combustion model to predict the primary chemical structure of the flame, as well as the temperature profile.

LIF has also been used to measure intermediate precursor species, e.g., TiO, AlO, SiO, SnO, PbO, and FeO, between gas-phase monomers and solid-phase nanoparticles. For flame synthesis and CVD process, the profiles of monoxide species are good indicators of the progress of precursor pyrolysis since they typically appear early in the decomposition process of metalorganics. On the other hand, the destruction of the monoxide specie in a flame is also sensitively linked to the particle formation process because it can condense onto solid particles and is likely a key intermediate in gas-phase metal oxide production.

Using LIF, Glumac et al.³⁶ detected the monoxides in flames using moderate laser powers and generated spatial number density profiles under varying conditions. Interference broadband fluorescence on TiO and AlO detection was suppressed by careful selection of excitation and collection wavelengths. The radical species SiO is found in nearly all reacting systems containing silicon and oxygen. For LIF measurements, the P(37) line in the (1-0) band of the A-X transition near 231 nm was used, which has a

very small dependence on temperature, minimizing the temperature correction required in the data processing³⁷. This line is particularly free from interferences of other transitions including those of O₂²². Similarly, LIF detections have been performed in flames on other metal monoxide species including SnO³⁸, FeO³⁹, and PbO⁴⁰.

3.2.2 Spontaneous Raman spectroscopy (SRS)

In situ Raman spectroscopy is suitable for CVD processes because it can be used at very high temperatures, with no restriction on the gas pressure. It has been employed to study gas-phase synthesis of carbon nanotubes (CNT)^{4,41,42}. *In situ* Raman spectroscopy of nanotubes grown by chemical vapor deposition has mainly been focused on investigating the D–G band of carbon nanotubes – in most cases the amount of carbon nanotubes present is related to the evolution of the integrated G-band area. In Ref. 4, high-purity single-walled carbon nanotubes (SWNTs) was produced by alcohol catalytic CVD (ACCVD) without use of an electric furnace or a hot filament. A vacuum chamber unit for a scanning probe microscope (SPM) was used as a simple CVD apparatus. A typical 2 mW Raman excitation laser was focused to a 2 μm spot and the scattered light was collected through a top observation window of the vacuum chamber unit. *In situ* Raman scattering was then applied during the growth stage in the vacuum chamber to measure surface temperature by a systematic shift in the silicon signal. Raman scattering also showed that the G-band intensity of the SWNT Raman spectrum increased nearly linearly with time in the growth stage after an initial rapid increase.

Recently, *in situ* Raman spectroscopy characterization was extended by Kaminska *et al*^{41,42} to obtain the so called global Raman imaging (GRI) for the CVD growth of CNT. GRI is accomplished by illuminating an area of interest on the sample by a defocused

spot, collecting the Raman scattered light with an objective and then detecting the signal with an electron multiplying charge coupled detector (CCD) camera. A lens is used to focus the incident beam before the objective in order to obtain a defocused spot necessary to produce global illumination on the sample. The optical setup also allows simultaneous spectroscopy measurements that complement the imaging data. The same technique was employed by Dittmer *et al.*⁴³ to monitor the onset of growth and to investigate the diameter distribution of the nanotubes as a function of time.

Gas phase synthesis is the most promising method for diamond growth, from both technical and economical points of view⁴⁴. The *in situ* characterization of a diamond film during synthesis can contribute to the understanding of the growth mechanism. Ref. 5 carried out *in situ* Raman analysis during the growth of diamond films on single-crystal alumina substrates in a microwave plasma reactor. Raman peak shifts dependences on temperature and stress were studied. Ref. 6 obtained the Raman spectra of diamond films in real time during their growth in plasma CVD reactors. Both studies used a pulsed laser and gated detection to reduce substantially the level of the thermal photons emitted by the substrate and to minimize the visible spectrum of the plasma.

Transition metal oxides supported on inorganic oxides play a crucial role as heterogeneous catalysts in chemical industries^{45, 46}. Raman spectroscopy can obtain detailed information about the molecular structure of the metal oxide overlayer on oxide supports. Raman spectroscopy was applied for studying the structural changes of the surface metal oxide species under *in situ* conditions where the temperature and gas composition of the catalyst could be controlled^{47, 48}. The supported metal oxide systems studied to date with *in situ* Raman spectroscopy include molybdenum oxide, tungsten

oxide, vanadium oxide, rhenium oxide, niobium oxide, which have been reviewed by Wachs⁴⁸ in detail.

The phase or crystallinity change of the materials during a chemical process can be monitored by their Raman signature^{7,8,49,50}. In Ref. 7, titania film prepared by ion-beam sputtering on a glass substrate was studied by Raman spectroscopy. The phase composition of the film, which includes a mixture of anatase, rutile, and amorphous phases, was monitored by detecting the anatase peak “*in situ*”; rutile growth was determined indirectly by sequential annealing. Although this is not a direct *in situ* study, it is an effort to monitor the continuous process. The technique can be applied to probe the deposition process *in situ*.

In situ Raman spectroscopy was also applied to the phase transition of boron nitride induced by laser heating⁸. By monitoring the Raman peaks at 790 and 1366 cm⁻¹, the cubic phase was found to transform to the rhombohedral phase above 1795 ± 80K. Solid-phase temperatures have been determined using the Stokes and anti-Stokes intensity ratios by Refs. 8 and 51.

As shown in this section, the Raman spectroscopy for materials synthesis have been focused on the solid-phase final products. To the best of our knowledge and literature search, it appears that we are the only ones to use gas-phase Raman spectroscopy for such studies, as presented in this thesis.

3.2.3 Fourier transform infrared (FTIR)

Of the many *in situ* techniques for monitoring combustion processes, Fourier transform infrared (FTIR) spectroscopy is particularly attractive for online monitoring of flame-made particles, as it can simultaneously provide information on flame temperature in

the presence of particles, as well as on gas composition and particle concentrations during synthesis^{9,52}. This technique is based on the relationship between the measured infrared absorbance and the absorption of gases and extinction of particles. *In situ* FTIR spectroscopy can provide valuable information using a combination of emission and transmission measurements (E/T). The transmission measurements yield information on the gas-phase composition as well as the particle composition, mass fraction, and size; the emission measurements contain information on the temperatures of gases and particles^{53,54,55,56}.

In its applications to flame synthesis, FTIR was used to measure the effect of electric fields on the process temperature and composition during synthesis of titania powders by TiCl_4 oxidation in a premixed methane-oxygen flame⁹. The *in situ* temperature measurements during the electrically-modified flame synthesis of particles showed that, in most cases, the gas and particle temperatures were the same, and the flame temperature was fairly uniform across the flame width. Transmission measurements showed that all of the TiCl_4 was converted to TiO_2 either by direct hydrolysis or by oxidation followed by hydrolysis of the Cl_2 byproduct. The absorption spectrum of the TiO_2 indicated that, in the absence of electric fields, the particle mass concentration decreased by 20% from 0.3 to 1.3 cm above the burner by gas dilution. In the presence of electric fields, however, that concentration decreased by 70% over the same distance. Thus, FTIR spectroscopy was demonstrated as a powerful diagnostic tool for *in situ* information of the temperature, composition, and particle characteristics in electrically-modified flames.

To monitor the flame synthesis of TiO_2 particles by liquid titanium

tetraisopropoxide (TTIP, $\text{Ti}(\text{OC}_3\text{H}_7)_4$), the axial and radial flame temperatures were measured by *in situ* FTIR¹⁰. The emission/transmission analysis deduced the temperature information by comparing the normalized radiance as calculated from the actual radiance of a sample to a black body Planck function spectroscopy in the presence of particles. While it was found by the study that particle temperature measurements can be accurate to within $\pm 100\text{K}$, other studies concluded that the temperature accuracy can be within $\pm 50\text{K}$ ⁵⁵ or even $\pm 25\text{K}$ ⁵³.

Due to its high selectivity and sensitivity concerning a wide variety of gaseous species, FTIR spectroscopy has been used to monitor gas-phase processes, including industrial scale CVD processes^{57,58}. In addition, an *in-situ* FTIR monitoring system was adapted to a fiber growth reactor which allowed the detection of gas species involved in high temperature fiber synthesis⁵⁹. Correlation between the gas phase composition and the fiber properties permitted process control and led to a better understanding of the fiber growth process.

3.2.4 Laser-induced breakdown spectroscopy (LIBS)

Laser-induced breakdown spectroscopy (LIBS) uses a high-energy short pulsed laser to generate plasma to excite signature spectra from a sample⁶⁰. The intensities of excited emission lines of the species in the plasma allow a quantitative chemical analysis of the target material. It is often used to obtain qualitative elemental characterization of gases, solids, liquids, and aerosols. LIBS is a fast, non-contact method allowing large detection distances and can be easily used as an *in situ* tool for gas-phase synthesis processes. There have been several reviews covering different aspects of LIBS techniques^{61,62,63,64}.

Mukherjee *et al.*¹³ develop a methodology to use LIBS to quantify the composition of multi-component aerosols without the need for external materials standards. Using LIBS, they obtained time-resolved atomic-emission spectra and plasma temperature to study quantitatively the composition of oxygen in aluminum nanoparticles oxidized in air at various temperatures. Specifically, the plasma temperatures were calculated based on the Boltzmann equation under the assumption of local thermal equilibrium (LTE)⁶⁵. By using Ar as an internal standard and optimizing laser delay time to collect spectra for each of the elemental species of interest, relative population densities of oxygen and aluminum from the Boltzmann relations were calculated. These techniques showed that the extent of oxidation of aluminum nanoparticles as a function of furnace temperature can be studied *in situ* and quantitatively.

While most of the LIBS techniques requires approaching the sample in order to perform the analysis, the detection and characterization of energetic materials at distances up to 45 m using a stand-off LIBS system has been demonstrated⁶⁶. The remote analysis method offered real-time results maintaining a security distance from the sample. A single pulse was proven to be suitable for the analysis of organic compounds by using low delay times in the detection. The detection of energetic material in 1 fingerprint or one 100 ppm solution drop containing about 5 mg of explosive is a satisfactory limit of detection for this application.

More recently, LIBS has been combined with Raman spectroscopy for planetary science studies^{67,68,69}. LIBS yields elemental compositions information while Raman spectroscopy yields molecular vibrational information about a sample, and both share similar instrumentation configurations. The combination of LIBS and Raman

spectroscopy in a single instrument for planetary surface exploration is thus very valuable.

3.2.5 Laser induced incandescence (LII)

Laser-induced incandescence (LII) has proven to be a powerful *in situ* tool for particle-concentration and primary particle-size measurements in combustion, particle synthesis, and environmental applications. LII involves heating particles with a short pulse (typically 20ns) laser and measuring the resulting radiative emission. The spatially, temporally, and spectrally recognizable radiation lasts much longer (hundreds of nanoseconds) than the laser pulse, and decreases exponentially. The detection of the incandescence decay time (Time Resolved Laser Induced Incandescence, TR-LII) can be used to obtain useful, almost real-time indications about the particle size during synthesis¹⁴.

In combustion research, LII is well established for soot diagnostics^{70,71,72} and has the potential to be extended to non-soot particle size determination^{73,74}, especially in flame synthesis¹⁴. However, different from soot, synthesized particles cover a wide range of chemical compositions with a variety of optical properties. The structure is frequently crystalline, and many physical parameters can change widely from case to case. The application of LII for such studies is therefore not as straightforward as for soot.

Maffi *et al.*¹⁴ applied LII to TiO₂ nanoparticle synthesis in a flame reactor. The 4th harmonic of the Nd:YAG laser was used to excite the LII signal. Spectral checks were necessary to verify that the laser excitation actually produced incandescence only, since an exceedingly high fluence can rather easily affect the experiments, leading to signals originated by other sources than from incandescence. Only under proper laser fluence

can LII signals show the expected dependence on the particle size and can be used for on-line size monitoring in TiO_2 synthesis.

LII can be extended from atmospheric flames to low-pressure processing plasmas⁷⁵. The temporal behavior of LII signals emitted from nanoparticles has been studied for quantitative size monitoring of Si nanoparticles growth in an argon plasma diluted with 5% SiH_4 at a pressure of 20 mTorr. In this experiment, it is found that the signal-to-noise ratio of the LII signal was sufficient to allow the identification of particles larger than 10 nm in diameter, with a measurement uncertainty that was estimated to be less than 5%.

3.2.6 Ultra-small-angle x-ray scattering (SAXS)

Ultra-small-angle x-ray scattering (SAXS) techniques are useful to measure the size distribution of ultrafine particles in the size range between 1 and 100 nm in atmospheric pressure flames. The third-generation synchrotron X-ray produced at the Advanced Photon Source of Argonne National Laboratory was used to perform SAXS measurements of the distributions of soot particles in flames⁷⁶.

Kammler⁷⁷ demonstrated the monitoring of primary particle and aggregate growth dynamics of oxide nanoparticles in a flame with ultra-small-angle x-ray scattering. SAXS was realized by employing the third-generation synchrotron X-ray sources. More specifically, the evolution of primary-particle diameter, mass-fractal dimension, geometric standard deviation, silica volume fraction, number concentration, radius of gyration of the aggregate, and number of primary particles per aggregate were measured along the flame axis for two different premixed flames. All these particle characteristics were derived from a single and nonintrusive measurement technique.

The same group¹¹ recently reported an *in situ* SAXS study of nanoparticle growth in

flames with sub-millisecond resolution. Nanostructured silica was produced in a methane/oxygen diffusion flame doped with an organometallic vapor, hexamethyldisiloxane (HMDSO). With sufficient flux, SAXS can be easily used to probe time-resolved scattering signatures of nanoparticle growth in flames, even at volume fractions of the order of 10^{-6} . Direct 2D mapping of nanoparticle nucleation and growth can be made on size scales from 0.5 to 500 nm, and on timescales as short as 100 μ s, depending on the gas flow rates.

3.2.7 Laser light scattering (LLS)

Light scattering techniques are also employed for particle size measurement. One of the easiest is laser light scattering (LLS), using scattering of visible laser light to characterize particles in the size range from a few nanometers to a few microns. Scattered laser light has been used for several decades in combustion systems to study particle size and number density^{78,79,80,81}.

For the flame synthesis of SiO_x nanoparticles, Glumac¹ used a combination of laser light scattering and thermophoretic sampling to get local particle size and number density information. The mean particle diameter (d) from TEM analysis, was used in conjunction with LLS to yield a relative number density (N) profile since light scattering intensity varies as $Nd^{82,83}$. Measurements in a standard $\text{H}_2\text{-O}_2\text{-HMDS}$ synthesis flame indicated that the number density of particles in the gap region was also fairly constant from precursor pyrolysis location to just above the substrate. It was also mentioned that since the sampling experiments gave no direct value for local particle diameter, these scattering results cannot be definitively used to infer local particle number density in a quantitative sense.

More recently, nonspherical Al_2O_3 aggregates produced in a laminar counterflow nonpremixed methane flame were investigated with an *in situ* spatially resolved LLS technique in combination with a thermophoretic sampling–transmission electron microscope (TS–TEM) method⁸⁴. Particulate morphological evolution from precursor (trimethylaluminum hydrolysis) was measured by multi-angular absolute LLS measurements and interpreted based on the Rayleigh–Debye–Gans scattering theory⁸⁵ for fractal aggregates. Optically determined fractal dimension, mean radius of gyration, aggregate size distribution, and local particle volume fraction were found to be consistent with *ex-situ* TS–TEM experiments.

References

- ¹ N.G. Glumac, Y.J. Chen, and G. Skandan, Diagnostics and modeling of nanopowder synthesis in low pressure flames,” *Journal of Materials Research* 13, 9, 2572-2579 (1998).
- ² A. Colibaba-Evulet, A. Singhal, N. Glumac, Detection of AlO and TiO by laser-induced fluorescence in powder synthesis, *Flames Combustion Science and Technology* 157, 1, 129-139 (2000).
- ³ S. Bailey, and N.G. Glumac, Laser-induced-fluorescence detection of SnO in low-pressure particle-synthesis flames, *Applied Physics B: Lasers and Optics* 77, 4, 455-461 (2003).
- ⁴ S. Chiashi, Y. Murakami, Y. Miyauchi, and S. Maruyama, Cold wall CVD generation of single-walled carbon nanotubes and *in situ* Raman scattering measurements of the growth stage, *Chemical Physics Letters* 386, 1-3, 1, 89-94 (2004).
- ⁵ L. Fayette, B. Marcus, M. Mermoux, N. Rosman, L. Abello, and G. Lucazeau,, *In situ* Raman spectroscopy during diamond growth in a microwave plasma reactor, *J. Appl. Phys.* 76, 1604 (1994).
- ⁶ M. Mermoux, L. Fayette, B. Marcus, N. Rosman, L. Abello, and G. Lucazeau, *In situ* Raman monitoring of the growth of diamond films in plasma-assisted CVD reactors, *Diamond and Related Materials* 4, 5-6, 745-749 (1995).
- ⁷ L.S. Hsu, and C.Y. She, Real-time monitoring of crystallization and structural transformation of titania films with Raman spectroscopy, *Opt. Lett.* 10, 638 (1985).
- ⁸ J. Liu, Y.K. Vohra, J.T. Tarvin, and S.S. Vagarali, Cubic-to-rhombohedral transformation in boron nitride induced by laser heating: *In situ* Raman-spectroscopy studies, *Phys Rev B Condens Matter.* 51, 8591-8594 (1995).
- ⁹ P.W. Morrison, et al., *In situ* Fourier transform infrared characterization of the effect of electrical fields on the flame synthesis of TiO_2 particles, *Chem. Mater.* 9, 2702-2708 (1997).
- ¹⁰ O. I. Arabi-Katbi, S. E. Pratsinis, P.W. Jr Morrison, and C. M. Megaridis, Monitoring the flame synthesis of TiO_2 particles by *in-situ* FTIR spectroscopy and thermophoretic sampling, *Combust. Flame* 124, 560-572 (2001).
- ¹¹ G. Beaucage, Probing the dynamics of nanoparticle growth in a flame using synchrotron radiation, *Nature Materials* 3, 370-373 (2004).
- ¹² Y. Xing, et al., *In situ* Light-Scattering Measurements of Morphologically Evolving Flame-Synthesized Oxide Nanoaggregates, *Appl. Opt.* 38, 2686-2697 (1999).

- ¹³ D. Mukherjee, A. Rai, and M.R. Zachariah, Quantitative laser-induced breakdown spectroscopy for aerosols via internal calibration: Application to the oxidative coating of aluminum nanoparticles, *Journal of Aerosol Science* 37, 6, 677-695 (2006).
- ¹⁴ S. Maffi, F. Cignoli, C. Bellomunna, S. De Iuliisa, and G. Zizak, Spectral effects in laser induced incandescence application to flame-made titania nanoparticles, *Spectrochimica Acta Part B: Atomic Spectroscopy* 63, 2, 202-209 (2008).
- ¹⁵ A.C. Eckbreth, *Laser Diagnostics for Combustion Temperature and Species* (Gordon and Breach Publishers, Amsterdam, The Netherlands, 1996).
- ¹⁶ J. W. Daily, Laser Induced Fluorescence Spectroscopy in Flames, *Prog. Energy. Combust. Sci.* 23, 133-199 (1997).
- ¹⁷ K. Kohse-Höinghaus, Laser techniques for the quantitative detection of reactive intermediates in combustion systems, *Prog. Energy. Combust. Sci.* 20, 203-247 (1994).
- ¹⁸ K. C. Smyth, and P. J. H. Tjossem, Radical concentration measurements in hydrocarbon diffusion flames, *Appl. Phys. B* 50, 499 (1990).
- ¹⁹ W. G. Brieland, P. Ho, and M. E. Coltrin, Gas-phase silicon atoms in silane chemical vapor deposition: laser-excited fluorescence measurements and comparisons with model predictions, *J. Appl. Phys.* 60, 1505 (1986).
- ²⁰ R.K. Hanson, P.H. Paul, and J.M. Seitzman, Digital fluorescence imaging of gaseous flows, *Mat. Res. Soc. Symp.* 117, 227 (1988).
- ²¹ J. P. Booth, G. Hancock, N. D. Perry and M. Toogood, Plasma diagnostics by laser-induced fluorescence, *Mat. Res. Soc. Symp.* 117, 47 (1988).
- ²² M.R. Zachariah, and D.R.F. Burgess Jr., Strategies for laser excited fluorescence spectroscopy. Measurements of gas phase species during particle formation, *Journal of Aerosol Science* 25, 3, 487-497 (1994).
- ²³ N. Khadiya, Combustion Near Catalytic Surfaces: Laser Diagnostics and Modeling, PhD Dissertation, Rutgers University (2000).
- ²⁴ N. Khadiya and N. G. Glumac, Catalytic removal of NO from post-flame gases in low pressure stagnation-point flames over platinum, *Combustion and Flame* 125, 1-2, 931-941 (2001).
- ²⁵ N. Khadiya and N. G. Glumac, Destruction of NO during Catalytic Combustion on Platinum and Palladium, *Combustion Science and Technology* 165, 1, 249-266 (2001).
- ²⁶ J. Y. Hwang, Y. S. Gil, J. I. Kim, M. Choi, and S. H. Chung, Measurements of temperature and OH radical distributions in a silica generating flame using CARS and PLIF, *Journal of Aerosol Science* 32, 5, 601-613 (2001).
- ²⁷ M. Alden, H. Edner, G. Hdmstedt, S. Svanberg, and T. Hoegberg, Single-pulse laser-induced OH fluorescence in an atmospheric flame, spatially resolved with a diode array detector. *Applied Optics* 21, 1236-1240 (1982).
- ²⁸ G. Kychakoff, R.D. Howe, and R.K. Hason, Quantitative flow visualization technique for measurements in combustion gases. *Applied Optics* 23, 704-712 (1984).
- ²⁹ M. G. Allen, and R. K. Hanson, Digital imaging of species concentration fields in spray flames. *Twenty-first symposium (international) on combustion*, 1755-1762 (1986).
- ³⁰ D. Lee, and M. Choi, Control of size and morphology of nano particle using CO₂ laser during flame synthesis, *Journal of Aerosol Science* 31, 1145-1163 (2000).
- ³¹ N. G. Glumac, Flame temperature predictions and comparison with experiment in high flow rate, fuel-rich acetylene/oxygen flames, *Combustion Science and Technology* 122, 1-6, 383-398 (1997).
- ³² M. Tamura, et al., Laser-induced fluorescence of seeded nitric oxide as a flame thermometer, *Applied Physics B: Lasers & Optics* 66, 4, 503 (1998).
- ³³ W.G. Bessler, F. Hildenbrand, C. Schulz, Two-line laser-induced fluorescence imaging of vibrational temperatures in a NO-seeded flame, *Appl. Opt.* 40, 748-756 (2001).
- ³⁴ H. Kronemayer, P. Ifecho, C. Hecht, T. Dreier, H. Wiggers, and C. Schulz, Gas-temperature imaging in a low-pressure flame reactor for nano-particle synthesis with multi-line NO-LIF thermometry, *Applied Physics B: Lasers and Optics* 88, 3, 373-377 (2007).
- ³⁵ C. Hecht, H. Kronemayer, T. Dreier, H. Wiggers, and C. Schulz, Imaging measurements of atomic iron concentration with laser-induced fluorescence in a nanoparticle synthesis flame reactor, *Applied Physics B: Lasers and Optics* 94, 1, 119-125 (2009).
- ³⁶ A. Colibaba-Evulet, A. Singhal, and N. G. Glumac, Detection of AlO and TiO by Laser-Induced

- Fluorescence in Powder Synthesis Flames, *Combustion Science and Technology* 157, 468-475 (2000).
- ³⁷ N. G. Glumac, Formation and destruction of SiO radicals in powder synthesis flames, *Combustion and Flame* 124, 702-711 (2001).
 - ³⁸ S. Bailey and N. G. Glumac, Laser-induced-fluorescence detection of SnO in low-pressure particle-synthesis flames, *Applied Physics B* 77, 455-461 (2003).
 - ³⁹ B. K. McMillin, P. Biswas and M.R. Zachariah, *In situ* characterization of vapor phase growth of iron oxide-silica nanocomposite; Part I: 2-D planar laser-induced fluorescence and mie imaging, *J. Mat. Res.* 11, 1552-1561 (1996).
 - ⁴⁰ P. Biswas, and M.R. Zachariah, *In situ* immobilization of lead species in combustion environments by injection of gas phase silica sorbent precursors, *Env. Sci. Tech.* 31, 2455 (1997).
 - ⁴¹ K. Kaminska, J. Lefebvre, D. G. Austing, and P. Finnie, Real-time *in situ* Raman imaging of carbon nanotube growth *Nanotechnology* 18, 165707 (2007).
 - ⁴² K. Kaminska, J. Lefebvre, D. G. Austing, and P. Finnie, Real-time global Raman imaging and optical manipulation of suspended carbon nanotubes, *Phys. Rev. B* 73, 235410 (2006).
 - ⁴³ S. Dittmer, N. Olofsson, J. Ek Weis, O.A. Nerushev, A.V. Gromov, and E.E.B. Campbell, *In situ* Raman studies of single-walled carbon nanotubes grown by local catalyst heating, *Chemical Physics Letters* 457, 1-3, 206-210 (2008).
 - ⁴⁴ L. I. Berger, *Semiconductor materials* (CRC, 1996).
 - ⁴⁵ M. A. Vuurman, and I. E. Wachs, *In situ* Raman spectroscopy of alumina-supported metal oxide catalysts, *The Journal of Physical Chemistry* 96, 12, 5008-5016 (1992).
 - ⁴⁶ B. M. Weckhuysen, J-M Jehng, and I. E. Wachs, *In situ* Raman Spectroscopy of Supported Transition Metal Oxide Catalysts: $^{18}\text{O}_2$ - $^{16}\text{O}_2$ Isotopic Labeling Studies, *Journal of Physical Chemistry B* 104, 31, 7382-7387 (2000).
 - ⁴⁷ I. E. Wachs, Raman and IR studies of surface metal oxide species on oxide supports: Supported metal oxide catalysts, *Catalysis Today* 27, 3-4, 437-455 (1996).
 - ⁴⁸ I. E. Wachs, *In situ* Raman spectroscopy studies of catalysts, *Topics in Catalysis* 8, 1, 57-63 (1999).
 - ⁴⁹ S. K. Sharma, S. M. Angel, M. Ghosh, H. W. Hubble, and P. G. Lucey, Remote pulsed laser raman spectroscopy system for mineral analysis on planetary surfaces to 66 meters, *Applied Spectroscopy* 56, 699 (2002).
 - ⁵⁰ N. Everall, J. B. King, and I. Clegg, The Raman effect, *Chemistry in Britain* 36, 40 (2000).
 - ⁵¹ D. Bersani, P. P. Lottici, and X. Z. Ding, Phonon confinement effects in the Raman scattering by TiO_2 nanocrystals, *Appl. Phys. Lett.* 72, 73 (1998).
 - ⁵² S. Farquharson, S. Charpenay, M. B. DiTaranto, P. A. Rosenthal, W. Zhu, and S. E. Pratsinis, In: *ACS Symposium Series 681, Synthesis and Characterization of Advanced Materials* (M. A. Serio, D. M. Gruen, R. Malhotra (Eds.), Am. Chem. Society, Orlando, FL, 1998, p.681).
 - ⁵³ P. E. Best, R. M. Carangelo, J. R. Markham, and P. R. Solomon, *Combust. Flame* 66, 47 (1986).
 - ⁵⁴ P. R. Solomon, and P. E. Best, In: N. Chigier (Ed.), *Combustion Measurements* (Hemisphere Publishing Corp., New York, 1991, p385).
 - ⁵⁵ P. W. Morrison, Jr., J. E. Cosgrove, J. R. Markham, and P. R. Solomon, In: *MRS International Conference Proceedings Series: New Diamond Science and Technology* (Proceedings of the Second International Conference on New Diamond Science and Technology; Messier, R., Glass, J. T., Butler, J. E., Roy, R., Eds.; Materials Research Society: Pittsburgh, PA, 1991, p 219).
 - ⁵⁶ S. C. Bates, R. M. Carangelo, K. Knight, and M. A. Serio, Fourier transform infrared Hadamard tomography of sooting flames, *Rev. Sci. Instrum.* 64, 1213 (1993).
 - ⁵⁷ V. Hopfe, H. Mosebach, M. Meyer, D. Sheel, W. Grähler, O. Throl, and B. Dresler, FTIR monitoring of industrial scale CVD processes, *11th Fourier Transform Spectroscopy International Conference Proceedings* 430, 470-473 (1998).
 - ⁵⁸ V. Hopfe, H. Mosebach, M. Erhard, and M. Meyer, *Journal Molecular Structure* 347, 331-342 (1995).
 - ⁵⁹ U. Vogt, A. Vital, W. Graehlert, M. Leparoux, H. Ewing, A. Beil, R. Daum, and H. Hopfe, *In-situ* FTIR spectroscopic monitoring of a CVD controlled Si-N-O fibre growth process, *J. Phys. IV France* 10 (PR2), Pr2-43-Pr2-48 (2000).
 - ⁶⁰ L. J. Radziemski, and D. A. Cremers, Spectrochemical analysis using laser plasma excitation. In: *Laser-induced plasmas and applications* (L.J. Radziemski, D.A. Cremers (Eds.), Marcel Dekker, New York, 1989, pp6107-6118).
 - ⁶¹ K. Song, Y. Lee, and J. Sneddon, Recent developments in instrumentation for laser induced breakdown

- spectroscopy, *Appl. Spectrosc. Rev.* 37, 89 (2002).
- ⁶² D. A. Rusak, B. C. Castle, B. W. Smith, and J. D. Winefordner, Fundamentals and applications of laser-induced breakdown spectroscopy, *Crit. Rev. Anal. Chem.* 27, 257–290 (1997).
 - ⁶³ E. Tognoni, V. Palleschi, M. Corsi, and G. Cristoforetti, Quantitative micro-analysis by laser-induced breakdown spectroscopy: a review of the experimental approaches, *Spectrochimica Acta Part B: Atomic Spectroscopy* 57, 7, 31, 1115–1130 (2002).
 - ⁶⁴ C. Pasquini, J. Cortez, L. M. C. Silva, and F. B. Gonzaga, Laser induced breakdown spectroscopy, *J. Braz. Chem. Soc.* 18, 3, 463–512 (2007).
 - ⁶⁵ H. R. Griem, *Plasma spectroscopy* (McGraw-Hill, New York, 1964).
 - ⁶⁶ C. López-Moreno, S. Palanco, J. J. Laserna, F. DeLucia Jr, A. W. Miziolek, J. Rose, R. A. Walters, and A. I. Whitehouse, Test of a stand-off laser-induced breakdown spectroscopy sensor for the detection of explosive residues on solid surfaces, *J. Anal. At. Spectrom.* 21, 55–60 (2006).
 - ⁶⁷ I. Escudero-Sanz, B. t Ahlers, and G. B. Courreges-Lacoste, Optical design of a combined Raman--laser-induced-breakdown-spectroscopy instrument for the European Space Agency ExoMars Mission, *Opt. Eng.* 47, 033001 (2008).
 - ⁶⁸ C. Brian Dreyer, G. S. Mungas, P. Thanh, and J. G. Radziszewski, Study of sub-mJ-excited laser-induced plasma combined with Raman spectroscopy under Mars atmosphere-simulated conditions, *Spectrochimica Acta Part B: Atomic Spectroscopy* 62, 12, 1448–1459 (2007).
 - ⁶⁹ R. C. Wiens, S. K. Sharma, and J. Thompson, A. Misra, P. G. Lucey, Joint analyses by laser-induced breakdown spectroscopy (LIBS) and Raman spectroscopy at stand-off distances, *Spectrochim Acta A* 61, 2324–2334 (2005).
 - ⁷⁰ B. Axelsson, R. Collin, and P. E. Bengtsson, Laser-induced incandescence for soot particle size and volume fraction measurements using on-line extinction calibration, *Appl. Phys. B* 72, 367–372 (2001).
 - ⁷¹ B.F. Kock, T. Eckhardt, and P. Roth, In-cylinder sizing of Diesel particles by time-resolved laser-induced incandescence (TR-LII), *Proc. Combust. Inst.* 29, 2775 (2002).
 - ⁷² R. Hadeif, V. Kruger, K P Geigle, M S Tsurikov, Y Schneider-Kuhnle, and M Aigner, Measurements of soot size and concentration in the laminar premixed flame, *Oil & Gas Science and Technology* 61, 5, 691–703 (2006).
 - ⁷³ A.V. Filippov, M.W. Markus, and P. Roth, *In-situ* characterization of ultrafine particles by laser-induced incandescence: sizing and particle structure determination, *J. Aerosol Sci.* 30, 71–87 (1999).
 - ⁷⁴ R.L. Vander Wal, T.M. Ticich, and J.J.R. West, Laser-induced incandescence applied to metal nanostructures, *Appl. Opt.* 38, 5867–5878 (1999).
 - ⁷⁵ G. S. Eom, S. Park, C. W. Park, W. Choe, Y.-H. Shin, K. H. Chung, and J. W. Hahn, Size monitoring of nanoparticles growing in low-pressure plasma using laser-induced incandescence technique, *Jpn. J. Appl. Phys.* 43, 6494 (2004).
 - ⁷⁶ J.P. Hessler, S. Seifert, and R.E. Winans, Spatially resolved small-angle x-ray scattering studies of soot inception and growth, *Proceedings of the Combustion Institute* 29, 2, 2743–2748 (2002).
 - ⁷⁷ H. K. Kammler, G. Beaucage, D. J. Kohls, N. Agashe, and J. Ilavsky, Monitoring simultaneously the growth of nanoparticles and aggregates by *in situ* ultra-small-angle x-ray scattering, *J. Appl. Phys.* 97, 054309 (2005).
 - ⁷⁸ J. M. Bernard, *Particle Sizing in Combustion Systems Using Scattered Laser Light* (The Aerospace Corp, El Segundo, CA, 1988).
 - ⁷⁹ S.L. Chung, and J. L. Katz, The counterflow diffusion flame burner: A new tool for the study of the nucleation of refractory compounds, *Combustion and Flame* 61, 271 (1985).
 - ⁸⁰ Y. Xing, Ü.Ö. Köylü, and D.E. Rosner, Synthesis and restructuring of inorganic nano-particles in counterflow diffusion flames, *Combust. Flame* 107, 85 (1996).
 - ⁸¹ S-L. Chung, M-S. Tsai, and H-D. Lin, Formation of particles in a H₂-O₂ counterflow diffusion flame doped with SiH₄ or SiCl₄, *Combust. Flame* 85, 134 (1991).
 - ⁸² S. E. Pratsinis, W. Zhu, and S. Vemury, The role of gas mixing in flame synthesis of titania powders, *Powder Technology* 86, 87 (1996).
 - ⁸³ P. E. Bengtsson, and M. Alden, Application of a pulsed laser for soot measurements in premixed flames *Appl. Phys. B* 48, 155 (1989).
 - ⁸⁴ Y. Xing, U. Koylu, and D. Rosner, *In situ* Light-Scattering Measurements of Morphologically Evolving Flame-Synthesized Oxide Nanoaggregates, *Appl. Opt.* 38, 2686–2697 (1999).
 - ⁸⁵ U. O. Koylu, and G. M. Faeth, “Optical properties of soot in buoyant laminar diffusion flames,” *J. Heat*

Transfer 116, 971-979 (1994).

Chapter 4

Application of Gas-Phase Spontaneous Raman Spectroscopy to Study the Synthesis of 1-D Nanostructures

The goal of this chapter is to apply laser-based diagnostics techniques to study the critical gas-phase conditions at the local sites of nanomaterials synthesis. The obtained knowledge of the flame structures is used to better understand the fundamental mechanisms of the synthesis process. Specifically, spontaneous Raman spectroscopy (SRS) is employed to study two flame configurations, namely the inverse diffusion flame (IDF) and the counter-flow diffusion flame (CDF), at atmospheric pressure. The results of the measurements, namely, local gas-phase temperature and concentrations of precursor/oxidizer species involved in the growth of carbon nanotubes (CNT) and ZnO nanowires, are compared with computational simulations using detailed chemistry and transport. The variation of the obtained parameters strongly affects the formation, diameter, growth rate, and morphology of the nanomaterials. The SRS results also help to establish the correlation between flame parameters and nanomaterials synthesis. Nanostructures grown under similar local conditions in different flames have similar morphology, indicating that the local conditions can be translated between different synthesis configurations. Finally, error analyses of the SRS measurements are given.

As stated in the Preface, some of the content of this chapter appears verbatim from published papers^{26,27,28}, which includes co-authors.

4.1 Introduction

It is useful to provide background for CNT growth on substrate probes in a hydrocarbon-based flame. The first steps for CNT growth on a catalytic surface are carbonization followed by surface breakup and the formation of catalytic nanoparticles. Surface carbonization happens on the metal probe in the flame. If the dissolved carbon reaches a concentration sufficient to form a carbide phase, the resulting lattice mismatch between the carbide phase and the underlying metal creates stresses localized within the surface region¹. Surface breakup will proceed along the weakest sections such as grain boundaries and edge dislocations where lattice stresses are concentrated, and the carbon concentration will likely be the highest. This formation mechanism of catalyst nanoparticles generally creates a wide variety of sizes and geometries^{2,3,4,5}, which are determined by various factors, such as temperature, chemical species, and carbon solubility of the metal. Different metals and metal alloys show different carbon solubilities that also vary with temperature⁶. Additionally, hydrogen can facilitate the carbide breakup process by etching or removing surface-adsorbed carbon where the rate of carbon deposition exceeds that of solvation. All of these parameters affect the formed nanoparticle properties such as size and yield, which will impact CNT morphologies and properties.

In flame synthesis of 1-D nanostructures (carbon nanotubes, nanowires, etc.), two flame configurations, namely the inverse diffusion flame (IDF) and the counter-flow diffusion flame (CDF)⁷ are investigated in this work. An IDF is a coflow flame where oxidizer is issued from the center jet while fuel is issued from the surrounding co-flow, which is an “inversed” coflow arrangement from the normal diffusion flame (NDF). The

2-D geometry of this flame provides a large parameter space (i.e. local gas-phase temperature, gas-phase species concentrations, substrate temperature, catalyst composition, and substrate voltages bias, etc.) so that suitable conditions for nanostructure growth are more easily discovered in the flame. Another advantage to produce high CNT yield is that carbon-related growth species generated in IDFs can be higher than that produced in premixed flames. IDFs separate soot formation processes from oxidation processes more effectively. Understanding CNT growth versus soot formation is important because soot would compete with CNT formation routes, as well as contaminate the final yield.

The CDF is a flat flame formed in between two opposing jets of fuel and oxidizer issued from bottom and top burners. The flame has gradients existing only in the axial direction and thus can be considered a quasi-1D flame. In the radial direction, the conditions are almost constant along a range of several centimeters so that the growth of nanostructures on a large area is possible. The flame is well defined so it can be simulated with detailed chemical kinetics and transport. A comparison between laser-based diagnostics measurements and simulations is important for investigating the local conditions with appropriate variables for materials synthesis.

It is reasonable to predict that the favorable local conditions for the growth of 1D nanostructures should be the same regardless flame configurations, or even gas-phase synthesis methods. By keeping the same local flame conditions, we investigate the growth of CNTs and ZnO nanowires in IDFs and CDFs, to see if flames with different geometries will produce similar nanomaterials.

Spontaneous Raman scattering has been used for gas-phase measurements. Different

flame configurations are investigated. Eckbreth⁸ has reviewed the advancement of SRS techniques. Most of the measurements are usually limited to simple configurations, because these configurations are well understood through detailed theoretical and computational study^{9, 10, 11} and are easily characterized by laser spectroscopy with sufficient precision^{12, 13, 14}. In flame synthesis research, tailored flame configurations (IDF, CDF) are employed. While the CDF has a simple structure, the IDF is more difficult to study computationally. When used for flame synthesis, these two flame configurations are then well worthy of being investigated thoroughly.

Therefore, to increase the fundamental understanding of the mechanisms of the flame synthesis of CNTs and metal-oxide nanowires, laser diagnostics will be conducted for the local gas-phase conditions. The SRS measurements will include the gas-phase temperatures and concentrations of major species (i.e., N₂, H₂, CO, C₂H₂, O₂, and H₂O) at specific locations for CNT and ZnO growth. The crystallography, microstructure, and characteristics of organic and non-organic nanomaterials produced in well-defined flames can be correlated to local gas phase conditions and properties of the substrate. The flame structure of the CDF is also computed using detailed chemical kinetics (GRI-Mech 1.2) and molecular transport. By comparing simulation and measurements, the nature of the material processing flow field can be revealed.

4.2 Spontaneous Raman scattering of methane inverse diffusion flames

Vertically well-aligned multi-walled carbon nanotubes (MWNTs) with uniform diameters (~15 nm) are grown on catalytic probes at high yield rates in an inverse diffusion flame (IDF) of a co-flow jet configuration using methane as fuel. The coflow flame configuration of IDF has been briefly mentioned in Section 4.1, and more details can be

found in the literature^{15,16}. From the point view of flame synthesis, the inversed configuration makes it possible to separate CNT formation routes from oxidation processes¹⁷. More important, this kind of flame has rich sources of hydrocarbon and pyrolysis species (i.e., C_n and CO), the local concentrations of which must be characterized to understand the initial chemical reaction pathways and the conditions promoting their kinetic dominance. The forming of CNTs in flames is realized by inserting transition-metal alloy probes into specific location of the flame structure. Under favorable conditions, catalyst nanoparticles are formed, and carbon-based precursor species readily undergo dissociative adsorption and diffuse through the catalyst nanoparticles and grow into CNTs¹⁸. In this process, temperature is critical for the catalytic activities of the probes. Local gas-phase temperatures and concentrations of precursor species are measured at those locations of direct CNT formation.

4.2.1 Experiment arrangement

Fig. 1(a) shows the IDF used for CNT synthesis. The IDF is produced by a burner that consists of a center tube surrounded by a concentric outer tube. A mixture of 10 L/min CH_4 and 4.2 L/min N_2 flows through the outer annulus, and exits the burner through a ceramic honeycomb with a flat velocity profile. A visible laminar flame that is 15 mm in height is established with ~9 mm (bluish chemiluminescence from CH^*) of it at the base being from the primary reaction zone and ~6 mm (faint orange) of it at the top being from pyrolysis and sooting mechanisms. The flames are monitored by a cathetometer, showing minimal spatial displacement of the flames at the level of $\pm 75 \mu m$.

Air at 0.8 L/min flows through the center tube, which is sufficiently long to produce a

fully-developed laminar velocity profile at the burner exit. A quartz cylinder encompasses the entire setup to prevent oxidizer permeation from the ambient. Transition-metal alloy probes (i.e. Fe, Ni/Cu, and Ni/Cr/Fe) are inserted horizontally (Fig. 4.1) into the flame structure at specific vertical positions to induce catalyst nanoparticle formation and subsequent CNT growth.

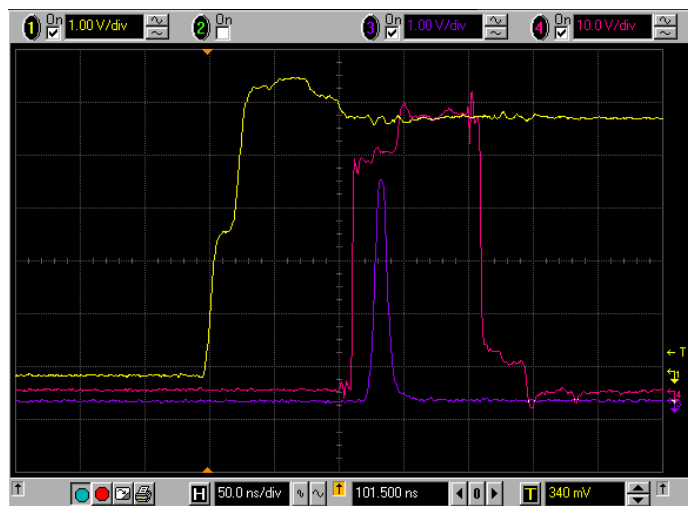
Spontaneous Raman spectroscopy (SRS) is utilized (Fig. 4.1b) to measure the gas-phase temperatures and concentrations of major species (i.e. N_2 , O_2 , H_2O , H_2 , CO , and C_2H_2) at specific locations of CNT growth. The excitation source is a vertically-polarized frequency-doubled (532 nm) Nd:YAG (Spectra-Physics Quanta Ray LAB-170) laser. The Nd:YAG laser is Q-switched to produce short pulse of 8~10 ns at a repetition rate of 10 Hz. The maximum output energy of the laser is 430 mJ/pulse. The laser line width is about 1.0 cm^{-1} , and the laser beam diameter is 10 mm with divergence smaller than 0.5 mrad. The laser beam is then passed through an iris aperture to prevent reflections back to the laser and to modify the beam shape before is focused into the test section with a 300-mm focal-length plano-convex fused silica lens (Thorlabs, L4855). The focused laser beam has a beam waist of $\sim 240 \text{ }\mu\text{m}$ at the focus point of the lens. The laser beam passes through the flame and is blocked by a beam dump behind the burner. A photodiode (Thorlabs, DET 210) is placed toward the beam dump to monitor the laser pulse energy and to provide a synchronized signal for the timing of the signal detection.

The vibrational Stokes Q-branch Raman signal from a $100 \text{ }\mu\text{m}$ diameter \times $100 \text{ }\mu\text{m}$ length measuring volume is focused by 400-mm and 300-mm achromat lenses onto the slit of a f/6.5 imaging spectrometer (Acton SpectrPro-2558), with ICCD camera (Princeton Instruments PIMAX 1300HQ, 1340×1300 pixels) as detector. A 2400 g/mm

UV grating (Richardson 53009BK01-150R) and 100 μm slit width of the spectrometer give a 15 nm spectral coverage with a resolution of ~ 0.04 nm. In the optics setup, a holographic notch filter (Kaiser Optical Systems, SuperNotch-Plus, 532 nm) filters out the laser wavelength. The scattered light passing through the notch filter should be collimated to suppress the elastically scattered component of light. The spectrometer possesses a vertical slit but the measuring volume is in the horizontal scattering plane. So, a two mirror “periscope” arrangement between the two achromat lenses is used, which achieves a 90 degree rotation and beam elevation change. However, this simple approach also changes the polarization of the scattered Raman signal from vertical to horizontal. A depolarizer is put in front of the spectrometer slit to scramble the polarization, optimizing the efficiency of the grating. The Raman signal recorded on the ICCD camera is acquired using “WinSpec/32” software (Princeton Instruments). The data processing can be carried out as described in Chapter 2.

Correct timing is essential to acquire the Raman scattering signal successfully. The intensified CCD PIMax camera and ST-133 controller with a programmable timing generator (Princeton Instrument) are synchronized to record the Raman signal with proper timing. The Nd:YAG laser pulse serves as the synchronizing source in the measurement. In the experiments, both the Nd:YAG laser (running in Q-switch internal trigger mode) and the ST-133 controller (running in external trigger mode) are triggered by a positive TTL signal from the Advanced Q-switch of the laser. A photodiode near the measurement position monitors when the laser pulse starts to excite the Raman signals. The PTG of the ST-133 controller determines the moment when the ICCD gate is opened for a series of Raman signals every 0.1s. Figure 4.1b shows the wiring between

instruments for timing synchronization proposes; Figure 4.1c shows the timing sequence. The ST-133 controls the gate width (Raman signal duration after the pulse, 40 ns in our experiments) and gate delay, which can be adjusted through the “WinSpec/32” spectroscopic software. The software also controls how many gates will be accumulated throughout the exposure, which will determine the total exposure time. A four-channel 1.5GHz oscilloscope (AGILENT TECH, 54845A) is used to monitor the signals from laser pulse, photodiode, and ST-133 gating operations to make sure the Raman signal is captured in the narrow gate width (Figure 4.1d). When the laser trigger is repetitive and when gate width and gate delay are optimized, the measurement will reflect the varied experimental parameters, such as temperature, concentration, or wavelength.



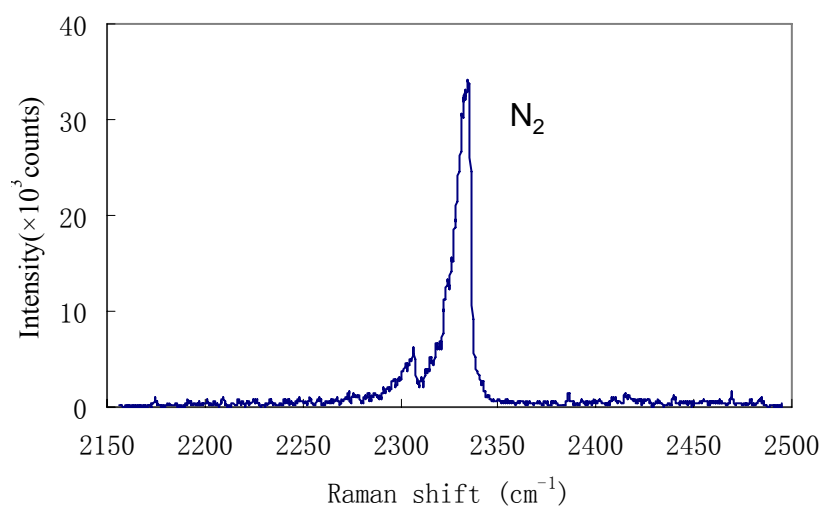
d

Figure 4.1. (a) Methane inverse co-flow jet diffusion flame. (b) Spontaneous Raman spectroscopy (SRS) diagnostic setup. (c) Experimental timing diagram (d) Time gate diagram on oscilloscope

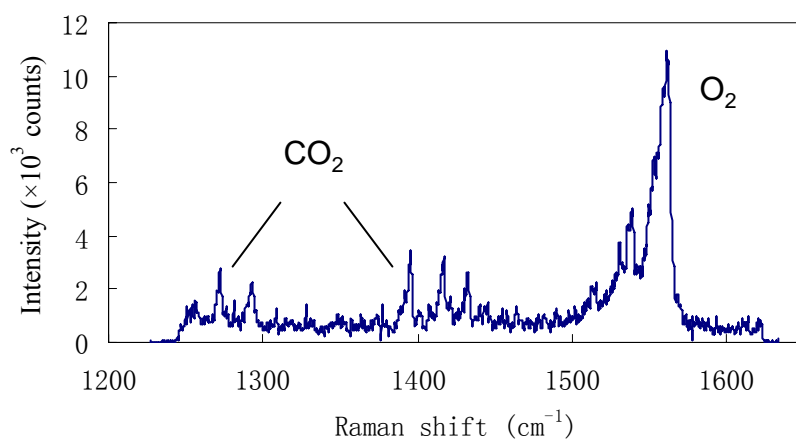
Temperature measurements are obtained by least-square fitting the shape of the N_2 Raman spectrum to theoretical library spectra spaced 50 K apart. The uncertainty in the fitted temperature is less than ± 50 K, and the reproducibility of the measurements is within ± 20 K. Species mole fraction profiles are determined from the strength of the Raman signal of individual species. The signals used to determine the concentrations of CH_4 , H_2 , CO , C_2H_2 , CO_2 , and H_2O are collected at Raman shifts of 2915, 4160, 2145, 1980, 1388, and 3657 cm^{-1} , respectively. The interference from the O-branch of N_2 on the CO spectrum is considered and subtracted. The reproducibility of the concentration measurements is within $\pm 5\%$.

4.2.2 Results

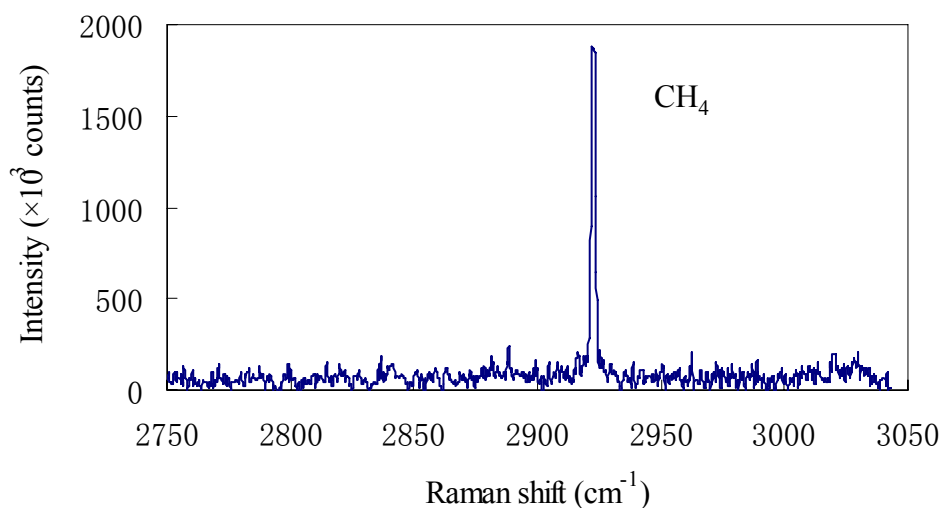
With Raman spectra taken for all the interested species (representative spectra are shown in Figure 4.2), concentration and temperature calculations can then be done in the manner described in Chapter 2. For practical measurements, however, some special issues related to the SRS techniques need to be addressed to get accurate results.



(a) N₂



(b) O₂ and CO₂

(c) CH₄**Figure 4.2.** Representative Raman spectra of major species at 1794K in flames.

First, for flames with strong gradients in refractive index n , the beam steering effect needs to be accounted for¹⁹. This effect, caused by the change of the propagation direction of the incident beam in the flame, leads to a “shadowgraph-type” distortion of the measuring volume. In real experimental conditions, an obstruction effect from the burner surface happens at the nozzle exit. Thus, it is normal to see some variation in collection efficiency in Raman measurements from various flames. It would be favorable to know the spatial profile of mole fraction of N₂, the reference species used for other species calculations, in the flame so that these effects on collection efficiency can be corrected. In most cases, however, this knowledge cannot be obtained easily, and some assumptions are needed, either from experience or from numerical simulation of the flame. In the coflow IDF flame, it may not be proper to assume that the mole fraction of N₂ has a linear distribution from the cold mixture to the hot reaction zone. In the next few sections, efforts are made to assess the nitrogen distribution along the axial centerline

using numerical simulation, and then to cross-validate those results with the experimental results.

Second, accounting for several interference effects between Raman spectra of different species is essential for accurate calculation of species concentrations. Based on the characteristics of the interference, different strategies for spectra correction must be performed on the raw data before the calculations described in Sec. 2.1.1.1 can be implemented. Those interference effects are most obvious at high temperatures. An overlap of the O_2 spectrum by the wing of the CO_2 spectrum, as shown in Figure 4.3, can be corrected by assuming that the wing of CO_2 is linear. The Q branch of CO overlaps the O branch of N_2 , making CO concentration results higher than the real condition, which can be corrected by subtracting the O branch of N_2 from the CO spectra. Both CO_2 and CO “suffer” from fluorescence interference in hydrocarbon flames at high temperatures. One solution to this problem is addressed in the counterflow flame measurement, where the interference becomes severe.

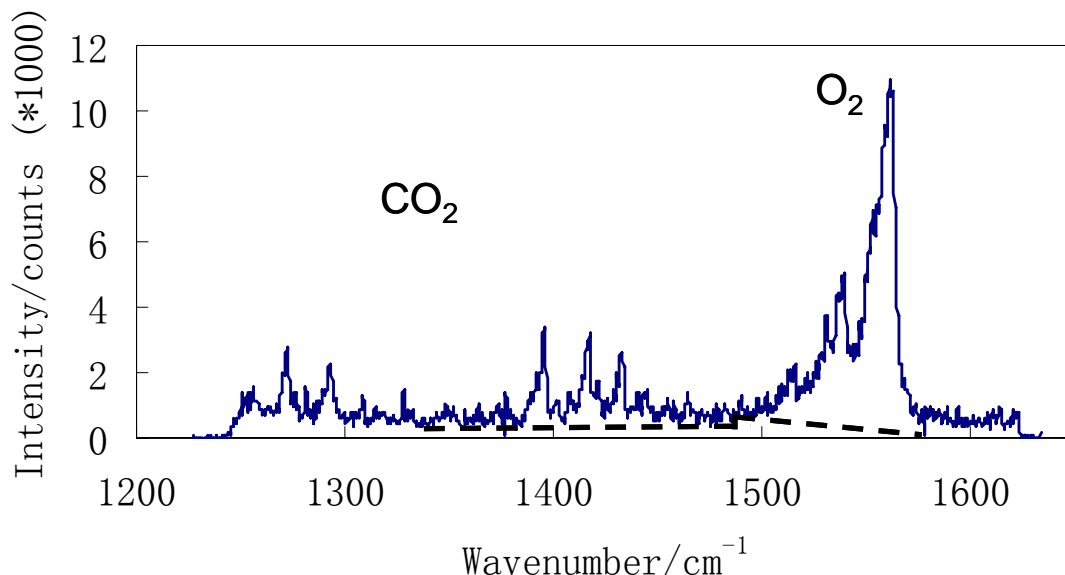


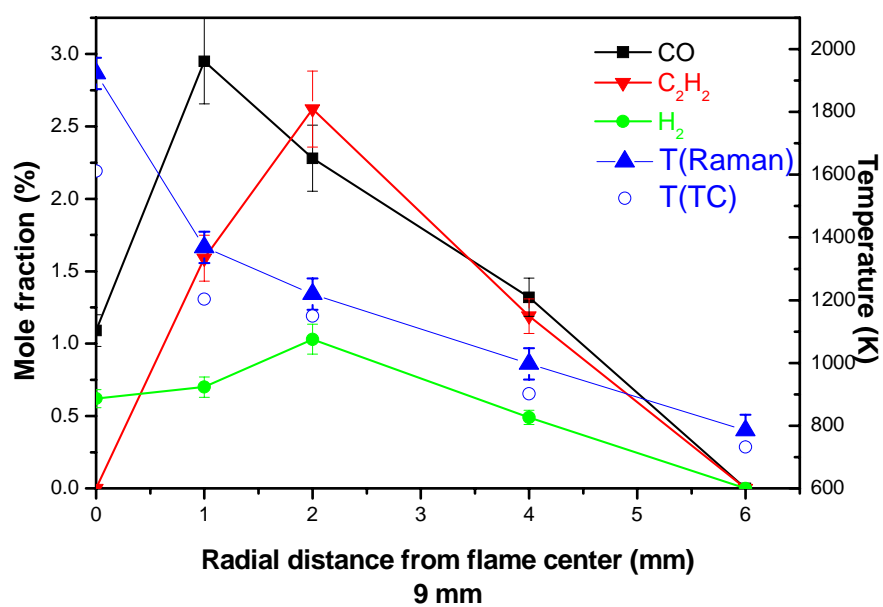
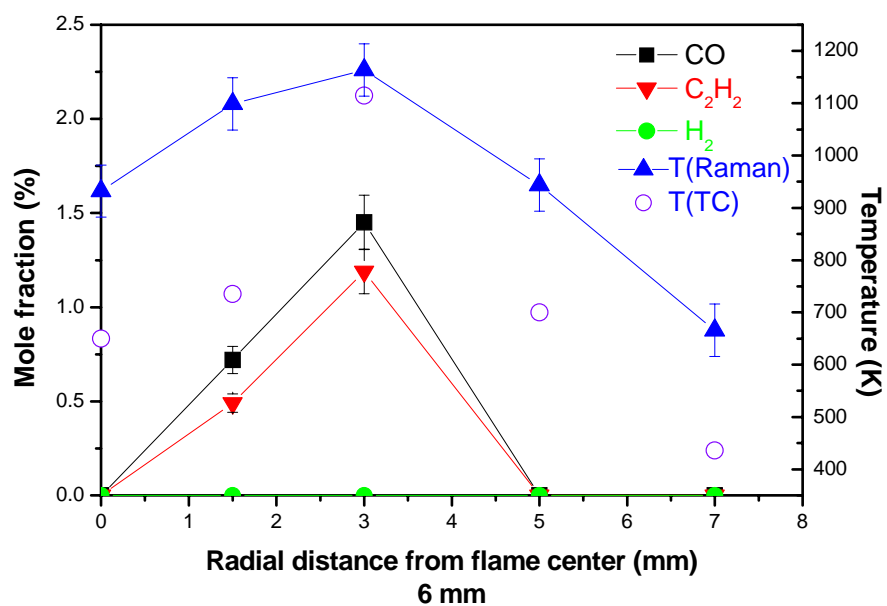
Figure 4.3. Experimental spectra of CO₂ and O₂ at T=1794 K, showing the overlap of O₂ spectrum by the wing of CO₂ spectrum at high temperature.

Gas-phase temperature and species mole fraction profiles measured from SRS are shown for 4 horizontal heights in the IDF (6mm, 9mm, 12mm, and 15mm) in Figure 4.4. For each height, the measurement points are not equally distributed. There are more points taken near the reaction zone of the flame to capture the larger gradient in parameters. The species measured are H₂, CO, and C₂H₂, which are important species involved in the formation of CNTs. Additional measurements of temperature using a thermocouple (TC) are made at the same positions as the Raman measurements. Comparison of the temperature results between SRS and TC are displayed in the plot to show the difference between gas phase and catalytic probe surface temperatures. The Raman scattering measurements of temperature and major species concentration at different vertical (z) and radial (r) sampling positions in the IDF (Fig. 4.1a) allow us to correlate the local conditions with resulting CNT morphology. After flame synthesis, the

surfaces of the probes are imaged using FESEM (Figure 4.5).

With the SRS results, along with the FESEM images, the growth mechanism of CNT in the IDF synthesis structures can be explored. Although the synthesis process is quite complex, involving catalytic nanoparticle formation and CNT growth, under very specific conditions, the setup allows for strategic control of the many process parameters involved.

At the height of $z = 6$ mm, where the highest concentrations of CO and C₂H₂ (1.45% and 1.19%, respectively) are detected on the edge of the bluish area of the flame (which corresponds to the reaction zone (Fig. 4.4a)), there are no CNTs or fibrous nanostructures grown along the probes. Another important parameter, temperature, which is well below 1200 K (Fig. 4.4a), may be too low (melting temperatures of Fe, Ni/Cu, and Ni/Cr/Fe 1535, 1220, and 1350 °C, respectively) for the formation/extraction of catalytic nanoparticles on/from the probes.



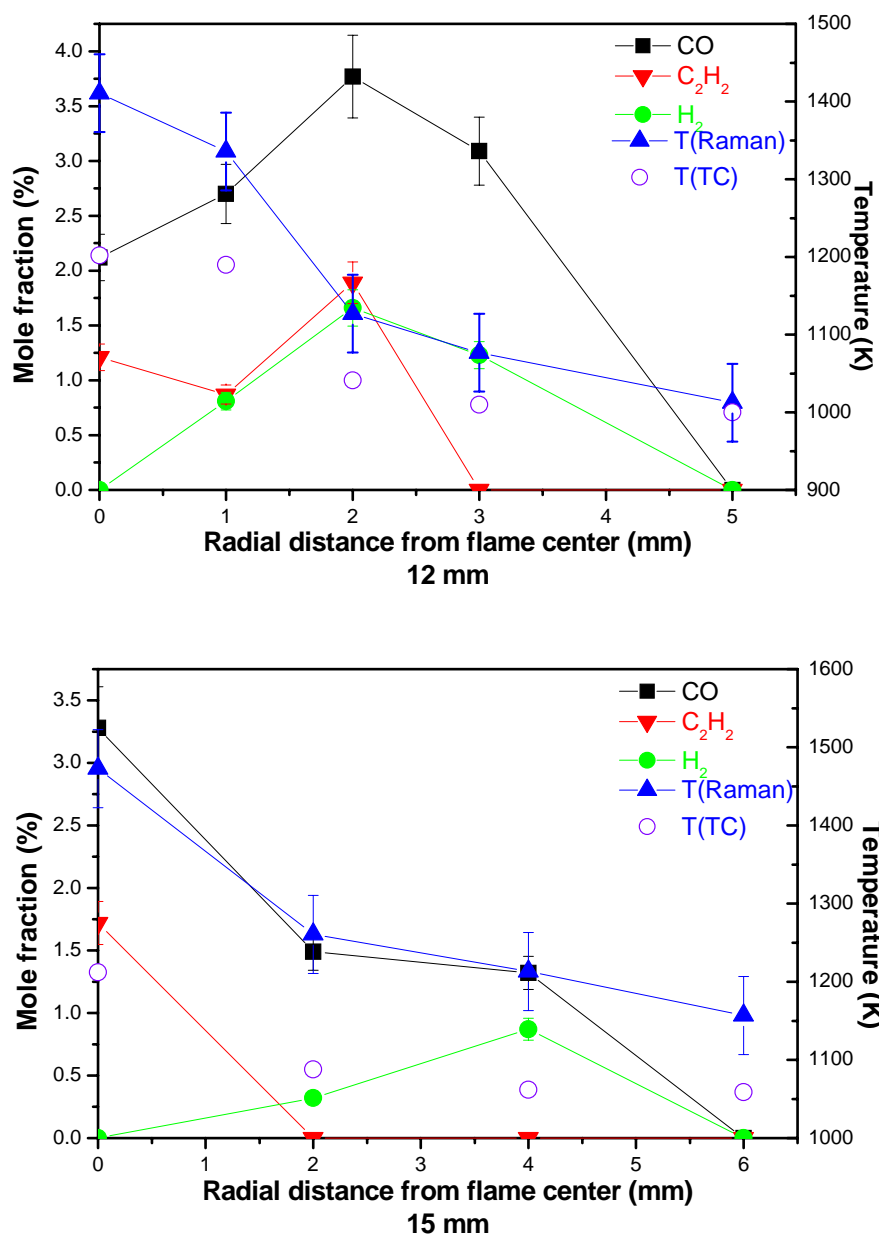


Figure 4.4. Gas-phase temperature (Raman) and species mole fraction profiles as measured by SRS, including thermocouple temperature (TC), at investigated sampling heights within the flame structure of Fig. 1: (a) $z = 6$ mm, (b) $z = 9$ mm, (c) $z = 12$ mm, and (d) $z = 15$ mm.

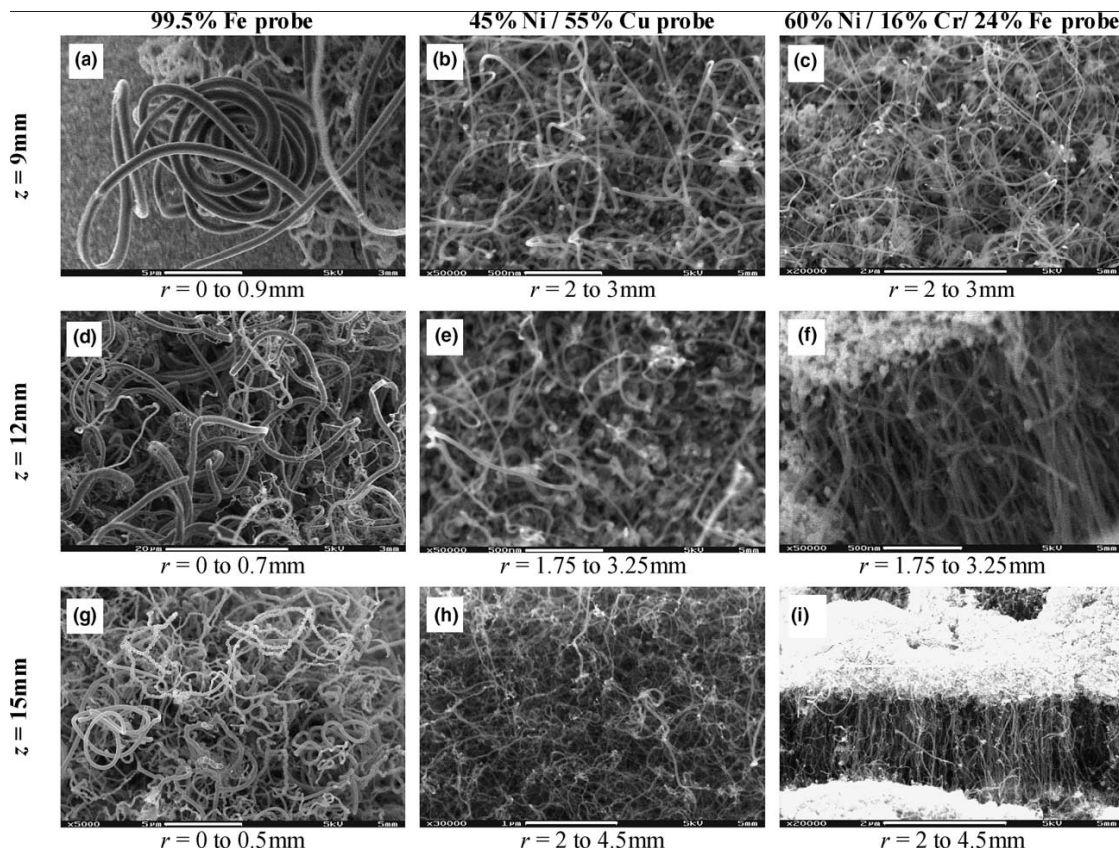


Figure 4.5. FESEM images of CNT morphology corresponding to catalytic probe composition (column) and flame sampling height (row) of Figure 4.1. (from Ref.28)

At the height of $z = 9$ mm, fibers and tubes can be seen growing on probes of different compositions at different radial positions (Fig. 4.5a-c). The center point is at the end of the bluish area and at the beginning of the orange area. Temperature at this point (1923K) is the highest in the flame--high enough to form catalytic Fe nanoparticles. Mole fractions of CO and C_2H_2 species (2.95% and 2.62%, respectively) are also high enough to induce CNT growth. Therefore, CNTs and carbon fibers are found to grow only near the centerline of the flame (Fig. 4.4b). For the Ni/Cu (Fig. 4.5b) and Ni/Cr/Fe (Fig. 4.5c) probes, CNTs are found only at $r = 2-3$ mm region, where the gas-phase temperature (around 1100 K) is high enough to produce Ni catalyst nanoparticles. Mole

fractions of CO and C₂H₂ are also high.

At the height of $z = 12$ mm, temperature is still highest (1411 K) at the flame center line. CO and H₂ have relatively high mole fraction at the $r = 2$ –4 mm region, while C₂H₂ can only be found near the center. This height turns out to be optimal for CNT growth. Nanomaterials grown on the iron probe are still found near the flame centerline (Fig. 4.4c) but the diameters are more uniform than at the previous height locations. For the Ni/Cu (Fig. 4.5e) and Ni/Cr/Fe (Fig. 4.5f) probes, $r = 1.75$ –3.25 mm is the region where CNTs are formed, where CO and C₂H₂ species generally have high mole fractions (3.77% and 1.89%, respectively). It also noted that well-aligned CNTs are formed near the $r = 3.25$ mm region where there is almost no C₂H₂, but plenty of CO, for the Ni-based probes.

At the height of $z = 15$ mm, the species mole fraction profile shows some similarity with that at previous height locations. Again, CNTs only grow near the flame centerline (Fig. 4.4d), which is the highest temperature area. For Ni/Cu (Fig. 4.5h) and Ni/Cr/Fe (Fig. 4.5i) probes, the CNTs have similar shapes but shorter lengths. The flatter temperature distribution and higher temperatures (all above 1150K) can perhaps explain the shorter CNT lengths and wider CNT growth regions ($r = 2$ – 4.5 mm of Fig.4.4d), as well as the orderly-arrayed patterns for Ni/Cr/Fe. It seems that CO is mainly responsible for CNT formation (Fig. 4.4d) here, as C₂H₂ is absent in these regions.

The large thermal and chemical gradients in the IDF are advantageous for determining CNT growth conditions due to the large parameter space. The SRS measurements quantitatively define the CNT growth conditions. As will be presented in the following sections, the SRS results also help to reveal the “universal” conditions between different synthesis methods.

There are also limitations of the SRS measurements in extracting flame synthesis conditions. As we have shown in the results, there are large gas-phase temperature gradients in the radial direction, but this may not be the same condition on the surfaces of the probes. For example, although gas-phase temperatures and CO and C₂H₂ mole fractions are comparable at locations [$z = 9$ mm, $r = 1.0$ mm] and [$z = 12$ mm and $r = 0$], as seen in Fig. 4.4b and 4.4c, the Fe probe inserted at the latter location is more conducive to CNT growth than at the former. In Section 4.4 of this chapter, we will show experiments using the quasi-1D counterflow diffusion flame, where the gradients only exist in the axial direction, and thus are negligible in the radial direction corresponding to the insertion orientation of the probes.

4.3 ZnO nanowires

CNTs are grown in the carbon rich region of the IDF on catalytic substrates. At the same time, metal-oxides nanowires can be grown directly from base-metal substrates using the same flame. Iron plated zinc, a low-melting-point metal, is examined as substrate in producing ZnO nanowires. Single-crystalline nanowires with uniform diameters, with growth rates of microns/min, without any pretreatment or catalysts, and in open environments, are grown directly on the zinc-plated substrates. Diameters ranging from 25-400 nm are selectable depending on local chemical species and temperature conditions.

Due to the sensitivity of ZnO nanostructures to their growth conditions (e.g. temperature and growth-related chemical species), examination of various temperatures and chemical species is required to understand the growth mechanism of ZnO nanostructures and to map the relations between ZnO nanostructures/morphologies and

their corresponding growth conditions in flames. Again, IDFs favor such examination as they present large gradients of temperature and chemical species in both axial (z) and radial (r) directions.

To get more detailed temperature and species profiles of the IDF for the nanowires synthesis, more rigorous measurements are done on the upper part of the flame cone where the flame synthesis conditions are most appropriate. First, detailed species concentration and temperature profiles are obtained at different height along the flames, and CFD simulations for the same flame configuration are compared with the experimental results. Second, in an effort to minimize system error, the CFD simulation results for N_2 concentrations are used to calibrate other species concentrations from the SRS measurements (see the post-processing details in Section 4.3.2). Both the improved measurements and simulation results are then adopted on a denser grid for the flame, which is shown in Figure 4.7-10. The 6 new heights (6 mm, 7 mm, 8 mm, 9 mm, 12 mm, and 15 mm) are still calculated from the exit of the inner tube of the burner. Based on flame shape, different intervals were used to get delineate the flame structure.

4.3.1 Experiment arrangement

The experiments for ZnO nanowire synthesis are conducted using the same flame configuration (Figure 4.6) as used for CNT synthesis, namely, an IDF established on a co-flow burner. Zinc-plated steel probes are used as substrates in the flame structure at various axial positions (z), as shown in Fig. 4.6, where local temperature and gas-phase chemical species are appropriate to promote reactions leading to zinc oxide. This geometry permits ready examination of the parameter space, as well as substrate probing of the fuel side of the flame structure for nanowire growth without piercing the reaction

zone and allowing oxygen leakage, thereby isolating O_2 versus H_2O reactions with Zn. The SRS measurement setup is the same as in Section 4.2, but additional considerations are placed on improving the accuracy of the species concentration measurements. In Section 4.2, to correct beam steering and defocusing effects, a linear distribution of N_2 mole fraction both in axial and radial direction is used as the calculation basis for the mole fractions of other species. However, a more accurate method is employed here to assess the N_2 mole fraction profile based on CFD simulation. This post-processing method is given in the next section.

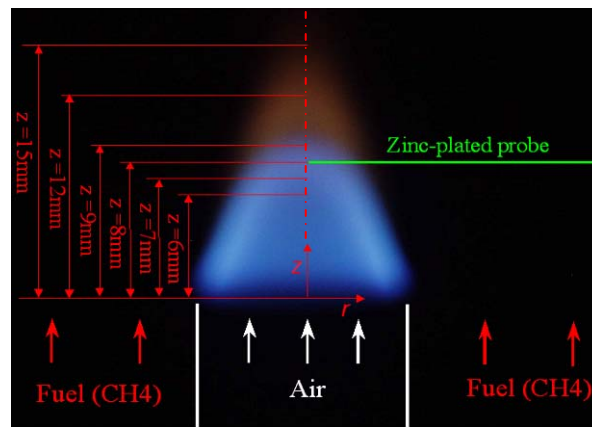


Figure 4.6. An IDF with investigated positions for ZnO nanostructure growth

4.3.2 N_2 Profiles from FLUENT simulation

The inverse diffusion flame (IDF) of a co-flow jet configuration using methane as fuel is studied and modeled using Fluent Computation Fluid Dynamics (CFD) software²⁰. Fluent software along with Gambit model and mesh builder is used to create a 2D axisymmetric geometry. A converging solution is obtained by iteration. Arrhenius kinetics is used to model a one and two-step laminar reaction of methane and air.

Specific properties for components are obtained through the built-in Fluent database based on Chapman-Enskog kinetic theory model²¹. From the simulation, temperature and major species profile along axial and radial direction can be obtained.

The simulation results for N_2 concentration can help to make accurate calculations of other species concentrations from the experimental data. In the counterflow diffusion flame (CDF), a quasi-one dimensional flame with ideally no gradients in the radial direction, a linear distribution assumption of N_2 concentration along the axial direction is appropriate. However, as will be shown in Section 4.4, an assumption of N_2 concentration from a computational simulation will increase the accuracy of the results of other species. Due to the complexity of the flame structure of the co-flow jet flame, however, a simple assumption of linear distribution of N_2 concentration is not accurate, either in axial or radial direction. With Fluent simulation results, temperature profiles are first verified by the SRS temperature measurement through curve-fitting N_2 Raman spectra with a N_2 spectra library (Figure 4.7). Since SRS temperature measurements (with high precision) are independent from concentration measurements, N_2 concentration profiles (Figure 4.8) from the same simulation predicting the experimental temperature “correctly” should provide a reasonable basis for concentration calculations for other species concentrations.

It is necessary to note that, due to the complexity of the flame structure and chemistry, the computations only serve to assess the N_2 (prevalent inert species) profiles, for which the SRS measured values are calibrated, and not to calculate the other species concentrations (or temperature) directly.

The comparisons of the simulation and experimental results are given in Figure 4.9 and Fig. 4.10. For major species, the profiles of O_2 , CO_2 , CH_4 , and H_2O are from the Fluent simulation results. The experimental results (based on the computed and experimental N_2 results) at specific measurement points are also given for comparison. The concentration of O_2 is highest at the exit of the burner and is continually consumed along the downstream direction of the flame structure. At the first measurement height, $z = 6\text{mm}$, the O_2 concentration at the centerline decreased to 14.06% from the result of SRS measurements; the simulation results at this point has only a 3% difference with experimental results. Towards the tip of the bluish flame area, O_2 concentration decreased to a negligible level at 9 mm, from both simulation and experiment. This corresponds to the end of the flame reaction zone where O_2 is consumed completely. By calibrating the simulation to the experimental data, basically by defining the reaction front, we can assess the accuracy of the post-processed values from the measurements for the other major species.

The comparisons for other species, i.e. CO_2 , CH_4 , and H_2O , are also shown individually for various measurement heights and radial locations (Figure 4.10). For those species with concentrations smaller than O_2 , the agreements between simulation and experimental data tend to be less close than that with O_2 . Nevertheless, the distribution profiles of these species still reflect the basic trend in their concentrations and shapes as those measured by SRS.

In comparing the profiles of major species with the N_2 concentration profile assumed linear and with the N_2 concentration profile obtained using FLUENT simulation, we find that for most of the major species (O_2 , CO_2 , and H_2O), the difference between two

profiles is under 10%; for CH₄, the discrepancy between two are larger, especially in the outer edge of the profiles. This is because CH₄ and N₂ are two major compositions of the outer area of the inverse diffusion flame, and CH₄ is more sensitive to N₂ profile assumption than the inner part of the profiles.

Although the aim is not to match simulation and experimental results for major species, the flame temperatures from simulation are still much higher than that for the actual case. Again, we are only interested in defining the flame boundaries so that the N₂ concentration profile is reasonable. However, the best route would be to determine the N₂ profile experimentally through Rayleigh scattering²². The Rayleigh scattering experiments usually employed a laser to illuminate the flow and the illumination line or sheet is detected normal to the incident laser. The intensity of the scattered light can be expressed as

$$I = KI_0N\sum_i\sigma_ix_i \quad (4.1)$$

K is the calibration constant of the collection optics, I_0 is the intensity of incident laser light, and N is the total number of molecules contained in the probe volume. The summation is over all species with the mole fraction x_i and Rayleigh cross-section of the i th gas in the mixture σ_i .

4.3.3 Results and discussion

SRS is employed to measure the gas-phase temperatures and concentrations of oxidizing species (i.e., O₂, H₂O, and CO₂) at the specific locations (r and z) where ZnO nanomaterials are produced. The result is illustrated in Fig. 4.11.

We first present the synthesis results at $z=8\text{mm}$ – a characteristic axial position where a variety of ZnO nanostructures (e.g. nanowire, nanoribbon and hierarchal structure) is

obtained. Both temperature and species are shown in Fig.4.11 ($z=8\text{mm}$). Specifically, ZnO nanostructures are produced in regions of high H_2O and CO_2 concentrations, where the H_2O route is likely based on homogeneous reactions with subsequent condensation, while the CO_2 route is probably due to heterogeneous surface reactions. In contrast, high concentrations of O_2 may actually hinder nanowire formation due to substrate surface oxidation. Along with substrate temperature and its associated gradient from solid to gas phase, such parameters are essential in producing a desired growth characteristic (e.g. morphology, diameter, and direction), and need further investigation. Nonetheless, EDX spectra (Fig. 4.12d) for all growth regions marked on Fig. 4.11c and shown in Fig. 4.12 reveal that the nanostructures are composed of only Zn and O, in proportions indicating that the as-synthesized nanomaterials are ZnO.

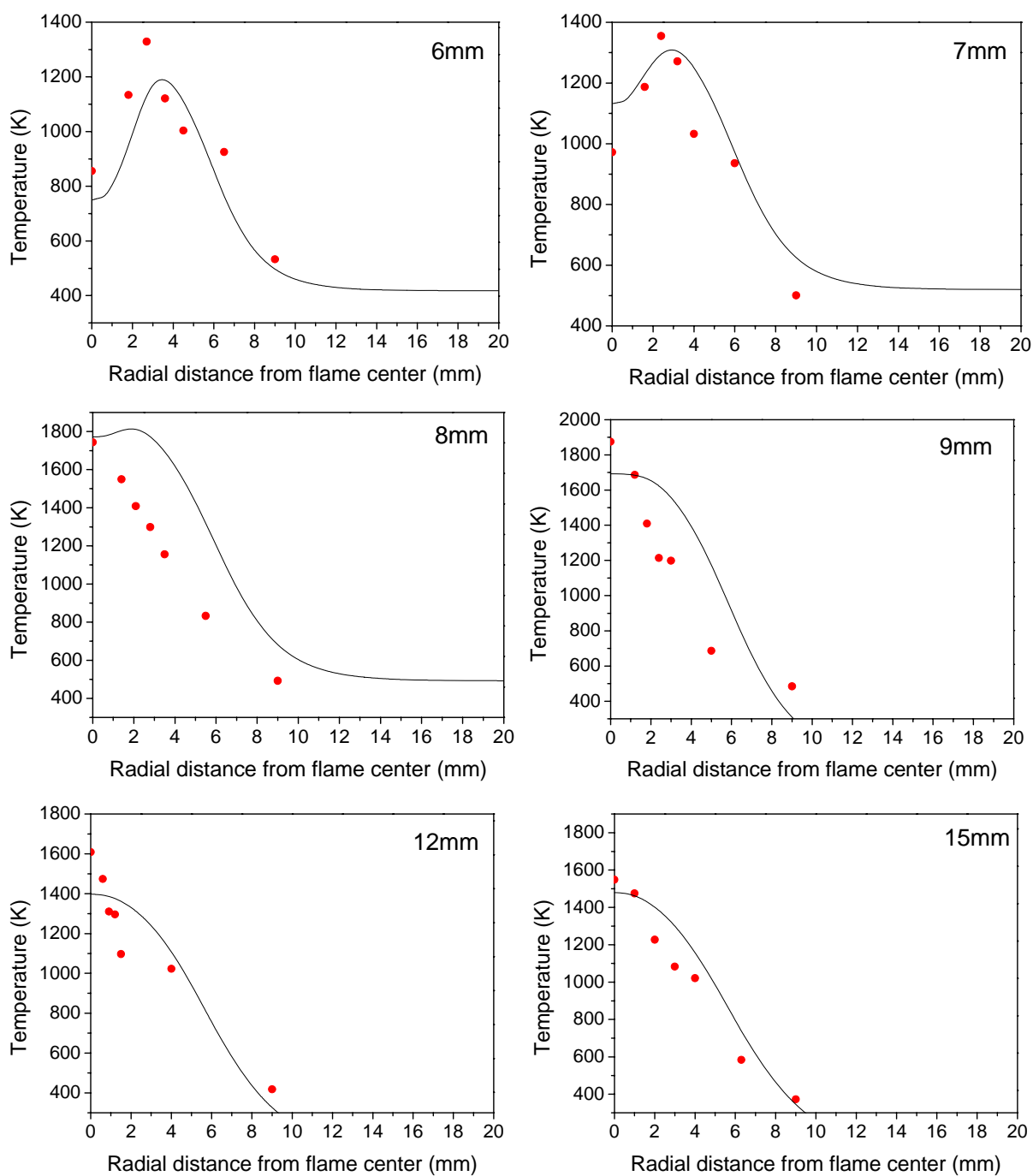
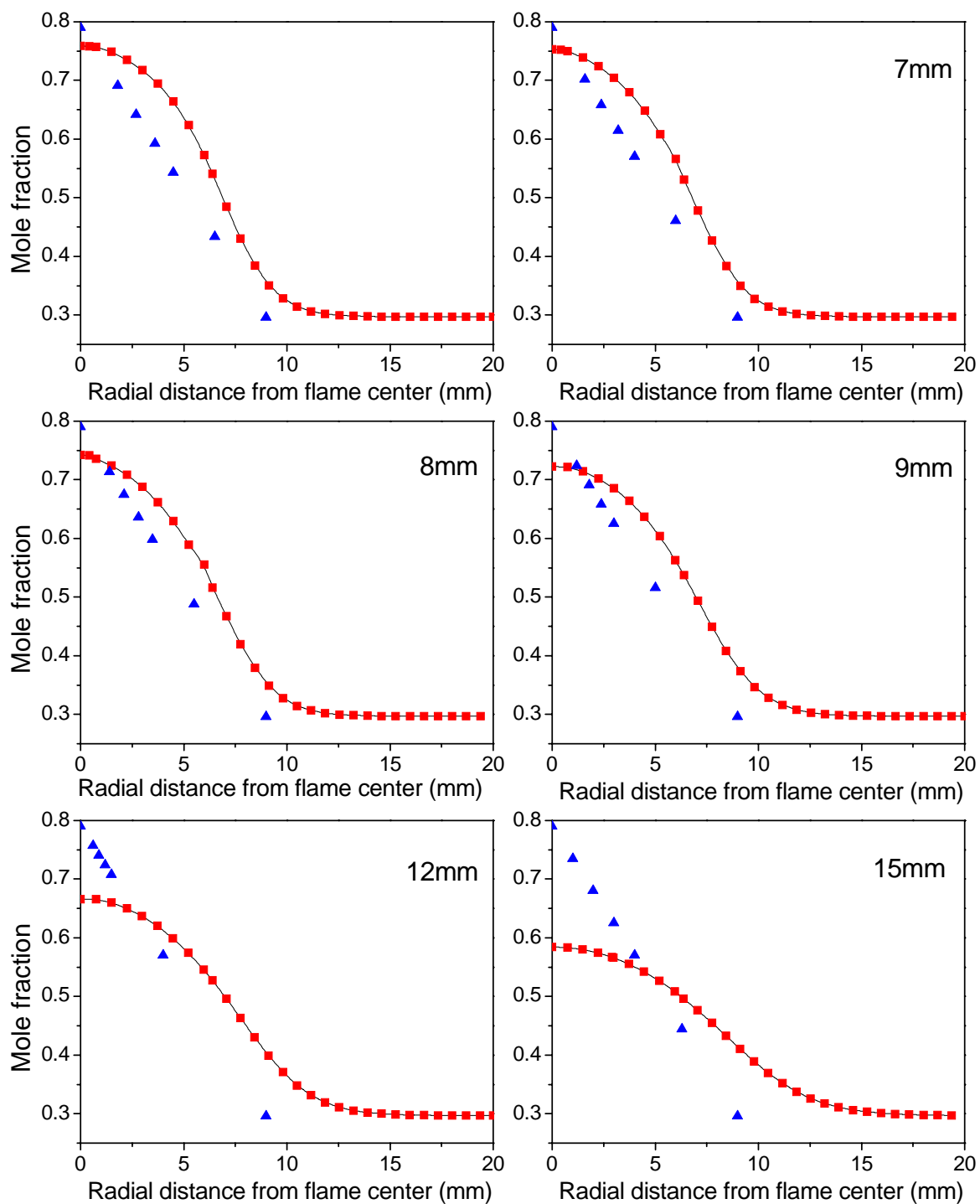
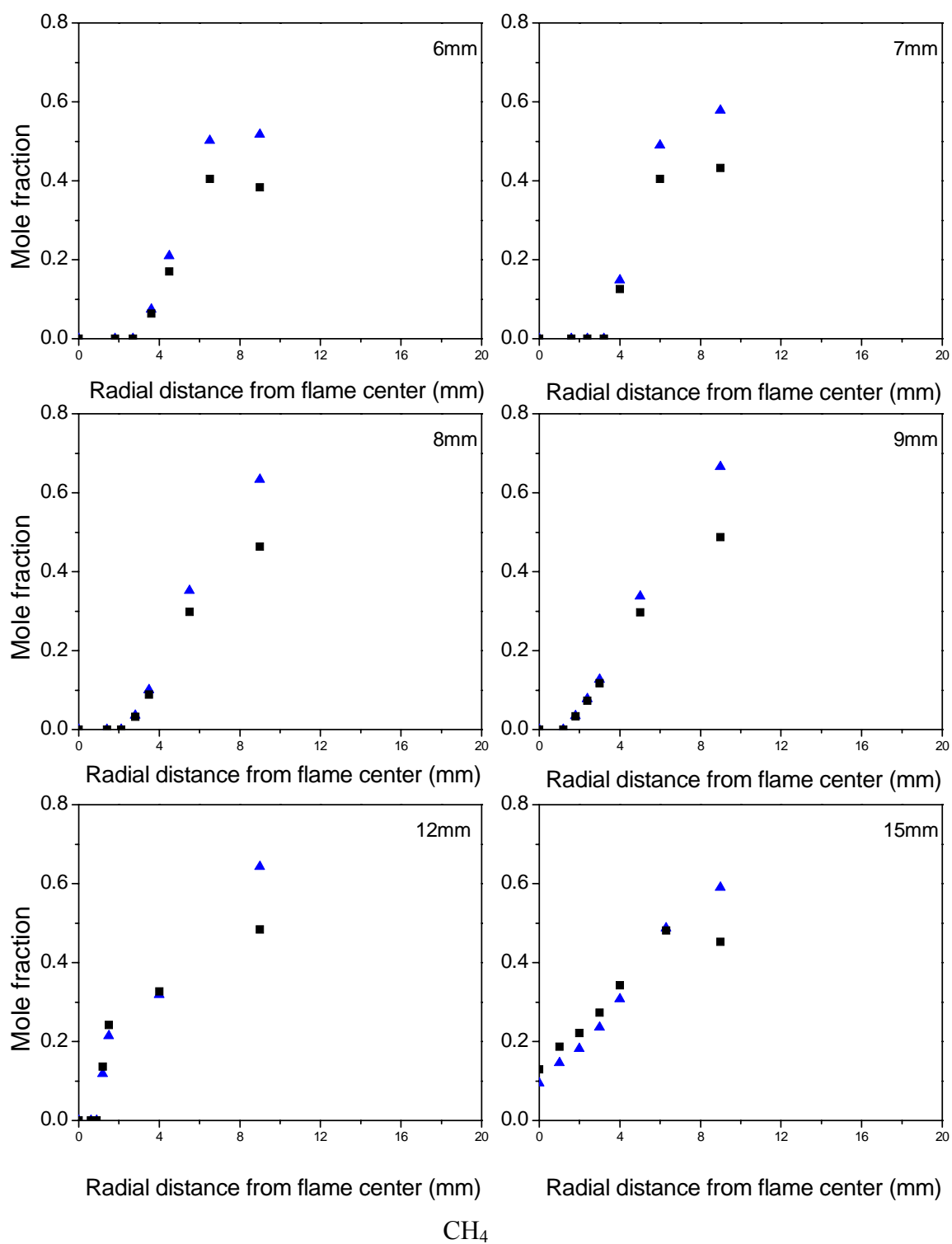
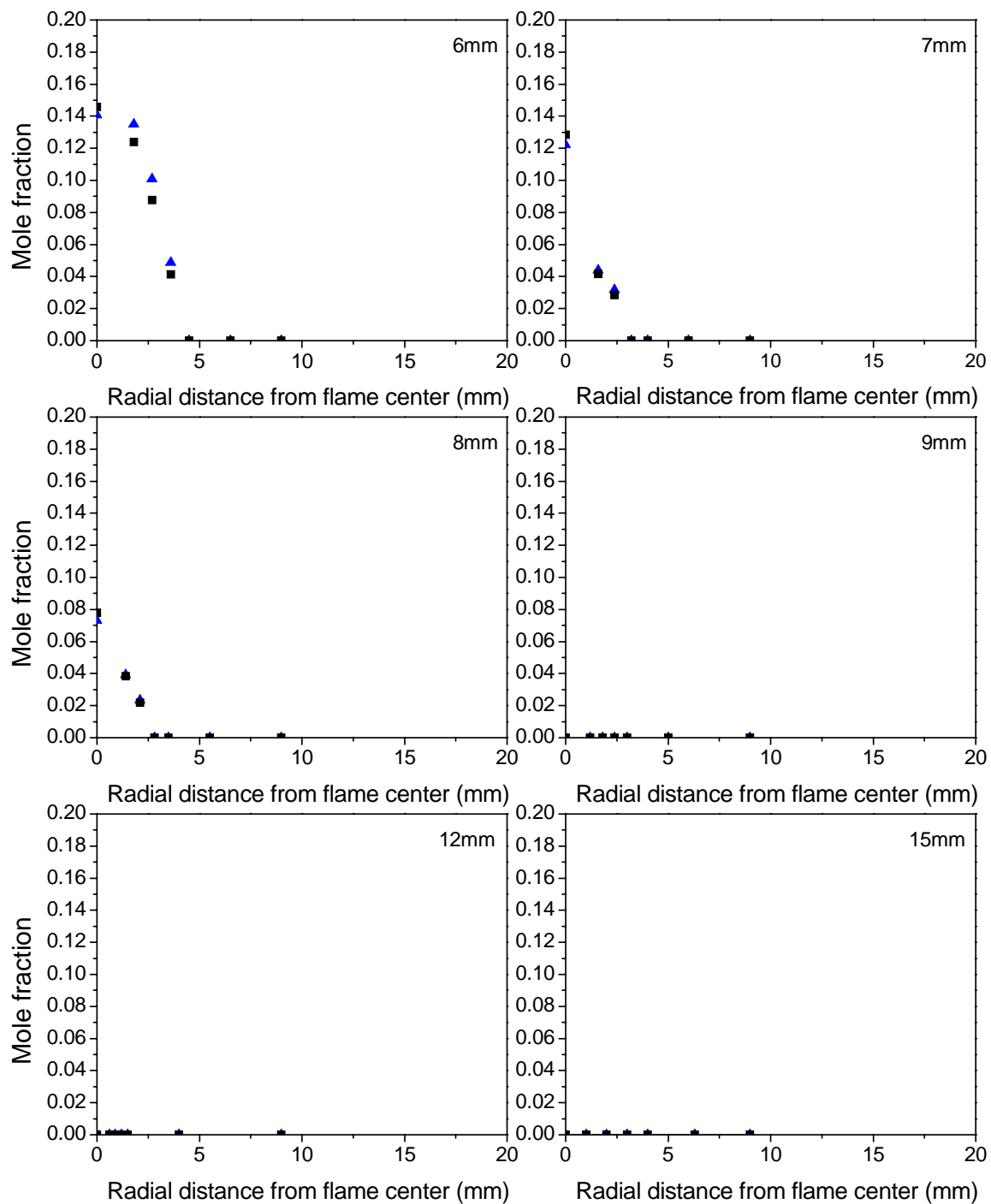
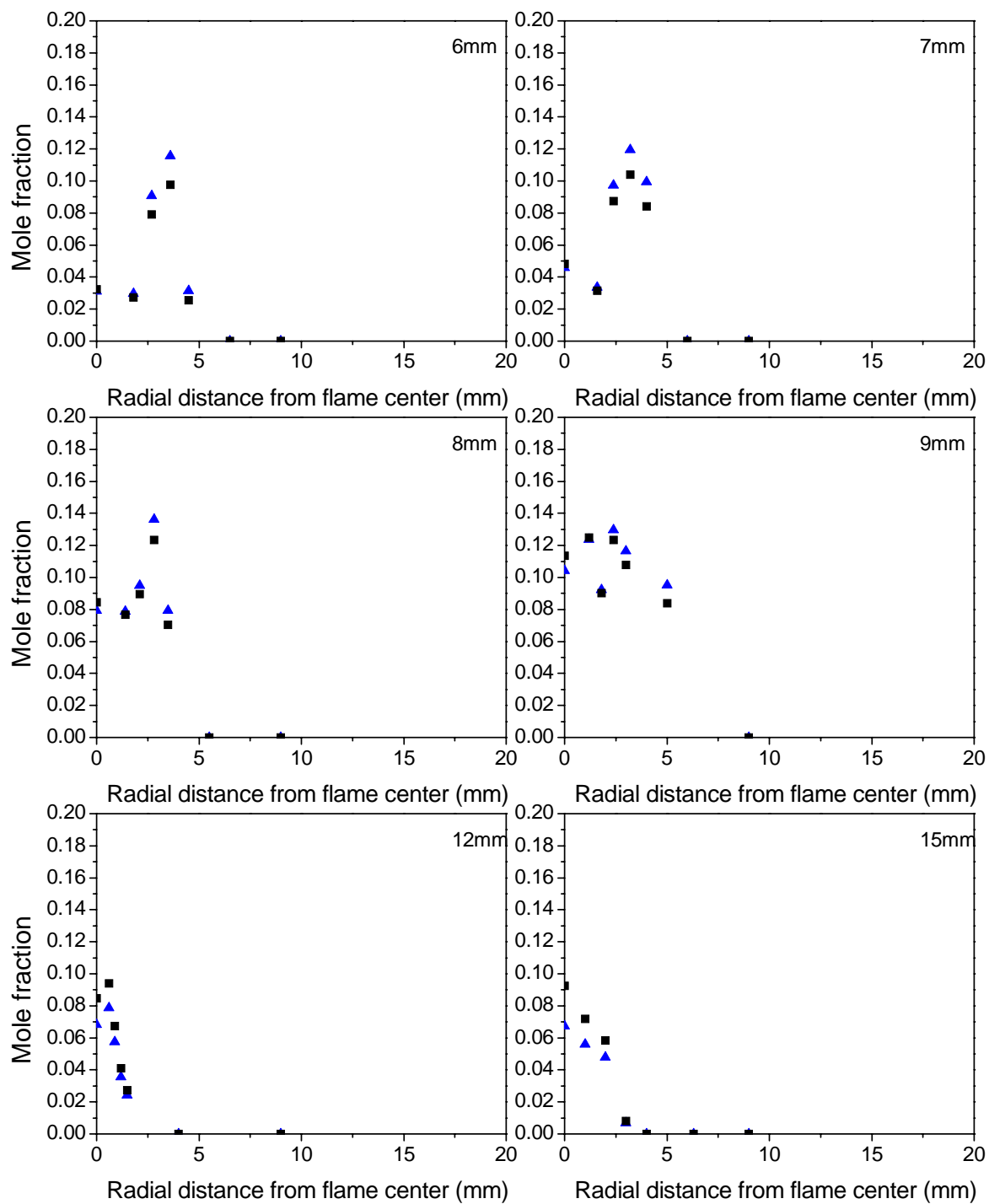


Figure 4.7. Comparisons of simulated and experimental results of flame temperature.

 N_2



 O_2



H_2O

Figure 4.8. N_2 profile simulation results from Fluent (■) vs. linear assumption (▲) and the comparisons of major species.

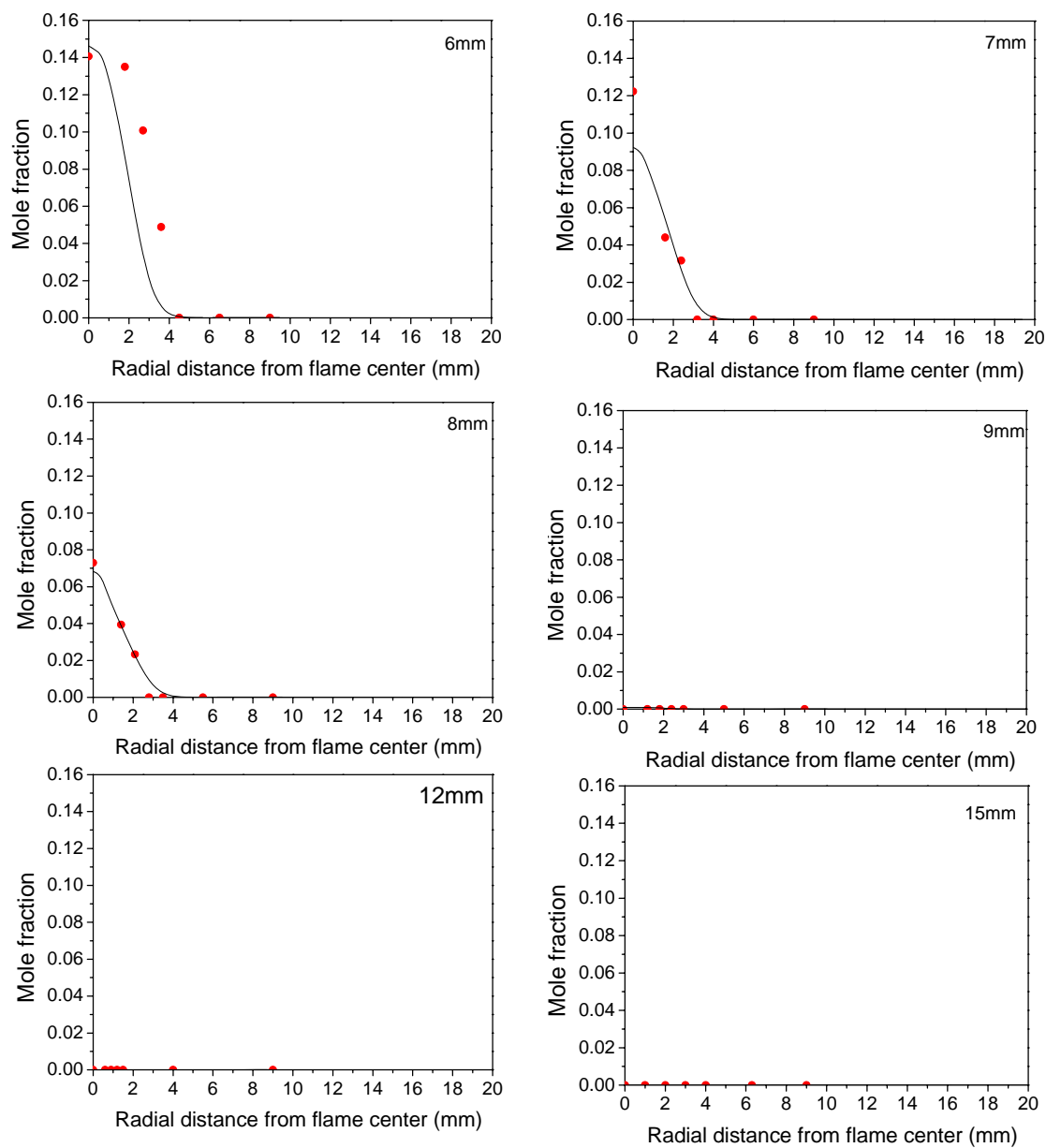
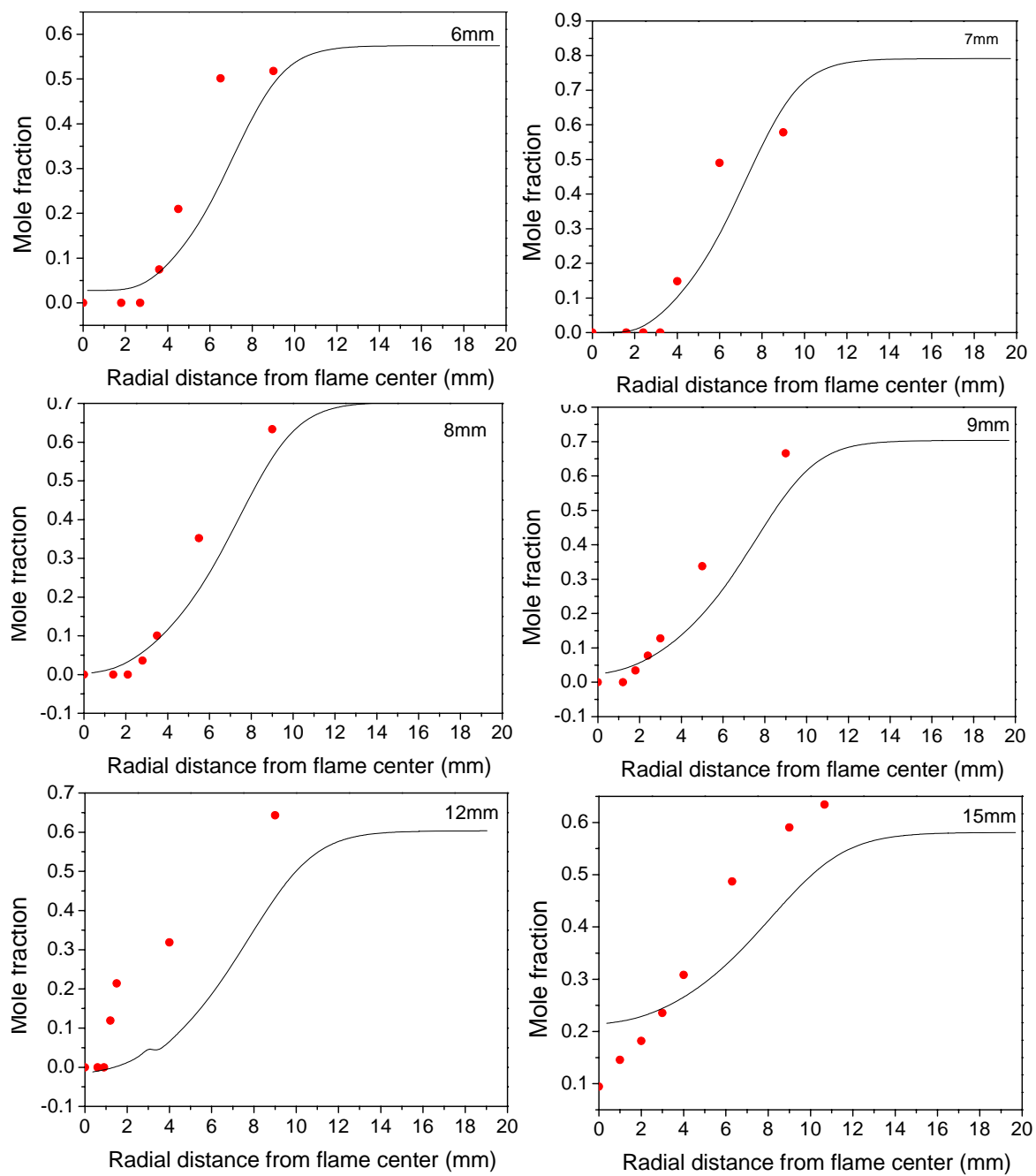
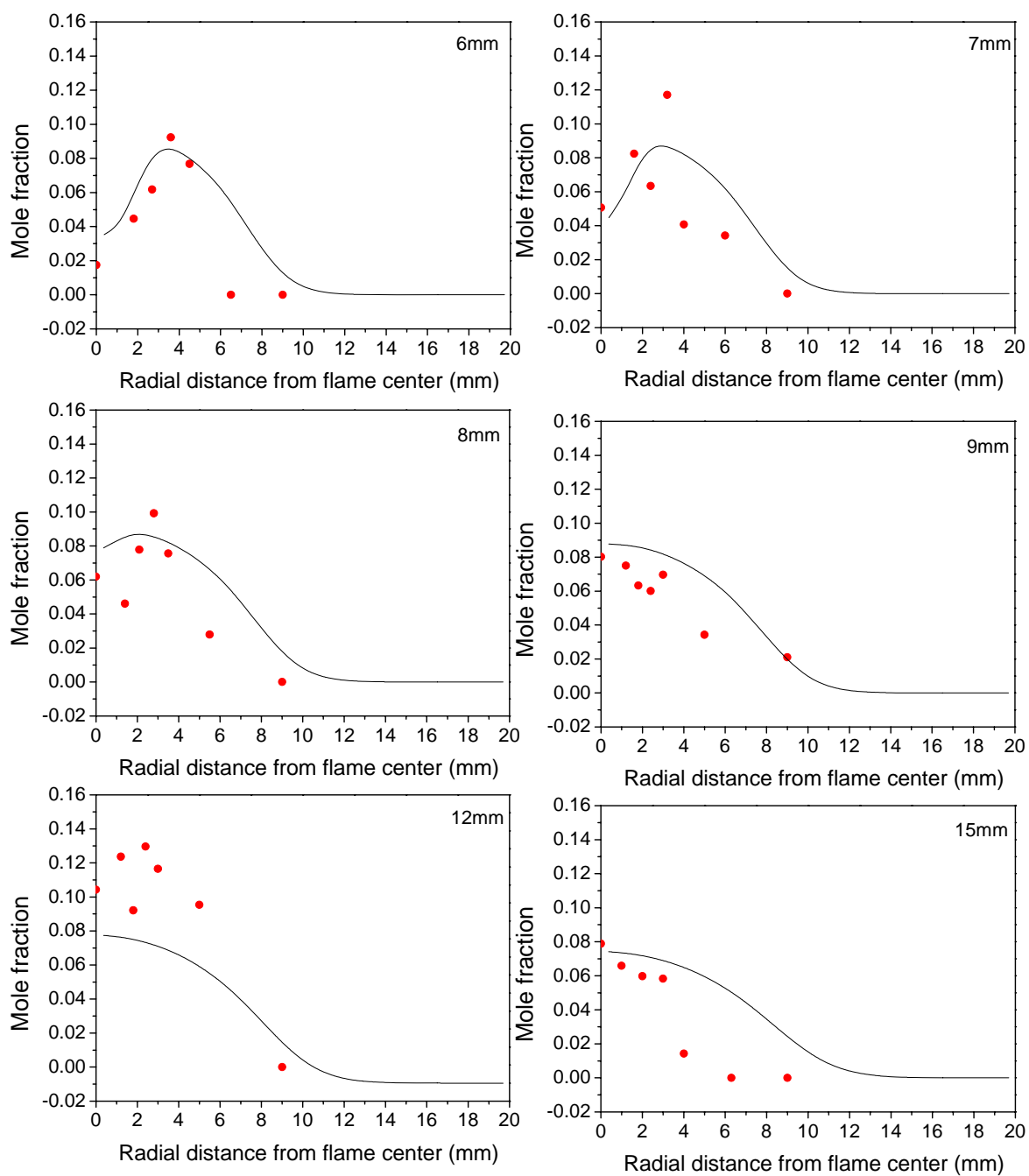
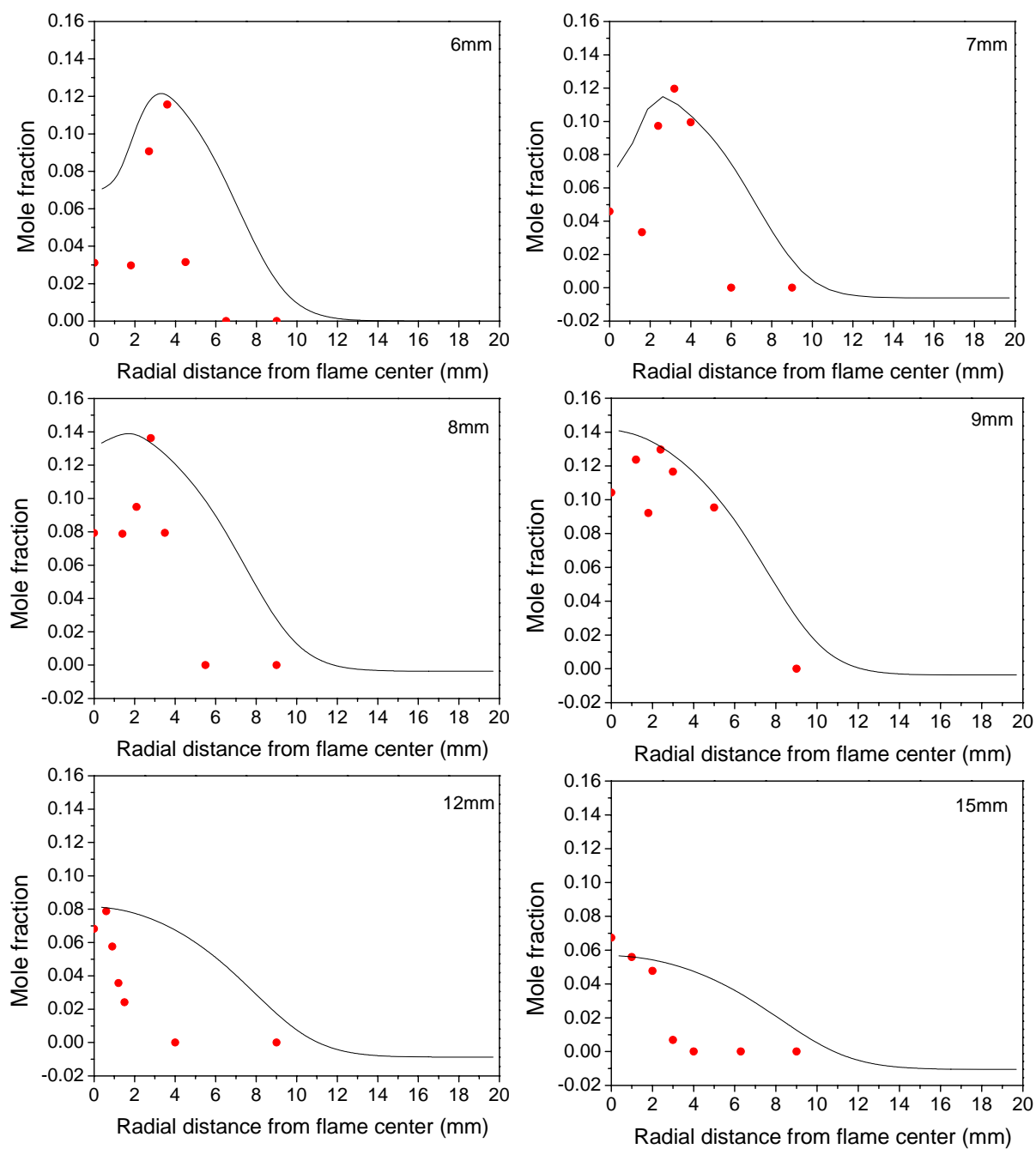


Figure 4.9. Comparisons of simulated and experimental results of O_2 mole fraction.

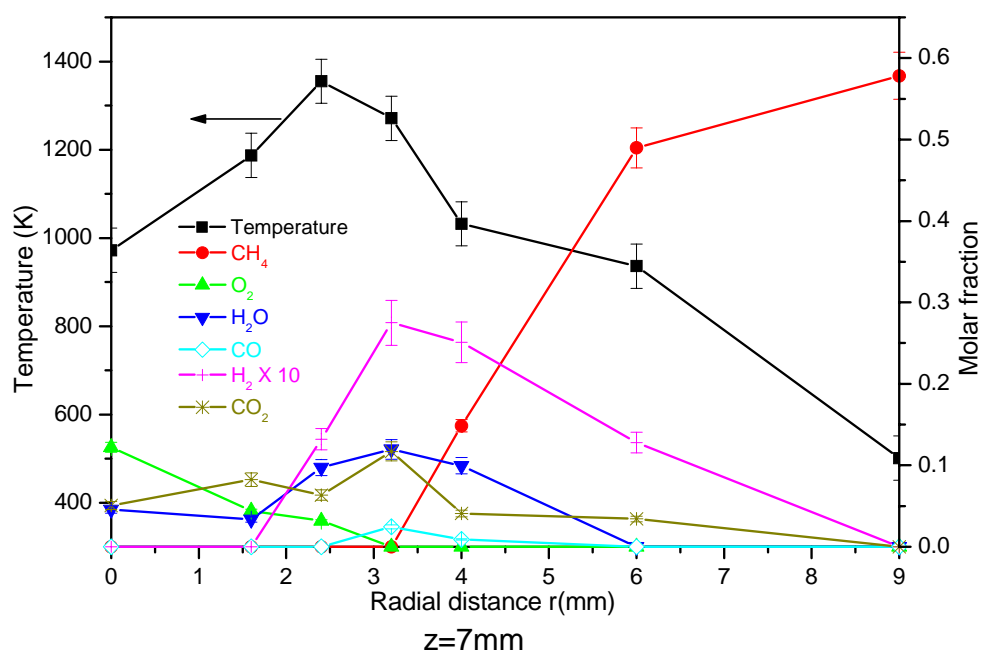
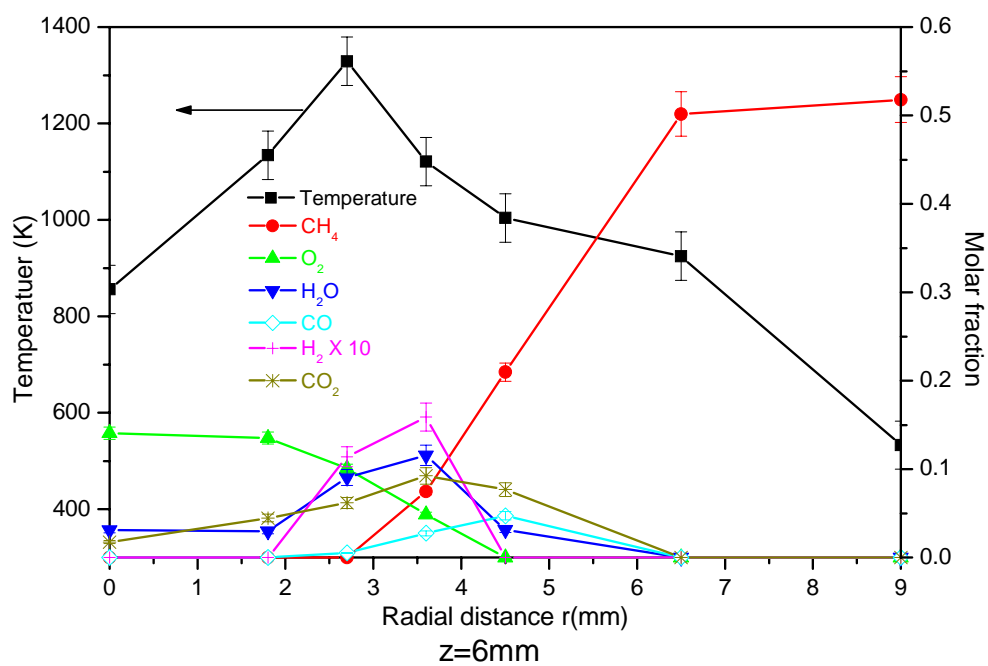
 CH_4

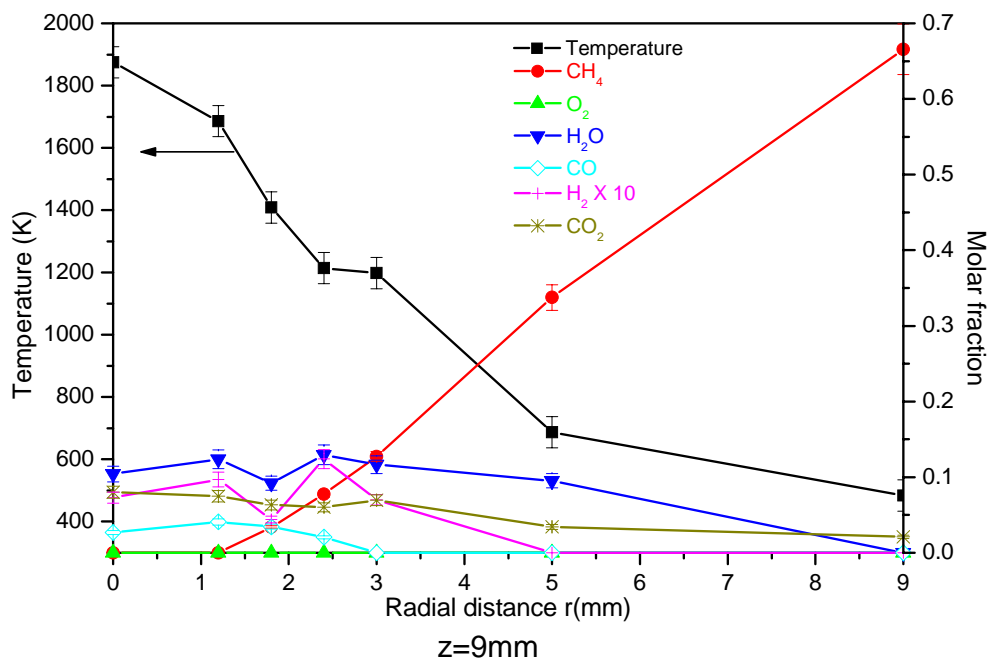
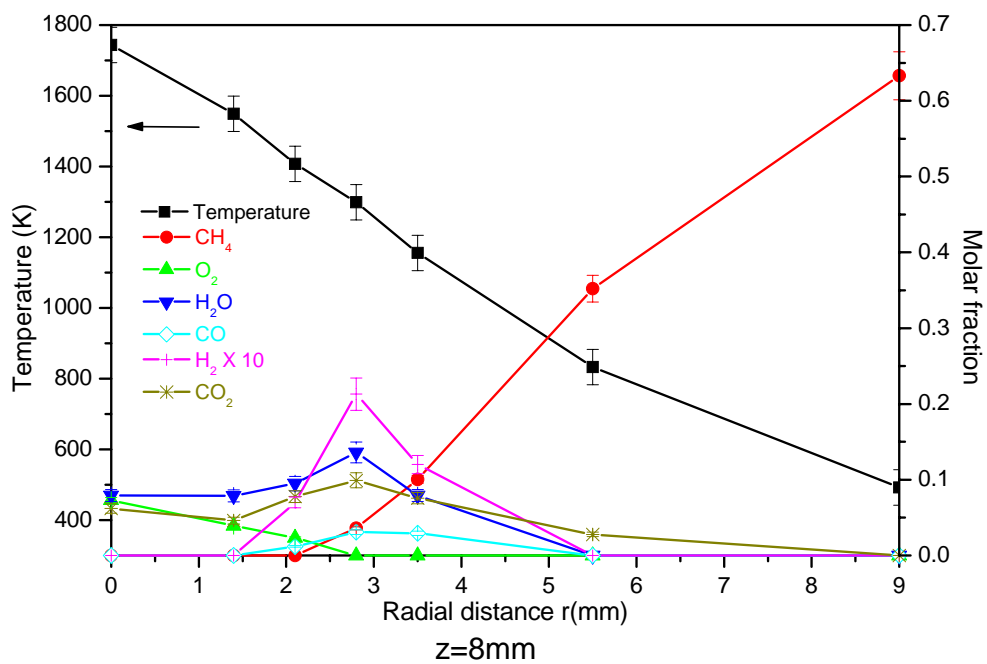
 CO_2



H_2O

Figure 4.10. Comparisons of simulated and experimental results of CH_4 , CO_2 , and H_2O at various heights in the flame.





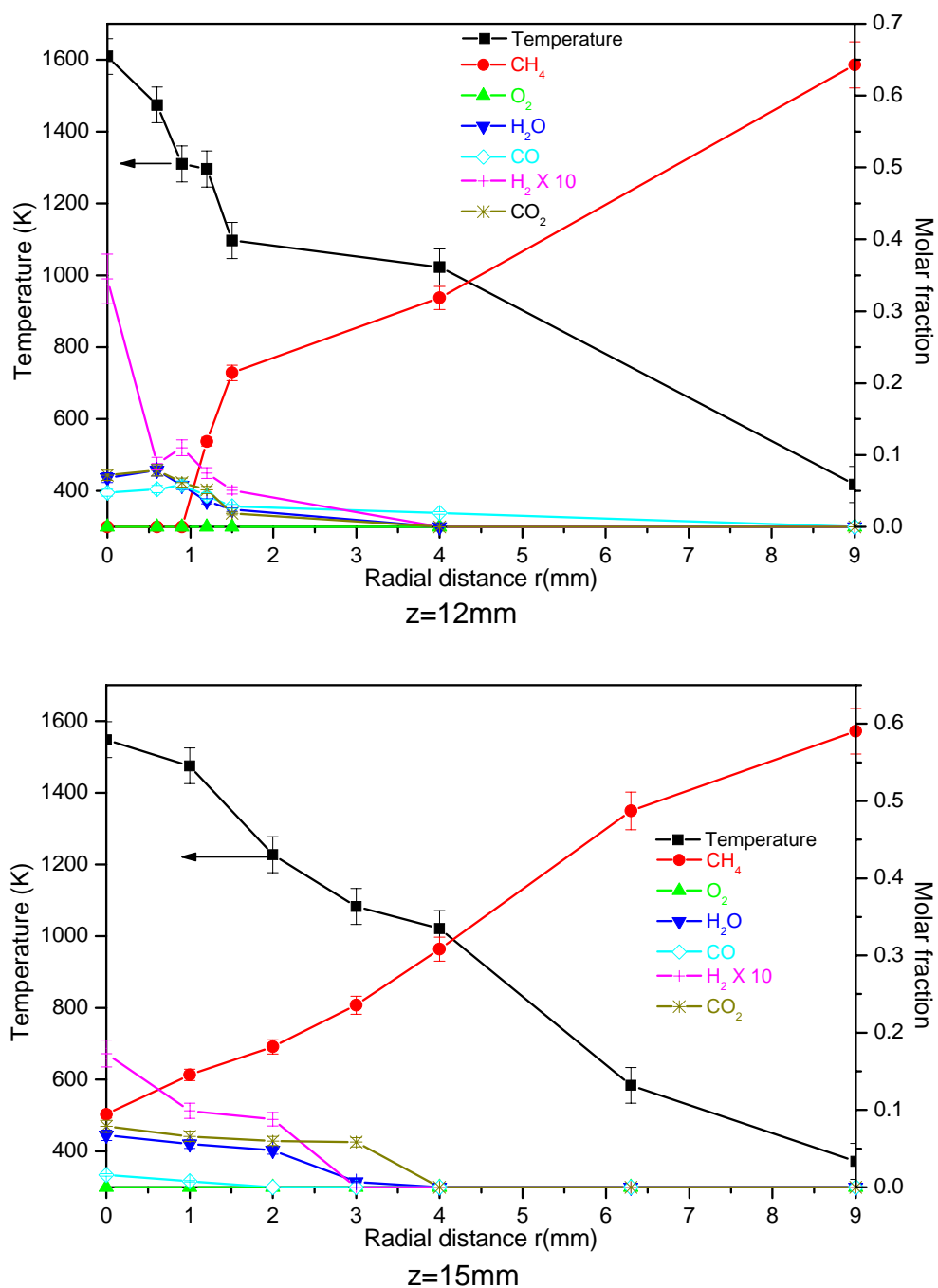


Figure 4.11. The profiles of temperature and major species measured by SRS for the production of ZnO nanostructures, at (a) $z=6\text{mm}$, (b) $z=7\text{mm}$, (c) $z=8\text{mm}$, (d) $z=9\text{mm}$, (e) $z=12\text{mm}$ and (f) $z=15\text{mm}$, along with the temperatures measured by thermocouple (TC)

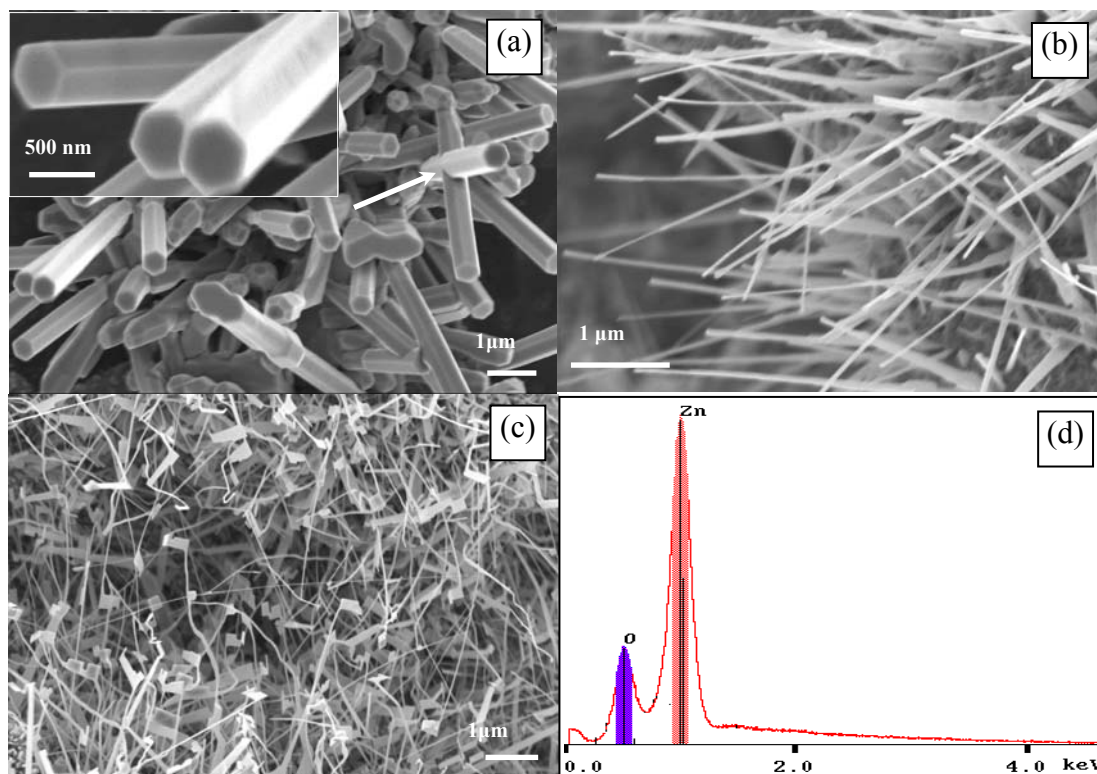


Figure 4.12. FESEM images corresponding to growth characteristics of (a) 100-400nm diameter nanowires, where arrows show interpenetrative growth, (b) < 50 nm diameter nanowires, and (c) nanowires with transition to nanoribbons at the tips. (d) EDX spectra of as-grown nanowires. (from Ref. 27)

The specific case of Fig. 4.11c ($z=8$ mm) shows gas-phase temperatures ranging from 800-1500K. While temperature decreases steadily with radius, the species concentrations are not fixed and are, in fact, non-monotonic. Thus, temperature is not the only variable governing nanostructure growth morphology as a function of radial position; and the departure from the “conventional” nanowire as seen in Fig.4.12c is not surprising. Nevertheless, other axial locations were investigated; and the results show that for the same quantitative local conditions (temperature and species), the same growth morphology is attained, corroborating that optimal local conditions for ZnO nanowire synthesis are “universal” and likely to be translatable to other methods and geometries of

gas-phase synthesis. For example, at both $z=12$ mm and 15 mm, the probed locations are in the post-flame zone where no oxygen is available (see Figs.4.11e and f). In these regions, only nanowire structures are obtained, similar to Fig.4.12b). At both $z=12$ mm and 15mm, where local conditions are ~ 1250 K with $\sim 3\%$ H_2O mole fraction and ~ 1050 K with $\sim 1\%$ H_2O mole fraction, respectively, nanowires of ~ 120 nm and ~ 40 nm in diameters are grown, respectively, similar to the characteristic case of Fig.4.11c for $z=8$ mm.

4.4 Spontaneous Raman scattering of counter flow diffusion flame

While the IDF is used to scan a large parameter space of conditions to find favorable local conditions for CNT growth, its 2-D geometry presents large gradients in the radial direction, making it difficult to isolate certain conditions. The CDF is a quasi-one dimensional flame with ideally no gradient in the radial direction. As such, conditions can be sought as a function of axial position. The specific flame configuration is a flat flame formed in between when the fuel and oxidizer issued from the bottom and top burners, as they impinge at atmospheric pressure. The flame is aerodynamically well-defined, with gradients existing only in the axial direction, and can be easily probed by SRS and compared with simulations involving detailed chemical kinetics and transport. A picture of an actual CDF is given in Fig. 4.13.

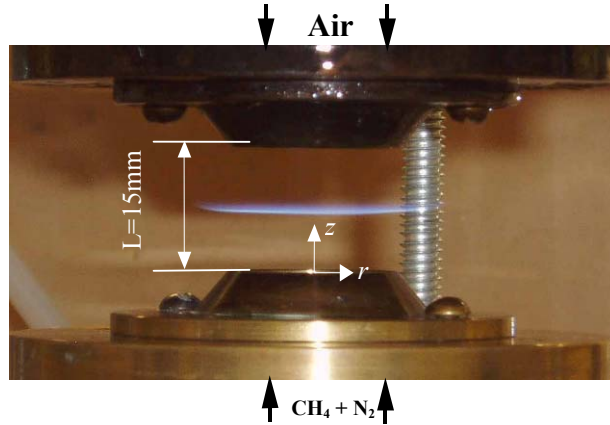


Figure 4.13. A CDF flame is established between the two burners.

The experiment utilizes the quasi-one-dimensional counterflow diffusion flame, with an air jet impinging onto an opposed jet of nitrogen-diluted methane (1.32 L/min fuel from a 19-mm-diameter nozzle) at atmospheric pressure. Spontaneous Raman scattering again is used to explore the temperature and species concentration profiles in the CDF. Favorable comparisons between the simulation and the measurement for the well-defined 1-D configuration give confidence to the SRS measurement of flame structures of IDFs.

4.4.1 Experiment arrangement

The SRS diagnostic setup is very similar with that used in methane inverse co-flow jet diffusion flame (Fig. 4.1b). The only difference is that the measuring volume is increased from a 100 μm diameter \times 100 μm length to 200 μm diameter \times 1500 μm length. Since the flame possesses only gradients in the axial direction, the light collection area in length is enlarged to increase collection power, with the SRS signal linearly proportional to the total energy of the laser pulse in the sampling volume.

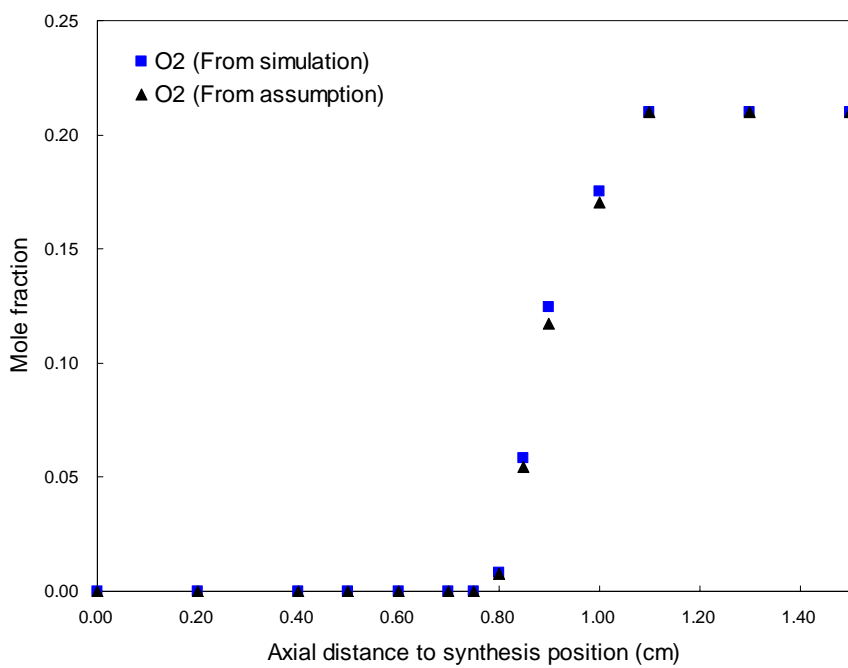
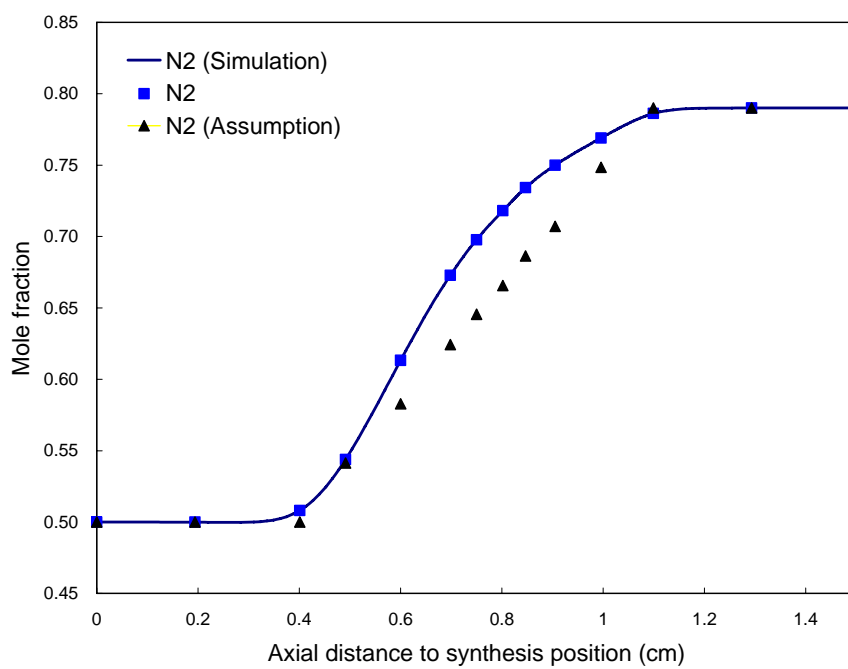
A detailed profile of temperature and major/minor species for the CDF includes 14 points in the axial centerline. The SRS signals collected at each point are for N_2 , O_2 , CH_4 ,

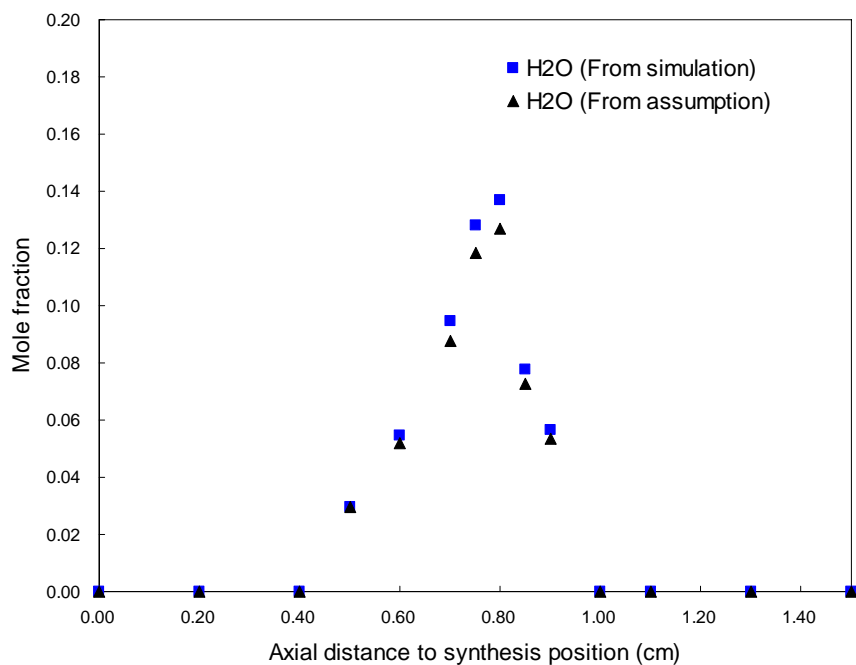
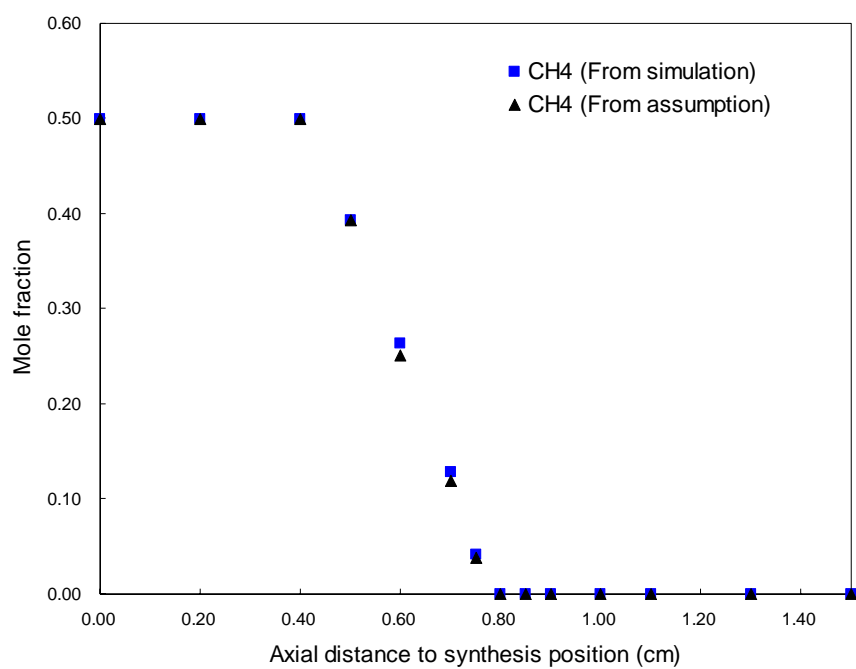
H₂O, CO₂, CO, C₂H₂, and H₂. The temperature is calculated from curve fitting the N₂ Q-branch Raman spectrum using a library of theoretical spectra at different temperatures (program code from Sandia). N₂ concentration is first assumed to linearly increase in the reaction zone, from fuel side of the burner (50%) to the fuel side of the burner (79%). Then the simulation results of N₂ mole fraction profile (CHEMKIN simulation software) is used as a base to calculate mole fractions of other species, which are deduced from the ratio between their SRS signal strength to N₂'s. And a program written in Visual Basic was modified and employed to facilitate the calculation processes. Both the linear distribution assumption and CHEMKIN simulation results for N₂ are shown in Fig. 4.14 for comparison. The details of the simulation can be found in Ref. 23. Fig. 4.14 also shows the concentrations of other major species (O₂, CH₄, H₂O, and CO₂), calculated using both the simulated and linear N₂ assumption, respectively. It can be seen from the comparison, there are maximum 7% differences between the results from the two assumptions. There are larger differences for H₂O in high temperature areas, resulted from larger uncertainties in measurements and simulations for species with lower concentrations. Finally, interference from the O-branch of N₂ on the CO spectrum, from O₂ on the CO₂ spectrum, and broadband fluorescence, which was believed to originate from PAHs and possibly incandescence from incipient soot nuclei were corrected for C₂H₂, CO and CO₂ spectrums. Broadband fluorescence from C-related species is also subtracted. The reproducibility of the concentration measurements is usually within $\pm 5\%$.

4.4.2 Fluorescence Interference on Raman measurement

In hydrocarbon flames, fluorescence interferences can arise from carbon containing radicals such as C₂, CN, CH, and PAHs. With 532 nm excitation, Dibble et al. and Masri

et al.²⁴ encountered 'fluorescence' interferences which were broadband and believed to originate from PAHs and possibly incandescence from incipient soot nuclei. While the "fluorescence" may be corrected for (using correction curves generated from measurements made in a laminar counterflow CH₄ diffusion flame and a diluted CH₄/N₂ = 1/2 (by vol.) laminar diffusion flame) measurements of CO and CO₂ are not reliable in the rich regions of the flame where the "fluorescence" is intense. As a solution to the problem, a simple assumption is made that the "fluorescence" is responsible for the broadband baseline of the CO or CO₂ spectra. Based on this assumption, corrections are made to those species with severe 'fluorescence' interferences. The results are shown in Figure 4.15. It is clearly shown that the corrected results are more close to the simulation results, which are considered very reliable, at least for methane flames in the counterflow diffusion geometry. Extra corrections based on this assumption produce a closer match to the flame structure simulation and is also made in the co-flow inverse diffusion flame of Section 4.3.





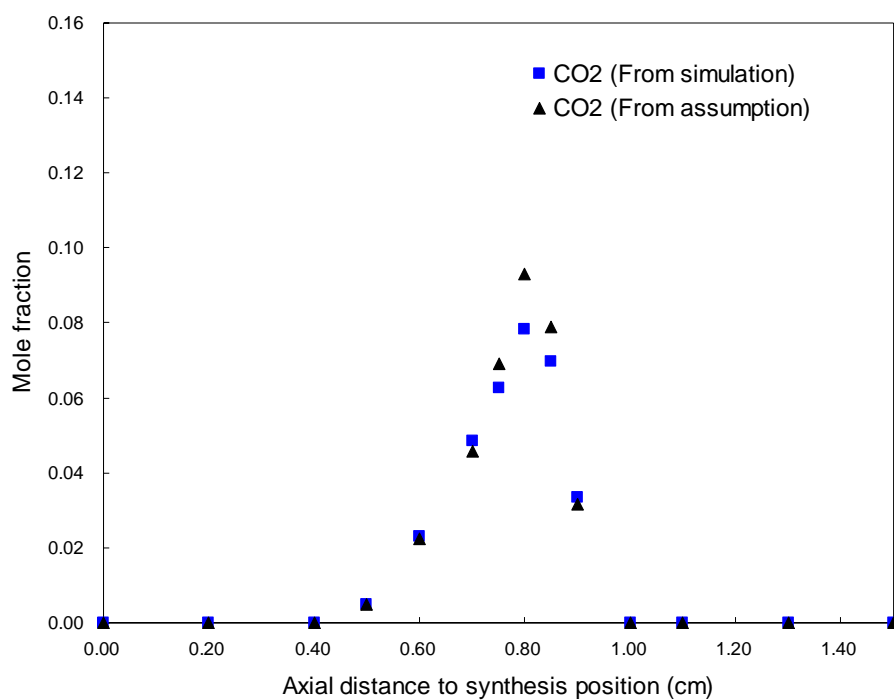
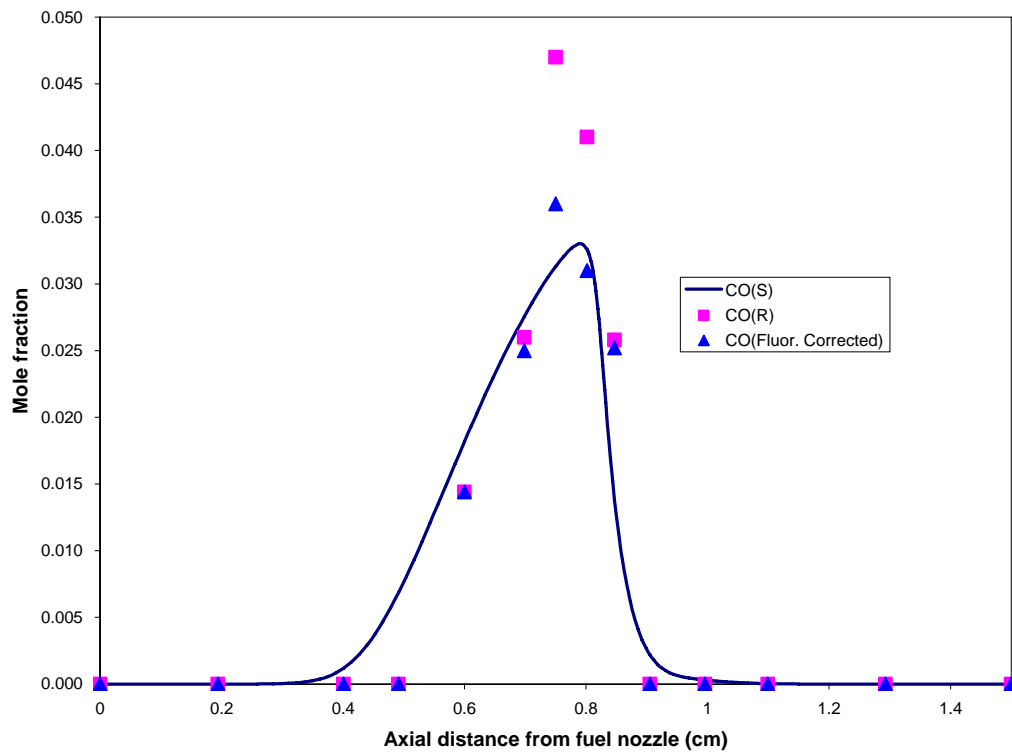
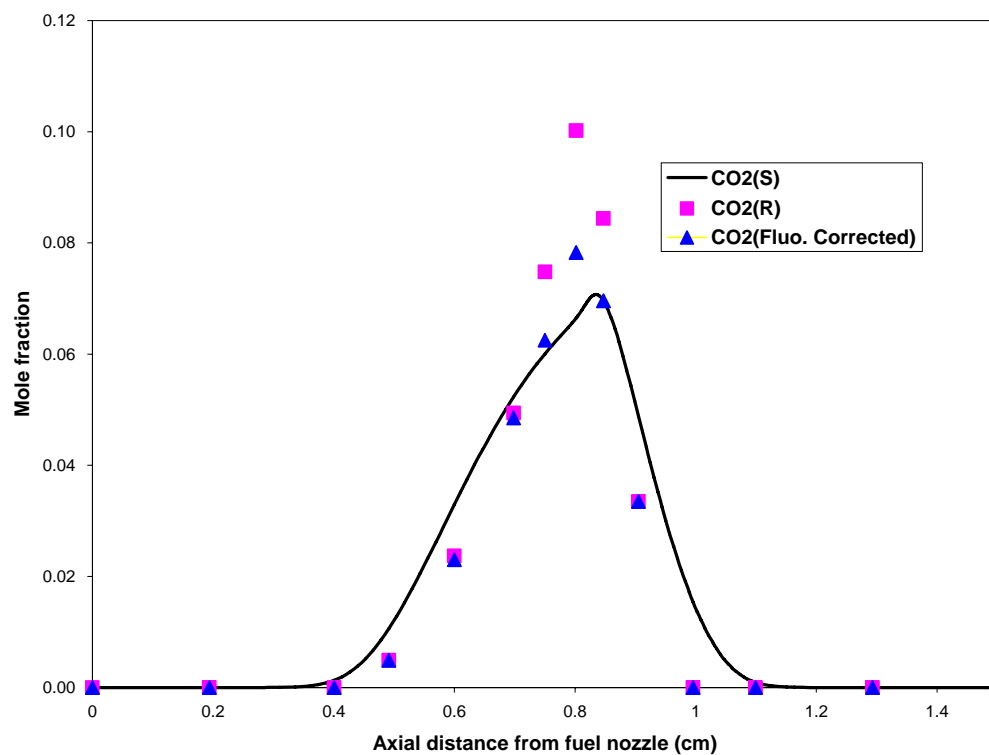


Fig. 4.14. Linear distribution assumption (\blacktriangle) and CHEMKIN simulation results (\blacksquare) of N_2 profile and the comparisons for major species.



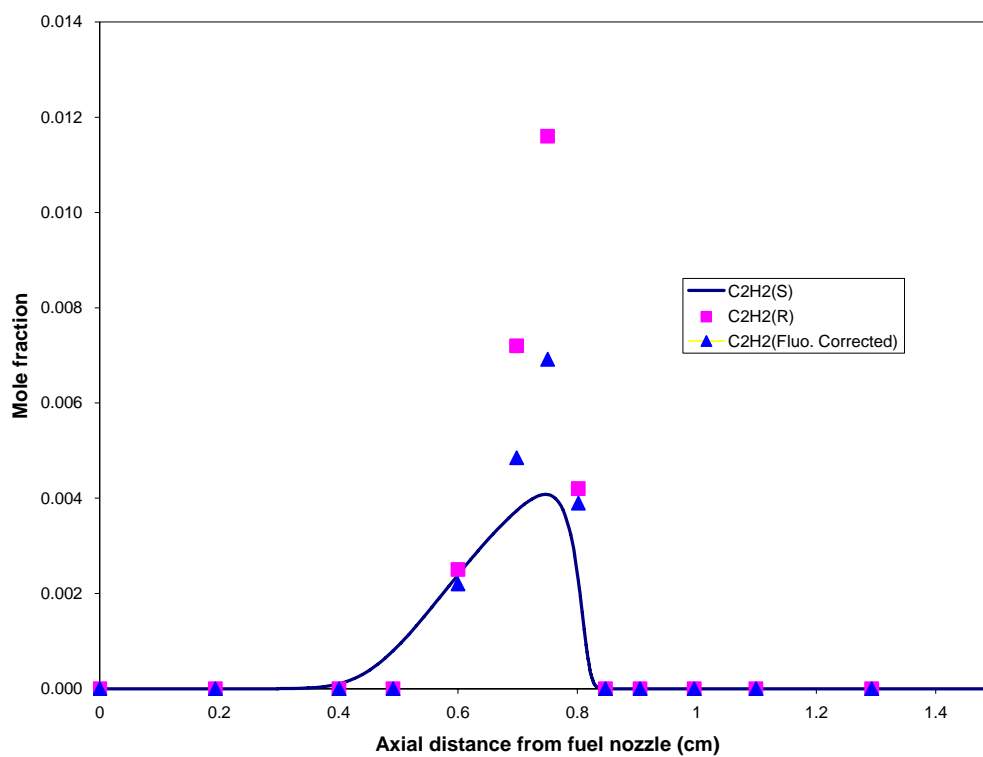


Figure 4.15. Concentration results from Raman scattering measurements with and without fluorescence interferences and their comparisons with computation simulation.

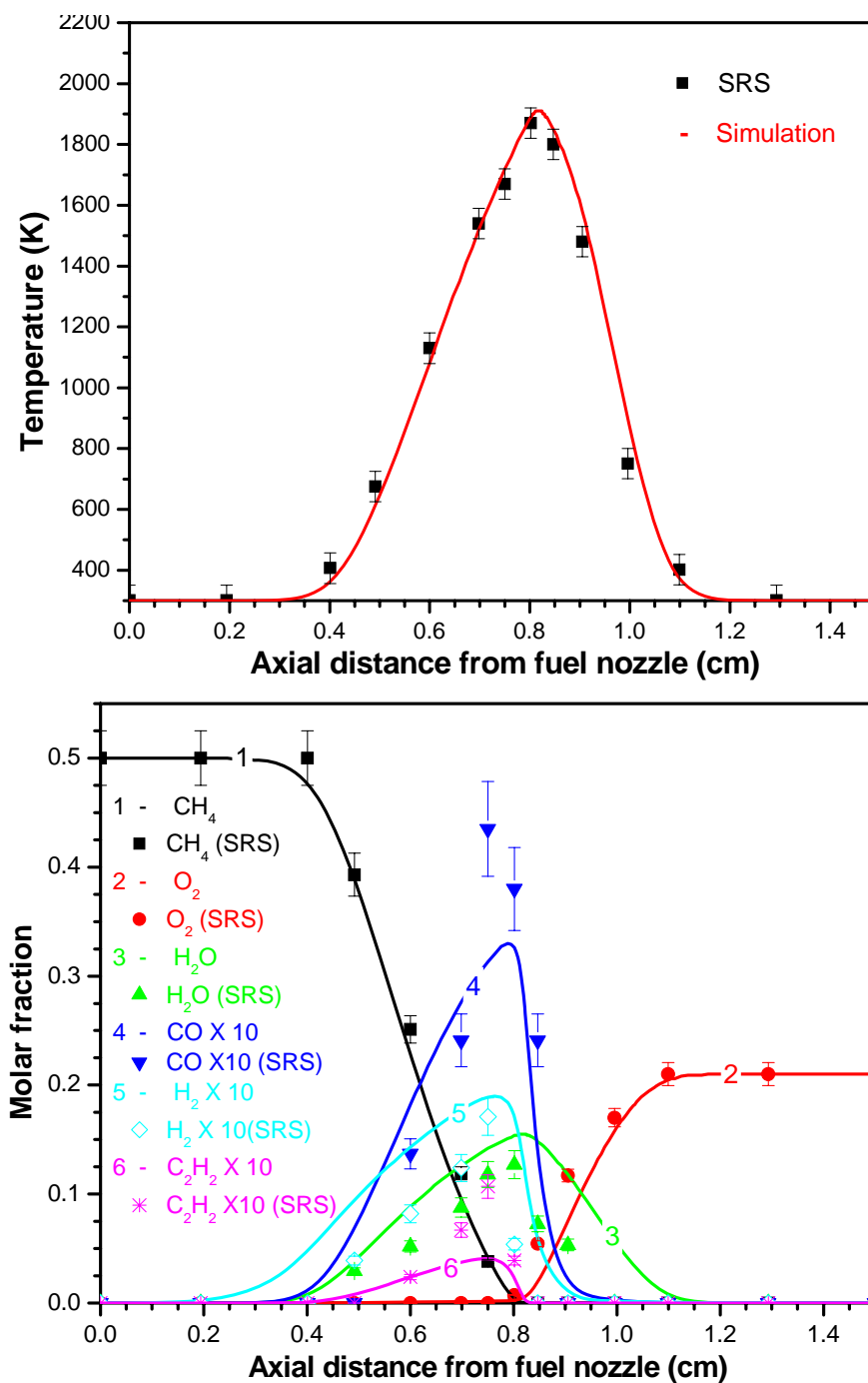


Figure 4.16. Flame structure with 50% CH₄ measured by SRS and compared with simulations, (a) temperature profile along the axial z direction, and (b) the molar fractions of major species along the axial z direction.

4.5 Results and Discussions

The measurements of the flame structure with 50% CH₄ by SRS are shown in Fig. 4.16. The Raman measurement results (symbols in the plots) has been compared with numerical simulations (curves in the plots) using GRI-Mech 1.2, which involves 32 species and 177 reactions. Additional reactions for CH^{*} chemiluminescence from Tse *et al*²⁵ have been included.

The agreement between measurements and simulation is very good for the results of temperature and seven species, evincing the accuracy of the simulations and their suitability in guiding experiments and interpreting results. Again, the shape of the nitrogen spectrum is used to determine the temperature profile. N₂ mole fraction distribution is not shown because N₂ is used as the base-line species for the calculation of the mole fraction of other species. A sum of the mole fractions of all 8 measured species is calculated to confirm the measurement accuracy since the sum should theoretically equal to one.

With laser-based diagnostics measurements of temperature and species matching well with the detailed simulations, the local growth conditions in CDF flames can be carefully selected to match the conditions employed in synthesis of CNTs on metal alloys in the IDFs (Section 4.2). The conditions determine the heat source and reaction reagents for the CNT synthesis in the hydrocarbon flame. Optimal local conditions for CNT synthesis should be “universal,” and such comparisons allow for assessment of the role of spatial gradients in temperature and species in affecting CNT morphologies and growth rates. Comparisons with previous work using IDFs in Section 4.2 reveal that local condition (i.e.

temperature and growth-related chemical species) for CNT growth and morphology can be translated between different configurations of synthesis²⁶.

Based on the details of the CDF obtained from SRS measurements and simulation, we can further manipulate the flame to get the optimized conditions for nanomaterial synthesis. For example, by adding C_2H_2 to the fuel of CDF, C_2H_2 mole fraction at the probe location is about 6 times higher than that produced in the original flame, while gas-phase temperature and CO mole fraction remain about the same^{26,27}, due to the small amount of C_2H_2 added. In this way, local gas-phase probe conditions (i.e. temperature, C_2H_2 , CO, H_2) for the new flame can be matched to that for optimal CNT growth in the IDF that resulted in vertically well-aligned CNTs for the Ni/Cr/Fe probe²⁸ (also seen in Section 4.2). The synthesized CNTs are vertically well-aligned, normal to the Ni/Cr/Fe alloy surface (Fig. 2j in Ref.26), showing that local conditions for CNT growth and morphology can be translated between different flame configurations of synthesis.

For the synthesis of ZnO nanostructures, appropriate local growth conditions (e.g. temperature and growth-related chemical species) in IDFs have been found. It is also true that non-uniformity of ZnO nanostructure exists in IDFs due to the large radial gradients, and the specific growth conditions of ZnO nanostructures should be better defined. Again, the CDF with quasi-one-dimensionality is employed, where the gradients vary mainly in the axial direction, to see if the obtained relations between ZnO nanostructures and their corresponding local conditions in IDFs can be translatable to another configuration of synthesis.

4.6 Error analysis

All experimental values are subject to uncertainties, which arise from inherent limitations in the instruments used. Even in the most carefully designed experiments, random effects influence results. Therefore, all experimental uncertainty is due to either random errors or systematic errors. Random errors are statistical fluctuations (in either direction) in the measured data due to the precision limitations of the measurement device. Random errors usually result from the experimenter's inability to take the same measurement in exactly the same way to get exact the same number. Random errors can be evaluated through statistical analysis and can be reduced by averaging over a large number of observations.

Systematic errors are often due to a problem that persists throughout the entire experiment. They are unique to specific techniques, difficult to detect, and cannot be analyzed statistically. Repeating measurements or averaging large numbers of results will not improve the results. Systematic errors may be studied through inter-comparisons, calibrations, and error propagation.

Both systematic and random error analyses of quantitative measurements of temperature and species concentrations using spontaneous Raman scattering will be discussed. The combined contribution of both error sources will be considered for each of the measurements.

4.6.1 Species concentration

In principle, the Raman signal is proportional to the molecular number density of the specific species. This can be complicated to determine in hydrocarbon flames due to the following two types of interferences. The first type is Raman signal from other species.

The overlap between Q branch of CO and the O branch of N₂, and the overlap of the O₂ spectrum by the wing of the CO₂ spectrum, both at high temperatures, give rise to cross-talk between the Raman channels. The other type is the broadband fluorescence interferences from heavy hydrocarbons such as polycyclic aromatic hydrocarbons (PAHs) and other soot precursors. The correction strategies applied to the raw Raman spectra to reduce the interferences (Chapter 2) inevitably introduce uncertainties into the species concentrations calculations. Those species mostly affected by spectra correction are CO, CO₂, H₂O, and H₂; the potential relative systematic errors are about 5-10%. For other species including O₂ and CH₄, systematic uncertainties of mole fraction measurements are typically 3-5%. The systematic errors are largely independent of the local flame conditions such as mole fraction and temperature.

Another important systematic uncertainty comes from the assumption of N₂ mole fraction profiles through numerical calculations. In counterflow diffusion flames (CDF), as shown in Figure 4.14, the assumption based on simulated N₂ profiles can improve the species concentration results by up to 7%, compared with a linear assumption of N₂ profiles. However, the numerical calculations have uncertainties, especially for the inversed diffusion flames (IDF).

In this chapter, the CH₄ diffusion flames (and H₂ premixed flame in Chapter 5) measured by SRS are generally clean. In such situations, background emissions are low, and soot formation is depressed or avoided. The short laser pulses used for Raman excitation provide for high peak Raman powers, and permit shorter sampling gate widths leading to reductions in collected background. It is also favored by using a good spatial resolution since the volume from which the background is collectable is diminished

considerably. Hence, with proper laser selection, background luminosities can be avoided.

The error due to spatial resolution has to be considered in the diffusion flame setup. Due to the large temperature gradient in the diffusion flame employed, the flame parameters can be very different within a distance of only fractions of a millimeter. It is critical to define the measuring volume small enough so that the spatial resolution adopted in the laser measurements is high enough to resolve the fine structure of the flame. A previous study²⁹ has shown that at spatial resolutions smaller than 500 μm the steep temperature increase with a gradient as high as 4000 K/mm can be well resolved. Although an inherent error associated with the experimental arrangement exists, the error is not considered to be substantial (typically under 5% for the 100 μm slit width used).

Another source of error lies in the uncertainty in the temperature-dependent bandwidth calibration factor $f(T)$, especially for intermediate temperatures. The bandwidth factor accounts for the temperature-dependent distribution of molecules in their allowed quantum states and depends on spectral location, shape, bandwidth of the detection system, and laser line width. Detection bandwidths are chosen so that the bandwidth factors are nearly constant over a wide range of temperatures (less than 3% variation), thereby reducing the error associated with the uncertainty in temperature.

While systematic errors arise from uncertainties in the calibration procedures, statistical or random errors in species concentrations are dominated by photon shot (statistical) noise of the detected Raman photons N_p in single-shot measurement.

The photon statistical fluctuation is inherent to the light emission/detection process and is due to the statistical temporal and spatial distribution of photons. The arrival of a

steady stream of photons is modeled by a random rate and may be described by the Poisson distribution. Its variance is equal to the total number of photoelectrons produced during the exposure time of the laser pulse:

$$\sigma_s^2 = N_p \quad (4.2)$$

The photoelectrons N_p can be obtained by the total number of the incident photons N , the transmission of detection lens systems ε , and quantum efficiency η , which is a measure of detector sensitivity, i.e., the probability for emission of a photoelectron from the detector due to an incident photon. The signal-to-noise ratio, SNR, is defined in terms of the root mean square deviation, or the square root of the variance, typically called the shot noise, and is given by

$$SNR = \sigma = \sqrt{N_p} = \sqrt{\eta \varepsilon N} \quad (4.3)$$

For our ICCD camera (PI MAX 1300HQ), the photocathode quantum efficiency for 532 nm is $\eta \approx 37\%$ and the transmission through the detection lens systems is estimated to be $\varepsilon = 0.8$. Typical laser energy of 150 mJ, a solid angle of 12.8° , and a spatial resolution of 100 μm give N_p the number of 3697 e^- (electrons).

In the low-light regime, the significant noise sources are read noise and dark current from ICCD cameras. Dark current arises from thermal energy within the silicon lattice comprising the CCD. Electrons are created over time and are independent of the light falling on the detector. These electrons are captured by the CCD's potential wells and counted as signal. Additionally, this increase in signal also carries a statistical fluctuation known as dark current noise. CCDs can be cooled to reduce this effect. Practically, the dark current noise should be reduced to a point where its contribution is negligible over a

typical exposure time. Since dark current noise follows Poisson statistics, the RMS dark current noise is the square root of the dark current and can be expressed as:

$$\sigma_{DC}^2 = \mu_{DC} \Delta t \quad (4.4)$$

where μ_{DC} is the accumulation rate with unit of electron/s (typical value: 3 e⁻/pixel/s@-20°C from the PIMAX ICCD datasheet).

The readout noise refers to the uncertainty introduced primarily from the on-chip preamplifier. It is independent of signal level and depends only on the readout rate. Its variance is expressed as

$$\sigma_{RO}^2 = \mu_{RO} \omega_{RO} \quad (4.5)$$

where ω_{RO} is the readout frequency with unit of pixels/s. The typical value for readout noise is 8 e⁻ from the PIMAX ICCD datasheet.

The total uncertainty can be expressed as

$$\sigma_T = \sqrt{\sigma_s^2 + \sigma_{RO}^2 + \sigma_{DC}^2} \quad (4.6)$$

where σ_T is in the unit of electrons. In order to convert this value into counts it must be divided by the gain G_{AD} :

$$\Delta S = \frac{1}{G_{AD}} \sqrt{\sigma_s^2 + \sigma_{RO}^2 + \sigma_{DC}^2} \quad (4.7)$$

The gain refers to the magnitude of amplification that the camera will produce, and it is given in the unit of electrons/ADU (analog-to-digital unit). In the ICCD camera the gain is adjusted by setting the parameter in WinSpec/32 software. By combining the three types of camera noise, we get $\Delta S = 60 \text{ e}^-$.

An additional random error is introduced in the interference correction procedure, as the photon noise on the fluorescence interference will affect the corrected concentrations.

Random error analysis above is performed for a single pulse. With hundreds to thousands shots measured in a typical SRS measurement, time averaging effect is to greatly increase N , by summing the individual pulse signal photons. Averaging over 3000 pulses (5 min) will reduce the relative error by 98.2%, decreasing the shot noise to near zero ($<1 e^-$) and thus the subtraction accuracy will improve considerably.

4.6.2 Temperature

As explained in Chapter 2, flame temperatures are obtained by curve-fitting the shape of the Raman spectra of N_2 , which is usually the most abundant species in the flame. The “quick-fit” approach employs library spectra spaced 50 K apart generated by convolving these spectra with the experimental slit function. A second program (Newqf.exe³⁰) performs a least-square fit to the data by interpolating between library spectra. A rigorous statistical treatment of the fitting errors is not applied in this study since the sources of error are not accurately known. Uncertainty in the fitted temperature is estimated conservatively by determining the temperature bounds at which the data and theory clearly disagree³¹. The uncertainty in the fitted temperature is thus determined to be less than ± 50 K shown in Fig 4.17 and the reproducibility of the measurements is within ± 20 K.

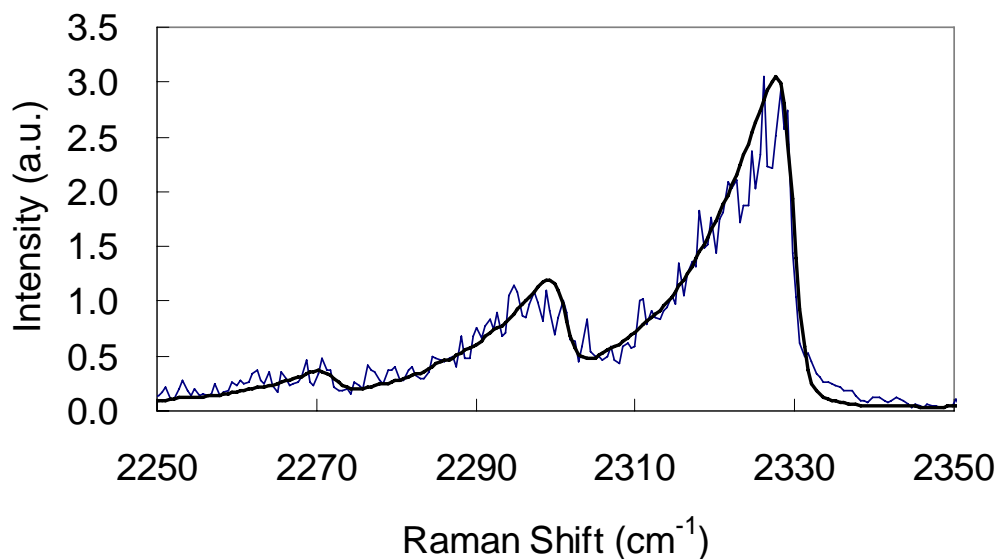


Figure 4.17. A typical theoretical least-square fit to the experimental Raman spectrum of N_2 .

When the spectrometer is used to record the Raman spectrum from an experiment, the measured spectrum is always slightly different from the true spectrum. The true spectrum is convoluted with the slit function of the spectrometer. During the convolution process, however, an error is brought to the measured profile due to the finite dimension of the slit width. The peak amplitude will drop and a slight broadening effect will occur as the slit width increases. In Raman spectroscopy measurements, temperature and species concentrations are quantitatively determined by the Raman spectra of combustion gases. It is critical to know how the spatial resolution defined by the slit width of the spectrograph will affect measured spectra and the temperature and concentrations measurement results.

If a light source emits a spectrum which consists of a single monochromatic wavelength λ_o (Figure 4.18a) and is analyzed by a perfect spectrometer, the output should

be identical to the spectrum of the emission (Figure 4.18b) which is a perfect line at precisely λ_0 .

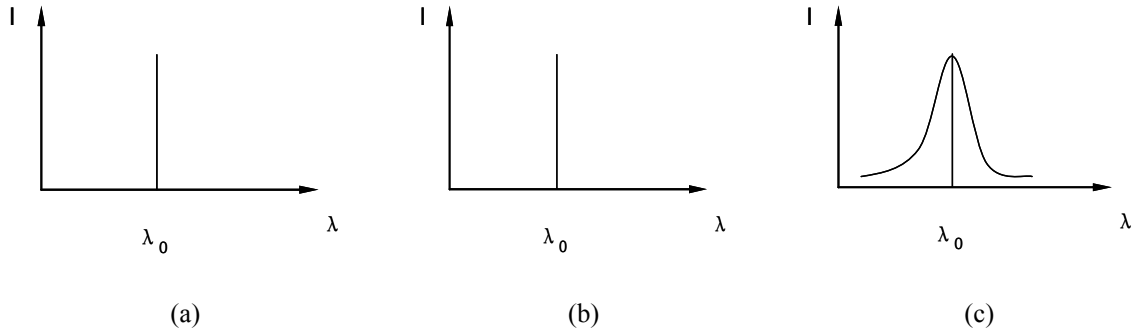


Figure 4.18. (a) Real spectrum of a monochromatic light source (b) Recorded spectrum of a monochromatic light source with a perfect instrument (c) Recorded spectrum of a monochromatic light source with a real instrument.

In reality, spectrometers are not perfect and produce an apparent spectral broadening of the purely monochromatic wavelength. The line profile now has finite width and is known as the "instrumental line profile" (instrumental bandpass, Figure 4.18c).

Any spectral structure may be considered to be the sum of infinite single monochromatic lines at different wavelengths. The recorded spectrum is the convolution of the real spectrum and the instrumental line profile.

Let $I(\lambda)$ be the real spectrum of the source to be analyzed, $O(\lambda)$ be the recorded spectrum through the spectrometer, and $S(\lambda)$ be the instrumental line profile, where

$$O(\lambda) = I(\lambda) * S(\lambda) \quad (4.7)$$

For spectrographs that have one entrance slit and a multichannel CCD detector, the shape of the instrumental line profile is mainly determined by the entrance slit. If $W_{en} =$

width of the image of the entrance slit, and $\Delta S = \text{linear dispersion} \times W_{en}$, then the slit's contribution to the instrumental line profile is the entrance slit function (Figure 4.19).

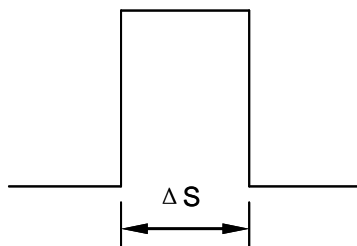


Image of Entrance Slit

Figure 4.19 Instrumental line profile of a spectrograph system used in Raman spectroscopy measurements

The linear dispersion of 2400g/mm grating used for the Raman measurement is 21.22 cm^{-1}/mm and the width of the image of the entrance slit is 100 μm . The ΔS is 2.112 cm^{-1} for the width of the slit function, which can be convoluted with the real spectrum to get the signal. An N_2 Raman spectrum at 1794 K and its convoluted spectrum, measured at 1799 K are shown in Figure 4.20. The convolution error, i.e., the 5 K difference, is quite small relative to the curve fitting uncertainty of ± 50 K. Additional testing shows that the convolution errors are typically under 15 K, which corresponds to an error of less than 3% even for low temperatures (~ 500 K). It can be concluded that, for the narrow (100 μm) slit width used in the experiment, an error of such a level is quite small for temperature measurements.

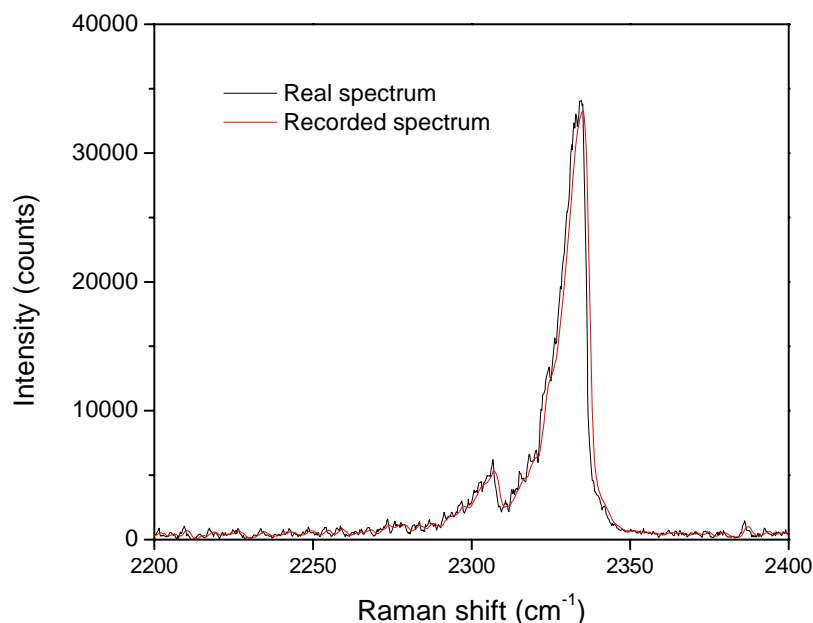


Figure 4.20 An N_2 Raman spectrum at 1794 K and its convoluted spectrum (1799 K)

The species concentrations are deduced by the strength of Raman signals. Since the convolution effect results in peak amplitude drop and spectrum broadening on the spectra of all species, concentration results will also bring errors from the convolution effect of the finite slit width. The convoluted spectrum shown in Figure 4.20, however, is only 0.1% different from the original spectrum, in terms of area under the peaks. Compared with other inherent uncertainties associated with species concentration measurements, which are usually at the level of several percent, errors from the convolution effect are extremely small.

4.6.3 Flame position

Since laser-based diagnostics measurements are associated with a finite volume in the flame, another source of error is the movement or vibration of the flame. The local Raman spectra are obtained at different axial (and radial for co-flow flames) locations

along the centerline by translating the burner assembly in three directions provided by the milling machine. The flames are monitored by a cathetometer during the course of the experiments. The flickering of these flames is minimal, and the support system is heavy enough to ensure spatial displacements (errors) with an accuracy of less than $\pm 75 \mu\text{m}$.

4.7 Conclusions

In-situ spontaneous Raman scattering (SRS) measurements have been conducted on two different flames for nanostructures synthesis. As a versatile laser-based diagnostic in combustion research, SRS has the advantages of providing non-intrusive, *in-situ*, spatially- and temporally-precise information about important chemical and thermodynamic parameters. In this chapter, this technique has been applied to the inverse diffusion flame (IDF) and the counter-flow diffusion flame (CDF) to measure temperatures and chemical species concentrations.

Special consideration has been made to improve the accuracy of the measurements, by selecting the right experimental instruments, adopting suitable measurement strategy, and conducting improved data post-processing. This is shown for the IDF case. The IDF has enough parameter capacity for flame structure manipulation to produce various nanomaterials, but its complex flame structure requires measurements with high spatial and temporal resolution, with high signal-to-noise ratio (SNR). Improved SRS measurements in this chapter provide satisfactory results with high reproducibility.

The experimental measurement results for the CDF can be readily compared with computational simulation with detailed chemical kinetics and transport properties. SRS allows for cross-validation of these flame structures. The measurement results are

compared with the simulated results, and are in excellent agreement with the simulations. The reliability of the SRS measurements makes it suitable for obtaining the profiles of temperature and major species for IDFs as well, especially when detailed simulation (e.g. chemical species) is a complex task given the 2-D IDF flame structure.

The establishment of correlations between flame parameters, especially species, and the corresponding nanostructures is not always straightforward in synthesis systems such as electric arc discharge and laser ablation. Utilizing well-defined flame systems, however, can be advantageous for the investigation, and further control of local temperature and growth-related species through comparative modeling of the flow field and diagnosing through laser-based spectroscopy becomes possible. The production of CNT and ZnO nanostructures in both flame configurations is discussed with respect to these measured parameters.

Finally, “universal” growth conditions for nanostructures in different flames are explored. By diagnosing and manipulating the flame structures, we have compared synthesized products under the same or similar conditions in different flames. The results show that local conditions (i.e. temperature and growth related chemical species) for CNT and ZnO growth and morphology can be translated between different configurations of synthesis.

References

¹ R.L. Vander Wal, L.J. Hall, and G.M. Berger, Optimization of flames synthesis for carbon nanotubes using supported catalyst, *J. Phys. Chem. B* 106, 13122-13132 (2002).

² G.A. Jablonski, F.W. Guerts, A. Sacco Jr., R.R. Biederman, Carbon deposition over Fe, Ni, and Co foils from CO-H₂-CH₄-CO₂-H₂O, CO-CO₂, CH₄-H₂, and CO-H₂-H₂O gas mixtures: I. Morphology, *Carbon* 30, 87 (1992).

³ G.A. Jablonski, F.W. Guerts, and A. Sacco Jr., Carbon deposition over Fe, Ni, and Co foils from CO-H₂-CH₄-CO₂-H₂O, CO-CO₂, CH₄-H₂, and CO-H₂-H₂O gas mixtures: II. Kinetics, *Carbon* 30, 99 (1992).

- ⁴ Y. Soneda, and M. Makino, The adsorption of water by active carbons, in relation to their chemical and structural properties, *Carbon* 38, 475 (2000).
- ⁵ T. Baird, J.R. Fryer, and B. Grant, Carbon formation on iron and nickel foils by hydrocarbon pyrolysis—reactions at 700°C, *Carbon* 12, 591 (1974).
- ⁶ A. Moisala, A.G. Nasibulin, and E.I. Kauppinen, The role of metal nanoparticles in the catalytic production of single-walled carbon nanotubes—a review, *J. Phys: Condens. Matter* 15, S3011-S3035 (2003).
- ⁷ R. M. Fristrom, *Flame Structure and Processes*, The Johns Hopkins University/Applied Physics Laboratory series in science and engineering (Oxford University Press, New York, 1995).
- ⁸ A.C. Eckbreth, *Laser Diagnostics for Combustion Temperature and Species* (Gordon and Breach Publishers, Amsterdam, The Netherlands, 1996).
- ⁹ I. Glassman, *Combustion* (Academic Press, New York, 1977).
- ¹⁰ K. K. Kuo, *Principles of combustion* (Wiley, New York, 1986).
- ¹¹ C. K. Law, *Combustion physics* (Cambridge University Press, New York, 2006).
- ¹² M. Lapp, L. M. Goldman, and C. M. Penney, Raman Scattering from Flames, *Science* 175, 1112 (1972).
- ¹³ R. W. Dibble, A. R. Masri, and R. W. Bilger, The spontaneous Raman scattering technique applied to nonpremixed flames of methane, *Combustion and Flame* 67, 189 (1987).
- ¹⁴ J. Kojima, and Q. Nguyen, Spontaneous Raman Scattering Diagnostics for High-Pressure Flames, *22nd AIAA Aerodynamic Measurement Technology and Ground Testing Conference* (2002).
- ¹⁵ G.W. Lee, J. Jurng, and J. Hwang, Synthesis of carbon nanotubes on a catalytic metal substrate by using an ethylene inverse diffusion flame, *Letters to the Editor/Carbon* 42, 667–91 (2004).
- ¹⁶ G.W. Lee, J. Jurng, and J. Hwang, Formation of Ni-catalyzed multiwalled carbon nanotubes and nanofibers on a substrate using an ethylene inverse diffusion flame, *Combust Flame* 139, 167–75 (2004).
- ¹⁷ G. Sidebotham, *An inverse co-flow approach to sooting laminar diffusion flames*, PhD thesis, Princeton University (1988).
- ¹⁸ R.T. Baker, *Carbon* 27, 315–23 (1989).
- ¹⁹ C-J Sung, On the structure, response, and stabilization of stretched flame, PhD Dissertation, Princeton University (1994).
- ²⁰ [Computer Software] FLUENT V. 6.2 for Windows. Fluent, Inc. 2005.
- ²¹ S. Chapman, and Cowling T. G., *The Mathematical Theory of Non-Uniform Gases: An Account of the Kinetic Theory of Viscosity, Thermal Conduction, and Diffusion in Gases* (Cambridge University Press, 1990).
- ²² J. Fielding, J.H. Frank, S.A. Kaiser, M.D. Smooke, and M.B. Long, Polarized/depolarized Rayleigh scattering for determining fuel concentrations in flames, *Proceedings of the Combustion Institute* 29, 2, 2703-2709 (2002).
- ²³ F. Xu, PhD thesis, Rutgers University (2007).
- ²⁴ A.R. Masri, et al., 'Fluorescence' Interference with Raman Measurements in Nonpremixed Flames of Methane, *Combust. Flame* 68, 2 (1987).
- ²⁵ S.D. Tse, D. Zhu, C.J. Sung, Y. Ju, and C.K. Law, Microgravity burner-generated spherical diffusion flames: Experimental and computation, *Combustion and flame* 125, 1265-1278 (2001).
- ²⁶ F. Xu, H. Zhao, and S.D. Tse, Carbon Nanotube Synthesis on Catalytic Metal Alloys in Methane/Air Counterflow Diffusion Flames, *Proceedings of the Combustion Institute* 31,2, 1839-1847 (2006).
- ²⁷ F. Xu, X. Liu, S.D. Tse, F. Cosandey, and B.H. Kear, Flame Synthesis of Zinc Oxide Nanowires, *Chemical Physics Letters* 449, 175-181 (2007).
- ²⁸ F. Xu, X. Liu, and S.D. Tse, Synthesis of Carbon Nanotubes on Metal Alloy Substrates with Voltage Bias in Methane Inverse Diffusion Flames, *Carbon* 44, 3, 570-577 (2006).
- ²⁹ C. J. Sung, J. B. Liu, and C. K. Law, Structural response of counterflow diffusion flames to strain rate variations, *Combustion and Flame* 102, 481 (1995).
- ³⁰ R.J. Hall, and L.R. Boedeker, CARS thermometry in fuel-rich combustion zones, *Appl. Opt.* 23, 1340-1346 (1984).
- ³¹ M.D. Allendorf, et al., Temperature measurements in a vapor axial deposition flame by spontaneous Raman spectroscopy, *J. Appl. Phys.* 66, 10, 5046-5051 (1989).

Chapter 5

Application of Gas-Phase Laser-Induced Fluorescence to Study Low-Pressure Synthesis of Nanoparticles

In this chapter, gas-phase synthesis of nanoparticles at low pressures is studied using *in situ* laser-based spectroscopy to investigate electric field and precursor loading effects on the flame structure. The synthesis flame and materials synthesis method are first introduced. Laser induced fluorescence (LIF) is employed to probe the gas-phase temperature profiles and OH species concentration distributions, which are compared with computational simulation with detailed chemistry and transport.

As stated in the Preface, much of the content of this chapter appears verbatim from published papers^{1,2}, which includes co-authors.

5.1 Introduction

Nanoparticles are made from gases by the so-called gas-to-particle conversion in flame reactors, hot-wall or furnace reactors, vapor-phase evaporation-condensation processes, plasma furnace reactors, and laser and sputtering reactors, to name a few. The advantages of gas-phase processes are the production of particles of high purity composed of nonporous primary particles with small sizes and relatively narrow size distribution. Disadvantages include difficulties in producing unagglomerated particles and multi-component materials³.

The gas-phase synthesis of nanoparticles starts from a supersaturated vapor mixture which is thermodynamically unstable and easy to form a condensed phase. If the supersaturation and condensation kinetics are favorable, particles will nucleate

homogeneously into solid or liquid phase, without the aid of any foreign surfaces. The remaining supersaturation can be relieved through condensation or surface reaction of the vapor-phase molecules on existing particles, where surface growth rather than further nucleation will occur. Therefore, in order to synthesize small particles, one needs to create a high degree of supersaturation by inducing a high monomer/cluster density, and then immediately quench the system, so that the particles have limited particle growth and/or agglomeration.

In summary, the research for flame synthesis of nanoparticles may include several components⁴, e.g. as outlined in Figure 5.1. In this work, anatase-phase TiO₂ nanoparticles are formed in a low-pressure premixed flat flame. Given the weakness of Raman scattering at low densities, the synthesis flame is characterized by LIF because its signal is 6 orders of magnitude stronger than that of Raman, making it a suitable tool for minor species detection and temperature measurement. The LIF results are compared with computational simulation (using the modified SPIN code). Particle growth dynamics coupled with the flow field and particle transport is modeled. The particle growth can also be studied by *in-situ* particle characterization and *in-situ* spectroscopic laser-based diagnostics. The detailed understanding of the synthesis process enables optimization whereby manipulating specific parameters such as electric field and precursor loading can directly affect the resulting particle properties.

As stated in the research outline, laser-based diagnostics – LIF – measurements on temperature and OH concentration profiles in the flow field will verify the flame structure. Measurements made under tailored flame conditions will examine parametric effects on nanoparticles synthesis. In the next chapter, another laser-based diagnostic

technique – spontaneous Raman spectroscopy (SRS) – will be employed for *in-situ* nanoparticle characterization, specifically to monitor particle composition and crystallinity.

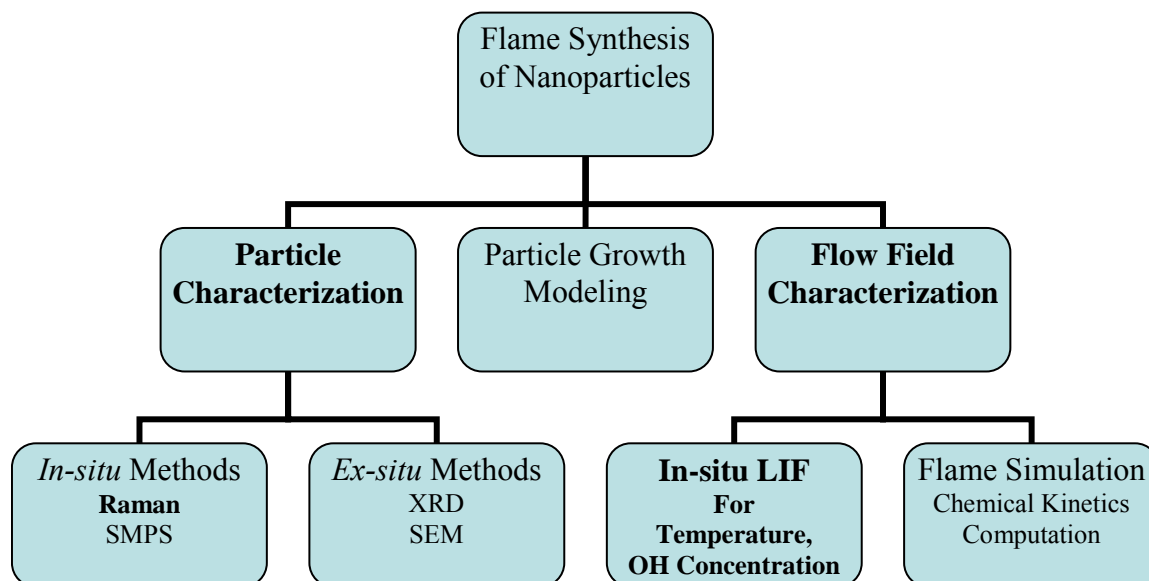


Figure 5.1. Outline of flame synthesis of nanoparticle research and the function of laser diagnostics techniques

5.2 Experiment

5.2.1 Flame synthesis setup

A typical flame aerosol reactor set-up is shown in Figure 5.2; it mainly consists of a precursor unit (bubbler or evaporator), a burner accompanied by a gas delivery system, and a cold substrate to provide the steep temperature gradient. Various studies utilize the premixed flame configuration for nanoparticle synthesis⁵. In a premixed flame, the precursor and the combustible gases are mixed before they enter the reaction zone (flame).

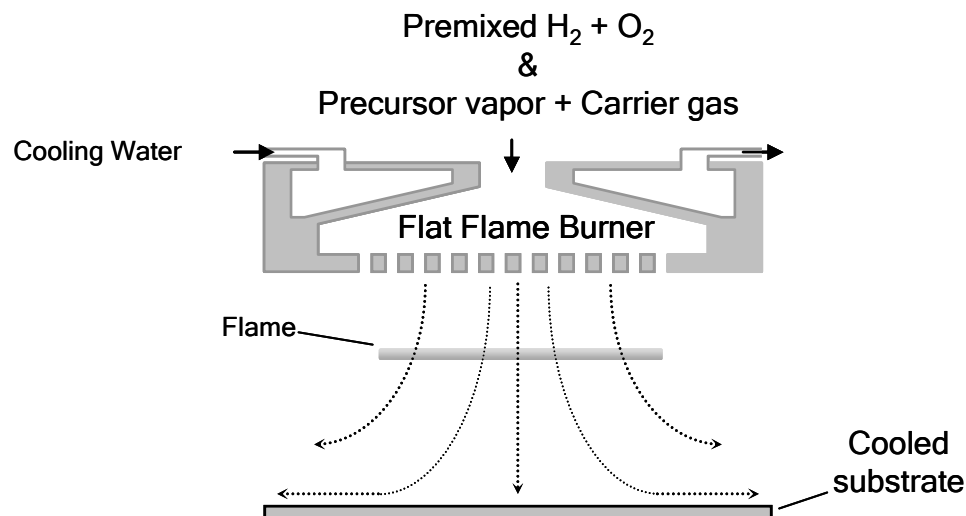


Figure 5.2. Premixed synthesis flame setup

Precursor molecules pyrolyze/oxidize at elevated temperatures into intermediate radicals and clusters that quickly grow to nano-sized particles, which then further grow through coalescence, coagulation, and/or surface reactions. For the ceramic nanopowders, i.e. TiO_2 , investigated in the current research, titanium tetro-iso-propoxide (TTIP) $\text{Ti}(\text{C}_3\text{H}_7\text{O})_4$ is used as precursor to synthesize TiO_2 nanoparticles. The liquid precursor is vaporized from a heated bubbling unit and entrained into a carrier gas and then combined with combustible premixed gases (e.g. hydrogen/oxygen) and delivered to the burner. The flow system is metered with mass flow controllers, and the flow lines are heated to prevent precursor condensation. A dual-polarity high-voltage source (0-10kV, 3-10mA) establishes the uniform electric field. The chemical precursors pyrolyze and oxidize in the flame and condense into nanoparticles as the gases cool upon reaching the substrate. The as-synthesized particles are characterized to obtain important nanopowder properties such as aggregate particle size, primary particle size, specific surface area, particle morphology, crystallinity, and phase composition.

It is important to know precisely the flame structure and flow field in the synthesis system. Particle image velocimetry (PIV) and laser Doppler velocimetry (LDV) can be used to measure the velocity of flow fields⁶. The tracer particles (with micron size range), however, may not follow the streamlines of the flow field, due to strong thermophoretic and electrophoretic forces in our setup. So, in our experiments, the flame structure is probed *in situ* using laser-induced fluorescence (LIF) to map the OH radical concentrations and gas-phase temperature distributions along the axial centerline. The simulation of the gas-phase flame structure is performed using the Sandia SPIN code, which assumes a quasi-1-D stagnation flow. By comparing the simulation with measurements, the flow field can be indirectly verified.

5.2.2 LIF diagnostics systems

The setup of the *in-situ* laser-based diagnostics is shown in Fig. 5.3, consisting of an injection-seeded Nd:YAG laser, a Nd:YAG-pumped dye laser, a spectrometer, an ICCD camera, and associated optics.

The injection-seeded 532nm 10Hz Nd:YAG laser (Spectra-Physics Quanta Ray LAB-170) pumps a dye laser (Sirah PrecisionScan D-24) with Rhodamine 6G dye (Rhodamine 590 chloride, $C_{28}H_{31}O_3N_2$) for the excitation of OH. The dye has a tuning range of 559-576 nm. In order to excite the selected OH transitions (~ 280 nm), the output laser beam from the dye (in visible range) is passed through a beta-barium borate (BBO) doubling crystal to get a ultraviolet (UV) range output. The output of the dye laser is then attenuated from 0.2W to 0.014W by the use of beam splitters, which pass part of the laser beam to a power meter (OPHIR, 30A-P-SH-V1) for power monitoring. The other part of the beam is then focused by a 500mm plano-convex fused-silica lens (Thorlabs, L4782)

at measurement positions between the burner and the substrate.

The OH fluorescence signal is collected with a UV lens (Universe Kogaku, UV1054B, 105 mm, F/4.0) at right angles into an f/6.5-imaging spectrometer (Acton SpectrPro-2558), with ICCD camera (Princeton Instruments PIMAX 1300HQ, 1340×1300 pixels) as detector. A 50 μm diameter pinhole is employed before the spectrometer for a probe volume corresponding to a spatial resolution of 150 μm in the flame. A pair of UV enhanced aluminum mirrors (Thorlab PF20-03-F01) provides the elevation change of the light path to bring the scattered light into the spectrometer. A 3600 g/mm UV grating (Richardson 53999BK01-170R) and 100 μm slit width of the spectrometer give an 11.5 nm spectral coverage with a resolution of 0.01 nm. The ICCD camera is externally-triggered by the 10 Hz Q-switch pulse from the Nd:YAG laser. A 100 ns gate width for each shot reduces background noise while retaining signal at the wavelengths of interest.

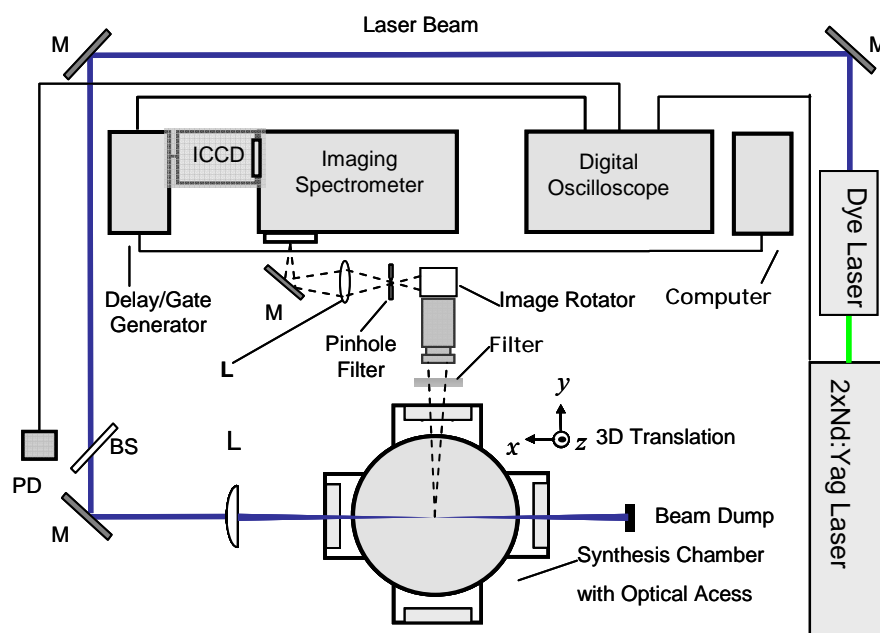


Figure 5.3. Laser induced fluorescence (LIF) measurement setup.

The strategy of LIF measurement has been described in Chapter 2. The main points are briefly included here. In our experiment, the laser-induced fluorescence of OH is collected at a wavelength different from the excitation wavelength of the dye laser in order to separate the LIF signal from other light sources. OH fluorescence sample spectra detected at the middle point between the flat flame burner and substrate are shown in Figure 5.4. The transition lines used for temperature and OH concentration measurements are labeled on the spectra.

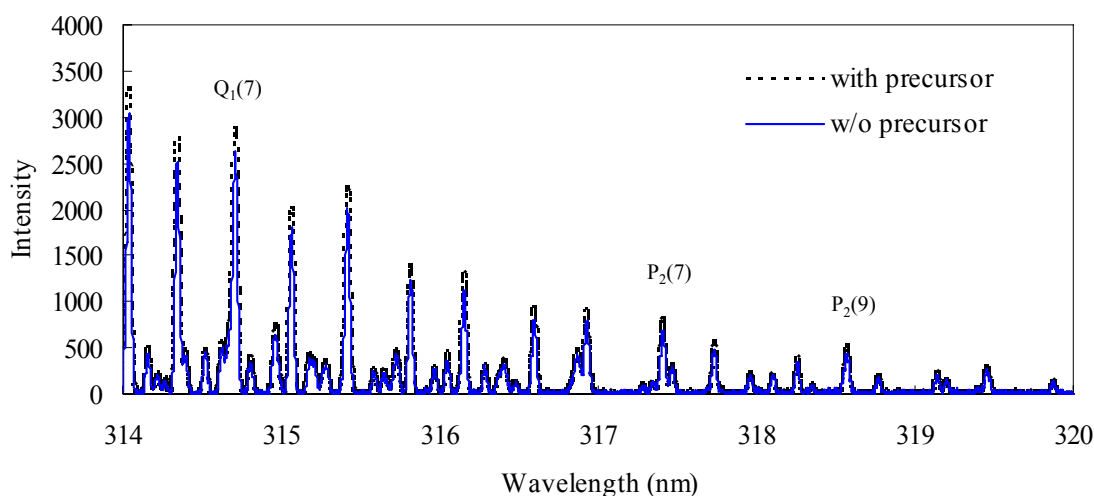


Figure 5.4. OH LIF spectra at the middle point between the burner and the substrate, with and without the precursor.

The $Q_1(7)$ transition is chosen to measure the relative OH concentration profile, since the relative population does not change much over the range of temperatures in the flame (Figure 2.6). This eliminates the need for temperature correction to the fluorescence signal profile. For temperature measurement using the two-line method, $P_2(7)$ and $P_2(9)$ transitions of the $(1-0)$ band of the $A^2\Sigma \leftarrow X^2\Pi$ are excited. These transitions have similar values of $B (g_1 + g_2) / g_2$, where B is the Einstein absorption coefficient and g_1 and g_2

are the upper and lower state degeneracies, respectively⁷. This reduces the effect of saturation on the derived temperature so that a linear and steady state regime can be assumed. The fluorescence signal is proportional to the population density of the ground state probed and the Einstein coefficients A and B . The population density is an exponential function of temperature and degeneracy. So the parameters that are required for the temperature measurement are either known (degeneracy), or taken from a table (Einstein coefficient), or measured (fluorescence area intensity). The equation⁸ for temperature calculation from the two intensities of the two transitions is:

$$T = \frac{(E_9 - E_7)/k}{\ln \left[\frac{(gB_{12}A_{21})_{P_2(7)}S_9}{(gB_{12}A_{21})_{P_2(9)}S_7} \right]} \quad (5.1)$$

The parameters⁹ applied in this calculation are listed in Table 5.1.

Table 5.1. Parameters used in temperature measurement.

Energy level E_9	3502.78 1/cm	Energy level E_7	2887.35 1/cm
Degeneracy g $P_2(9)$	15	Degeneracy g $P_2(7)$	11
Coefficient A $P_2(9)$	892	Coefficient A $P_2(7)$	924
Coefficient B $P_2(9)$	198	Coefficient B $P_2(7)$	193
Fluorescence intensity ratio S_9/S_7	Measured	k	0.6938 1/cm/K

The experimental procedure is as follows. A laminar premixed flame ($H_2/O_2/N_2 = 1.0:1.2:0.75$ with an equivalence ratio of 0.42) is stabilized by the burner. The substrate-burner-gap is 4cm. A 3-axis milling machine base is used to translate the chamber vertically to allow the laser beam to focus at different heights within the flame

structure, while the laser beam and the optics are kept fixed. The precision of the height control is 0.025 mm using the precision gauge on the milling machine positioner. For the precursor-free flame, more data points (fifteen points plus the burner and substrate) are taken. For the precursor-loaded flame, only five points are measured because the burner can become partially clogged when the experiment runs longer than 40 minutes. For each measurement location, three spectra are collected at center wavelengths of 317.438 nm ($P_2(7)$), 318.599 nm ($P_2(9)$), and 314.695 nm ($Q_1(7)$), by tuning the dye laser to the excitation wavelengths of 285.432 nm ($P_2(7)$), 286.567 nm ($P_2(9)$), and 283.222 nm ($Q_1(7)$), respectively.

The temperatures very near the burner and substrate are measured using LIF. These temperatures are not exactly equal to the temperatures of the substrate or burner plates. Due to the focusing angle of the laser beam, there is a minimum distance of 0.03785mm –“dead distance”– near the substrate and burner, which cannot be probed or measured by LIF, as shown in Fig. 5.5. The temperatures at the burner and substrate are instead measured using thermocouples.

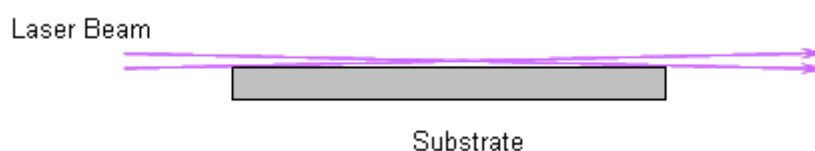


Figure 5.5. “Dead distance” in LIF when approaching surfaces.

5.3 Flame simulation – CHEMKIN¹⁰

The gas-phase flame structure of the premixed flame in the experiment is simulated using the Sandia SPIN¹¹ code (generally used for CVD processes) for stagnation flow geometry,

by turning off disk rotation and using the appropriate boundary conditions at the substrate. A flow/chemistry model treats the flow and transport between, as well as the chemical reactions occurring in the gas-phase and at the substrate surface. Gas-phase and surface chemical kinetics are handled by CHEMKIN¹² and SURFACE CHEMKIN subroutines¹³, respectively, while variable transport properties are determined by TRANSPORT¹⁴. Conservation equations are solved for continuity, radial and circumferential momentum, thermal energy, and chemical species, along with a pressure-explicit equation of state. The detailed chemical kinetic mechanism of Mueller et al.¹⁵ for hydrogen chemistry involving 9 species and 21 elementary reactions is applied for the gas phase.

The boundary conditions are: (i) experimentally specified inlet mass flux and temperature at the burner; (ii) no-slip condition and constant surface temperature at the substrate; (iii) recombination of H, O, OH, and HO₂ with unit sticking probability at the substrate surface; and (iv) the gas-phase mass flux of each species to the substrate j_k is balanced by the creation or depletion of that species by surface reactions, i.e.

$$j_k = \dot{S}_k M_k \quad (k=1, \dots, K_g) \quad (5.2)$$

The gas-phase mass flux of species k at the substrate is a combination of diffusive and convective processes, i.e.

$$j_k = \rho Y_k u + \rho Y_k V_k \quad (k=1, \dots, K_g) \quad (5.3)$$

where V_k is the diffusion velocity of the k th species. The surface reactions of Aghalayam et al.²⁴ are employed at the substrate, where surface recombination reactions are taken to have zero activation energy.

5.4 Results and discussions

5.4.1 Isolation of the electrophoretic effect

The effect on the gas-phase temperature profile by the electric fields in a typical synthesis flame (e.g. -500V applied to substrate and burner grounded) is studied. The temperature and OH concentration profiles with and without an electric field are shown in Fig. 5.6 and Fig. 5.7, respectively. As shown in Fig. 5.6, the measurements and the simulation agree with each other very well in terms of the temperature profile. Furthermore, the LIF measurements reveal that there are negligible differences with and without uniform electric field application.

OH radical is an important combustion intermediate for any modeling effort. The OH concentration profiles from the LIF measurements in the flames with and without electric field are compared to the simulation results in Fig. 5.7. Again, the agreement between computations and measurements is good, and the application of electric fields has negligible effect on the OH profile. It is also found that flame chemiluminescence has no noticeable change when applying negative/positive voltages to the substrate, showing that although chemical effects induced by transposing and re-distributing ionic species by the action of the electrical fields may exist, they seem to play a very minor role in terms of our synthesis flow field. It is then possible to isolate the electrophoretic effect so that we can study its effect on particle residence time under fixed gas-phase conditions. In addition, the agreement between the quasi one-dimensional flow field simulation model and the LIF measurements is very good for these stagnation point flames, suggesting that the model predicts accurately the material processing flow fields. Thus, the temperature and velocity profiles from the simulations can be utilized in particle transport and growth

modeling.

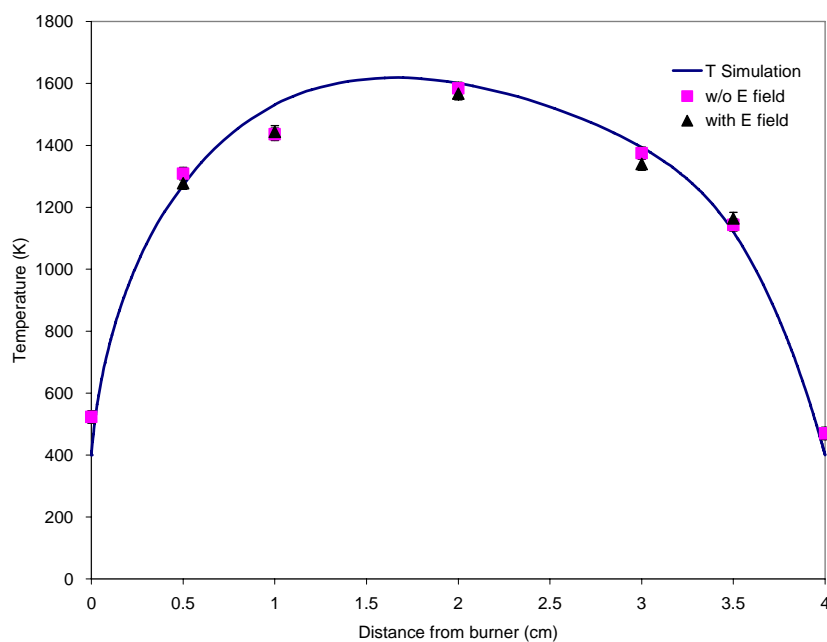


Figure 5.6 Axial temperature profile without precursor. Comparison between simulation, with and without an electric field at 20 torr. The symbols are the results of LIF measurements and the line is model prediction. -500V is applied to the substrate and the burner is grounded.

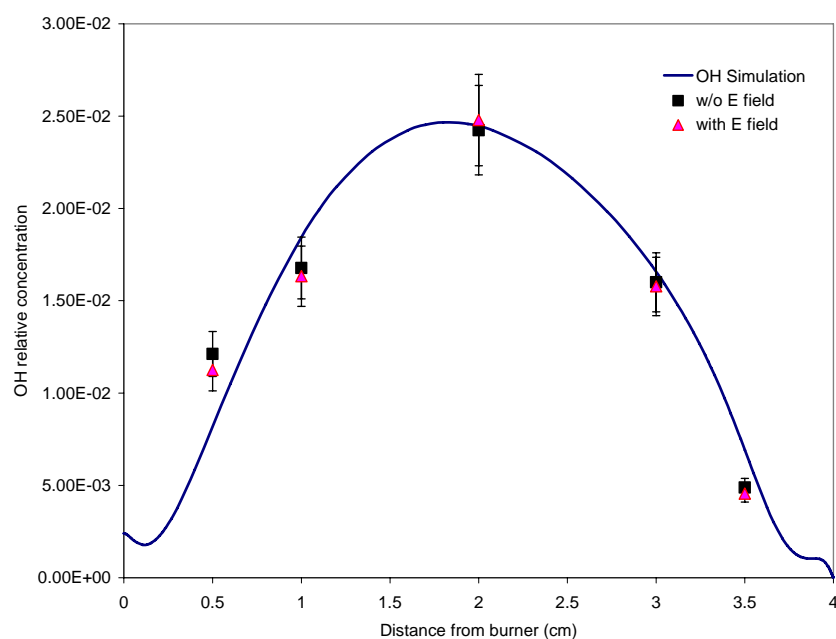


Figure 5.7 Axial OH concentration without precursor. Comparison between simulation, with and without an electric field at 20 torr. The symbols are the results of LIF measurements and the line is the model prediction. -500 V is applied to the substrate and the burner is grounded.

5.4.2 Effect of the precursor loading on T and OH concentration

Visible luminescence of the synthesis flames, with and without precursor loading, changes dramatically (Fig. 5.8). The temperature and OH concentrations profiles in the same synthesis flame with and without the addition of precursor TTIP (a typical precursor loading rate of 3.83×10^{-4} mol/min) are shown in Fig. 5.9 and Fig. 5.10, respectively. In both cases, no electric field is applied to the synthesis flame. As seen from Fig. 5.9, the addition of precursor (TTIP) has only a small effect on the flame temperature. Figure 5.10 shows an increasing OH concentration on the burner side of the flame and the peak value increases by about 10%. However, closer to the substrate side, the decay of OH concentration is similar to the case without the precursor. This behavior is similar to that seen in hydrogen/oxygen flames to which a trace hydrocarbon is added, showing that the precursor is decomposing in a manner similar to a hydrocarbon fuel additive.

Usually the loading of a precursor will increase the flame temperature through the oxidation of TTIP and the further oxidation of the intermediate product, e.g., C_3H_6 . The carbon content can be presumed to have burned off by the center of the burner-substrate-gap from the OH concentrations as shown in Fig. 5.10. On the other hand, the presence of TiO_2 particles can increase the radiative losses from the flame (as seen from the strong luminescence when the precursor is loaded—the result of the particles thermally radiating at high temperatures), which will lower the precursor-free flame temperature.

Those two factors seem to cancel each out, which might be the reason that the gas-phase temperatures with precursor loading only experienced a mild temperature increase (2%, 28 K in Fig. 5.9) over that of the precursor-free flame. This is an important result because, in the particle modeling effort, we use the TTIP-free flame temperature

distribution.

(a)



(b)

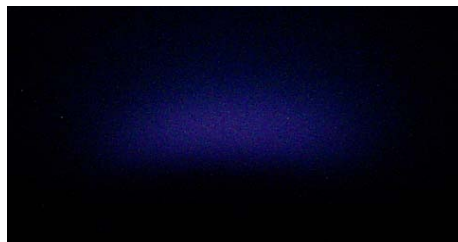


Figure 5.8. Comparison of visible luminescence of the synthesis flames, (a) with, and (b) without precursor loaded.

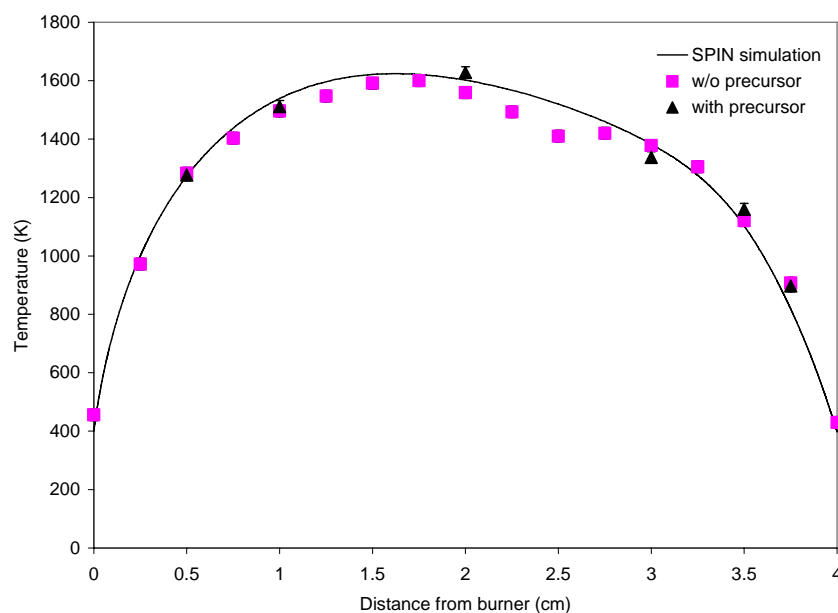


Figure 5.9. Axial temperature profile. Comparison between simulation, with and without precursor, at 20torr. The symbols are the results of the LIF measurement and the line is the model prediction.

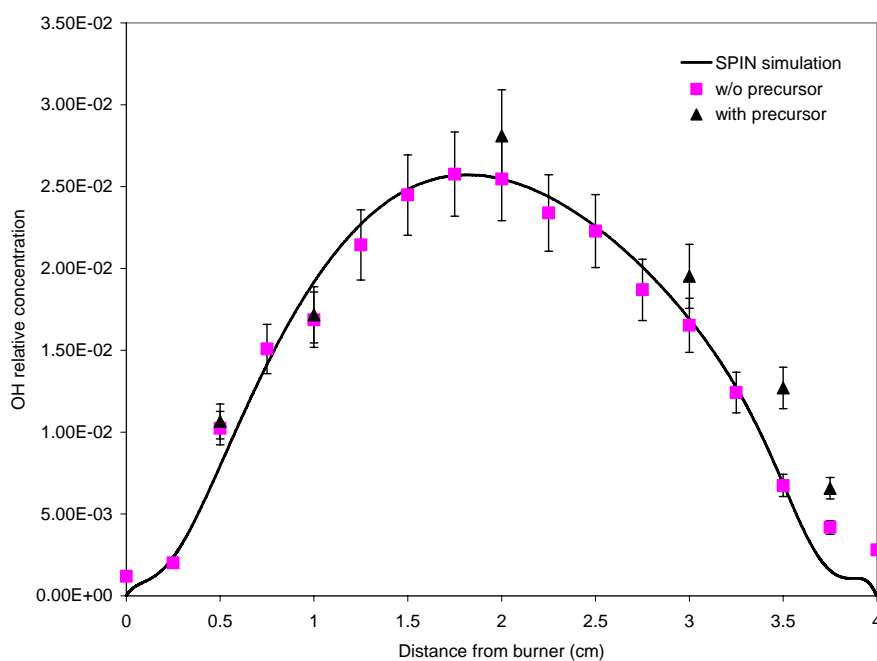


Figure 5.10. Axial OH concentration. Comparison between simulation, with and without precursor at 20torr. The symbols are the results of the LIF measurement and the line is the model prediction.

5.5 Error analysis

5.5.1 Relative OH concentration errors from systematic uncertainty

The OH-PLIF measurements are obtained by excitation of the $A^2\Sigma \leftarrow X^2\Pi(1,0)$ band of OH, near 283nm combined with detection of the strong (1,1) band near 315nm (ranging from ~308-325 nm). This excitation strategy, which can be performed using a frequency-doubled dye laser, is chosen to avoid fluorescence trapping, the absorption of the emitted OH fluorescence by other OH molecules¹⁶. In addition, the limited pulse energies (~1-30 mJ) available from the frequency-doubled dye laser sources provide a linear fluorescence measurement regime.

The isolated $Q_1(7)$ transition at 283.222nm is selected to minimize signal dependence on temperature (i.e., ground state population). For $J''=7.5$, the population term is only weakly sensitive to temperature over a wide range of temperatures (i.e., 1500-3000 K). By using the $Q_1(7)$ transition, we eliminate the need for a temperature correction to the fluorescence signal profile. The relative uncertainty in number density for a nearly constant pressure region is approximately 10% due to Boltzmann temperature variations¹⁷.

If the concentration of the target species or some other absorbing species is large enough, absorption will reduce the local laser irradiance and thus the excitation rate, depressing the LIF signal. Laser trapping by both gas and particle absorption may occur, but it is apparent that in our premixed flames, the absorption can be ignored because these flame are usually “clean.”

There are several possible scattering interferences that need to be reduced. From the analysis in Chapter 2, scattering from windows and other optics surfaces can be

minimized by careful attention to the optical layout and by coating windows to reduce scattering losses. Rayleigh and Raman scattering from other species in large concentrations may interfere with the signal. Because the Rayleigh and Raman scattered signals are highly polarized while the fluorescence signal is not, the optical layout is set such that the ratio of Rayleigh or Raman to fluorescence is significantly reduced. Particle scattering can interfere with the optical measurement only if present in sufficient concentration. In a H_2/O_2 premixed flame, even with TiO_2 precursor added, the particle number density is very low so that the probability of a particle being in the focal volume is small and the particle scattering effect can be discarded. When particle number density limit is researched, one can use discrimination criteria¹⁸ to reject the signal when its amplitude suggests a particle may be present.

A consequence of laser excitation and collisional redistribution is that the laser energy deposited in the focal volume eventually ends up as thermal energy. By heating the focal volume and raising the local temperature, the energy will bring signal distortion to the LIF measurement. The laser heating effect becomes obvious when energy deposition in the focal volume is significant with respect to the rate of diffusion of energy away from it. An estimation by considering the conservation of energy¹⁹ shows that the typical temperature rise in the focal volume is at most ~ 30 K over a 5-ns pulse duration. Although the heating rate will be reduced by volumetric expansion effects at high temperatures, it can certainly be relatively large at a measuring point at low temperatures.

5.5.2 Temperature errors from systematic uncertainty

The strategy of two-line temperature measurements uses excited $\text{P}_2(7)$ and $\text{P}_2(9)$ transitions of the (1-0) band, which have similar $B(g'g'')/g'$ values (Chapter 2). This

reduces the effect of saturation on the derived temperature, since the difference in temperature obtained by assuming linear conditions and assuming fully saturated conditions is less than 20 K.

5.5.3 Temperature errors from photoelectron statistics

In LIF, the temperature is determined with two-line thermometry by the use of rotational states j_1 and j_2 . The ratio R of the population in the two states, if assuming the same nuclear degeneracy, is related to temperature by

$$R = \left[(2j_1 + 1) / (2j_2 + 1) \right] \exp(\Delta E / kT) \quad (5.4)$$

Differentiation yields the relative error:

$$\Delta T / T = (\Delta R / R)(kT / \Delta E) \quad (5.5)$$

where R is obtained as the ratio of N_{p1}/N_{p2} , and N_p the number of photoelectrons. The error of ΔR is then

$$\Delta R = \left| dR / dN_{p1} \right| \Delta N_{p1} + \left| dR / dN_{p2} \right| \Delta N_{p2} \quad (5.6)$$

and the relative error is, according to linear error propagation, the sum of the individual errors:

$$\Delta R / R = 1 / (N_{p1})^{1/2} + 1 / (N_{p2})^{1/2} \quad (5.7)$$

We use the typical data in Chapter 2, that is,

$$g_N = 2N + 1 \quad (5.8)$$

$$k = 0.6938 \text{ cm}^{-1} \text{ K}^{-1} \quad (5.9)$$

and

$$E_7 = 2887.35 \text{ cm}^{-1} \quad (5.10)$$

$$E_7 = 3502.78 \text{ cm}^{-1} \quad (5.11)$$

Then

$$\Delta R / R = (1.3 N_{p2})^{-1/2} + (N_{p2})^{-1/2} = 1.88 (N_{p2})^{-1/2} \quad (5.12)$$

so that

$$\Delta T = T \Delta R/R = 1.88 T N^{-1/2} \text{ with } N = N_p. \quad (5.13)$$

In single-shot experiments, the measurement precision is usually determined by N_p .

From Poisson statistics, the absolute error is $\Delta N_p = N_p^{1/2}$, and the relative error is $\Delta N_p / N_p = N_p^{-1/2}$, with S/N ratio of $N_p / N_p^{1/2} = N_p^{1/2}$. When signals are integrated over many laser shots (hundreds to thousands), statistical errors become negligible. This is similar with the signal-to-noise ratio and the resulting random error S/σ_s in the Raman spectroscopy measurement,

$$\frac{S}{\sigma_s} \propto \sqrt{N} \quad (5.14)$$

where σ_s is the RMS of the collected LIF signal S . For a 30 second LIF measurement which includes 300 shots, the statistical errors are only 6% of those in single-shot measurements.

5.6 Conclusion

The agreement between the simulation and the LIF measurements is very good for these stagnation point flames, suggesting that the flow field is appropriately captured by the stagnation-point flow model. It is verified that the application of electric fields in this geometry (and at the magnitudes examined) has virtually no effect on the flame structure. It does, however, induce electrophoretic transport of nanoparticles that are innately charged by the combustion processes through thermionic emission. In the precursor-loaded flame, the OH concentration profile is similar to one where a trace hydrocarbon is added to the hydrogen flame, showing that the metalorganic precursor is decomposing in a manner similar to a hydrocarbon fuel additive. The precursor-loaded flame experiences only a mild temperature increase since particles thermally radiating decreases the magnitude of the temperature increase. Nonetheless, the measurements show that it is

appropriate to model particle transport and growth based on the temperature and velocity profiles given by the simulations.

In the future work of this research, spectroscopic flame emission characteristics at various locations should be examined, which can provide information on pyrolysis and reaction kinetics. LIF should be further employed to probe radical monomer species distributions, i.e., AlO, TiO. Spontaneous Raman spectroscopy (SRS) should be used to measure the temperature and major species concentration (e.g., H₂, O₂, N₂, H₂O) at higher pressures. In the next chapter, SRS is applied to directly detect TiO₂ nanoparticle composition and crystallinity. Since other *in-situ* and *ex-situ* characterizations on nanoparticles provide physical information, such as particle size and particle morphology, SRS can be used to diagnose phase transition, providing complementary *in-situ* information on chemical aspects of particle growth.

References

- ¹H. Zhao, X. Liu, and S.D. Tse, Control of Nanoparticle Size and Agglomeration through Electric-Field-Enhanced Flame Synthesis, invited paper, *Journal of Nanoparticle Research* 10, 907-923 (2008).
- ²H. Zhao, X. Liu, and S. D. Tse, Effects of pressure and precursor loading in the flame synthesis of Titania Nanoparticles, *Journal of Aerosol Science*, In Press (available online 6 Aug 2009).
- ³M. S. Wooldridge, Gas-phase combustion synthesis of particles, *Progress in Energy and Combustion Science* 24, 1, 63-87 (1998).
- ⁴H.K. Kammler, L. Madler, and S.E. Pratsinis, Flame synthesis of nanoparticles, *Chemical Engineering and Technology* 24, 6, 583-596 (2001).
- ⁵B. Zhao, K. Uchikawa, J. R. McCormick, C. Ni, J. Chen, and H. Wang, Ultrafine anatase TiO₂ nanoparticles produced in premixed ethylene stagnation flame at 1atm, *Proceedings of the combustion institute* 30, 2569-2576 (2005).
- ⁶R. J. Goldstein, *Fluid Mechanics Measurements* (Washington: Hemisphere Pub. Corp, 1983)
- ⁷N.G. Glumac, Y.J. Chen, and G. Skandan, Diagnostics and modeling of nanopowder synthesis in low pressure flames, *Journal of Materials Research* 13, 9, 2572-2579 (1998).
- ⁸A. Colibaba-Evulet, Nanoparticle synthesis in low pressure flames, Ph.D. dissertation, Rutgers University, 2000.
- ⁹Y.J. Chen, Nanocrystalline-oxide ceramics: synthesis, diagnostics, and processing, Ph.D. dissertation, Rutgers University, 2000.
- ¹⁰H. Zhao, Experimental and computational studies of flame synthesis of nanoparticles: Effects of pressure, precursor loading, and electric field, Ph.D. Thesis, Rutgers University, 2007.
- ¹¹SPIN, A Program For Modeling One-Dimensional Rotating-Disk /Stagnation-Flow Chemical Vapor Deposition Reactors, SPI-036-1, 2000.

-
- ¹² R.J. Kee, F.M. Rupley, E. Meeks, J.A. Miller, CHEMKIN-III: A fortran chemical kinetics package for the analysis of gas-phase chemical and plasma kinetics, Rept. SAND96-8216, Sandia national laboratories, 1996.
- ¹³ M.E. Coltrin, et al., Surface Chemkin: A general formalism and software for analyzing heterogeneous chemical kinetics at a gas-surface interface, *International Journal of Chemical Kinetics* 23, 12, 1111-1128, 1991.
- ¹⁴ R.J. Kee, G. Dixon-Lewis, J Warnatz., M.E. Coltrin, J.A. Miller, and H.K. Moffat, A Fortran computer code package for the evaluation of gas-phase, multicomponent transport properties, Rept. SAND86-8246B, Sandia national laboratories, 1998.
- ¹⁵ M.A. Mueller, T.J. Kim, R.A. Yetter, and F.L. Dryer, *Int. J. Chem. Kinet.* 31, 113-125 (1999).
- ¹⁶ J. M. Seitzmann, and R. K. Hanson, Comparison of excitation techniques for quantitative fluorescence imaging of reacting flows, *AIAA Journal* 31, 3, 513-519 (1993).
- ¹⁷ T. E. Parker, et al., Measurements of OH and H₂O for reacting flow in a supersonic combustor, *Journal of Propulsion and Power* 11, 6, 1154-1161 (1995).
- ¹⁸ A.R. Masri, R.W. Dibble, and R.S. Barlow, Raman-Rayleigh scattering measurements in reacting and non-reacting dilute two-phase flows, *J. Raman Spectrosc.* 24, 83-89 (1993).
- ¹⁹ J.W. Daily, Laser induced fluorescence spectroscopy in flames, *Prog. Energy Combust. Sci.* 23, 133-199 (1997).

Chapter 6

***In-situ* Raman Characterization of Nanoparticle Aerosols during Flame Synthesis**

In the previous chapter, LIF measurements of temperature and OH concentration profiles were made to verify the flow field predicted by the computational simulation. As a result, a rigorous parametric study on nanoparticle synthesis could be properly conducted, revealing fundamental growth mechanisms. Under standard conditions (specified in Ch.4), nanoparticles with small primary particle sizes and good crystalline structure are readily produced. Particle growth modeling was compared with *in-situ* TEM sampling and *in-situ* particle size distribution characterization (using nano-SMPS). Nevertheless, the as-synthesized nanoparticles are ultimately characterized by *ex-situ* methods, as described in Chapter 2, to determine their aggregate particle size, phase, crystallinity, primary particle size, morphology, specific surface area, and extent of pyrolysis.

In this chapter, *non-intrusive* Raman spectroscopy is applied to diagnose nanoparticle presence and characteristics in a gaseous flow field. Specifically, *in-situ* monitoring of the Raman-active modes of TiO_2 and Al_2O_3 nanoparticles in aerosol form is demonstrated in high-temperature flame environments. The effect of temperature on the solid-particle Raman spectra is investigated by seeding nanoparticles into a co-flow jet diffusion flame, where local gas-phase temperatures are correlated by shape-fitting the N_2 vibrational Stokes Q-branch Raman spectra. The technique is also applied to low-pressure premixed flame synthesis as described in Ch.4.

As stated in the Preface, much of the content of this chapter appears verbatim from a paper¹ submitted for publication, which includes co-authors.

6.1 Introduction

Of the numerous techniques developed for the production of nanoparticles, one of the most popular methods is gas phase synthesis due to its high rate of synthesis, capability for continuous operation, and good control of particle size, crystallinity, and degree of agglomeration. Flame synthesis is a method that has drawn interest from a variety of research communities because of its potential for large-scale manufacture of a wide range of new materials^{2,3}. However, it can be a complex chemical and physical transition process, involving complicated aerodynamics, unknown precursor decomposition kinetics, fast chemical reactions, and multiple particle transport and growth processes. As a result, fundamental understanding of flame synthesis of nanostructured materials remains a major challenge, despite detailed study by a variety of scientific communities.

Utilization of advanced spectroscopic diagnostics enables non-intrusive *in-situ* characterization of velocity, temperature, and chemical species concentration fields, along with nanoparticle composition and size, permitting fundamental understanding of the mechanisms of particle nucleation, growth, crystallization, and aggregation. This knowledge in turn affords the ability to define process conditions that enable repeatable, high purity, and large yields of various nanomaterials.

Several laser-based spectroscopic diagnostics have been applied *in-situ* to study flame synthesis, ranging from premixed to diffusion and from laminar to turbulent. For examples, laser-induced fluorescence (LIF) has been used to measure intermediate

combustion and metalorganic precursor species (along with temperature) which play important roles in the transition from gas-phase monomers to solid-phase nanoparticles^{4,5,6}. Spontaneous Raman scattering (SRS) has been employed to quantify major species concentration and temperature information^{7,8,9}. Fourier transform infrared (FTIR) spectroscopy has been utilized to measure temperatures and concentrations of gases and particles¹⁰. Ultra-small-angle x-ray scattering (SAXS) has been applied to measure temperature and primary particle size by probing time-resolved scattering signatures of nanoparticles, even at volume fractions on the order of 10^{-6} ¹¹. Laser light scattering (LLS) has been used to measure fractal dimension, mean radius of gyration, aggregate size distribution, and local volume fraction of particles¹². Laser-induced breakdown spectroscopy (LIBS) has been used to characterize particle composition¹³, and laser-induced incandescence (LII) has been used to measure nanoparticle size¹⁴. By combining these techniques, many aspects of the synthesis process can be quantified. However, a technique to unambiguously identify an evolving nanoparticle's composition and crystallinity is still needed.

Raman spectroscopy is a robust technique that can characterize temperatures and concentrations of gases, liquids, solids, and, as will be shown, even multi-phase systems. Recent developments in instrumentation, i.e. intense laser source, high-performance notch filters, and sensitive charge-coupled devices, have overcome many of the difficulties associated with the inherently weak Raman effect. Raman spectroscopy of thin films^{15,16,17,18}, nanopowders^{19,20,21,22,23,24}, and fullerenic materials^{25,26} are routinely performed using microscopy techniques with high spatial resolution. However, such characterization is performed *ex-situ*; and various applications require *in-situ* or real-time

response (e.g. in industry process control ²⁷), remote sensing design ²⁸, or other flexibilities. In this work, we introduce the novel application of Raman spectroscopy to characterize nanoparticle composition and crystallinity in aerosol form in high-temperature flame environments, particularly highlighting its utilization during gas-phase synthesis. Such a diagnostic is envisioned to become an indispensable tool in a production setting, where the properties of end-product materials can be verified (and optimized) during the run, prior to final collection.

6.2 Experimental Arrangement

6.2.1 *In-situ* Spontaneous Raman Scattering Setup

Figure 6.1 shows a schematic of the spontaneous Raman scattering (SRS) system used to probe the experiments *in-situ*. An injection-seeded frequency-doubled (532nm) Q-switch Nd:YAG laser (Quanta-Ray Lab-170, Spectra Physics) operating at 10Hz (8.4ns FWHM) serves as the excitation source. The laser beam is focused by a 300-mm (500-mm for the synthesis experiments) focal-length plano-convex fused-silica lens to a probe volume with a waist diameter of approximately 200 μ m. For gas-phase molecule excitation, the energy is \sim 50mJ/pulse; while for solid-phase nanoparticle excitation, the energy is attenuated to \sim 6.5mJ/pulse, due to the much larger Raman signal. The scattered light from a 100 μ m diameter by 100 μ m length measuring volume is collected at 90° by a 400-mm focal-length achromat lens, passed through a Raman holographic notch filter (Kaiser HSPF-532.0-2.0), image rotated, depolarized, and focused by a 300-mm focal-length achromat lens into a 0.5-m imaging spectrometer (Acton SpectrPro-2558, f/6.5) with a 2400 groove/mm grating (Richardson 53009BK01-150R) onto an ICCD detector (Princeton Instruments PIMAX 1300HQ). The spectrometer magnification is unity, and

the slit width is $75\mu\text{m}$, with a wavelength resolution of $\sim 0.04\text{nm}$. The use of the pulsed laser source and gated detector improves the signal to noise ratio (SNR). For both gas-phase molecule and nanoparticle detection, typically 3000 shots (300 shots on the chip with 10 accumulations) using a 100ns gate width are taken to increase SNR. The aerosol experiments are mounted on a 3-D translator, which allows spatial profiling with micrometer precision.

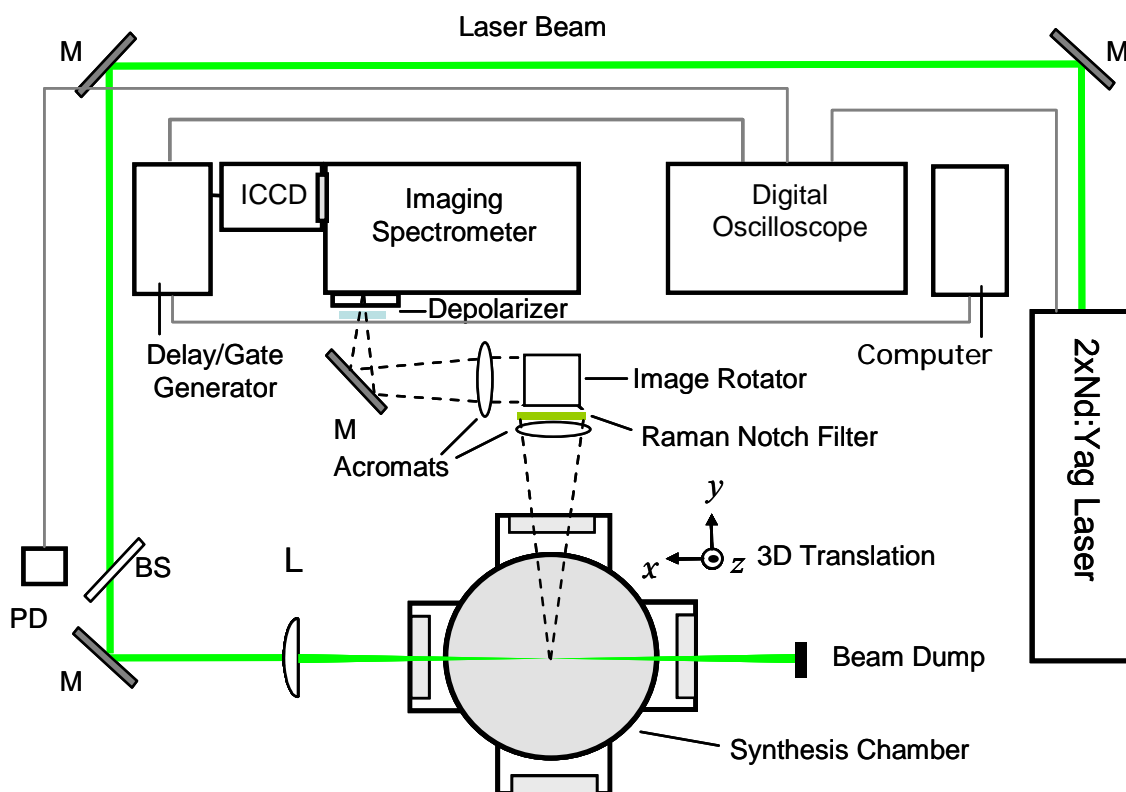


Figure 6.1. Schematic of the *in-situ* Raman scattering system. BS: beam splitter; L: lens; M: mirror; PD: photodiode.

6.2.2 Gas-phase SRS

Spontaneous Raman spectroscopy is employed to determine local gas-phase temperatures at locations corresponding to nanoparticle detection, for atmospheric flame experiments. The temperature measurements are obtained by least-square fitting²⁹ the shape of the Q-

branch N_2 Raman spectrum (Raman shift of 2330 cm^{-1}) to a library of theoretical spectra³⁰ spaced 50K apart. The uncertainty in the fitted temperature is less than $\pm 50\text{K}$, and the reproducibility of the measurements is within $\pm 20\text{K}$.

6.2.3 Nanoparticle SRS

Solid-phase Raman scattering shares many common features with gas phase from the basic principles to the experimental setups. Raman spectroscopy of titania has been carried out by various investigations^{15,20,21,31,32,33,34}. Titania has 3 main polymorphs, i.e. anatase (tetragonal), rutile (tetragonal), and brookite (orthorhombic). For anatase single crystal, Ohasaka³⁵ detected the six Raman active modes from factor group analysis, identifying them at 144cm^{-1} (E_g), 197cm^{-1} (E_g), 399cm^{-1} (B_{1g}), 513cm^{-1} (A_{1g}), 519cm^{-1} (B_{1g}), and 639cm^{-1} (E_g). For rutile single crystal, Porto et al.³⁶ detected the four Raman active modes, identifying them at 143cm^{-1} (B_{1g}), 447cm^{-1} (E_g), 612cm^{-1} (A_{1g}), and 826cm^{-1} (B_{2g}). Although the 143cm^{-1} (B_{1g}) peak overlaps with anatase, Ref. 15 finds it to be extremely small for rutile, especially in relation to the other peak heights and thus should not be of concern in discriminating between anatase and rutile phases. Little information exists for brookite, which is not investigated in this work. Other works have found that the distinguishing phonon frequencies in single-crystal Raman spectra are similar to those in the spectra of polycrystalline^{37,38,39} and nanophase⁴⁰ materials, such that all the Raman active modes can be associated (albeit with slight shifts) to that for the single crystal spectra²⁰. In this work, the Raman modes in TiO_2 (and Al_2O_3) nanoparticles are referenced to those reported in the literature for the bulk phase.

Alumina has several crystalline phases. $\gamma\text{-Al}_2\text{O}_3$ with $Fd\bar{3}m$ (cubic) does not have Raman modes⁴¹. Yet, $\alpha\text{-Al}_2\text{O}_3$ (corundum), the equilibrium phase, with $R3c$ space group

(rhombohedral), gives rise to seven Raman active phonon modes, $2A_{1g}+5E_g$ ⁴², i.e., 378cm^{-1} (E_g), 418cm^{-1} (A_{1g}), 432cm^{-1} (E_g), 451cm^{-1} (E_g), 578cm^{-1} (E_g), 648cm^{-1} (A_{1g}), and 755cm^{-1} (E_g). This Raman signature of $\alpha\text{-Al}_2\text{O}_3$ has been used to detect the transformation of $\gamma\text{-Al}_2\text{O}_3$ to $\alpha\text{-Al}_2\text{O}_3$ in laser treatment of as-sprayed coatings⁴³.

In this work, Raman particle scatter is targeted by using a low excitation power, purposely relegating the much weaker Raman gas-phase scatter to the instrumental detection threshold.

6.3 Validation and Calibration of Technique

6.3.1 *Ex-Situ* TiO₂ nanoparticle characterization on glass slides at room temperature

The capability of the optical arrangement of our *in-situ* Raman setup (Fig. 6.1) to characterize nanopowders is validated by comparing its performance to that of a commercial Raman microscope for static nanoparticles on a glass slide. Figure 6.2 displays the setup for the slide configuration. The excitation power is kept under 2 mJ/pulse and is monitored using a power meter. Specular reflection is eschewed by adjusting the angle of the glass slide (see Fig. 6.2) so that only diffuse scatter from the nanopowder is collected by the Raman system.

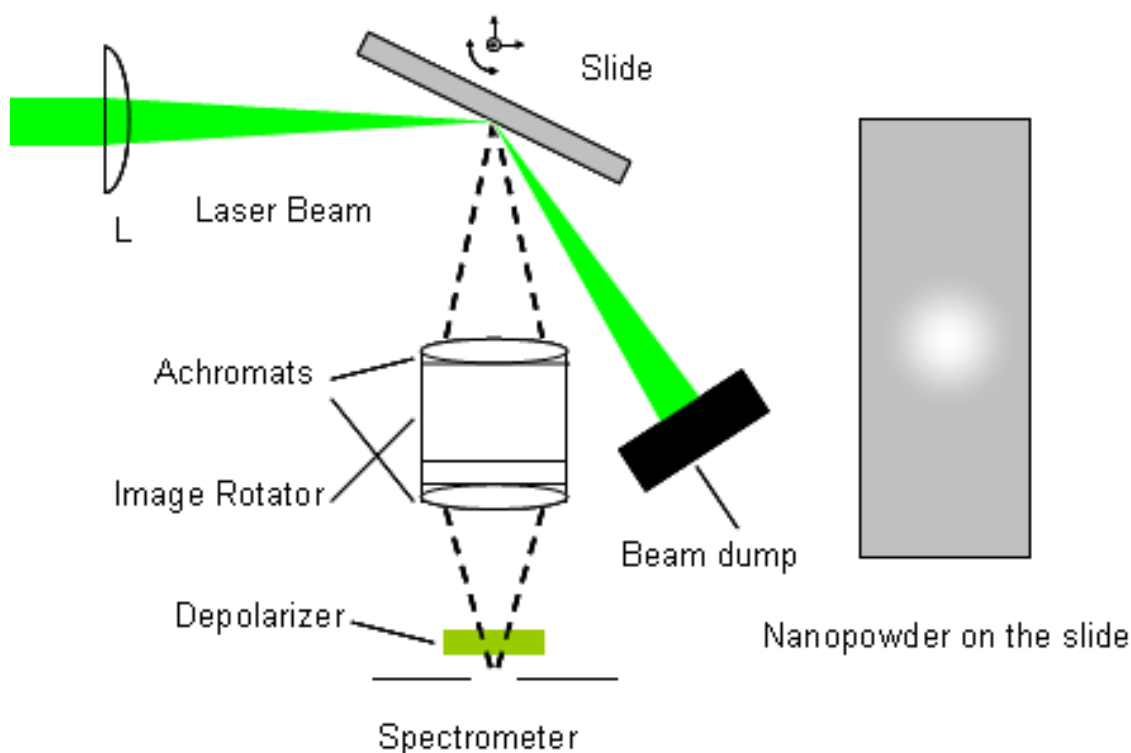
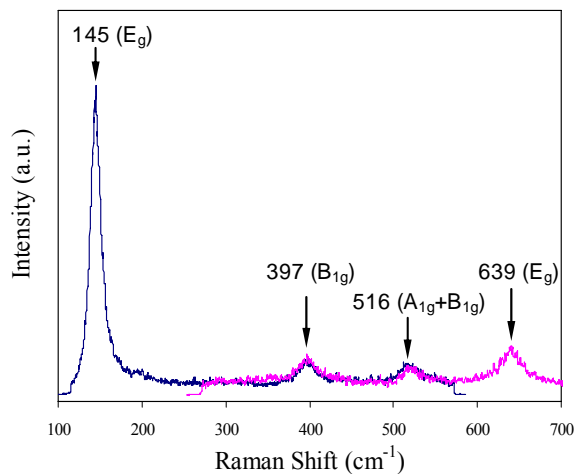


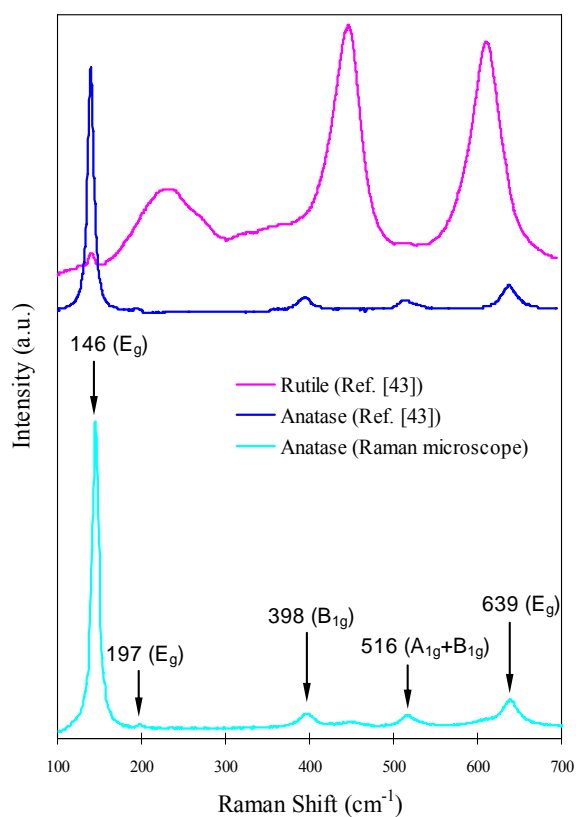
Figure 6.2. Schematic of the setup for the nanopowder on glass slide calibration configuration.

Figure 6.3(a) shows a high-SNR Raman spectrum of anatase TiO_2 nanopowder produced by our system, without any background subtraction or smoothing. As can be seen, the spectrum is a combination of two smaller coverage spectra, centered at 350cm^{-1} and 500cm^{-1} , due to the use of a 2400g/mm grating for high resolution. The main Raman peaks are those for anatase at 145cm^{-1} (E_g), 397cm^{-1} (B_{1g}), 516cm^{-1} ($A_{1g}+B_{1g}$), and 639cm^{-1} (E_g). The same nanopowder-coated glass slide is tested with a Renishaw inVia Raman microscope with 785-nm excitation; and the spectrum is shown in Fig. 6.3(b), with Raman peaks at 146cm^{-1} (E_g), 398cm^{-1} (B_{1g}), 516cm^{-1} ($A_{1g}+B_{1g}$), and 639cm^{-1} (E_g). As reference, Fig. 6.3(b) also displays the known spectra for anatase and rutile for film samples as given in Ref. 44. The main Raman peaks detected using our *in-situ* setup and the Raman microscope agree very well with each other, substantiating the competence of

our system to characterize nanoparticles with high-quality spectra. Although the Raman peak at 197cm^{-1} (E_g) is discernable by our system, it is more evident in the microscope system. Background subtraction would have better resolved this peak. Nevertheless, this peak is characteristically small and is not necessary to be resolved to verify the anatase phase, as shown in other works^{20,40}.



(a)



(b)

Figure 6.3. Raman spectrum of anatase titania on a glass slide: (a) taken using our *in-situ* Raman setup. Spectrum is composed of two smaller coverage spectra, with the grating centered at 350 cm^{-1} and 500 cm^{-1} ; (b) taken using Renishaw inVia Raman microscope. Known spectra of anatase and rutile films given in Ref. 44 are also shown.

6.3.2 *In-Situ* Aerosol Characterization

6.3.2.1 *Setup of Nanoparticle-Seeded Calibration Flame*

The Raman spectroscopy of TiO₂ nanoparticles seeded into a co-flow jet diffusion flame is investigated to demonstrate the ability of our system to characterize nano-aerosols, as well as to study temperature and species interference effects on the collected spectra. The schematic in Fig. 6.4 displays the burner and the supporting gas-flow instrumentation producing the jet diffusion flame. The burner is composed of a center tube surrounded by a concentric outer annulus, which is filled with 3-mm glass beads to distribute an airflow that exits the burner through a ceramic honeycomb with a flat velocity profile. Nitrogen-diluted methane flows through the center tube, which is sufficiently long to produce a fully-developed laminar velocity profile at the burner exit. Nanoparticles are injected into this center tube. A quartz cylinder encompasses the flame and flow field to isolate the aerosol from the ambient surroundings. Raman measurement of the TiO₂ nanoparticles is examined along the axial centerline (proceeding downstream of the burner exit) of the axi-symmetric flow field. At the same locations where TiO₂ Raman signals are taken, N₂ Raman spectra are also collected to determine the local gas-phase temperatures.

As seen from Fig. 6.4, the gas flow system comprises an N₂ line which bypasses the aerosol feeder, so that conditions can be examined sans nanoparticle seeding while maintaining the same flow rate and thus flame state. By comparing Raman spectra with and without the presence of TiO₂ nanoparticles, gas-phase temperatures can be cross-validated; and interference modes can be identified and accounted for. For example, the low frequency N₂ rotational Raman spectra and the low-frequency E_g mode of TiO₂ are both found in the same Raman shift range of 100 to 200cm⁻¹.

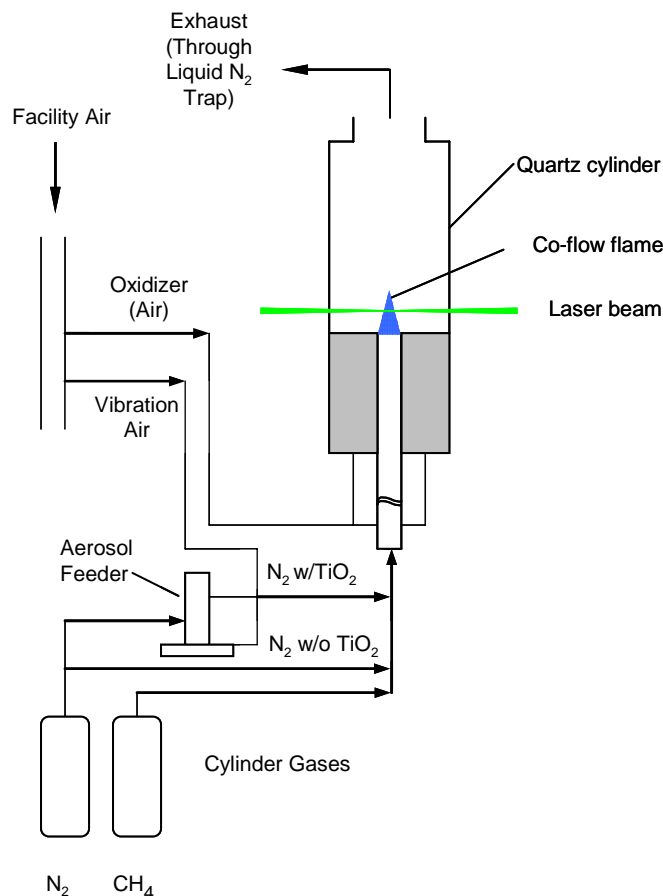


Figure 6.4. Schematic of the setup for the nanoparticle-seeded co-flow jet diffusion flame.

6.3.2.2 Results and Discussion

Measurements are taken at points with a 2.5-mm interval along the axial centerline of the flame. As previously mentioned, the Q-branch of the N_2 vibrational Raman spectra at these points are also obtained and used to determine the gas-phase temperatures.

For the TiO_2 nanoparticle Raman investigations, a very low feeding rate of the TiO_2 nanopowder is used to approximate the conditions in the flame synthesis environment (described later). A low particle density ($\sim 10^{17}$ particles/ m^3) precludes heavy interference of the particles, facilitating analysis. As will be seen, under the current experimental situation, the SNR is sufficient to recognize coexisting rutile and anatase

content in the particles. Background luminosity can be reduced by gating (on the order of 10^6 with a 100ns detection window), and broadband fluorescence from flame species can be corrected for based on empirically determined characteristics⁴⁵. For the low-frequency E_g mode of TiO_2 , interference from the N_2 rotational Raman modes can exist. Figure 6.5 shows a typical N_2 rotational spectrum for our flame when no particles are present. However, such gas species spectra can be easily subtracted out by using the “clean” (without TiO_2 powder) N_2 bypass line (Fig. 6.4) to obtain the “background” gas-phase spectra.

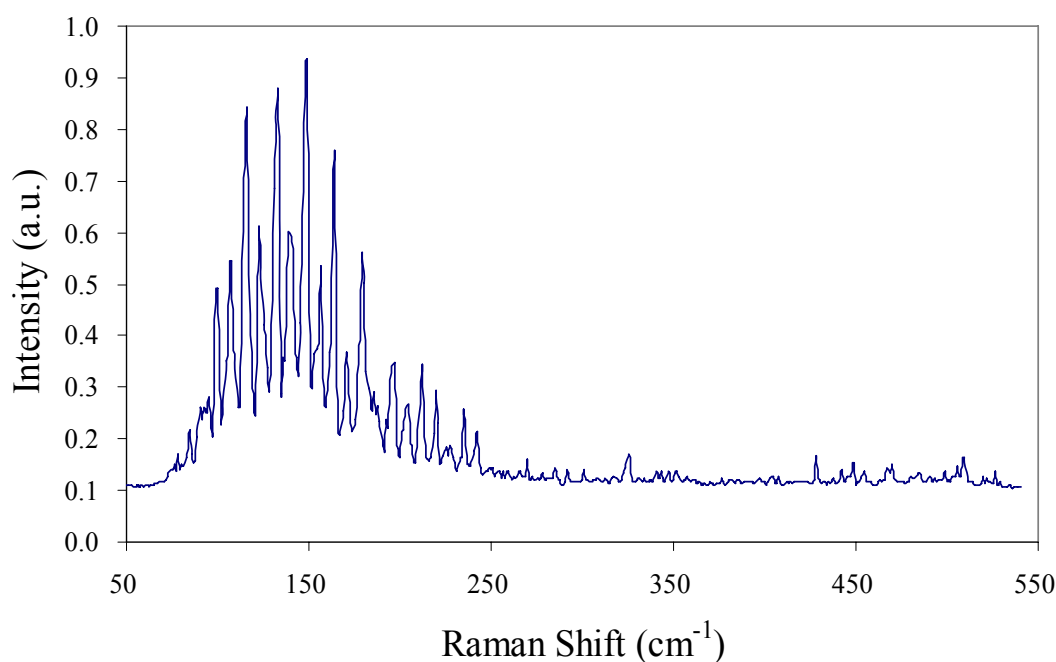


Figure 6.5. Typical N_2 rotational Raman spectrum detected *in-situ* in the co-flow jet diffusion flame without TiO_2 nanoparticle seeding.

Another consideration in taking Raman spectra for aerosols is that photons may randomly ‘diffuse’ by scattering at particle boundaries and then reemerge to be detected with a delay⁴⁶. In the current study, such a response is observed for the TiO_2 nanoparticle aerosol. In contrast to the $<50\text{ns}$ gate width that we generally need for our

laser-pulse-synchronized ICCD camera to detect the Raman signal from gas molecules, a longer gating interval of 100 to 200ns is required for the detection of nanoparticles, implying that inter-powder diffusion extends the lifetime of the Raman scattering signal. Further study is needed to explore this effect as a function of nanoparticle concentration, size, and composition.

A sequence of processed *in-situ* TiO₂ Raman spectra of the anatase nanoparticles seeded into the diffusion flame, at different distances along the axial centerline from the burner exit, is given in Fig. 6.6. Near the burner exit, at relatively low temperatures (points a and b), very strong peaks at $\sim 150\text{cm}^{-1}$ (E_g), $\sim 407\text{cm}^{-1}$ (B_{1g}), $\sim 528\text{cm}^{-1}$ ($A_{1g}+B_{1g}$), and $\sim 645\text{cm}^{-1}$ (E_g) indicate the dominance of the anatase phase. The temperature dependence of the lowest E_g mode manifests itself as a red shift (Stokes regime) from 145cm^{-1} , at room temperature (300K) from the glass slide measurement to 150cm^{-1} , at elevated temperatures within the flame (e.g. 664 and 763K, points a and b). A combination of size confinement and anharmonic effects likely contribute to red shifting and broadening of the spectral peaks²². Refs. 21 and 47 found red shifting (Stokes regime) of the peaks with decreasing particle size, due to phonon confinement. At high temperatures, however, the anharmonic effect was found to be more prominent²².

Above 1000K, a phase transition from anatase to rutile is revealed in the Raman spectra. As seen in Fig. 6.6 at point c, the $\sim 150\text{cm}^{-1}$ (E_g) peak has decreased greatly; and new broad peaks at $\sim 440\text{cm}^{-1}$ (E_g), and $\sim 617\text{cm}^{-1}$ (A_{1g}) appear that are comparable in height with the 150cm^{-1} peak, along with the previous anatase peaks. The new peaks correspond to the well-known Raman spectra of rutile, reported as 447cm^{-1} (E_g) and 612cm^{-1} (A_{1g}) in Ref. 36 (see Fig. 3(b)). Again, the redshift (Stokes regime) for these two

peaks are mainly due to the elevated temperature effect. From points d to g, the nanoparticles are now rutile. In addition, there exists a strong broad band at $\sim 235\text{cm}^{-1}$ (which cannot be assigned to fundamental modes allowed by symmetry in the rutile phase³⁶) that is consistent with what others have found for heated TiO_2 powders (see Fig. 3(b)) that mark the anatase-rutile transformation^{36,38,39}. Porto et al.³⁶ ascribed it to a combination band; Hara and Nicol³⁸ proposed that it is disorder-induced; and Blachandran et al. Ref. 39 suggested that it is due to the second-order scattering from a multiphonon process. Nonetheless, the entire Raman-spectra sequence of Fig. 6 evinces the phase transformation of TiO_2 nanoparticle due to in-flight heat treatment from the hot flame. The measurements indicate the suitability of the technique to monitor and characterize TiO_2 nanoparticle formation from metalorganic precursors during gas-phase synthesis, which is discussed in the next section.

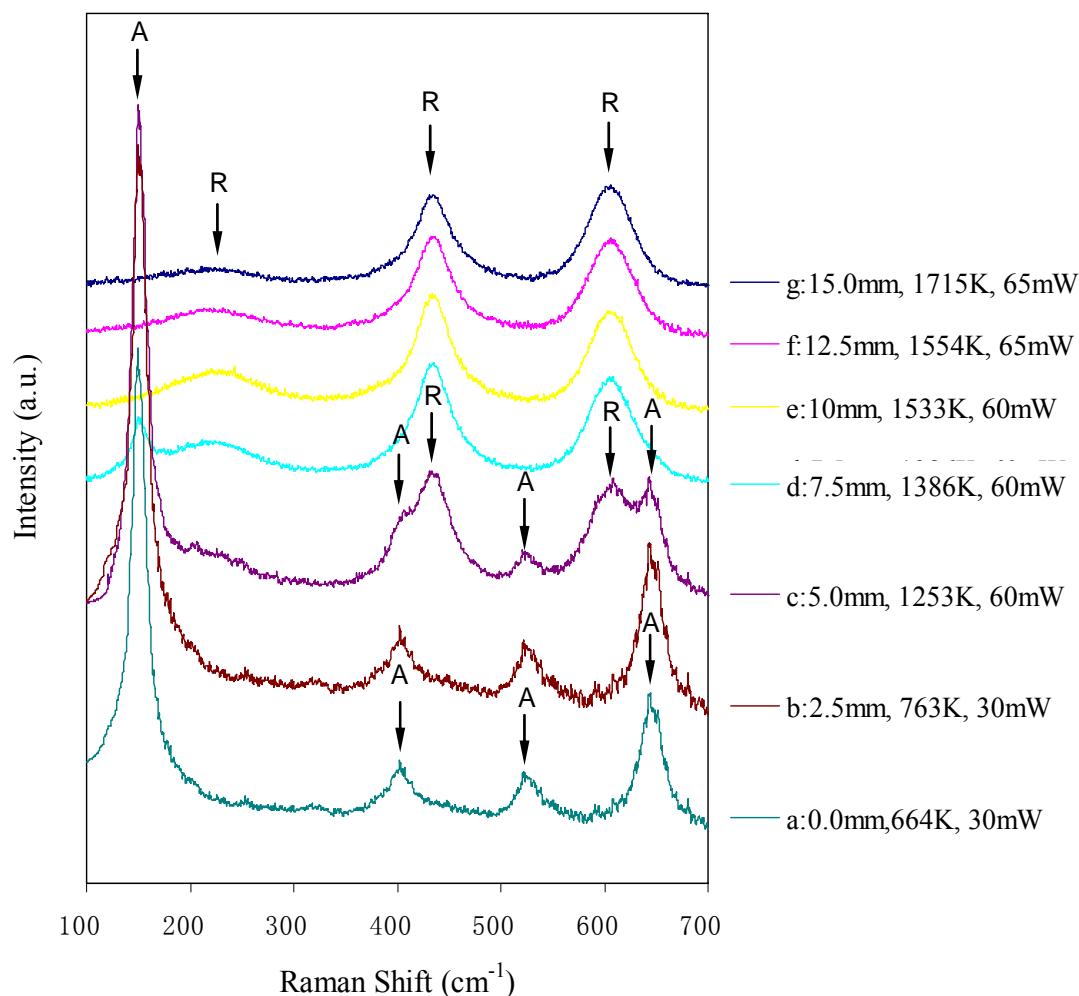


Figure 6.6. *In-situ* Raman spectra of seeded TiO_2 nanoparticles flowing through the co-flow jet diffusion flame, along the axial centerline at different heights above the burner exit. Gas-phase temperature is given and made by SRS on N_2 . Figure shows the transformation from anatase to rutile of the originally anatase seeded nanoparticles.

To extend and generalize the capability of using Raman scattering to characterize aerosol particles *in-situ*, $\gamma\text{-Al}_2\text{O}_3$ nanoparticles are examined by feeding them into the diffusion flame. From the spectra (Fig. 6.7), $\alpha\text{-Al}_2\text{O}_3$ is detected only at the highest gas temperature (1715K at $h = 15\text{mm}$). This observation is consistent with the reported high transition temperature from $\gamma\text{-Al}_2\text{O}_3$ to $\alpha\text{-Al}_2\text{O}_3$,^{48,49} which begins at $T \geq 950^\circ\text{C}$ and finishes at $T \leq 1100^\circ\text{C}$. Our measured transition temperature is higher due to a difference

between gas-phase and solid-phase temperatures since the nanoparticles exit the burner cold and heat up as they traverse the hot flame. A straightforward calculation to estimate the particle temperature can be made as follows.

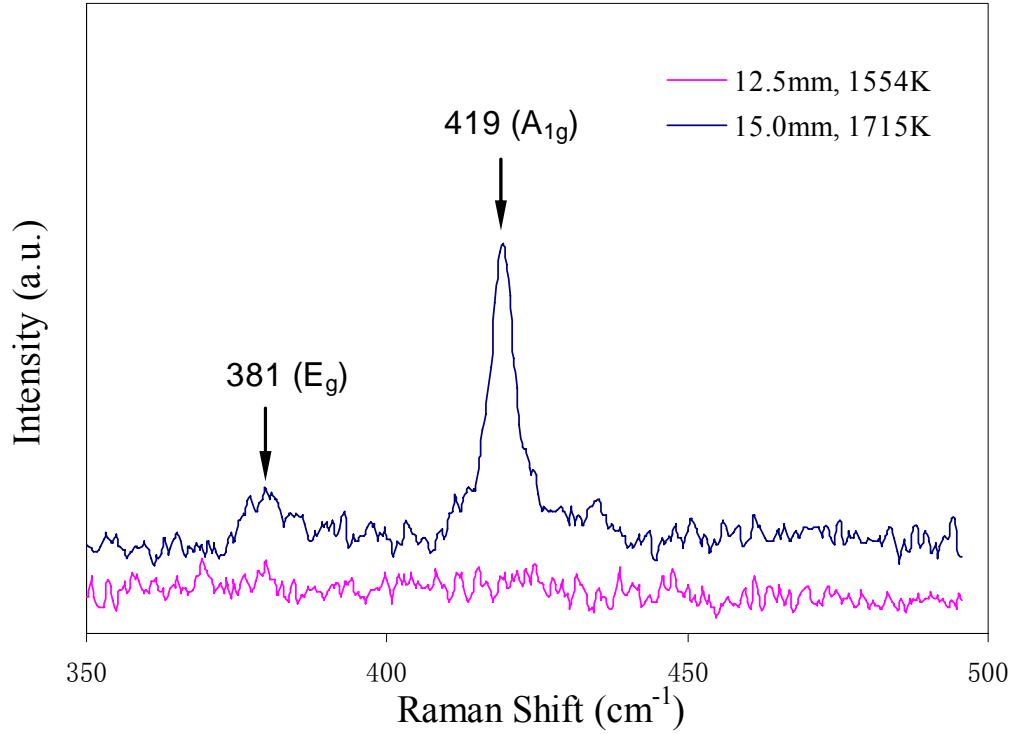


Figure 6.7. *In-situ* Raman spectra of seeded Al_2O_3 nanoparticles flowing through the co-flow jet diffusion flame, along the axial centerline at two heights above the burner exit. Gas-phase temperature is given and made by SRS on N_2 . Figure shows the transformation from γ -alumina (no Raman signature) to α -alumina of the originally γ -alumina seeded nanoparticles.

By applying the *lumped-heat-capacity* model⁵⁰ for a uniform-temperature TiO_2 particle, such that,

$$q = hA(T - T_\infty) = -c\rho V \frac{dT}{d\tau} \quad (6.1)$$

the instantaneous particle temperature is:

$$T_p = T_\infty + (T_{gas} - T_\infty) e^{-[hA/\rho cV]\tau} \quad (6.2)$$

We examine an Al_2O_3 particle with diameter $d=100\text{nm}$, specific heat $c=880\text{J/Kg}\cdot\text{K}$, density $\rho=3.69\times 10^3\text{ Kg/m}^3$. τ is the traveling time of the particle from the exit of the burner to the tip of the flame (a 15mm distance). The particle velocity, which is assumed to be the flow velocity, can be calculated from the flow rate of the jet diffusion flame $V=0.8\text{ L/min}$, with center tube $D=0.01\text{m}$, assuming a fully-developed laminar velocity profile, to be 33 cm/s along the centerline. Exposing a particle initially at $T_\infty=300\text{ K}$ to a flame at $T_{gas}=1715\text{ K}$, with convection heat transfer coefficient $h=100\text{ W/m}^2\text{ }^{50}$, the calculation gives a particle temperature $T_p=920^\circ\text{C}$, which corresponds to the beginning of the Al_2O_3 phase transition temperature range given above. Again, the *in-situ* Raman technique has revealed a phase transition. Although, a similar calculation can be made to assess the solid-phase temperature of TiO_2 nanoparticles traveling through the flame, it may be possible to measure directly the particle temperature using spontaneous Raman spectroscopy. Ref. 22 studied the temperature dependence of the first E_g Raman mode of TiO_2 nanopowder prepared by laser-induced pyrolysis, where the local temperature (with uncertainties of $\pm 100\text{K}$) was determined by the Stokes/anti-Stokes intensity ratio of the first E_g mode of particles themselves. This technique of probing nanoparticle temperatures in an aerosol is the subject of on-going work.

6.4 Application of Technique to Flame Synthesis of Nanoparticles

6.4.1 TiO₂ Nanoparticle Synthesis Flame Setup

Figure 6.8 displays the low-pressure flame synthesis setup. The axisymmetric, stagnation-point premixed flame is formed by flowing premixed reactants, added with chemical precursor vapor, through a flat-flame burner impinging onto a cold substrate. Liquid precursor (i.e. titanium tetra-iso-propoxide (TTIP)) is vaporized and entrained into a carrier gas via a heated bubbling unit and then combined with combustible premixed gases (e.g. hydrogen/oxygen) and delivered to the burner. The flow system is metered with mass flow controllers, and the flow lines are heated (and temperature controlled) to prevent precursor condensation. The chemical precursors pyrolyze and oxidize in the flame and condense into nanoparticles as the gases advect toward the cool substrate.

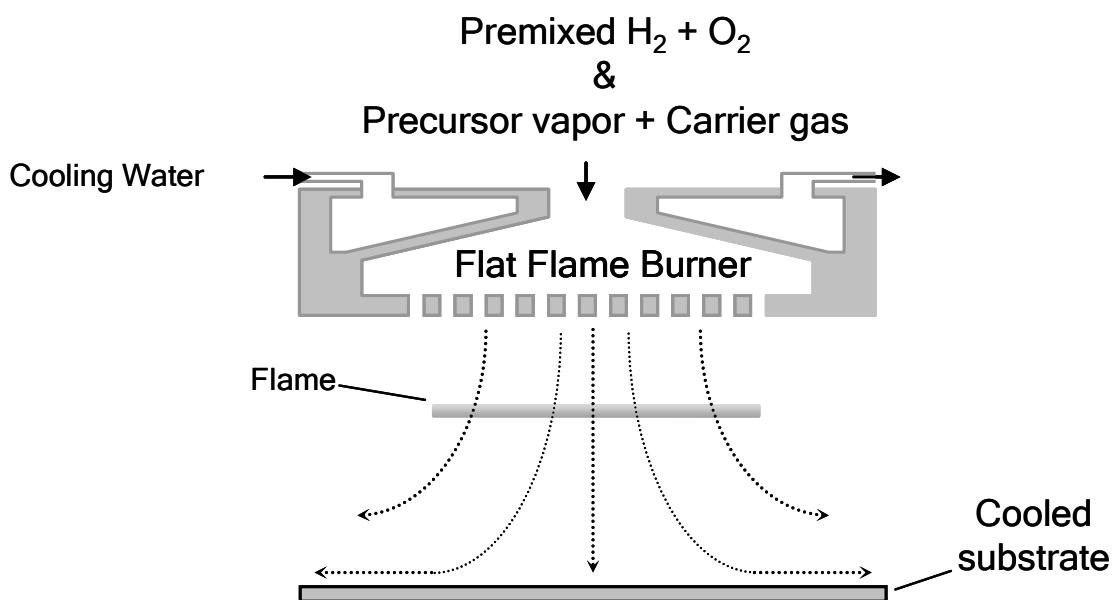


Figure 6.8. Schematic of the axisymmetric, stagnation-point premixed flame synthesis setup.

The synthesis reactor (see Fig. 6.1) consists of a 47-cm diameter cold-wall vacuum chamber, which is maintained at the desired pressure by a roughing pump, throttle valve, and closed-loop pressure controller. Inside the chamber, the burner and substrate are fixed at a set distance apart. Both the burner and substrate are water-cooled, and their temperatures are monitored with K-type thermocouples. The chamber is configured with four orthogonal quartz view ports for optical access, and the entire chamber is mounted to a 3-axis positioner to enable spatial mapping of the aerosol flow field by laser-based diagnostics.

Given the weakness of the gas-phase Raman scattering signal at low pressures, the flame structure is probed *in-situ* using two-line laser-induced fluorescence (LIF) of the hydroxyl radical generated innately by the flame reactions to determine the gas-phase temperature distributions along the axial centerline. Nevertheless, the weak gas-phase Raman scatter under these low-pressure, high-temperature (resulting in very low density) conditions aid in isolating particle Raman scattering. Simulation of the gas-phase flame structure of our quasi-one-dimensional flow field using detailed chemical kinetics and transport is performed using the Sandia SPIN code. By comparing the simulation with measurement, the nature of the material processing flow field is revealed. Further details can be found in Ref. 51. Moreover, a sectional model, coupled with the simulated flow field and flame structure, is employed to model particle growth dynamics, computing aggregate and primary particle size distribution, geometric standard deviation, and average primary particle size. The computations are compared with the experiments, for which *in-situ* characterization of the nanoparticles in the flow field is accomplished by a

low-pressure aerosol sampling system connected to a nano-scanning mobility particle sizer, as well as by TEM sampling.

The flames examined in this study use premixed hydrogen and oxygen with an equivalence ratio of ~ 0.42 , mass flux of 2.519 mg/s/cm^3 , and a system of pressure of 20torr. For titania synthesis, a precursor loading rate of $7.185 \times 10^{-4} \text{ mol/min}$ of TTIP is used.

6.4.2 Results and Discussion

A sequence of *in-situ* Raman spectra obtained along the central line of the gas-synthesis flow field is presented in Fig. 6.9. The local gas-phase temperatures are determined using two-line LIF of OH and confirmed with numerical simulation using detailed chemical kinetics and transport. Here, particle temperatures are expected to be close to gas-phase temperatures, as the particles are homogeneously formed and grow mainly through coalescence and coagulation⁶. Particles with anatase characteristics are first detected about midway between the burner and the substrate (see point d of Fig. 6.9). As evinced, the strong E_g Raman peak at $\sim 150 \text{ cm}^{-1}$ (red shifted due to the previously-discussed temperature and phonon confinement effects) provides a good indication of the anatase phase, along with confirming peaks at 399 cm^{-1} (B_{1g}), 513 cm^{-1} ($A_{1g} + B_{1g}$), and 639 cm^{-1} (E_g). All the same, we are not using the shifts to determine either temperature or particle size. Instead, we analyze the Raman peaks to establish crystalline nature and particle composition, so, as long as the peaks can be associated with identifying features of a particular polymorph, then any minor shift is immaterial. As shown, the peaks become stronger and more distinct near the substrate (e.g. point a of Fig. 6.9). In fact, the small E_g peak at $\sim 200 \text{ cm}^{-1}$ is clearly visible here. This favorable spectrum endorses our

technique since the nanopowder collected at the substrate is characterized post-experiment as anatase using both XRD (Fig. 6.10) and Raman. Additionally, *in-situ* TEM sampling at locations near the substrate also confirm the anatase phase (Fig. 6.11).

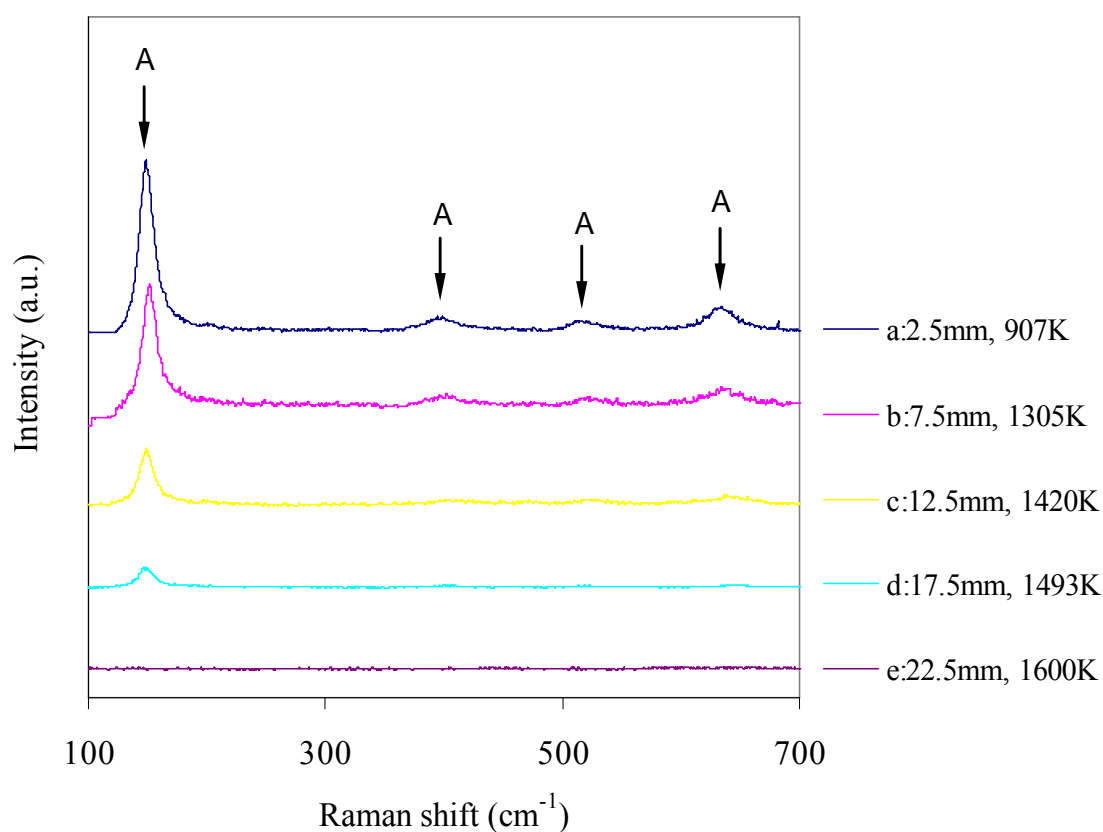


Figure 6.9. *In-situ* Raman spectra of TiO_2 nanoparticles formed during low-pressure premixed flame synthesis (see Fig. 6.8), along the axial centerline at different distances from the substrate (0mm). Burner exit is located at 40mm. Gas-phase temperature is given and made by LIF on OH. Figure shows the increasing anatase content as the nanoparticles approach the substrate.

In Figure 6.10, the phases and the crystallinity of the as-synthesized TiO_2 nanoparticles are identified by XRD. From the relative intensities of the primary peaks shown in XRD pattern (Fig. 6.10), the rutile phase (primary peak at (110)) is determined to be less than 5% weight fraction of the produced powders.

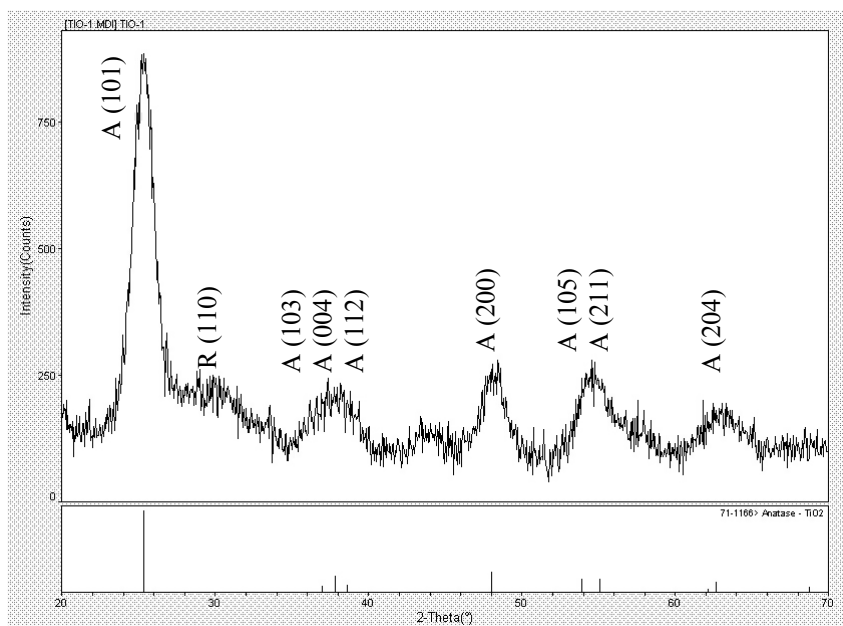


Figure 6.10. XRD of TiO_2 (A for anatase, R for rutile) (From Ref. 51)

The morphologies of the nanoparticles can be revealed by TEM imaging as shown in Fig. 6.11. Here, the nanoparticles appear to be compact and almost spherical. A statistical evaluation of ~ 50 particles from the TEM images gives a narrow primary particle size distribution, with an average primary particle size of 6.09 nm. The SAD ring pattern (inset of Fig. 6.11) matches all of the peaks obtained from the XRD pattern, confirming that the TiO_2 nanoparticles are polycrystal anatase.

However, the present “direct” measurement cannot quantitatively deduce the relative degree of crystallization because the spectral intensities (i.e. peak height or integration of peak area) have not been normalized. Additional studies are needed to calibrate spectral intensity with respect to particle size (aggregate and primary), shape, and concentration. The flame environment and particle dynamics make this a non-trivial task.

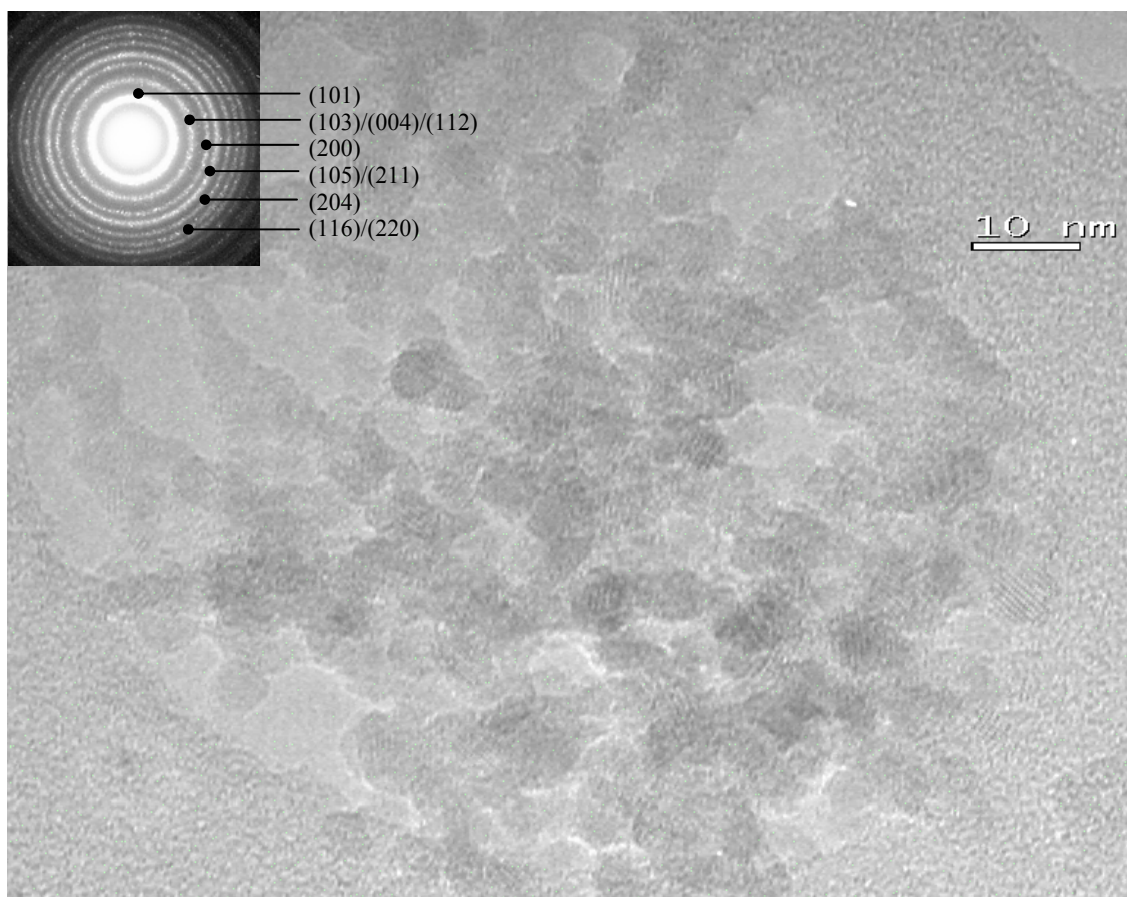


Figure 6.11 TEM image of TiO₂ nanoparticles and the insert showing the SAD pattern (From Ref. 51)

Elastic laser light scattering (LLS) is employed to identify the presence of particles, which Raman cannot conclusively substantiate unless they are crystalline in nature. Additionally, LLS can be used to infer local particle size (d) and number density (N) [4] because light scattering intensity varies as Nd . In conjunction with measurements of aggregate particle size d from *in-situ* PSD characterization using nano-SMPS sampling⁵¹, a relative number density profile can be extrapolated. Much lower laser energy of 5 mJ/pulse is used for excitation, with the Rayleigh scatter collected at 90°. The

spectrometer grating is centered at 532nm with the Raman notch filter removed from the system.

Figure 6.12 shows that the particle-scattering signal rises to a maximum value within 5mm of the burner exit and then stays somewhat constant until it begins to decay on approaching the substrate. Using the nano-SMPS data for the aggregate particle size d , along with the computational results from the sectional particle growth model, we calculate a relative number density profile (Fig. 6.12). Thus the low LLS intensity near the substrate does not denote the absence of nanoparticles (which the Raman technique evinces are present), but simply reflects the diminishing number density of nanoparticles due to the radial divergence of the streamlines in the stagnation-point flow field.

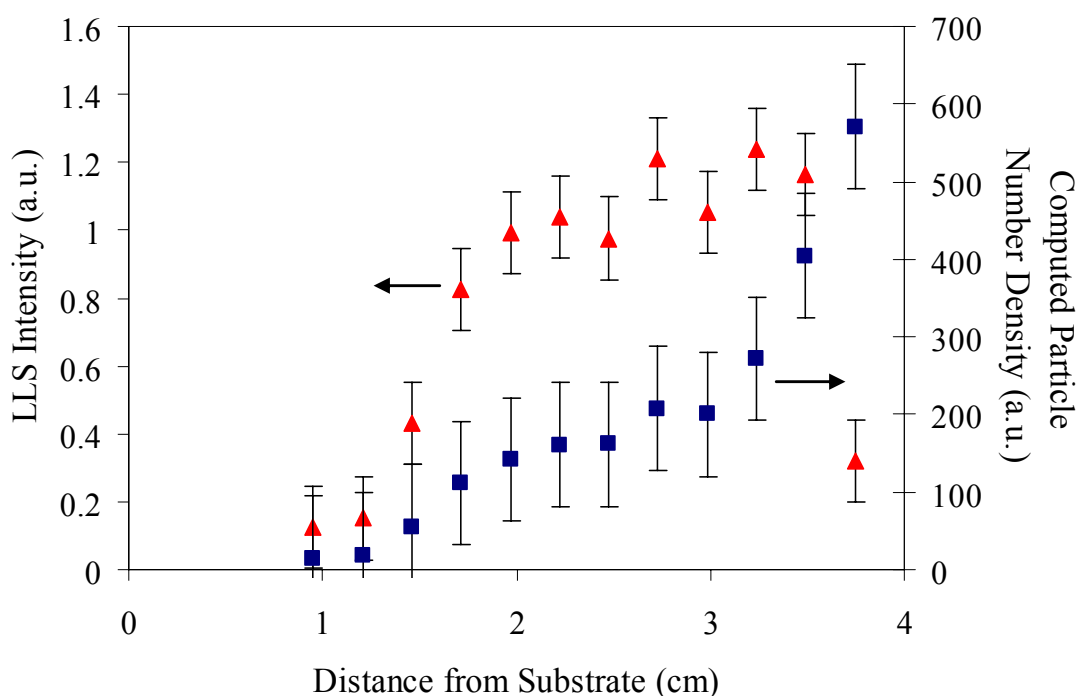


Figure 6.12. Elastic laser light scattering from nanoparticles synthesized in the flame, as a function of distance from the substrate. Burner exit is located at 4cm. A relative number density is computed using nano-SMPS data for the aggregate particle size.

The agreeing sectional model and nano-SMPS results, along with the LLS data, suggest that significant TTIP decomposition and nanoparticle formation occurs near the burner at the beginning of the flow field. However, as mentioned above, the *in-situ* Raman spectra of TiO₂ nanoparticles in Fig. 6.9 do not divulge anatase phases within the TiO₂ nanoparticles until half way to the substrate, with increasing crystallinity upon approaching it. Therefore, although nanoparticle nucleation occurs almost from the beginning, the synthesized nanoparticles are amorphous. Amorphous particles are formed very fast, explaining the sharp rise in LLS (Fig. 6.12) intensity near the burner exit. However, the particles are not identifiable by Raman spectroscopy, until they experience the transformation to crystalline form. Anatase crystallization kinetics is a relatively fast process at low temperature⁵², which has been shown to take 12-30ms in our flame synthesis system⁶. Figure 6.13 plots computed particle residence time, along with temperature, as a function of location between the substrate and burner. It is seen that 12ms particle residence time for our synthesis condition corresponds to a location of ~5mm from the substrate. This finding is in accord with the Raman data of Fig. 6.9, where full anatase crystallization is shown to occur within ~7.5mm of the substrate. Furthermore, as expected, rutile is excluded in our synthesis condition, unlike that for the particle-seeded diffusion flame used for validation. Formation of rutile from anatase requires about one second of residence time at 1473K⁵³. Consequently, the low temperature history and the short characteristic residence time (12-30ms) in this flame synthesis condition are the reasons for the absence of rutile and the dominance of anatase. As evidenced, our *in-situ* Raman technique captures properly the crystallization progress of synthesized nanoparticles in-flight during flame synthesis (Fig. 6.9).

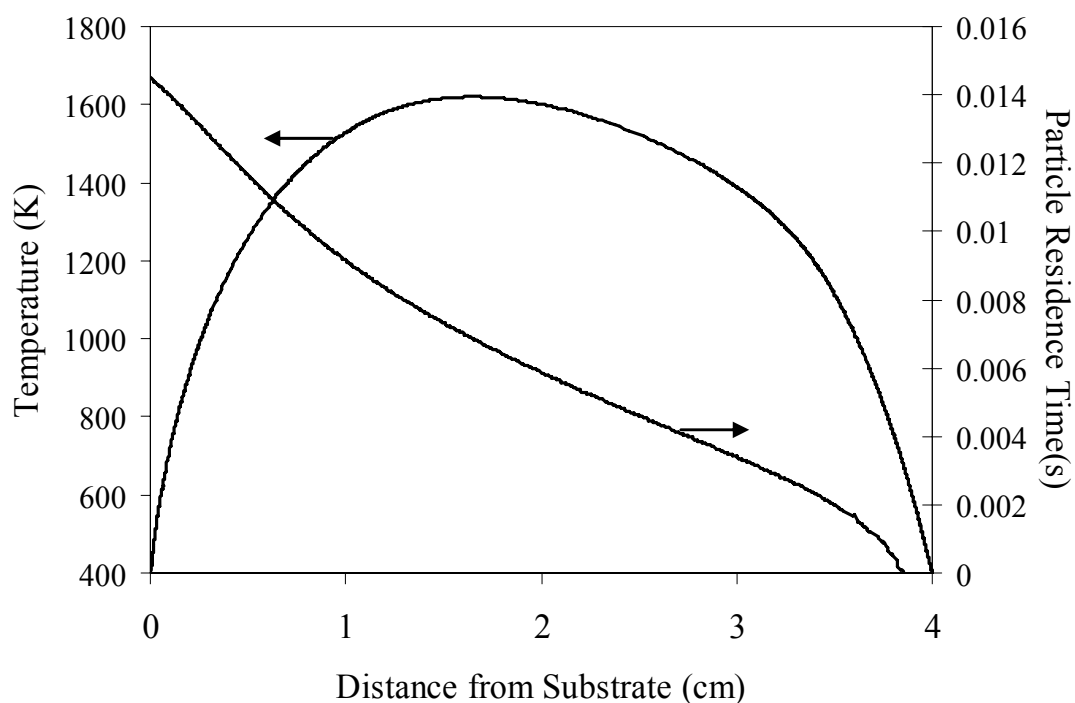


Figure 6.13. Computed particle residence time and temperature between the substrate and burner.

6.5 Error Analysis

The quantitative results in this chapter are mainly related to the temperature measurements by N_2 SRS (Section 6.2.2) and TiO_2 particle number density results by LLS (Section 6.4.2). It has been analyzed that the uncertainty in temperature measurement is mainly due to the system error, which relates to the least-square fitting technique. Again, the uncertainty in the fitted temperature is less than $\pm 50K$, and the reproducibility of the measurements is within $\pm 20K$.

The uncertainty in TiO_2 particle number density can be deduced by the individual uncertainty of LLS intensity (I) and local particle size (d). It has been discussed in

Section 6.4.2, LLS infers local particle size (d) and number density (N), *i.e.*, $I \propto Nd$.

From the propagation of the uncertainty,

$$\frac{\Delta N}{N} = \sqrt{\left(\frac{\Delta I}{I}\right)^2 + \left(\frac{\Delta d}{d}\right)^2} \quad (6.3)$$

if we estimate the relative uncertainties of LLS intensity and local particle size both are 5%, the relative uncertainty of calculated number density will be 7%. As a practical consideration, there are larger errors for lower LLS intensity and smaller particle size measurements. A careful way for the estimation is to use maximum absolute uncertainty in all measurement point as the overall uncertainty for all. The error analysis results have been shown in Figure 6.12.

6.6 Conclusions

In-situ Raman scattering has been employed to characterize particle crystallinity (e.g. anatase titania, α -alumina) and delineate phase conversion within nano-aerosols at high temperatures. The reliability and precision of the technique are demonstrated using a nanoparticle-seeded jet diffusion flame at atmospheric pressure and a nanoparticle-synthesizing premixed stagnation-point flame at low pressure. Concurrent use of gas-phase SRS or LIF provides correlation with local gas-phase temperatures. Ongoing work involves assessing the particle temperature (which may or may not differ from the gas-phase temperature) by using the Stokes/anti-Stokes Raman intensity ratio for the nanoparticles themselves. Combined with other *in-situ* diagnostics, mapping of chemical species concentrations, quantitative determination of thermodynamic properties and assessment of nanoparticle properties are made possible to properly characterize material processing flow fields. Such explicit information is essential for the modeling of

governing mechanisms, along with detailed computational simulation for quantitative realism, fundamental understanding, and predictive capability. Particularly innovative, our diagnostic technique has the potential to be used as an online diagnostic in large-scale synthesis facilities to monitor nanoparticle properties so that process conditions can be actively adjusted through real-time feedback, ensuring high-purity yields of materials with specific user-defined properties.

Another application of *in-situ* Raman scattering will be shown in Chapter 6, where nitride-based (non-oxide) nanomaterials, e.g. cubic boron nitride (*c*-BN), is produced by an inductively coupled RF plasma. *In-situ* Raman scattering is applied in the post-plasma synthesis region to monitor the synthesis process of *c*-BN. Again, same-point gas-phase temperature is measured by examining the rot-vibrational Raman spectrum of N₂ there.

References

- ¹ X. Liu, M. Smith, and S.D. Tse, In-Situ Raman Characterization of Nanoparticle Aerosols during Flame Synthesis, submitted to *Applied Physics B* (2009).
- ² S. E. Pratsinis, Flame aerosol synthesis of ceramic powders, *Progress in Energy and Combustion Science* 24, 197 (1998).
- ³ M. S. Wooldridge, Gas-phase combustion synthesis of particles, *Progress in Energy and Combustion Science* 24, 63 (1998).
- ⁴ N.G. Glumac, Y.J. Chen, and G. Skandan, Diagnostics and modeling of nanopowder synthesis in low pressure flames, *Journal of Materials Research* 13, 9, 2572-2579 (1998).
- ⁵ Zhao, H., Liu, X., and Tse, S.D., Control of Nanoparticle Size and Agglomeration through Electric-Field-Enhanced Flame Synthesis, invited paper, *Journal of Nanoparticle Research* 10, 907-923 (2008).
- ⁶ H. Zhao, X. Liu, and S. D. Tse, Effects of pressure and precursor loading in the flame synthesis of Titania Nanoparticles, *Journal of Aerosol Science*, In Press (available online 6 Aug 2009).
- ⁷ F. Xu, X. Liu, and S.D. Tse, Synthesis of Carbon Nanotubes on Metal Alloy Substrates with Voltage Bias in Methane Inverse Diffusion Flames, *Carbon* 44, 570-577 (2006).
- ⁸ F. Xu, H. Zhao, and S.D. Tse, Carbon Nanotube Synthesis on Catalytic Metal Alloys in Methane/Air Counterflow Diffusion Flames, *Proceedings of the Combustion Institute* 31, 1839-1847 (2007).
- ⁹ F. Xu, X. Liu, and S.D. Tse,, F. Cosandey, and B.H. Kear, Flame Synthesis of Zinc Oxide Nanowires, *Chemical Physics Letters* 449, 175-181 (2007).
- ¹⁰ P.W. Morrison, et al., *In Situ* Fourier Transform Infrared Characterization of the Effect of Electrical Fields on the Flame Synthesis of TiO₂ Particles, *Chem. Mater.* 9, 2702-2708 (1997).
- ¹¹ G. Beaucage, Probing the Dynamics of Nanoparticle Growth in a Flame using Synchrotron Radiation, *Nature Materials* 3, 370 – 373 (2004).

- ¹² Y. Xing, et al., *In Situ* Light-Scattering Measurements of Morphologically Evolving Flame-Synthesized Oxide Nanoaggregates, *Appl. Opt.* 38, 2686-2697 (1999).
- ¹³ D. Mukherjee, A. Rai, and M.R. Zachariah, Quantitative laser-induced breakdown spectroscopy for aerosols via internal calibration: Application to the oxidative coating of aluminum nanoparticles, *Journal of Aerosol Science* 37, 6, 677-695 (2006).
- ¹⁴ S. Maffi, F. Cignoli, C. Bellomunna, S. De Iuliisa, and G. Zizak, Spectral effects in laser induced incandescence application to flame-made titania nanoparticles, *Spectrochimica Acta Part B: Atomic Spectroscopy* 63, 2, 202-209 (2008).
- ¹⁵ L. S. Hsu and C. Y. She, Real-time monitoring of crystallization and structural transformation of titania films with Raman spectroscopy, *Opt. Lett.* 10, 638 (1985).
- ¹⁶ C. R. Aita, Raman scattering by thin film nanomosaic rutile TiO₂, *Appl. Phys. Lett.* 90, 213112 (2007).
- ¹⁷ M.P. Moret, R. Zallen, D.P. Vijay, S.B. Desu, Brookite-rich titania films made by pulsed laser deposition, *Thin Solid Films* 366, 8-10 (2000).
- ¹⁸ I. De Wolf, Micro-Raman spectroscopy to study local mechanical stress in silicon integrated circuits, *Semicond. Sci. Technol.* 11, 139-154 (1996).
- ¹⁹ Z.L. Wang, *Characterization of nanophase materials* (Wiley-VCH, 2000).
- ²⁰ W. Ma, Z. Lu, and M. Zhang, Investigation of structural transformations in nanophase titanium dioxide by Raman spectroscopy, *Applied Physics A: Materials Science & Processing* 66, 621 (1998).
- ²¹ D. Bersani, P.P. Lottici, and X.Z. Ding, Phonon confinement effects in the Raman scattering by TiO₂ nanocrystals, *Appl. Phys. Lett.* 72, 73 (1998).
- ²² M.J. Scepanovic, M. Grujic-Brojcic, Z.D. Dohcevic, and Z.V. Popovic, Temperature dependence of the lowest frequency Eg Raman mode in laser-synthesized anatase TiO₂ nanopowder, *Applied Physics A* 86, 365 (2007).
- ²³ S.-M. Oh and T. Ishigaki, Preparation of pure rutile and anatase TiO₂ nanopowders using RF thermal plasma, *Thin Solid Films* 457, 186-191 (2004).
- ²⁴ S. R. Emory and S. Nie, Near-Field Surface-Enhanced Raman Spectroscopy on Single Silver Nanoparticles, *Analytical Chemistry* 69, 2631-2635 (1997).
- ²⁵ M.S. Dresselhaus, G. Dresselhaus, G. Saito, and R. Jor, Raman spectroscopy of carbon nanotubes, *Physics Reports* 409, 47-99 (2005).
- ²⁶ D.S. Bethune, G. Meijer, W.C. Tang, H.J. Rosen, The vibrational Raman spectra of purified solid films of C60 and C70, *Chemical Physics Letters* 174, 219-222 (1990).
- ²⁷ N. Everall, J. B. King, and I. Clegg, The Raman effect, *Chemistry in Britain* 36, 40 (2000).
- ²⁸ S.K. Sharma, S.M. Angel, M. Ghosh, H.W. Hubble, and P.G. Lucey, Remote Pulsed Laser Raman Spectroscopy System for Mineral Analysis on Planetary Surfaces to 66 Meters, *Applied Spectroscopy* 56, 699 (2002).
- ²⁹ R. J. Hall and L. R. Boedeker, CARS thermometry in fuel-rich combustion zones, *Appl. Opt.* 23, 1340-1346 (1984).
- ³⁰ R. L. Farrow, R. P. Lucht, G. L. Clark, and R. E. Palmer, Species concentration measurements using CARS with nonresonant susceptibility normalization, *Appl. Opt.* 24, 2241-2251 (1985).
- ³¹ A. K. Misra, S. K. Sharma, and P. G. Lucey, Single pulse remote Raman detection of minerals and organics under illuminated condition from 10 meters distance, *Lunar and Planetary Science XXXVI* (2005).
- ³² A. Li Bassi, et al., Raman spectroscopy characterization of titania nanoparticles produced by flame pyrolysis: The influence of size and stoichiometry, *Journal of Applied Physics* 98, 074305 (2005).
- ³³ W. F. Zhang, Y. L. He, M. S. Zhang, Z. Yin, and Q. Chen, Raman scattering study on anatase TiO₂ nanocrystals, *Journal of Physics D: Applied Physics* 33, 912-916 (2000).
- ³⁴ C. Pighini, D. Aymes, N. Millot, and L. Saviot, Low-frequency Raman characterization of size-controlled anatase TiO₂ nanopowders prepared by continuous hydrothermal syntheses, *Journal of Nanoparticle Research* 9, 309-315 (2007).
- ³⁵ T. Ohaka, Temperature Dependence of the Raman Spectrum in Anatase TiO₂, *J. Phys. Soc. Jpn.* 48, 1661 (1980).
- ³⁶ S. P. S. Porto, P. A. Fluery, and T. C. Damen, Raman Spectra of TiO₂, MgF₂, ZnF₂, FeF₂, and MnF₂, *Phys. Rev.* 154, 522 (1967).
- ³⁷ P.P. Lottici, D. Bersani, M. Braghini, and A. Montenero, Raman scattering characterization of gel-derived titania glass, *J. Mater. Sci.* 28, 177 (1993).

-
- ³⁸ Y. Hara and M. Nicol, Raman spectra and the structure of rutile at high pressures, *Phys. Status Solid B* 94, 317 (1979).
- ³⁹ U. Balachandran and N. G. Eror, Raman spectra of titanium dioxide, *J. Solid State Chem.* 42, 276 (1982).
- ⁴⁰ C. A. Melendres, A. Narayanasamy, V. A. Maroni, and R. W. Siegel, Raman spectroscopy of nanophase TiO_2 , *J. Mater. Res.* 4, 1246 (1989).
- ⁴¹ A. Mortensen *et al.*, Raman spectra of amorphous Al_2O_3 and $\text{Al}_2\text{O}_3/\text{MoO}_3$ obtained by visible and infrared excitation, *J. Raman Spectrosc.* 22, 47 (1991).
- ⁴² A. Misra, *et al.*, Thin film of aluminum oxide through pulsed laser deposition: a micro-Raman study, *Mater. Sci. Eng. B* 79, 49 (2001).
- ⁴³ R. Krishnan *et al.*, Raman spectroscopic and photoluminescence investigations on laser surface modified $\alpha\text{-Al}_2\text{O}_3$ coatings, *Scripta Materialia* 48, 1099 (2003).
- ⁴⁴ R. Lewis and H. G. M. Edwards, *Handbook of Raman spectroscopy: from the research laboratory to the process line* (Marcel Dekker, 2001).
- ⁴⁵ C. Eckbreth, *Laser diagnostics for combustion temperature and species* (Gordon and Breach Publishers, 1996).
- ⁴⁶ N. Everall, T. Hahn, P. Matousek, A. W. Parker, and M. Towrie, Picosecond Time-Resolved Raman Spectroscopy of Solids: Capabilities and Limitations for Fluorescence Rejection and the Influence of Diffuse Reflectance, *Applied Spectroscopy* 55, 1701 (2001).
- ⁴⁷ V. Swamy, A. Kuznetsov, L.S. Dubrovinsky, R.A. Caruso, D.G. Shchukin, and B.C. Muddle, Finite-size and pressure effects on the Raman spectrum of nanocrystalline anatase TiO_2 , *Phys. Rev. B* 71, 184302 (2005).
- ⁴⁸ S. Cava, *et al.*, Structural and spectroscopic analysis of $\gamma\text{-Al}_2\text{O}_3$ to $\alpha\text{-Al}_2\text{O}_3\text{-CoAl}_2\text{O}_4$ phase transition, *Materials Chemistry and Physics* 97, 102-108 (2006).
- ⁴⁹ S. Cava, *et al.*, Structural characterization of phase transition of Al_2O_3 nanopowders obtained by polymeric precursor method, *Materials Chemistry and Physics* 103, 394-399 (2007).
- ⁵⁰ J.P. Holman, *Heat Transfer* (McGraw-Hill 1989).
- ⁵¹ H. Zhao, Experimental and computational studies of flame synthesis of nanoparticles: Effects of pressure, precursor loading, and electric field, Ph.D Thesis, Rutgers University (2007).
- ⁵² A.J. Rulison, P.F. Miquel, and J.L. Katz, Titania and silica powders produced in a counterflow diffusion flame, *J. Mater. Res.* 11, 12, 3083 (1996).
- ⁵³ R. D. Shannon, and J. A. Pask, Topotaxy in the anatase-rutile transformation, *Am. Mineral.* 49, 11-12, 1707 (1964).

Chapter 7

Application of *In-Situ* Raman Spectroscopy to Study the Plasma Synthesis of Cubic Boron Nitride Nanoparticles

In Chapters 3 and 5, *in-situ* spontaneous Raman spectroscopy (SRS) was employed to measure gas-phase chemical species and thermodynamic properties and to diagnose solid-phase nanomaterials, in flame environments. In this chapter, SRS measurements are extended to characterize Group-III-Nitride nanoparticles (i.e. cubic boron nitride) synthesized in an inductively coupled RF plasma reactor in a stagnation-point geometry. A brief overview of synthesis methods and diagnostics techniques is provided. Raman spectroscopy is applied for both *ex-situ* and *in-situ* characterizations of as-synthesized *c*-BN nanopowders, as well as to determine gas-phase temperatures near the cold substrate.

As stated in the Preface, some of the content of this chapter appears verbatim from a published conference proceedings paper¹, which includes co-authors.

7.1 Introduction

III-Nitride materials, e.g., cubic boron nitride or *c*-BN, gallium nitride and aluminum nitride, have potential as hosts for high-power laser gain media. This type of polycrystalline material, with high thermal conductivities, hardnesses, and radiative and chemical stabilities, make the fabrication of high energy solid-state lasers possible.

Studies have involved the synthesis of GaN^{2,3}, AlN^{4,5}, and *c*-BN^{6,7,8,9} materials. Those synthesis methods can be divided into two categories, physical vapor deposition (PVD) and chemical vapor deposition (CVD)²⁴. PVD methods include electron beam evaporation¹⁰, ion beam deposition¹¹, pulsed laser deposition¹², sputtering¹³, etc. The

CVD method is a practical technique suitable for industry scale-up. There are different types of CVD for the synthesis of *c*-BN, e.g., plasma-assisted CVD^{6,7}, metal-organic CVD without use of plasma¹⁴, low pressure CVD¹⁵, thermal-heating CVD¹⁶, etc. Specifically, for *c*-BN, the most often used energetic synthesis technique is plasma-assisted chemical vapor deposition (PACVD). During the synthesis process, both B and N ions from a microwave (2.45 GHz) or RF (13.56 MHz) plasma are deposited to a biased substrate. Several kinds of source/carrier gases have been used, including B₂H₆ in N₂¹⁷ or NH₃¹⁸, BH₃-NH₃ in H₂¹⁹, BF₃ in N₂+H₂^{6,7}, etc.

In this work, the *c*-BN powders are synthesized using a novel, aerodynamically-enhanced plasma process. Plasma is a hot, partially ionized gas, with significantly higher gas temperatures and less reactive chemical environments compared to flames. The plasmas are energized with high-frequency electromagnetic fields (e.g. RF or microwave energy) or with direct current. The inductively coupled RF plasma is the most prevalent and is used in our gas-phase synthesis studies. Cases where rare earth (RE), e.g. Er, Nd, Yb, is doped directly during the plasma synthesis process are also investigated. Although not addressed in this thesis, both powders and ceramic pellets are characterized spectroscopically for photoluminescence, absorption/emission characteristics, and emission life times.

Similar to the flame studies, to better understand the fundamental mechanisms of the processes involved, *in-situ* laser-based diagnosis of the gas-phase flow field and as-synthesized nanoparticles are needed. Various techniques have been used for the *in-situ* study of the materials produced in such high-temperature environments. For example, *in situ* FTIR reflection spectroscopy is sensitive enough to determine the phase of the

growing film due to the different phonon absorption frequencies of hexagonal BN (*h*-BN) and *c*-BN²⁰. Electron energy loss spectroscopy (EELS) has been used to study the *c*-BN film composition and electronic properties *in situ*²¹. As mentioned in Chapter 5, laser-induced breakdown spectroscopy (LIBS) has been used to characterize particle composition²², and laser-induced incandescence (LII) has been used to measure nanoparticle size²³. For gas-phase *in-situ* diagnostics, it is still feasible to apply LIF and SRS to monitor both the temperature and chemical species in the flow field. As shown in the preceding chapter, *in-situ* Raman scattering can be a powerful tool to determine the composition and crystallinity of the as-synthesized nanoparticles.

7.2 Experiment Arrangement

7.2.1 *In-situ* Spontaneous Raman Scattering Setup

Raman spectroscopy is applied to the present study of BN nanoparticles during plasma synthesis, with the same configuration as that used for *in-situ* Raman scattering of TiO₂ during flame synthesis (please see the previous chapter). Gas-phase temperatures, using SRS, are measured only near the substrate where atomic N has recombined to form N₂. A “relatively” short signal collection time (30s) is sufficient for each measurement location, indicating the possibility of using the technique as an online diagnostic.

7.2.2 Gas-phase SRS

Again, we determine the gas-phase temperatures from the shapes of the N₂ Raman spectra. Details are the same as that described in previous chapters.

7.2.3 *c*-BN nanoparticle SRS

Boron nitride has been widely studied by Raman spectroscopy. Boron nitride displays four primary crystal structures, including two diamond-like sp^3 -bonded phases (cubic boron nitride, *c*-BN, and wurtzitic boron nitride, *w*-BN), two graphite-like sp^2 -bonded phases (hexagonal, *h*-BN, and rhombohedral boron nitride, *r*-BN)²⁴. Another “turbostratic” boron nitride (*t*-BN) is a disordered phase.

The main Raman peak of *h*-BN appears at 1306 cm^{-1} (LO mode)^{25, 26} as representative of sp^2 hybridized, planar bonding. The structure of *c*-BN belongs to the face-centered-cubic lattice with space-group $F\bar{4}3m$, consisting of highly covalent B-N bonds. Its Raman spectrum has two strong peaks: the Brillouin zone center transverse optical mode (TO) at 1054 cm^{-1} and the longitudinal-optical mode (LO) at 1367 cm^{-1} , as representative of sp^3 tetrahedral bonding^{27,28}. The relative intensity of the TO and LO modes for *c*-BN can vary as BN has strong Raman anisotropy²⁹. The intensity of the LO line relative to the TO line varies with excitation wavelength due to resonance effects and with polarization angle of the laser and analyzer. Furthermore, the phonon spectra depend somewhat on the process used to fabricate the *c*-BN powders³⁰. Nevertheless, the TO mode of *c*-BN and the LO mode of *h*-BN can be used as “signature” of their corresponding phases (Figure 7.1)³².

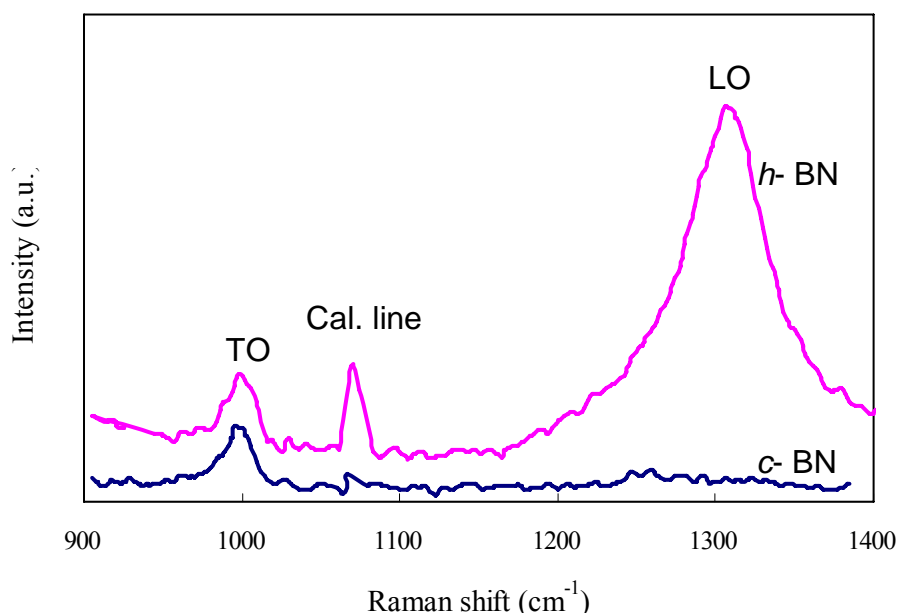


Figure 7.1. TO mode of *c*-BN and the LO mode of *h*-BN Raman spectra. (Reproduced from Ref. 32)

In this work, Raman scattering of boron nitride particles is excited by using low excitation power. The objective is to discriminate the different phases of boron nitride as the particles are synthesized.

7.2.4 *c*-BN Nanoparticle Plasma Synthesis Setup

Figure 7.3 shows the plasma setup used for the synthesis of *c*-BN nanopowders. The setup is contained in a stainless steel chamber filled with nitrogen at atmospheric pressure. The chamber has two quartz windows for the laser beam to enter and the Raman signal to be collected. The plasma setup itself consists of a quartz plasma torch with a diameter of 2.5 cm, encompassed by a silver radio frequency (RF) coil. An RF plasma generator (Seren II600, 40 MHz) provides the power to the coil through a matching network. The output power is adjustable from 0 to 1.5 kilowatts. Argon (ultra high purity, 99.9%, Airgas) is used as the plasma and sheath/auxiliary gas. The precursor, borane-ammonia

(90%, Aldrich, USA), is heated and sublimed in a bubbler outside the chamber, and then transported into the plasma region by a nitrogen carrier gas. The cold substrate is an aluminum plate with dimension of $15.4 \times 9.2 \times 1.2 \text{ cm}^3$ and is placed below the plasma torch with a distance of 6.50 cm. During the experiments, the RF coil and deposition plate are always cooled by cold water circulated by a temperature-controlled water bath at 4°C.

The measurement locations for temperature and *c*-BN characterization by SRS are shown in Figure 7.2. The RF ICP plasma can be divided into three different regions for characterization purposes. The highest gas temperature region is in the plasma core, inside the induction coil and extending a few millimeters down. The core region appears as a bright white, nontransparent zone. Spectrally, this core is characterized by an intense continuum and the atomic lines of Ar. Because of the continuum, the core region is of limited analytical utility. A short distance downward, the plasma becomes slightly transparent, and the continuum is greatly reduced. This region extends 1-3 cm below the induction coil and provides the highest S/N ratios for atomic emission spectroscopy. The background consists primarily of Ar lines and some other molecular bands. The next lower region, called “tailflame” region, has lower temperatures similar to those of an ordinary combustion flame. This is the region where we study the formation mechanisms of *c*-BN nanoparticles, and where laser-based spectroscopic techniques can infer useful information for the synthesis process.

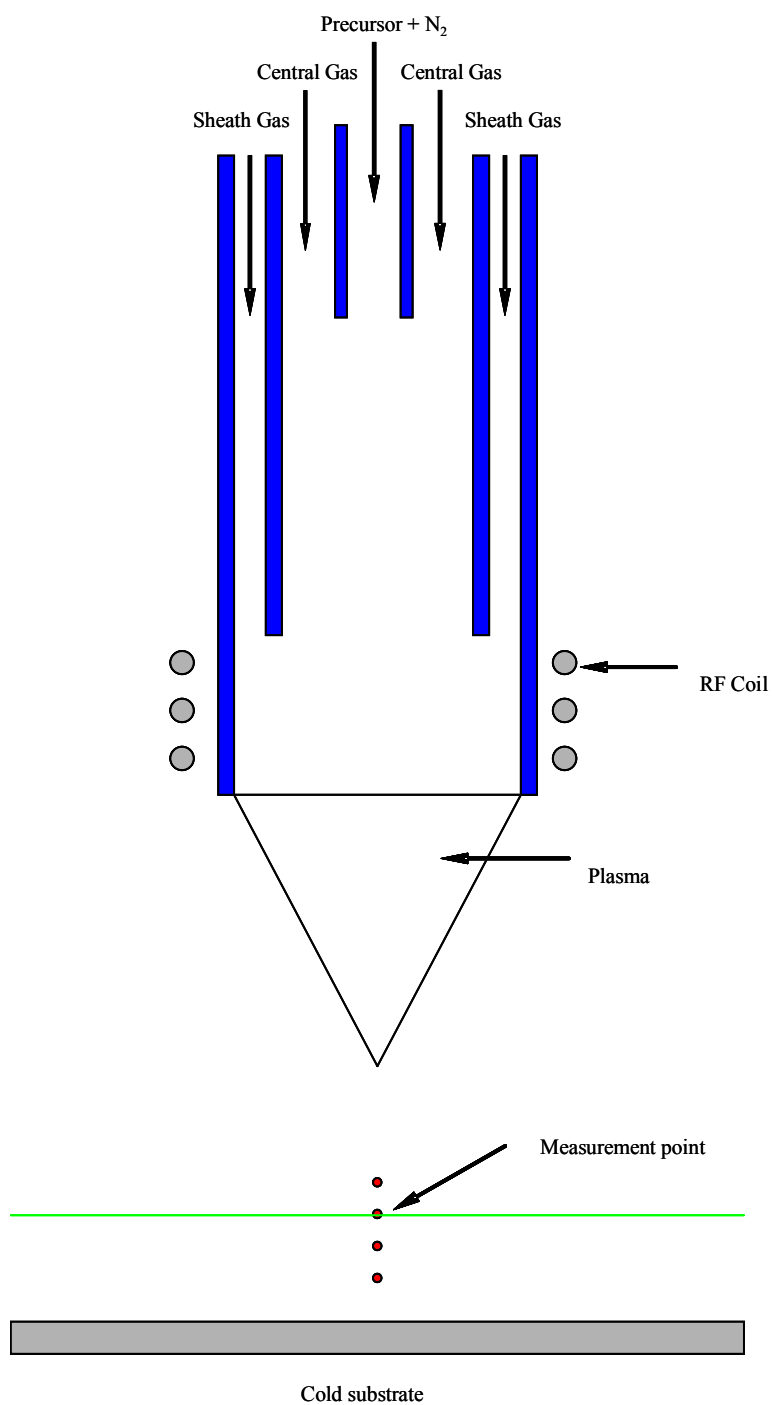


Figure 7.2. The schematic diagram of the r.f. ICP-CVD system inside the plasma chamber measurement locations for temperature and *c*-BN characterization by SRS

7.2.5 *Ex-Situ* *c*-BN nanoparticle characterization on glass slides at room temperature

The setup for the slide configuration is the same as that given in Figure 6.2. The excitation power is kept under 2 mJ/pulse and is monitored using a power meter. The angle of the glass slide (see Fig. 6.2) is also adjusted to ensure that only diffuse scatter from the nanopowder is collected by the Raman system.

The properties of the *c*-BN nanopowders are also obtained *ex situ* using X-ray diffraction (XRD) and transmission electron microscopy (TEM).

7.3 Results and discussion

Formation of boron nitride material by chemical reaction at atmospheric pressure generally yields the hexagonal modification *h*-BN, which may be transformed into small *c*-BN crystallites by using high pressure, high temperature (HPHT) synthesis³¹. In the settings of the r.f. ICP-system, it is necessary to analyze the form of the synthesized BN. We conduct diagnostics and characterization on the material both *in-situ* and *ex-situ*.

7.3.1 *Ex-situ* characterization

As-synthesized nanopowders are collected from the substrate for characterization. Similar to the *ex-situ* testing of TiO₂ in Section 6.2, the nanopowder is tested using Raman on glass slides. A low laser power of 5 mJ/pulse is used for excitation. The Raman spectrum (Figure 7.3) shows a strong peak 1060 cm⁻¹, with FWHM of ~50 cm⁻¹, which corresponds to the TO Raman mode of *c*-BN. The absence of a peak at 1306 cm⁻¹ (corresponding to the *E_g*, or LO mode of hexagonal boron nitride, i.e., *h*-BN) indicates the form of *c*-BN instead of *h*-BN^{32,33}.

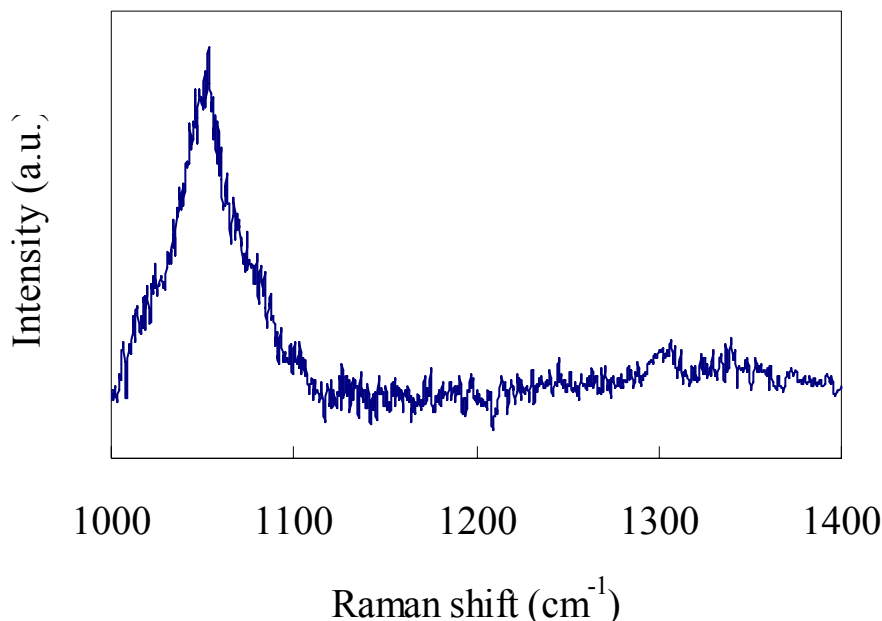


Figure 7.3. Raman spectrum of *c*-BN powder samples on the slides

The FWHM is much larger than that of *c*-BN crystals with the size of $1\text{-}\mu\text{m}$ ³⁴, which is normally $20\text{-}30\text{ cm}^{-1}$. The powder collected from the substrate has been characterized by TEM to obtain the morphologies of the nanoparticles. Fig. 7.4 shows the powders deposited at a generator power of 800 W. It is observed that the powders are composed of many fine particles. Some crystal facets are also observed with the size of 50-100 nm. It is therefore concluded that the broadening of the peak (50 cm^{-1}) is due to the small size of crystallites³⁵.

Further investigations are carried out by XRD measurement. Fig. 7.5 shows the XRD pattern of the same sample in Figs. 7.3 and 7.4. Strong peaks of *c*-BN clearly characterize the cubic phase. The content of *c*-BN in the sample is larger than 95%. Scherer's equation for the broadening of the XRD peaks gives a crystallite size of 40 nm. As a result, the Raman measurements are confirmed, showing that the nanoparticles are metastable *c*-BN in phase.

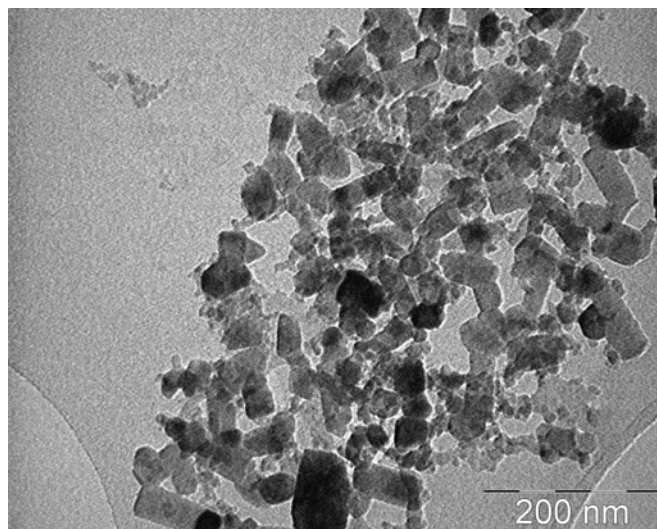
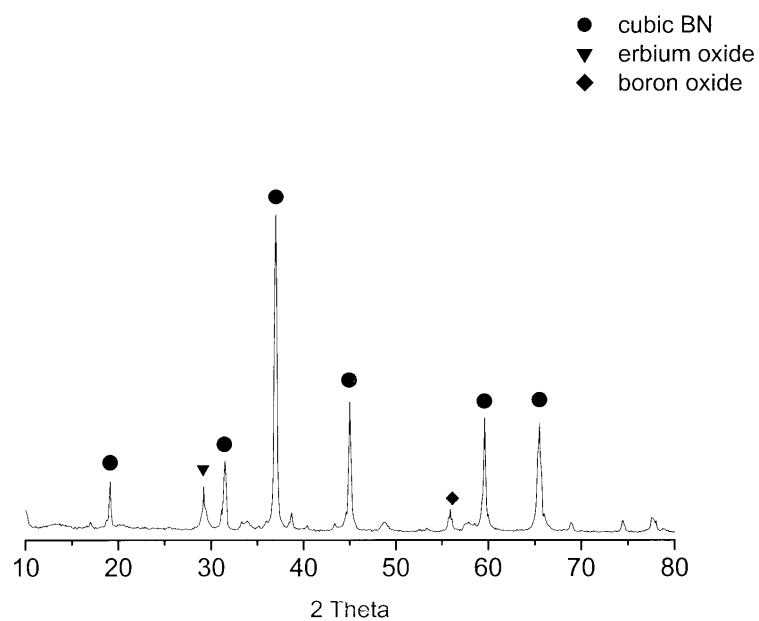


Figure 7.4. TEM image of *c*-BN powders (from Ref.1)



XRD profile of the sample on Sep. 11, 2008.

cBN: >95%
erbium oxide: ~3%
boron oxide: <2%

Figure 7.5. XRD pattern of *c*-BN powders shows the dominant phase of *c*-BN (from Ref. 1)

7.3.2 *In-situ* characterization

Temperature

A steep temperature gradient is crucial for the formation of metastable *c*-BN nanoparticles in our ICP system. The *in-situ* temperature diagnostics are well suited for this measurement.

In-situ diagnostics of gas-phase temperature has been realized in other flame synthesis systems where temperatures range up to 2200K. For our Raman technique, the limit is set by the thermal stability of N₂, the characteristic species for the temperature calculation. Nevertheless, although the plasma can be up to 10,000°C, the nucleation of nanoparticles is at much lower temperatures. As pointed out in Ref. 32 and the references therein, cubic boron nitride is converted to hexagonal form at ~1840 K. Thus, we measure temperatures using Raman starting from the cold substrate, moving upwards toward the plasma until N₂ dissociates. Figure 7.6 shows the temperature profile above the cold substrate but below the hot plasma zone during the synthesis of *c*-BN. The temperature gradient near the substrate can reach 100K/mm.

However, to completely understand the molecular chemistry and particle formation routes, the plasma region (within the flow field) needs to be characterized as well. Of course, spectroscopy-based methods are used most often, as they do not disturb the plasma flow. The intensities of radiation emitted at certain wavelengths are related to temperature and excited level population. There are different types of temperatures defined in a plasma³⁶: for a given species, the Maxwellian distribution defines the translational temperature T_k ; the Boltzmann distribution of two excited levels i and j

defines the excitation temperature T_{ex} ; the mass action law defines the reactional temperature T_{re} , of the concerned species; and Planck's law defines the radiation temperature T_{rad} . Complete thermodynamic equilibrium (CTE) ($T_k = T_{ex} = T_{re} = T_{rad}$) is not realized in laboratory plasmas which are optically thin (Planck's law is not valid). But the mass action law, the Boltzmann distribution and Maxwell distribution may be obeyed by a unique local temperature such that $T_k = T_{ex} = T_{re} = T^{36}$, then one introduces the (complete) local thermodynamic equilibrium (LTE). Due to the complexity of thermodynamic equilibrium in the plasma and given our focus on gas-phase synthesis aspects, temperature measurement is performed in the regions where LTE is realized.

With Argon gas as the major species in the plasma, it is also possible to obtain an excitation temperature of Ar by calculating the relative intensities of argon-ion (ArI) emission lines or the Boltzmann plot³⁷. A sample Ar emission spectrum in the plasma is displayed in Fig. 7.7, where the ratio of emission intensities of transitions can be used to determine temperature^{38,39}. In the so-called line pair intensity ratio method, two lines of the same element in the same ionization state are used. The excitation temperature can be deduced from the ratio of the two line intensities, I_1 and I_2 :

$$T = \frac{1}{k} \frac{(E_1 - E_2)}{\ln\left(\frac{g_1 A_1 \lambda_2}{g_2 A_2 \lambda_1}\right) - \ln\left(\frac{I_1}{I_2}\right)} \quad (7.1)$$

with $k = 0.695 \text{ cm}^{-1} \text{ K}^{-1} = 8.617 \times 10^{-5} \text{ eV K}^{-1}$, and $\ln 10 = 2.302$. E_m , excitation energies, g_m , statistical weights of the upper excited level, and A_{nm} , transition probabilities, are obtained from the literature⁴⁰. The subscripts 1 and 2 refer to the first and second line intensities, respectively.

By selecting the two lines of $\lambda_1 = 603.2128$ nm and $\lambda_2 = 610.5636$ nm from the Ar I emission collected from our plasma, and $g_1=9$; $g_2=5$, $A_1=2.46e+6$ s⁻¹; $A_2=1.21e+6$ s⁻¹, the plasma temperature at 5 cm above the cold substrate is calculated to be 6233 K.

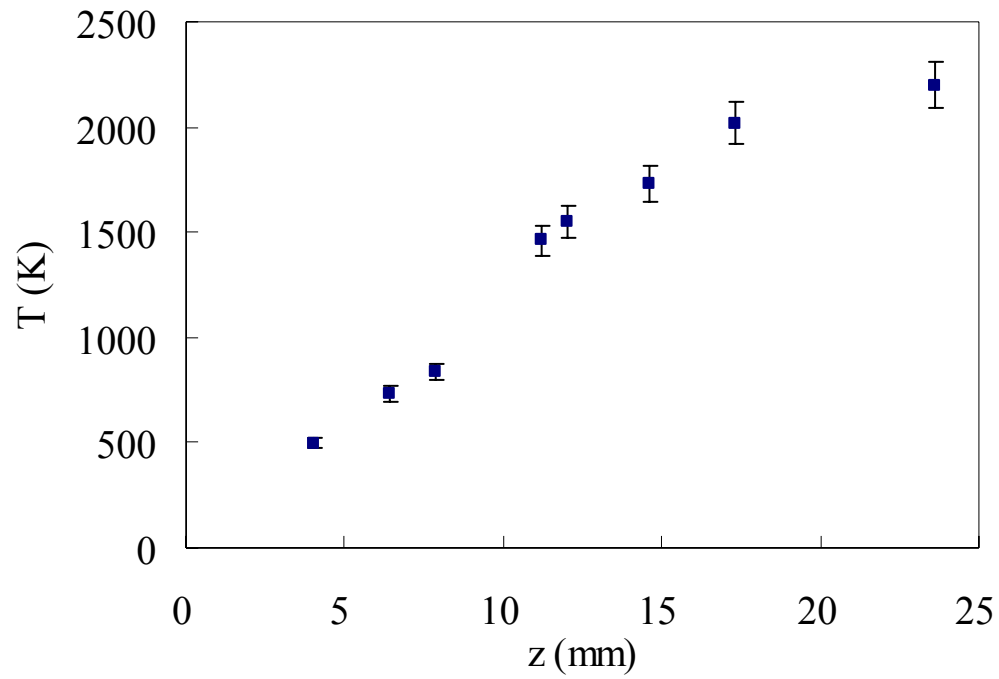


Figure 7.6. Temperature measurements in post-plasma region using SRS of N₂

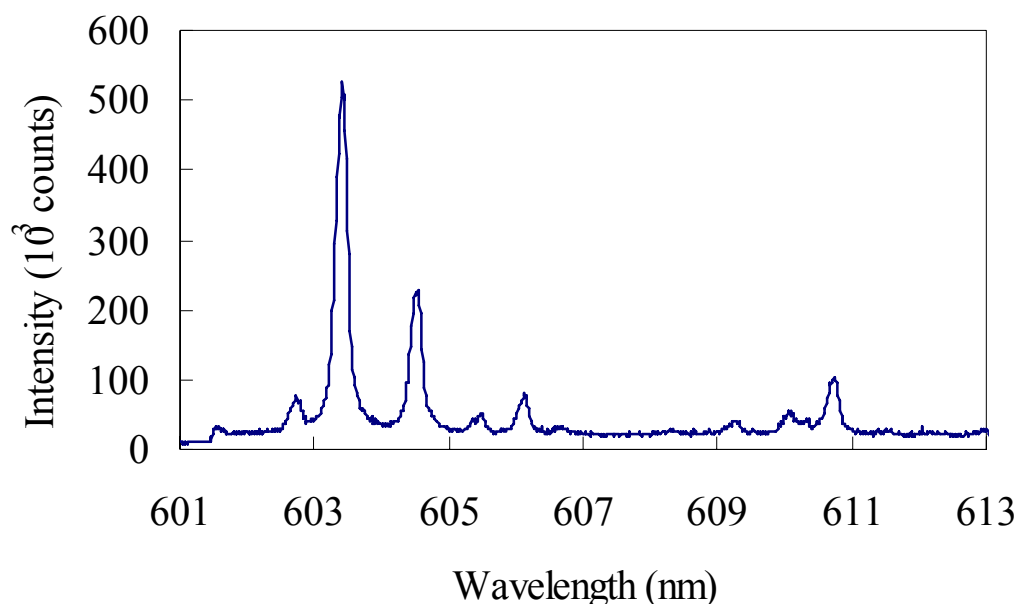


Figure 7.7. Ar I emission lines in plasma region at 5cm above the cold substrate.

***c*-BN nanopowders**

From a preliminary study of *in-situ* Raman characterization of the plasma system, *c*-BN nanoparticles are detected in the regions near the cold substrate. Close to the substrate, two Raman spectra show noticeable peaks at 1087 cm^{-1} and 1098 cm^{-1} , respectively, at two positions (point a and b in Fig. 7.8, which are 6.4 mm and 12.0 mm above the substrate), where *c*-BN is detected at gas-phase temperatures of 730 K and 1547 K, respectively (Fig. 7.6). Probing higher upstream, no obvious peaks in the spectra (not shown in the plot) can be detected in our system.

The Raman peak of 1087 cm^{-1} at point a (closest to the substrate) is well defined, indicating good crystallinity, and corresponds to the TO active mode of *c*-BN^{31,32,33,34}. The peak also has a broad FWHM of 70 cm^{-1} , mainly due to the relatively high

temperature (730 K gas-phase temperature). At point b, which is closer to the plasma (gas-phase temperature is 1547 K), the spectrum displays a less pronounced peak at 1098 cm^{-1} . From point a to point b, with the increased temperatures, a Stokes Raman shift towards larger wavenumbers (red shift) is observed (Fig. 7.8). This is consistent with what we found for TiO_2 in the previous chapter, where for the Stokes spectra, there was a red shift towards larger wavenumbers due to elevated temperatures. However, for *c*-BN single crystals, an opposite trend of Raman shift with the temperature is found in the literature⁴¹. For example, the temperature dependence of *c*-BN Raman lines, as studied by Herchen and Cappelli³², was found to blue shift (for the Stokes Raman) 1060 cm^{-1} at room temperature to about 1000 cm^{-1} at 1700K. This discrepancy with our results, as well as with our anatase titania results from the previous chapter, needs to be resolved.

One of the possible reasons for the discrepancy is the laser heating effect on the Raman spectra. The laser energy used for this experiment ($>10\text{mJ/pulse}$) is much larger than that for TiO_2 ($<6.5\text{mJ/pulse}$, Chapter 6). The larger particles near the substrate move slower, with more heating time. Larger volume also makes heat accumulation in the particles more likely. These factors may give the powders near the substrate (point a) a higher temperature than point b, making the Raman shift at point a with a smaller Raman shift.

It is then concluded that the forming of *c*-BN actually starts from the point b. The Raman peaks observed in the range of 1000 cm^{-1} to 1400 cm^{-1} are all belong to *c*-BN. There is no peak corresponding to *h*-BN in the same region, which should be around 1306 cm^{-1} as indicated by literature³². This indicates that our synthesis conditions using ICP plasma are favorable for forming metastable *c*-BN.

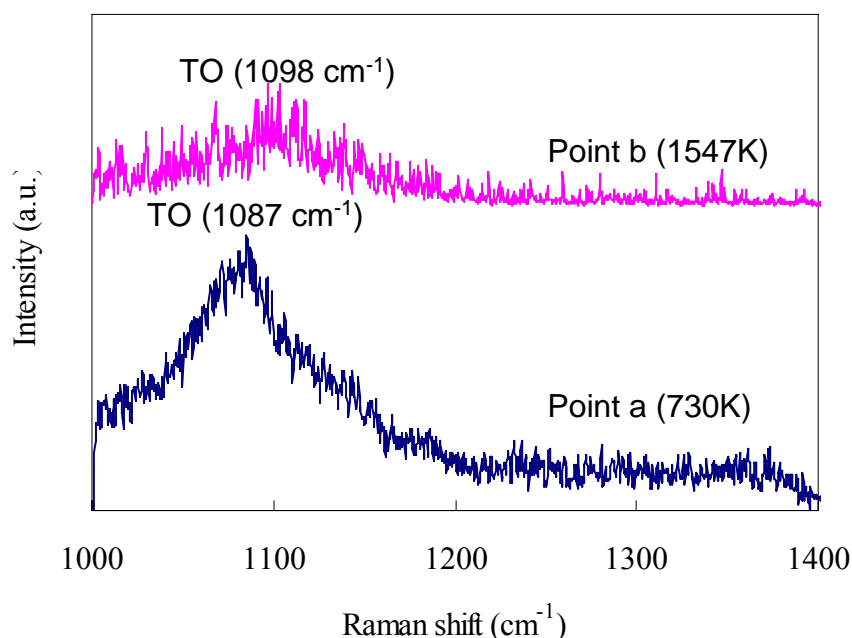


Figure 7.8. Raman spectra of *c*-BN detected in the region nearby the substrate

7.4 Conclusion

III-Nitride nanoparticles (e.g. boron nitride) have been produced by an inductively coupled RF plasma method, with *in-situ* Raman scattering identifying them as metastable *c*-BN. Our results indicate that for the nanoparticle aerosols of *c*-BN, there is a red shift in the Stokes Raman peaks with higher temperatures, similar to what we found for TiO₂ in the previous chapter. However, there appears to be conflicting experimental data for single crystal *c*-BN in the literature that shows an opposite trend. Perhaps this may be due to the difference between bulk single crystal and nanoparticles. Nonetheless, more study is needed.

References

¹ S.D. Tse, G. Sun, X. Liu, et al, Development of RE-Doped III-Nitride Nanomaterials for Laser Applications, Symposium D: Rare-Earth Doping of Advanced Materials for Photonic Applications, 2008 MRS Fall Meeting, December 1 - 5, Boston, MA.

- ² T. I. Shin, and D. H. Yoon, Growth behaviour of bulk GaN single crystals grown with various flux ratios using solvent-thermal method, *Cryst. Res. Technol.* 40, 9, 827 – 831 (2005).
- ³ E. D. Readinger, et al., GaN doped with neodymium by plasma-assisted molecular beam epitaxy, *Appl. Phys. Lett.* 92, 061108 (2008).
- ⁴ I.C. Huseby, Synthesis and Characterization of a High-Purity AlN Powder, *J. American Ceramic Society*, 66, 3, 217-220 (1983).
- ⁵ Y. Kai, et al., Synthesis of Low-Resistivity Aluminum Nitride Films Using Pulsed Laser Deposition, *Jpn. J. Appl. Phys.* 42, L229 (2003).
- ⁶ J. Yu, S. Matsumoto, Growth of cBN films by d.c.-bias assisted inductively-coupled r.f. plasma chemical vapor deposition, *Diamond and Related Materials* 12, 1903–1907 (2003).
- ⁷ J. Yu, S. Matsumoto, Controlled growth of large cubic boron nitride crystals by chemical vapor deposition, *Diamond and Related Materials* 12, 1539–1543 (2003).
- ⁸ T.A. Friedmann, P.R. Mirkarimi, D.L. Meddlin, K.F. McCarty, E.J. Klaus, D.R. Boehme, et al., *J. Appl. Phys.* 76, 3088 (1994).
- ⁹ D.J. Kester, R. Messier, Phase control of cubic boron nitride thin films, *J. Appl. Phys.* 72, 504 (1992).
- ¹⁰ K. Inagawa, K. Watanabe, H. Ohsone, K. Saitoh, and A. Itoh, *J. Vat. Sci. Technol. A* 5, 2696 (1987).
- ¹¹ H. Hofsass, C. Ronning, U. Griesmeier, M. Gross, S. Reinke, and M. Kuhr., Cubic boron nitride films grown by low energy B⁺ and N⁺ ion beam deposition, *Appl. Phys. Lett.* 67, 46 (1995).
- ¹² S. Mineta, M. Kolrata, N. Yasunaga, and Y. Kikuta, Preparation of cubic boron nitride film by CO₂ laser physical vapour deposition with simultaneous nitrogen ion supply, *Thin Solid Films* 189, 125 (1990).
- ¹³ H. Ltihtje, K. Bewilogua, S. Daaud, M. Johansson, and L. Hultman, Preparation of cubic boron nitride films by use of electrically conductive boron carbide targets, *Thin Solid Films* 257, 40 (1995).
- ¹⁴ A.R. Phani, S. Roy, V.J. Rao, Growth of boron nitride thin films by metal-organic chemical vapour deposition, *Thin Solid Films* 258, 21 (1995).
- ¹⁵ A. Bartl, S. Bohr, R. Haubner, and B.Lux, A comparison of low-pressure CVD synthesis of diamond and c-BN, *International journal of refractory metals & hard materials* 14, 1-3, 145-157 (1996).
- ¹⁶ F.-H. Lin, C.-K. Hsu, T.-P. Tang, P.-L. Kang, and F.-F. Yang, Thermal-heating CVD synthesis of BN nanotubes from trimethyl borate and nitrogen gas, *Materials Chemistry and Physics* 107, 115-121 (2008).
- ¹⁷ W. Dworschak, K. Jung, and H. Ehrhardt, Growth mechanism of cubic boron nitride in a r.f. glow discharge, *Thin Solid Films* 254, 65 (1995).
- ¹⁸ K.J. Liao, W.L. Wang, *Phys. Stat. Sol.* 147, K9 (1995).
- ¹⁹ H. Saitoh, T. Hirose, H. Marsui, Y. Hirotsu, Y. Ichinose, *Surf. Coat. Technol.* 39/40, 265 (1989).
- ²⁰ P. Scheible, and A. Lunk, *In situ* characterization of boron nitride layer growth by polarized FTIR reflection spectroscopy, *Thin Solid Films* 364, 1, 40-44 (2000).
- ²¹ P. Reinke, P. Oelhafen, H. Feldermann, C. Ronning, and H. Hofsass, Hydrogen-plasma etching of ion beam deposited c-BN films: An *in situ* investigation of the surface with electron spectroscopy, *J. Appl. Phys.* 88, 5597 (2000).
- ²² D. Mukherjee, A. Rai, and M.R. Zachariah, Quantitative laser-induced breakdown spectroscopy for aerosols via internal calibration: Application to the oxidative coating of aluminum nanoparticles, *Journal of Aerosol Science* 37, 6, 677-695 (2006).
- ²³ S. Maffi, F. Cignoli, C. Bellomunna, S. De Iuliisa, and G. Zizak, Spectral effects in laser induced incandescence application to flame-made titania nanoparticles, *Spectrochimica Acta Part B: Atomic Spectroscopy* 63, 2, 202-209 (2008).
- ²⁴ P.B. Mirkarimi, K.F. McCarty, and D.L. Medlin, Review of advances in cubic boron nitride film synthesis, *Materials Science and Engineering R: Reports* 21, 2, 47-100 (1997).
- ²⁵ Nemanich R. J., Solin S. A. and Martin R. M., Light scattering study of boron nitride microcrystals, *Phys. Rev. B* 23, 6348 (1981).
- ²⁶ R. Geick, C.H. Perry, G. Rupprecht, *Phys. Rev.* 146, 543 (1966).
- ²⁷ J. A. Sanjurjo, E. Lo'pez-Cruz, P. Vogl, and M. Cardona, *Phys. Rev. B* 28, 4579 (1983).
- ²⁸ O. Brafman, G. Lengyel, S.S. Mitra, P.J. Gielisse, J.N. Plendl, and L.C. Mansur, *Solid State Commun.* 6, 523 (1968).
- ²⁹ P. Huong, *Diamond Relat. Mater.* 1, 33 (1991).
- ³⁰ L. Vel, G. Demazeau, and J. Etourneau, Cubic boron nitride: synthesis, physicochemical properties and applications, *Mater. Sci. Eng. B* 10, 149 (1991).

-
- ³¹ T. Werninghaus, et al., Raman spectroscopy investigation of size effects in cubic boron nitride, *Appl. Phys. Lett.* 70, 958 (1997).
- ³² H. Herchen, and M. A. Cappelli, Temperature dependence of the cubic boron nitride Raman lines, *Phys. Rev. B* 47, 14193 – 14199 (1993).
- ³³ J. Liu, et al., Cubic-to-rhombohedral transformation in boron nitride induced by laser heating: *In situ* Raman-spectroscopy studies, *Phys. Rev. B* 51, 8591 – 8594 (1995).
- ³⁴ W.J. Zhang, et al, Deposition of large-area, high-quality cubic boron nitride films by ECR-enhanced microwave-plasma CVD, *Appl. Phys. A* 76, 953–955 (2003).
- ³⁵ W.J. Zhang, S. Matsumoto, Investigations of crystallinity and residual stress of cubic boron nitride films by Raman spectroscopy, *Phys. Rev. B* 63, 201 (2001).
- ³⁶ M. Venugopalan, and S. Vepřek, ed., *Plasma chemistry I Topics in current chemistry* (Springer-Verlag, 1980).
- ³⁷ P. Fauchais, ed., *First report on spectroscopic methods of temperature measurements*. IUPAC, Rep. of the committee on standards and measurements in plasma chemistry (Limoges Univers., 1980).
- ³⁸ K. Muraoka, and M. Maeda. *Laser-Aided Diagnostics of Plasmas and Gases*. Series in plasma physics (Institute of Physics Pub, Bristol, 2001).
- ³⁹ A. A. Ovsyannikov, and M. F. Zhukov. *Plasma Diagnostics* (Cambridge International Science Pub, Cambridge, UK, 2000).
- ⁴⁰ NIST Atomic Spectra Database, <http://physics.nist.gov>.
- ⁴¹ A.D. Alvarenga, et al, Raman scattering from cubic boron nitride up to 1600K, *J. Appl. Phys.* 72, 1955 (1992).

Chapter 8 Concluding Remarks

8.1 Review of results and conclusions

Spectroscopic laser-based diagnostics are utilized in flame synthesis of nanostructured materials for remote, non-intrusive, *in-situ*, spatially-precise measurements of important chemical and thermodynamic parameters. Whereas flame synthesis is promising, the combustion itself can be a complex process, combining detailed chemistry and transport, where characteristics are determined within milliseconds and influenced by numerous process variables. Laser-based diagnostics provide the local quantitative measurements to improve the understanding of the materials synthesis process. In our atmospheric-pressure studies, spontaneous Raman spectroscopy (SRS) is utilized to determine local gas-phase temperatures, as well as the concentrations of precursor/oxide species at specific locations of nanomaterials growth. Through the measurements, “universal” chemical and thermodynamic conditions for nanomaterial growth are extracted under different flame configurations. At low pressures, laser induced fluorescence (LIF) is employed to probe gas-phase temperatures and OH species concentrations in the synthesis of metal-oxide nanoparticles. Finally, Raman spectroscopy is employed, for the first time, to characterize nanoparticles *in-situ* in aerosol form during synthesis, for both flame and plasma processes.

8.1.1 Flame structure for nanostructure synthesis by SRS

Spontaneous Raman spectroscopy (SRS) is employed to determine the local gas-phase growth conditions for the synthesis of carbon nanotubes (CNTs) and zinc oxide (ZnO) nanowires in inverse diffusion flames (IDFs) and counterflow diffusion flames (CDFs).

Computations for the N_2 profile are used to improve the measurement calculations for other major species concentrations. The measurements are compared with computational simulation with detailed chemical kinetics and transport properties to get cross-validation of the flame structures. The relationship between the morphologies of synthesized nanostructures in both flame configurations and the measured local conditions is discussed. It is found that local conditions for CNT and ZnO growth and morphology can be translated in different synthesis flame configurations.

8.1.2 Flame structure for nanoparticle synthesis by LIF

Laser induced fluorescence (LIF) is employed to probe the gas-phase temperature profile and OH species concentration distribution in a low-pressure premixed stagnation flame used for oxide nanoparticle synthesis. The LIF results agree well with the computational simulation with detailed chemistry and transport, confirming that the flow field is quasi-1-D. By varying the synthesis parameters, LIF reveals that the application of uniform electric fields has virtually no effect on the flame structure, thus isolating the electrophoretic effect on particle transport. With precursor loading, there are minor changes in the temperature and OH concentration profiles, indicating the effect of the combustion of the metalorganic precursor.

8.1.3 *In-situ* laser diagnostics of nanoparticle growth in flame synthesis

In-situ Raman scattering system is developed and calibrated in a novel application to characterize particle crystallinity and phase conversion in nano-aerosols at high temperatures. The capability of the system is evinced in a nanoparticle-seeded jet diffusion flame at atmospheric pressure and a nanoparticle-synthesizing premixed

stagnation-point flame at low pressure. Gas-phase temperatures are correlated with particle Raman spectra in the study of the synthesis process from particle nucleation to crystallization. This technique is envisioned to be a promising technique as an online diagnostic for large-scale synthesis facilities.

8.1.4 *In-situ* laser diagnostics of energetic material growth in aerodynamically-assisted plasma synthesis

The robust design of the *in-situ* SRS systems is extended to characterize nanoparticles formed in an inductively-coupled RF plasma. The crystallinity process in the post-plasma synthesis region is shown to be favorable for the synthesis of the metastable *c*-BN nanoparticles. Temperature measurements are performed by N₂ SRS and emission spectroscopy in the post-plasma region.

8.2 Suggestions for future work

In-situ Raman spectroscopy has been demonstrated for its unique advantages to diagnose nanoparticles (TiO₂, Al₂O₃, and *c*-BN) in a variety of reactive flow environments. Presently, this technique has not been extended to CNTs, which are only characterized by Raman spectroscopy *ex-situ*. Several advancements of Raman spectroscopy have appeared in CNT research, namely, stimulated Raman scattering, SERS, and the potential for *in-situ* development should be explored. By selecting suitable excitation laser wavelengths, different types of CNT (i.e., conducting or semi-conducting) can be identified during the synthesis process. Some preliminary work on Raman scattering of single-wall carbon nanotubes (SWNTs) is given in the Appendix A.

Along with temperature and OH concentration profiles, LIF from the diatomic precursor monomer molecules (e.g. AlO, SiO) can provide further information on

nanoparticle formation. LIF techniques can also be extended to 2D, named planar laser induced fluorescence or PLIF. Other laser diagnostics can be used to study other nanoparticle properties, such as using the Stokes/anti-Stokes Raman intensity ratio to determine the nanoparticle temperatures, which may be different than the gas-phase. Laser-induced breakdown spectroscopy (LIBS) for particle composition and laser-induced incandescence (LII) for nanoparticle size can also be utilized in our systems.

In the previous study, premixed flat flame was utilized because low operating pressures and low flame temperatures significantly reduce the particle residence time and inter-particle collisions, which will reduce both aggregate and primary particle sizes. Several diffusion flames (inverse diffusion flame, counterflow diffusion flame) are favorable because, when burning stoichiometrically, the flame speed and cellular stabilization problems related to premixed flames are avoided. It can be proposed that a burner-generated, steady, spherically symmetric diffusion flame can be used for flame synthesis study. We have demonstrated that by issuing air from a spherical burner into a low-pressure, low-molecular-weight, fuel environment, a nearly 1-D spherical flame with weak buoyancy can be realized. By controlling the temperature profile, a cooled substrate would not be needed for particle nucleation. Moreover, the divergent flow in such a flame would minimize particle agglomeration. Preliminary work on examining this flame structure is given in Appendix B.

Appendix A

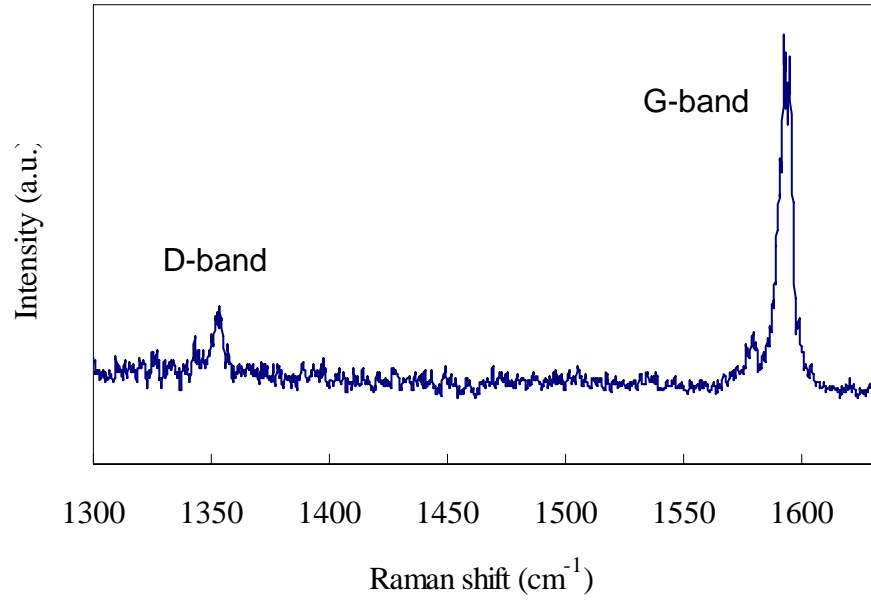
Resonance Raman Spectroscopy Characterization on Single-Wall Carbon Nanotubes (SWNT)

Using the Raman system and the glass slide sampling configuration for nanopowder *ex situ* characterization, single wall carbon nanotubes (SWNT) produced during flame synthesis process in our lab are characterized. The laser excitation wavelength is 532 nm (2.33 eV) from a pulsed Nd:YAG. SWNTs demonstrate both metallic and semiconductor properties as a result of the different electronic structure related to the helical arrangement of the ring structures and the tube radius. By exciting the molecule with an excitation wavelength corresponding to the electronic transition of the nanotube, resulting in Resonance Raman Scattering, information on the structure of the tube and tube radius can be obtained.

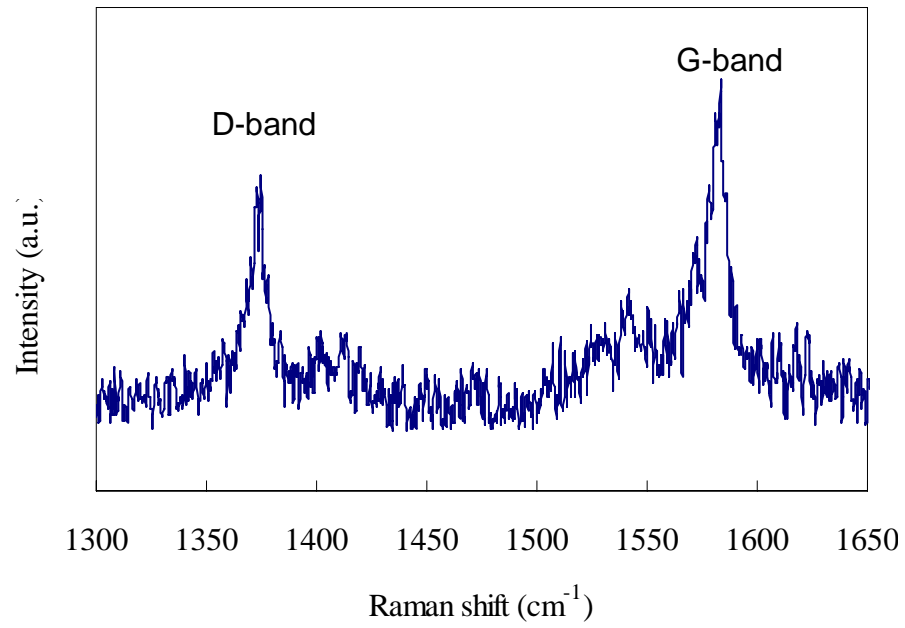
Due to the one dimensional structure of SWNT, distinctive Raman bands are found in many studies^{1,2,3,4}. Figure A.1 shows the Raman spectra of 2 samples, where three specific bands are observed, which is comparable with those in Ref. 5. G-type mode (or TM- Tangential Mode) near 1600 cm^{-1} corresponds to the graphite stretching mode. A Breit-Wigner-Fano (BWF) spectrum is observed for the lower wavenumber range of the G-band, indicating a metallic carbon nanotube. The D-band of the SWNT spectrum is often utilized for the evaluation of the nanotube crystallinity. In addition, the band observed in the low wavenumber region of the spectrum is designated as the Radial Breathing Mode (RBM), which can be correlated with the stretching of the nanotube diameter, the peak position inversely proportional to the tube diameter. The diameter estimated by the peak position (279 cm^{-1}) is 0.82 nm using Equation A.1⁶:

$$\omega = 228 / D \quad (\text{A.1})$$

where D is the diameter of SWNT in nm, and ω the Raman shift in cm^{-1} .



a



b

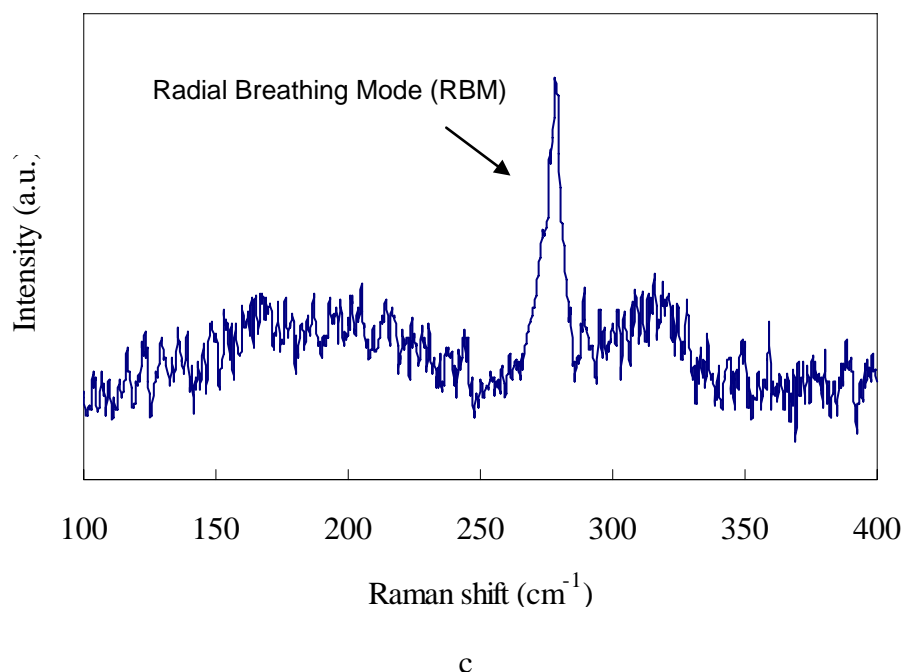


Figure A.1. Raman spectra of single-wall carbon nanotubes: a. G/D mode of sample 1; b. G/D mode and c. RBM mode of sample 2.

Like what we did for TiO_2 , our *in-situ* Raman technique can be developed to characterize CNTs during the catalytic aerosol synthesis method.

Reference

- ¹ M.S. Dresselhaus, G. Dresselhaus, R. Saito, and A. Jorio, Raman spectroscopy of carbon nanotubes, *Physics reports* 409, 2, 47-99 (2005).
- ² A. M. Rao, E. Richter, Shunji Bandow, Bruce Chase, P. C. Eklund, K. A. Williams, S. Fang, K. R. Subbaswamy, M. Menon, A. Thess, R. E. Smalley, G. Dresselhaus, and M. S. Dresselhaus, Diameter-Selective Raman Scattering from Vibrational Modes in Carbon Nanotubes, *Science* 275, 187 (1997).
- ³ A. Hartschuh, H. N. Pedrosa, L. Novotny, and T. D. Krauss, Simultaneous Fluorescence and Raman Scattering from Single Carbon Nanotubes *Science* 301, 1354 (2003).
- ⁴ M.S. Dresselhaus, G. Dresselhaus, A. Jorio, A.G. Souza Filho, and R., Saito, Raman spectroscopy on isolated single wall carbon nanotubes, *Carbon* 40, 2043-2061 (2002).
- ⁵ Jasco Inc., Carbon Nanotube Analysis by Raman Spectroscopy, *The Application Notebook, Spectroscopy Magazine*, September 2004.
- ⁶ A. Jorio, et al., Structural (n, m) determination of isolated single-wall nanotubes by resonant Raman scattering, *Phys. Rev. Lett.* 86, 1118-1121 (2001).

Appendix B

Laser Diagnostics Applied to Low-Grashof Nearly Spherical Inverse Flames

In this appendix, a burner-generated, steady, spherically symmetric diffusion flame is examined. By issuing air from a spherical burner into a low-pressure, low-molecular-weight, fuel environment, a nearly 1-D spherical flame with weak buoyancy can be realized. Furthermore, given the size of the flames produced, the structure can be probed at high spatial resolution. The 1D structure may have unique advantages in the flame synthesis of nanoparticles.

B.1 Background and objectives

A burner-generated, steady, spherically symmetric flame has been established to study the chemical kinetic mechanisms¹. This type of flame can be realized in the Earth's gravity by issuing air from the spherical burner into a low-pressure, low-molecular-weight, fuel environment. The advantages of the spherical flames include its simple aerodynamic structure, minimum buoyant distortion, extended dimension and thereby improved spatial resolution. The spherical flame has been experimentally studied for OH* and CH* chemiluminescent structures, which was compared with computational simulation in terms of the kinetics of formation of OH* and CH*. The current work uses OH LIF/PLIF to characterize the flame structure.

B.2 Experiment setup

B.2.1 Low-pressure chamber

Experiments are conducted in a low-pressure chamber under normal gravity, as shown in Figure B.1a. Here nitrogen-diluted oxidizer mixture is issued from a porous, bronze burner (20 μm pore diameter, 1.27 cm sphere diameter, Figure B.1b; custom ordered from GKN SINTER METALS (Auburn Hills, MI) and are carefully machined to be connected and supported by 1/16" tubing) into the low-density fuel (e.g. H_2) environment at chamber pressures of 0.1 atm. A stainless-steel capillary (1.5 mm o.d.) supported the burner and is situated horizontally. Frontal images therefore do not show the tube support or its possible distorting effects. The chamber is continuously supplied with fuel at very low velocity and ventilated to maintain constant pressure. Ignition is achieved by a high voltage spark discharge near the burner surface.

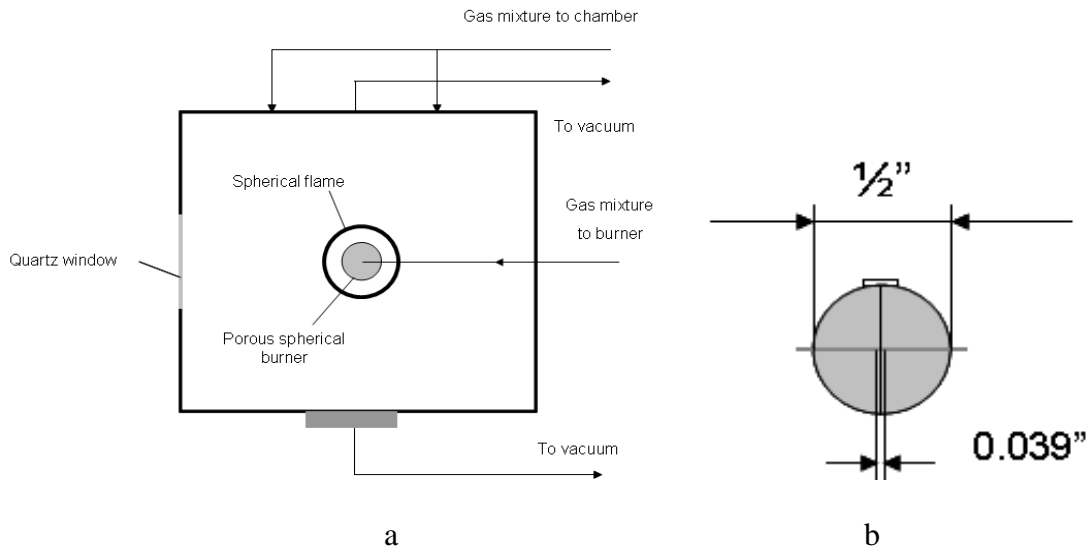


Figure B.1. a: Schematic of spherical inverse diffusion flame combustion apparatus. Inner dimension is $40 \times 40 \times 40 \text{ cm}^3$. b: Design of 1.27 cm spherical diameter porous, bronze burner.

B.2.2 LIF experiment setup

Laser induced fluorescence (LIF) has been conducted in the experiments to obtain the information for the temperature and OH concentration profiles. The setup of the *in-situ* diagnostics is same as that described in Chapter 5.

Modifications can be made to the LIF setup to get the capacity of 2-D OH distribution, namely planar-LIF (PLIF). The ultraviolet laser beam from the dye laser is reshaped into a planar sheet beam of 1mm thickness using a combination of a 50mm cylindrical lens and a 200mm convex lens. As in the LIF point measurement, $Q_1(7)$ is chosen to image the OH radicals by their fluorescent emission at the cross-section of the flame. The fluorescence signal is filtered with WG-305 and UG-11 color glass filters. To get maximum signal-to-noise ratio, an image gate width of 50ns is chosen for the ICCD camera.

B.2.3 Experiment procedure

The hydrogen flame is formed by issuing a 9% O_2 /91% N_2 mixture of mass flow rate 0.078 g/s from a 1.27 cm diameter bronze burner into a pure hydrogen environment at a chamber pressure of 0.079 atm. The hydrogen/methane experiments use the 0.635 cm diameter burner and involve issuing a 17% O_2 /83% N_2 oxidizer mixture at a mass flow rate of 0.024 g/s into a 19% H_2 /5% CH_4 /76% He environment at a chamber pressure of 0.1 atm.

The procedure to operate the spherical flame is listed as follows.

Setting up spherical burner:

- Upon coming to the setup, all of the gauges and readings should be off.

- There are separate lines for air, hydrogen, methane, cooling water, and electric charge all going into the chamber.
- The regulators should be fully open (no flow); the flow meter valve should be shut, as well as the rough valve and the fine tuning valve, which are downstream from the regulators. This should be the case for the hydrogen and air lines.
- For the methane line, the rough valve and fine-tuning valve should both be shut. The valve on the chamber for refilling it with air should be closed.
- DO NOT proceed with this setup until the above conditions are met.
- The first thing to do is connect the quick connect air hose to the air regulator, and turn the air supply on, then fully open the valve on the hydrogen and methane bottles.
- With the regulators on the hydrogen and methane bottles, dial the pressure to 20 psi and open the valves on the bottles.
- At this time, also turn on the water flow.
- Now the system is ready to go.
- First turn on the vacuum pump and evacuate the chamber and leave the pump on.
- Next you want to use the on board hydrogen regulator to let some hydrogen in to the setup.
- Open the flow meter valve for hydrogen FULLY and then the rough valve and finally the fine tune valve and try to get the flow to be about 4 cm so that the pressure in the chamber rises to about 3 inches Hg, which reads 27 on the gauge.
- Now you can let a little-bit of methane in, open the rough valve all the way and then use the fine tune valve to let the right amount of methane in, just enough to see the flame.

- Finally, turn the air regulator to let air in and then open the air flow meter fully and the rough valve and keep the fine valve closed.
- Get the sparker in one hand and use the other hand to let the air in.
- Gradually let air in and use the sparker until you see the flame at which point you let more air in to sustain the flame.
- If at any time it doesn't spark turn the air off to avoid making a mix of H_2 and air in the chamber.
- After you are done with the sparker, rotate it out of the way of the flame.
- Once you have a steady flame, you will probably notice that the pressure has gone up, this is because of the heat in the chamber.
- To remedy this, you can do a few things: decrease the methane flow, decrease the hydrogen flow, and open the vacuum valve more.
- Once you reduce hydrogen, you will also have to reduce the air too so the flame doesn't get too big, but make sure to keep the flame off of the burner so it doesn't heat it up too much.
- We want to keep checking things at this point, such as flow rates and pressure.
- If at any point, the burner becomes red colored, shut off the air immediately.
- If at any point anything goes wrong, shut off the air immediately.
- You can now vary the flows to get a desirable flame.

Shutting down the spherical burner:

- First thing is to shut off the airflow, the flame will go out.
- Next turn off the valve for the methane and the hydrogen and let the rest of the extra gas to be pumped out through the vacuum pump.

- Now you can open the regulators and shut the valves on the H_2 and CH_4 tanks, also open the regulator for the H_2 and turn off the rest of the valves and do the same for the methane.
- Once the methane and H_2 are evacuated, you can turn the air off from the source, and let the excess air be sucked out through the pump.
- Finally, turn off all the valves for the air, and turn off the vacuum pump.
- Open the valve on the chamber and let the air back in.
- Check to make sure all the valves are shut off and everything is in order the way it was at the beginning of this procedure.

B.3 Experiment results

B.3.1 Direct observations on the flames

Various types of flame are setup and recorded during the experiments. Keeping the chamber pressure at 0.1 atm, a pure hydrogen flame is observed after a spark ignition with a little methane. Increasing the methane into the hydrogen environment, one can see the blue flame evolve into a diffusion flame with two layers of luminous zone separated by a dark zone appeared, blue inside and green outside. Images in Figure B.2 show the three different type of flame produced in the experiments. The pure methane flame in c of Figure B.2 is very bright and its shape is obviously off spherical because methane is much heavier than hydrogen. In such an environment, the upward buoyant force is reduced, but the buoyancy of methane cannot be ignored. Similar phenomenon has also been observed in Ref.2.



Figure B.2. Spherical diffusion flames of different fuels. a) Pure hydrogen. b) Hydrogen/methane mixture. c) Pure methane

With those direct observations on the flames, systematic experimental trials are carried out to achieve spherical symmetry. Sphericity of the flame (defined as the ratio of the horizontal to the vertical diameters of the flame) and its concentricity (defined as the distance between center of the burner and bottom of the flame divided by half of the vertical diameter of the flame) can be measured..

The hydrogen/methane mixture flame is specially investigated because, although good consistency between experimental and computational data is observed for the pure hydrogen diffusion flame, an outward shift relative to the burner is apparent for the hydrogen/methane flame.

B.3.2 Temperature measurements by OH LIF

Ref. 2 used a K-type thermocouple for temperature measurement, including burner surface temperature and radial temperature profile in the flame. The method is inaccurate in that intrusive measurements required elaborate and always uncertain corrections. Laser induced fluorescence (LIF) can be employed to get *in-situ* temperature measurements.

The three kinds of spherical flames are investigated for the temperature distributions across the flame zone. Two-line OH temperature technique is used to attain the temperature of the local points at certain distance from the burner surface. Most of the points are selected at an interval of 2 mm, beginning at 1mm from the surface, up to 20mm from the surface. Only the downward direction of the hydrogen flame is measured considering its perfect radial symmetry, which results from the low buoyancy of the flame. The same scheme is used on the hydrogen/methane mixture flame. For the pure methane flame, the shape cannot be considered as spherical, so three directional measurements are made: vertical upward, vertical downward, and horizontal. (Note: the upward measurements are made every 5 mm since the flame is longer in this direction.

As can be seen from Figure B.4, the temperature peak extends outwards with the small mount of methane added into the hydrogen fuel. The peak positions also correspond to the luminous zone of the flame, where the most heat release occurs. From Figure B.4, the methane flame shows an egg shape resulting from the buoyancy.

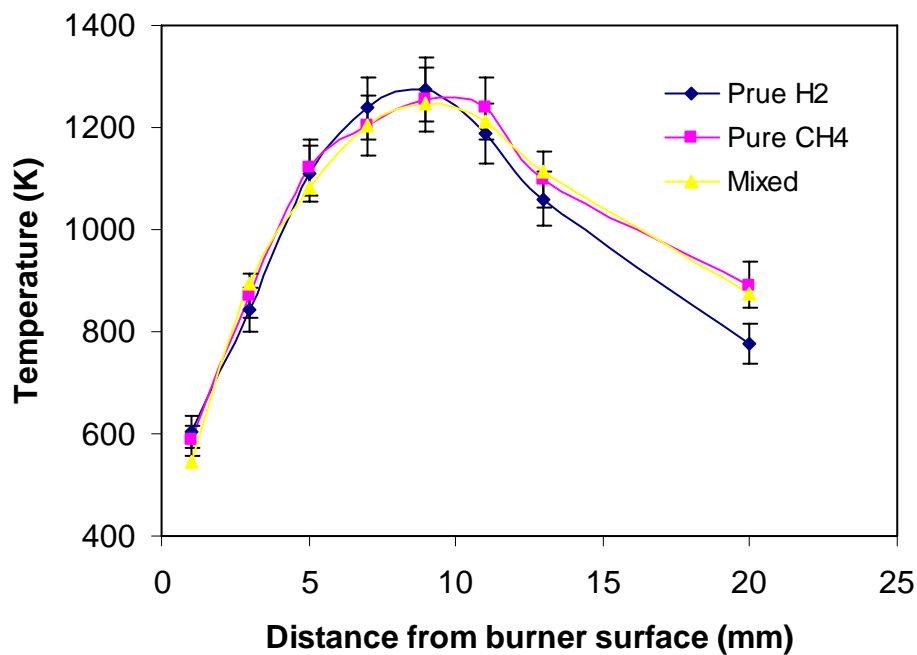


Figure B.3 Comparison of temperature profile along downward direction between three flames

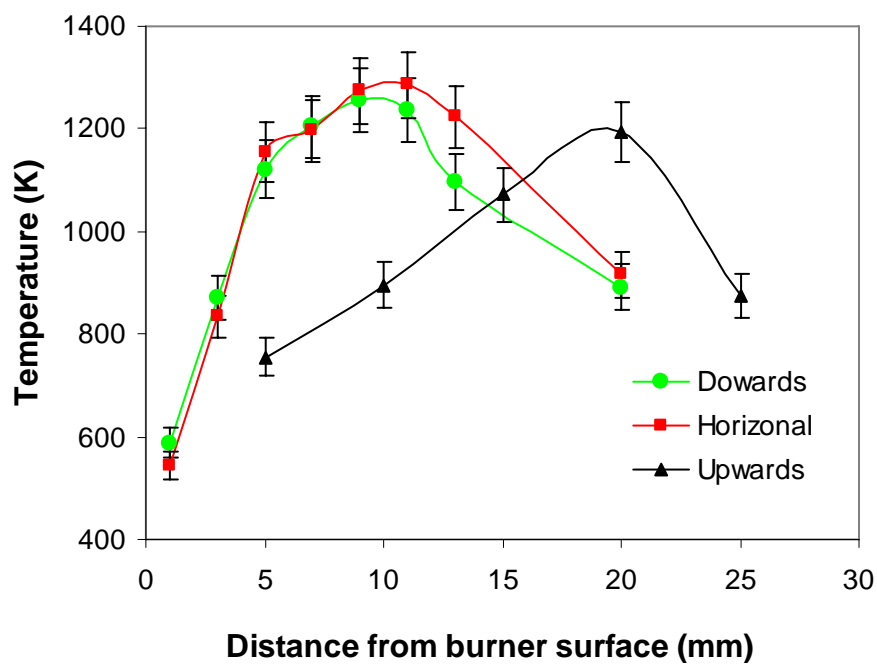


Figure B.4. Temperature distribution profile along three directions in the methane inversed spherical flame.

B.4 Conclusion

A weakly buoyant, almost spherical inverse diffusion flames is setup. LIF is applied for the first time to determine the structure of the chemiluminescent species OH (OH^*) in this flame. The results will be used to determine if such flames are a promising candidate for flame synthesis applications.

References

¹ C. J. Sung, D. L. Zhu, and C. K. Law, On Micro-buoyancy Spherical Diffusion Flames and a Double Luminous Zone Structure of the Hydrogen/Methane Flame, *Proc. Combust. Inst.* 27, 2559–2566 (1998).

² S.W. Yoo, C.K. Law, and S.D. Tse, Chemiluminescent OH^* and CH^* flame structure and aerodynamic scaling of weakly buoyant, nearly spherical diffusion flames, *Proc. Combust. Inst.* 29, 1663–1670 (2002).

Appendix C

Intensity Calibration of Raman Spectroscopy System

The Raman system includes a series of components. A typical Raman system is explained in detail in Chapters 2 and 4. The final spectrum recorded by ICCD camera is the result of all the individual components in the optical collection path, including transmission of optical elements, efficiency of diffraction gratings, the silicon quantum efficiency curve of the CCD detector elements, and pixel-to-pixel variation in CCD detector responsivity. Intensity calibration is required to compensate for the variations of the intensity transfer function of the spectroscopy system.

Intensity calibration involves tracing the system's response to a standard light source. The light source should be broad band with spectral radiance over a relatively wide dynamic range. A tungsten halogen light source (Ocean Optics, LS-1-CAL) is used to calibrate the absolute spectral response of the Raman system (picture shown in Figure C.1).



Figure C.1. Tungsten halogen light source (LS-1-CAL)

LS-1-CAL uses bulbs with a bulb life of 900 hours. Each lamp also features a 12 VDC regulated power supply. The lamps are effective in calibrating the absolute spectral response of a system from 300-1050 nm. It provides known absolute intensity values at several wavelengths, expressed in $\mu\text{W}/\text{cm}^2/\text{nm}$. The spectral output of the LS-1-CAL is shown in Figure C.2. Since the spectral intensity of the LS-1-CAL is traceable to the National Institute of Standards and Technology (NIST), it is specifically designed for calibrating the absolute spectral response.

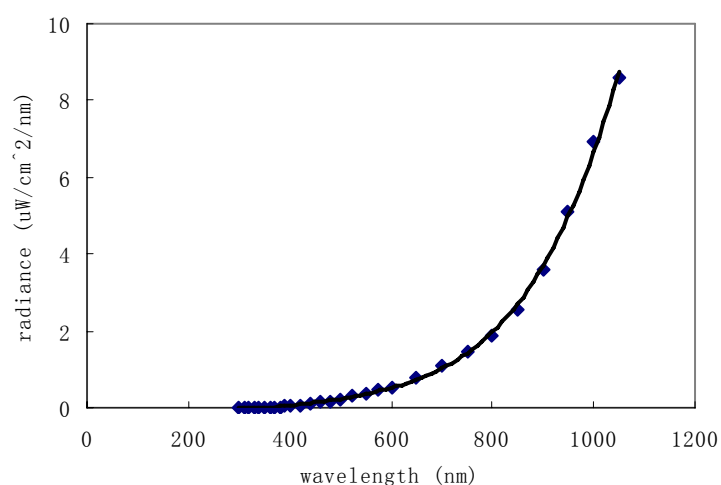


Figure C.2. Spectral Output of the LS-1-CAL

The calibration procedure is given here. The imaging spectrometer (Acton SpectrPro-2558, 500 mm, f/6.5) is equipped with 3 gratings, i.e., 150 g/mm (blazed at 500 nm), 600 g/mm (blazed at 500 nm), and 2400 g/mm holographic grating (David Richardson Gratings). The spectrograph is coupled to an intensified charged coupled device (ICCD, Princeton Instruments PIMAX 1300HQ, 1340×1300 pixels) as a detector. The optics setup, including a holographic notch filter, an image rotator, two achromat lenses, a

mirror, and a depolarizer, is used for collimating and focusing the lamp light to the entrance slit of the spectrograph. The wavelength calibration of the set up is performed using the Mercury-Argon lamp (Ocean Optics, HG-1).

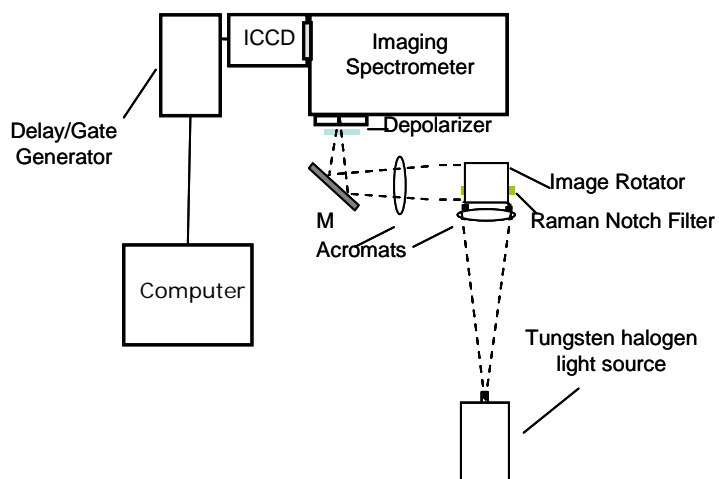


Figure C.3. The set-up used for calibrating the Raman system.

The lamp spectra are recorded using the spectrograph-ICCD. The raw data obtained with 150g/mm grating is given in Figure C.4.

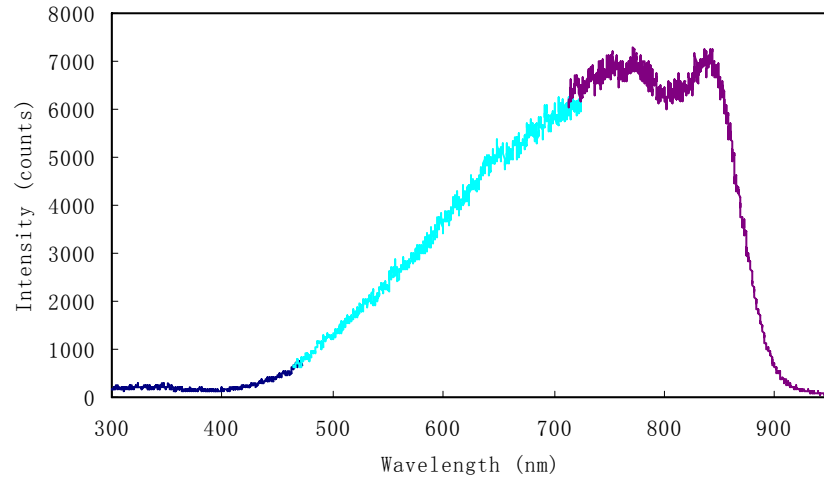


Figure C.4. The lamp spectrum recorded using 150 g/mm grating

Knowing the spectrum from tungsten halogen light source (indeed a Planck curve at around 3000 K), one can calculate the spectral responsivity function $F(\lambda)$.

$$I(\lambda) \bullet F(\lambda) = R(\lambda) \quad (\text{C.1})$$

$I(\lambda)$ is the spectral irradiance from the light source and $R(\lambda)$ is the measured response of the spectrograph. The function $F(\lambda)$ is then determined from the equation above. Figure C.5 shows the responsivity function determined in this manner for the 150 g/mm grating.

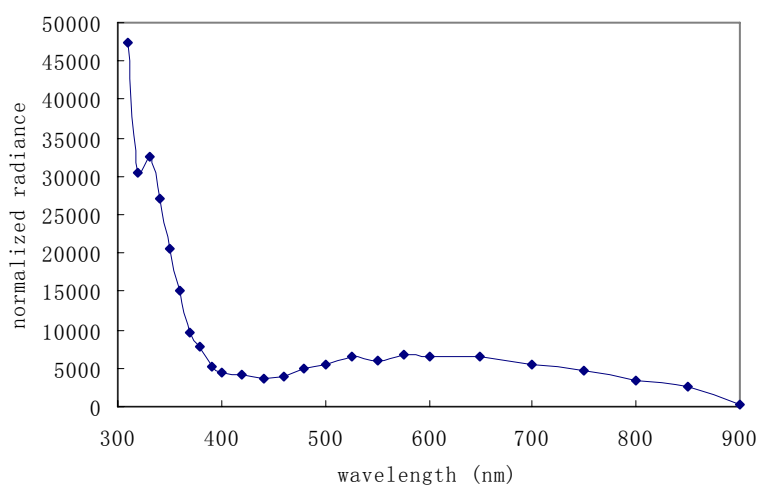


Figure C.5. Spectral response curve of Spectrograph + ICCD + 150g/mm grating.

For all the species measured with Raman spectroscopy, the detection wavelength range is between 550 nm and 700 nm. The spectral response curve (Fig. C.5) within this range is quite constant, which indicates no intensity correction is needed for the spectra of different species.

The spectral response of the Spectrograph and ICCD are not measured in the UV region due to the poor emissivity of the lamp in this region.

Appendix D

Standard Operation Procedure for Laser-Based Diagnostics

In this appendix, the standard operation procedure related to laser-based diagnostics research is listed for major instruments and experiments. The SOP should be carefully followed to ensure successful experiments. It is also very important to follow the safety procedures for the safety of the experimenters.

D.1 General Operation Procedure for Optical and Electronic Instruments

D.1.1 Nd:YAG Laser

Before experiment:

0. Keep the circulation nitrogen gas running;
1. Turn on the cooling water;
2. Turn on the laser power;
3. Turn on the Laser Enable button on the control panel;

After experiment:

4. Turn off the Laser Enable button on the control panel;
5. Turn off the laser power;
6. Turn off the cooling water.

D.1.2 Dye Laser

Before experiment:

0. Keep the circulation nitrogen gas running (Nd:YAG);

1. Turn on the cooling water (Nd:YAG);
2. Turn on the Dye circulator system;
3. Turn on the Dye laser power;
4. Turn on the Sirah Dye laser control software;
5. Turn on the Nd:YAG laser power;
6. Turn on the Nd:YAG laser Enable button on the control panel;

After experiment:

7. Turn off the Nd:YAG laser Enable button on the control panel;
8. Turn off the Nd:YAG laser power;
9. Turn off the Dye laser power;
10. Turn off the Dye circulator system;
11. Turn off the Sirah Dye laser control software;
12. Turn off the cooling water (Nd:YAG).

D.1.3 ICCD Camera/Spectrograph

Before experiment:

1. Turn on the ICCD Controller power;
2. Turn on the Spectrometer power;
3. Turn on the WinSpec/32 Software;
4. Turn on the cooling of ICCD camera;
5. Turn on ICCD camera;

After experiment:

6. Turn off ICCD camera;;
7. Turn off the WinSpec/32 Software;

8. Turn off the Spectrometer power;
9. Turn off the ICCD Controller power.

D.2 Raman and LIF Experimental Procedure

D.2.1 Raman

1. Turn on ICCD Camera/Spectrograph and configure proper experimental settings in software for specific applications. To be safe, keep minimum the signal light into ICCD camera to start the experiments;
2. Turn on lasers to excite gas or solid phase samples;
3. Collect signals onto ICCD camera. Keep CCD chips from saturation;
4. Turn off lasers when experiments are done;
5. Turn off the ICCD Camera/Spectrograph.

D.2.2 LIF

1. Turn on the dye laser;
2. Configure proper settings in Sarah software to tune the laser wavelength for specific experiments;
3. Collect signal onto ICCD camera. Keep CCD chips from saturation;
4. Turn off lasers when the experiment is done;
5. Turn off the ICCD Camera/Spectrograph.

D.3 Safety Procedures

D.3.1 Lasers

Keep the laser warning light shining during any laser operation. Make sure all other people are safe from unwanted laser beams. Don't look directly at the laser. Always wear a safety goggle during a laser experiment.

D.3.2 Dye

All the dye powder should be stored in dark glass bottle. Wear gloves when operating with the dye. Be careful not to sprinkle the powder or the solution when a dye solution is made. If this happens, clean the powder or the solution and wash the place with methanol. Always keep the dye circulation system running when the dye laser is on. Replace the dye every 3 months or less.

D.3.3 Gas cylinders

Make sure gas cylinders are closed when you finish the experiment. Fasten the bottles to avoid falling over.

D.3.4 Hazardous waste

Put hazardous waste you generate into secure containers and store them in SAA area in the lab. Don't just drop any waste into a sink or dustbin. Call REHS (732-445-2550) to remove the waste when the containers are near full.

Reference

¹Nd:YAG laser manual (Spectra-Physics Quanta Ray LAB-170)

²Sarah dye laser manual (Sirah PrecisionScan D-24)

³Imaging spectrometer manual CD (Acton SpectrPro-2558)

⁴ICCD camera manual (Princeton Instruments PIMAX 1300HQ)

Curriculum Vita

Xiaofei Liu

Education

Ph.D. Mechanical and Aerospace Engineering, October 2009
Rutgers University, Piscataway, NJ

M.S. Engineering Mechanics, July 2002
Tsinghua University, Beijing, China

B.S. Engineering Mechanics, July 2000
Tsinghua University, Beijing, China

Experience

2003-2008, Graduate and Teaching Assistant, Dept. MAE, Rutgers University, USA

1990-2002, Dept. DEM, Tsinghua University, Beijing, China

Publications

Liu X., Smith M., and Tse S.D., *In-Situ* Raman Characterization of Nanoparticle Aerosols during Flame Synthesis, submitted to *Applied Physics B* (2009).

Zhao, H., Liu, X., and Tse, S.D., Effects of Pressure and Precursor Loading in the Flame Synthesis of Titania Nanoparticles, *Journal of Aerosol Science*, in press (available online 6 Aug 2009).

Tse, S.D., Sun, G., Liu, X., *et al*, Development of RE-Doped III-Nitride Nanomaterials for Laser Applications, *Symposium D: Rare-Earth Doping of Advanced Materials for Photonic Applications*, 2008 MRS Fall Meeting, December 1 - 5, Boston, MA.

Zhao, H., Liu, X., and Tse, S.D., Control of Nanoparticle Size and Agglomeration through Electric-Field-Enhanced Flame Synthesis, Invited paper, *Journal of Nanoparticle Research* 10, 907-923 (2008).

Xu, F., Liu, X., Tse, S.D., Cosandey, F., and Kear, B.H., "Flame Synthesis of Zinc Oxide Nanowires on Zinc-Plated Substrates," *Chemical Physics Letters* 449 (1-3): 175-181 (2007).

Xu, F., Liu, X., and Tse, S.D., "Synthesis of Carbon Nanotubes on Metal Alloy Substrates with Voltage Bias in Methane Inverse Diffusion Flames," *Carbon* 44(3): 570-577 (2006).